Developing luminescence chronometers to establish the timing of late Quaternary environmental changes in South Africa

Debra Colarossi

Thesis submitted for the requirements of the

degree PhD

Aberystwyth University

January 2017

Abstract

The predominantly dryland climate of interior South Africa precludes the widespread preservation of organic proxy records. Various potential geoproxy records exist, but their exploitation requires accurately constrained chronologies. This study investigates the development of two luminescence chronometers, quartz OSL and K-feldspar post-IR IRSL. At four sites across the eastern interior (Moopetsi, Voordrag, St Paul's and Goedgedacht), these chronometers are used to constrain the timing of: (i) the late Quaternary initiation of deposition; (ii) intervening phases of erosion, deposition and pedogenesis; and (iii) the current deep erosional phase.

The value of using paired ages (i.e. determining quartz and K-feldspar ages from the same sample) becomes apparent, particularly at Voordrag where quartz OSL reaches saturation within the limit of radiocarbon dating. Paired chronologies show good agreement for younger samples (<24 ka) but systematic underestimation of quartz ages for older samples.

Investigation of the post-IR IRSL protocol showed that signal transfer between the L_x and T_x measurements caused systematic underestimation of older feldspar ages. Dose recovery tests showed that it was not possible to recover a large given dose (400 Gy) when using a small (5 Gy) test dose. Two solutions were investigated, specifically increasing the size of the test dose to ~30 % of the D_e value and increasing the IR stimulation time. This led to the development of a 'modified' post-IR IRSL protocol.

The derived quartz and K-feldspar single grain chronologies show that the initiation of deposition was not synchronous at the four study sites, and ranges from ~153 – 65 ka. Intervening phases of erosion, deposition and pedogenesis remain difficult to constrain but broad inferences regarding climatic and geomorphic drivers can be made. The current phase of deep erosion appears to be linked to two periods of abrupt climate change, the 3.8 – 4.2 ka arid event and the Little Ice Age.

Word count of thesis: 46736

DECLARATION

This work has not previously been accepted in substance for any degree and is not being concurrently submitted in candidature for any degree.

Signed: .....
Date: .....

STATEMENT 1

This thesis is the result of my own investigations, except where otherwise stated. Where **correction services* have been used, the extent and nature of the correction is clearly marked in a footnote(s).

Other sources are acknowledged by explicit references and a bibliography is appended.

Signed: .....
Date: .....

*this refers to the extent to which the text has been corrected by others

STATEMENT 2

I hereby give consent for my thesis, if accepted, to be available for photocopying and for inter-library loan, and for the title and summary to be made available to outside organisations.

Signed: .....
Date: .....

'Those who complete the course will do so only because they do not, as fatigue sets in, convince themselves that the road ahead is still too long, the inclines too steep, the loneliness impossible to bear and the prize itself of doubtful value.'

Thabo Mbeki

Acknowledgements

As with any journey, the experience is made all the richer by the people we meet on the way. My time spent in Aberystwyth pursuing my PhD studies (and travelling in the name of field work and conference attendance) has been immensely enjoyable but this thesis would not have been possible without the support of many people and organisations. For their generous financial support, I would like to thank the Aberystwyth University Doctoral Career Development Scheme, the Geological Society of South Africa (GSSA) Research Education and Investment fund, the Quaternary Research Association (QRA) New Research Workers Award, the British Society for Geomorphology (BSG) Postgraduate Research Grant and the Department of Geography and Earth Science (DGES) Postgraduate Discretionary Fund.

My supervisors, Geoff Duller and Stephen Tooth have been instrumental in my progress as a scientist, and my growth as a person over the last three years. Whether in the office or the field your advice, support and guidance have been invaluable. Thank you. Also Helen Roberts, not an official supervisor, but a fantastic unofficial one.

The members of the Aberystwyth Luminescence Research Laboratory for their support and understanding. Melissa Chapot (and Tom) for going above and beyond the duty of an office mate and friend, for amusing me and feeding me on the weekends, you're the reason I'm still sane. Hollie Wynne for everything from lab schedules to sorting out the kettle, you're my hero! Rachel Smedley for the feldspar coffee sessions, enjoyable and practical at the same time. Geraint Jenkins for all the general office chatter, because some days you just need to talk about the rugby.

My international cohort of friends for reminding me that there is life beyond a graduate degree. There are too many names to mention everyone but thank you for teaching me about your homes, your countries and your quirks. Thank you for sharing my journey and allowing me to be a part of yours. And thank you for all the coffees, chats, random train/bus journeys, movies, theatre productions and stimulating discussions.

Most importantly, to my parents for their long-distance support via frequent Skype sessions and for believing in me when I doubted myself. You have always done your best to help me through life and I would not have been able to finish this without the determination, focus and indefatigable work ethic that you taught me. Also to my gran, who was here for the start but not the finish.

And finally, this thesis was fuelled by coffee and chocolate, not always together and not necessarily in that order...

Contents

List of Figures

List of Tables

List of Abbreviations

α	Alpha
Ac	Actinium
Ar	Argon
β	Beta
BSS	Brown silty sand
BT	Black turf palaeosol
C	Carbon
^{14}C	Radiocarbon
Ca	Calcium
CAM	Central Age Model
CF	Channel fill
Cl	Chlorine
$\dot{D}$	Environmental dose rate
D_0	Characteristic saturation dose
D_e	Equivalent dose
D_α	Alpha dose rate
D_β	Beta dose rate
D_γ	Gamma dose rate
DRC	Dose response curve
DSE	Double saturating exponential
FGS	Field gamma spectrometry
FMM	Finite Mixture Model
γ	Gamma
GD	Given dose
GMBC	Geiger-Mueller beta counting
Gy	Grays
HCl	Hydrochloric acid
HF	Hydrofluoric acid
H_2O_2	Hydrogen peroxide
IEU	Internal External Consistency Criterion
IntCal98	International calibration curve
IR	Infrared
IRSL	Infrared stimulated luminescence

K	Potassium
ka	Kilo-annum (one thousand years)
LIA	Little Ice Age
LED	Light emitting diode
LGS	Lower gravelly sand
L_n	Natural luminescence signal
L_x	Regenerative dose luminescence signal
Ma	Mega-annum (one million years)
MAM	Minimum Age Model
MgO	Magnesium Oxide
MWP	Medieval Warm Period
N	Number of grains that passed acceptance criteria
n	Number of grains in a distribution
n_{sat}	Number of saturated grains
N_T	Total number of grains measured
OD	Overdispersion
OGP	Olive grey palaeosol
OIS	Oxygen Isotope Stage
OSL	Optically stimulated luminescence
Pb	Lead
Ph_{regen}	Preheat prior to the regenerative dose measurement
Ph_{test}	Preheat prior to the test dose measurement
Po	Polonium
post-IR IRSL	Post-infrared infrared stimulated luminescence
Ra	Radium
Rb	Rubidium
Rn	Radon
$t_{1/2}$	Half-life
Td	Test dose
Th	Thorium
TL	Thermoluminescence
TSAC	Thick source alpha counting
T_n	Test dose measurement for the natural signal
T_x	Test dose measurement for the regenerative dose
Rb	Rubidium
SAAD	Single aliquot additive dose
SAR	Single aliquot regenerative dose
SEM	Scanning electron microscope
SEPL	Single saturating exponential plus linear
ShCal13	Southern Hemisphere calibration curve
SPT	Sodium polytungstate
Sr	Strontium
SRZ	Summer rainfall zone

SSE	Single saturating exponential
SST	Sea surface temperature
U	Uranium
UGS	Upper gravelly sand
WC	Water content
WRZ	Winter rainfall zone
Y	Yttrium
years BP	Years before present
ZnS	Zinc sulphide

Chapter 1

Introduction

1.1 Quaternary research in South Africa

The Quaternary Period is the most recent geological time period (~2.58 Ma to present), during which modern humans evolved, and was characterised by a highly variable climate. Understanding environmental changes, particularly during the late Quaternary, is of great importance when attempting to reconstruct past and predict future climatically-driven land surface changes and direct anthropogenic impacts on the environment.

The reconstruction of Quaternary environmental changes within interior South Africa is hampered by the dominantly arid to semi-arid and highly seasonal climate, which largely precludes the accumulation and preservation of organic-based proxy records (Lyons et al., 2014; Meadows and Finch, 2016; Thomas and Burrough, 2012). This has resulted in a scarcity of long, continuous, robustly-dated palaeoenvironmental records to help reconstruct the nature, spatial patterns and forcing mechanisms of Quaternary climatic changes (Chase and Meadows, 2007). Several review papers covering various

aspects of proxy records within the interior of southern Africa are available (e.g. Chase and Meadows, 2007; Gasse et al., 2008; Singhvi and Porat, 2008; Thomas and Burrough, 2012; Thomas and Shaw, 2002) and these show that whilst a number of proxy records exist for shorter time spans, typically covering short periods during the last ~50 ka (e.g. Holmgren et al., 2003; Holzkämper et al., 2009; Neumann et al., 2010; Scott et al., 2012), only a few records span longer time periods (e.g. Partridge et al., 1997; Ziegler et al., 2013).

One set of potential proxy records, however, have been less well utilised. Palaeoenvironmental data can be extracted from *geoproxy* records, defined as spatially pervasive geomorphological landforms. Geoproxies can aid in the reconstruction of palaeoenvironments because their sedimentology, morphology and spatial distribution may have been controlled by past environmental changes (Thomas and Burrough, 2012). Geoproxies include features such as dunes (e.g. Holmes et al., 2008; Telfer and Thomas, 2006), palaeolake shorelines (e.g. Burrough et al., 2007), cave sediments associated with archaeological sites (e.g. Feathers, 2002; Jacobs et al., 2008a) and river deposits (Keen-Zebert et al., 2013; Lyons et al., 2014; Rodnight et al., 2005; Tooth et al., 2007). To date, however, dunes, palaeolake shorelines and cave sediments have been most widely investigated, whilst river deposits have been less well studied. Given that geoproxies offer the potential to characterise the landscapes in which early humans existed, they are of particular importance in southern Africa for understanding the relationship between climate change, human evolution and dispersal (Thomas and Burrough, 2012).

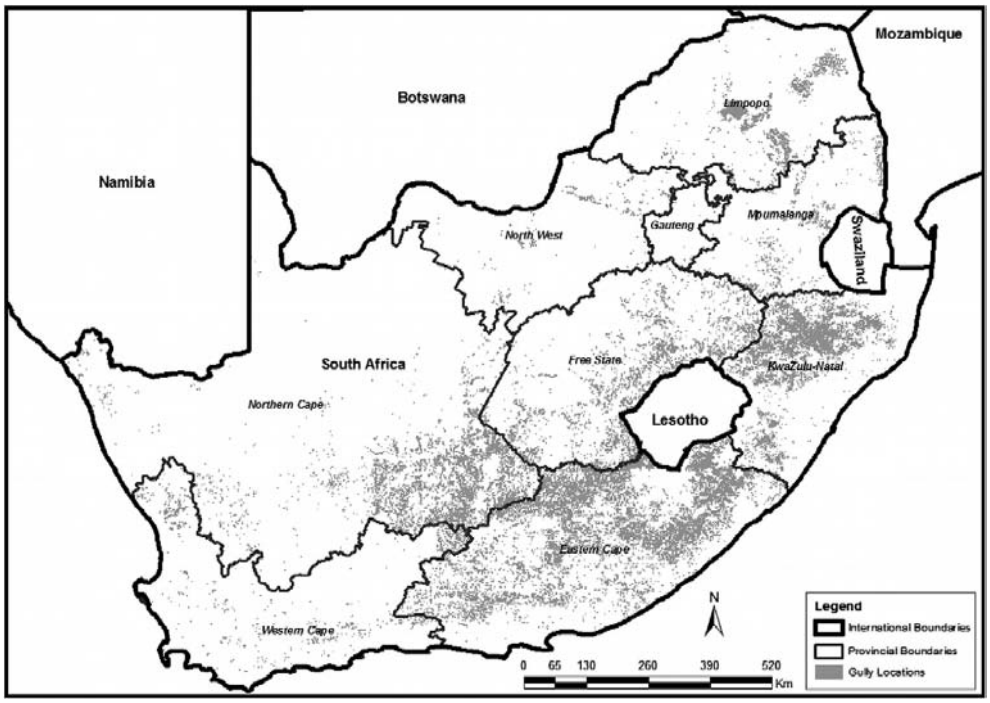

Figure 1.1: Map of South Africa showing the extent of dongas (gullies), reproduced from Mararakanye and Le Roux (2012).

Across the southern African interior, a large proportion of the land surface is characterised by dongas (extensive gullies and badland-type terrain, Figure 1.1). These erosional features provide access to a wealth of Quaternary sedimentary and archaeological records, but to exploit their potential the timing of their formation needs to be accurately constrained through appropriate dating techniques. Early work (e.g. Botha, 1996; Wintle et al., 1995a,b) used radiocarbon (^{14}C) and luminescence dating to constrain the timing of late Quaternary environmental changes, but subsequent developments in geochronology make this an opportune time to revisit previously dated sites. Furthermore, applying newly developed techniques more widely will result in better constraints on the timing and spatial expression of environmental change. This study will focus on improving the reliability of geoproxy chronologies by developing multiple

luminescence chronometers, to date four sites across the interior of South Africa and establish the timing of colluvial sedimentation during the late Quaternary.

1.2 Luminescence dating

Luminescence dating belongs to a family of radiometric dating techniques (Walker, 2005), and is based on counting the electrons trapped within structural defects and impurities in the crystal lattice, following exposure to ionising radiation. Electrons can be liberated from these traps to produce a pulse of light (a luminescence signal) using heat, in which case the signal is termed *thermoluminescence* (TL), or light, termed *optically stimulated luminescence* (OSL). In its application to sediments, the event being dated is not the formation of the mineral but rather the amount of time that the mineral has been storing radiation since it was last exposed to daylight (Figure 1.2), i.e. a burial age. The luminescence age equation (Equation 1.1) requires two values for the calculation, the laboratory equivalent of the amount of radiation stored within the crystal lattice during burial, termed the equivalent dose (D_e), and the amount of ionising radiation that the samples received during burial over a given period, the environmental dose rate ($\dot{D}$).

$$Age\,(ka) = \frac{Equivalent\ dose\,(Gy)}{Dose\ rate\,(Gy/ka)} = \frac{D_e\,(Gy)}{\dot{D}\,(Gy/ka)} \tag{1.1}$$

Numerous reviews have been written on the general principles of luminescence dating (e.g. Aitken, 1985, 1994; Duller, 2004; Prescott and Robertson, 1997; Preusser et al., 2008; Wintle and Murray, 2006) and also

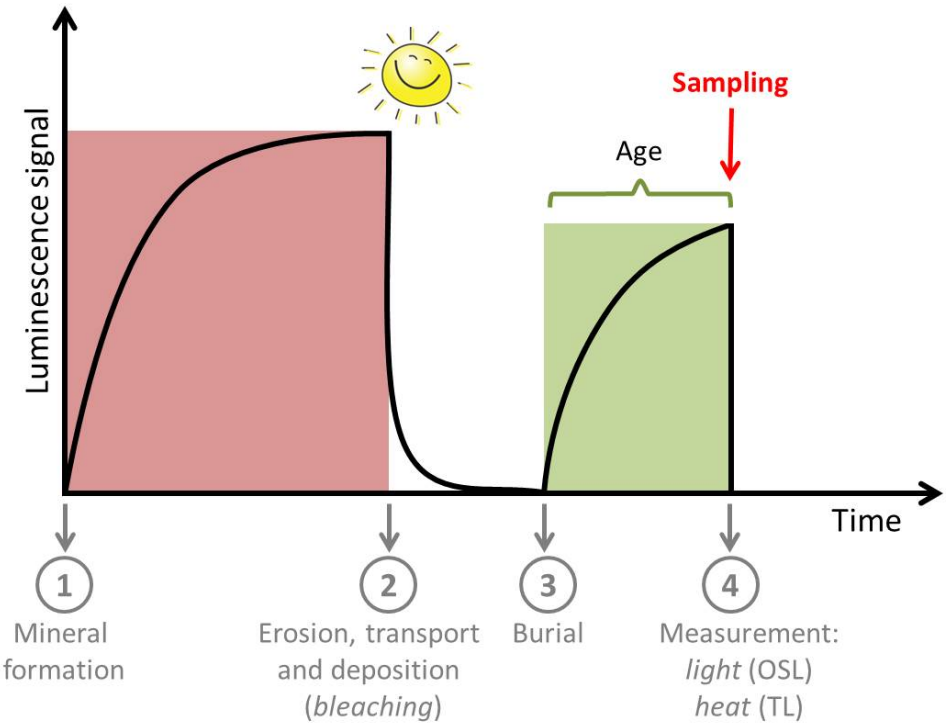

Figure 1.2: Schematic diagram of the event being dated by luminescence dating using unconsolidated sediment. Once buried (1) the sediment absorbs ionising radiation from the surrounding environment and the luminescence signal accumulates until the sediment is exposed to light during weathering and erosion (2). The traps are stimulated by sunlight and the stored charge released as energy, this is the *bleaching* process. After deposition, the sediments are buried once again (3) and removed from direct sunlight. The luminescence signal begins to accumulate until the time of sampling (4). The second (green) period between the bleaching event and sampling, provides the age determined by luminescence dating.

its application to specific environments, including fluvial (e.g Rittenour, 2008; Wallinga, 2002b), colluvial (e.g. Fuchs and Lang, 2009), dryland (e.g. Singhvi and Porat, 2008), coastal and marine (e.g. Jacobs, 2008) and glacial (e.g. Fuchs and Owen, 2008) environments. The dating of young (<1 ka) sediments has also been reviewed (e.g. Madsen and Murray, 2009), although no review paper focuses explicitly on the dating of old sediments (i.e. those near the maximum age limit of the technique).

The value of luminescence for dating geoproxies, lies in the ability to date constituent mineral grains of a sedimentary deposit or landform, as opposed to non-mineral matter incorporated within the deposit (i.e. organic material such as charcoal used in radiocarbon dating). This allows the timing of the formation of the sediment deposit or landform to be dated directly. Many natural materials are capable of behaving as luminescence dosimeters, such as biogenic carbonate (Duller et al., 2009; Stirling et al., 2012), apatite (Smith et al., 1986), zircon (Smith et al., 1986; Smith, 1988) and volcanic ash deposits (Berger and Huntley, 1994). However, the most widely available materials for luminescence dating in an environmental context, and the ones which form the focus of this study, are quartz and feldspar.

1.3 Quartz as a luminescence dosimeter

The mechanism responsible for the luminescence process in quartz is best described using the energy level diagram for non-conducting ionic crystalline materials (Aitken, 1998). In this model (Figure 1.3) electrons occur within discrete energy bands, specifically the valence and conduction

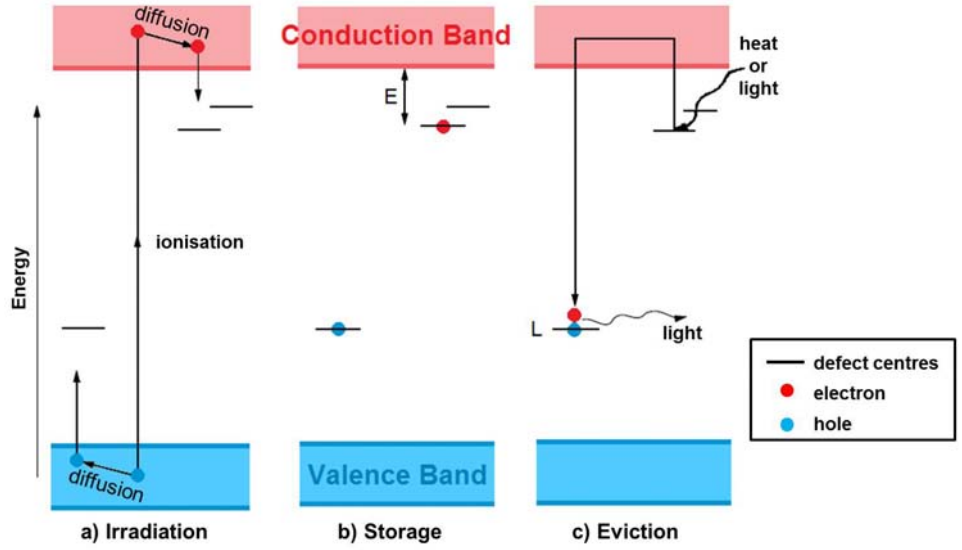

Figure 1.3: Energy-level diagram depicting the three stages of the luminescence process: (a) electrons are forced into the conduction band by ionising radiation, where (b) they become trapped within defects in the crystal lattice until (c) stimulation of the crystal with heat or light releases the trapped electrons which then recombine at luminescence centres (L) and emit a luminescence signal (redrawn from Duller (2008a), original in Aitken (1998)).

bands. Between these two bands lies the 'forbidden gap', where in perfect crystals electrons are not hosted. However, electrons can occur in this forbidden gap, when defects, such as impurities or missing atoms, are present within the crystal lattice. Ionising radiation from the surrounding environment can interact with the crystal, exciting an electron from the valence band to the conduction band (Figure 1.3(a)) and producing a hole or electron vacancy (Aitken, 1998). The electrons and holes move freely throughout the crystal, however if trapped in the defect sites, the energy will be stored in the crystal lattice temporarily (Figure 1.3(b)). In order to free the electrons from the traps, energy is required, with the amount of energy related to the depth of the trap below the conduction band. Thus the energy stored in deeper traps is more stable than the energy stored in

shallower traps, with the luminescence signal resulting from eviction of the more stable, deeper traps. Stimulation of the crystal with sufficient light or heat, results in eviction of the electrons (Figure 1.3(c)), and they are either trapped again or recombine with available holes to produce luminescence at recombination centres. The light emitted by this process is the luminescence signal.

1.3.1 The single aliquot regenerative dose (SAR) protocol

Whilst several techniques exist for using measurements of the luminescence signal of sedimentary quartz grains to calculate a D_e, the advent of the single aliquot regenerative dose (SAR) protocol of Murray and Wintle (2000) revolutionised OSL dating. This protocol uses additional OSL measurements to monitor sensitivity changes caused by laboratory treatment, by applying a fixed test dose after each OSL measurement (Figure 1.4). The SAR protocol comprises a series of cycles, the first of which measures the radiation accumulated in the sample during burial in nature (denoted by L_N, Figure 1.4). Each subsequent cycle measures the response of the sample (L_1, L_2, etc, Figure 1.4) after exposure to varying amounts of radiation in the laboratory; these are referred to as regeneration doses. The second part of each cycle sees the application of a fixed radiation dose (the test dose), which is measured (T_N, T_1, etc, Figure 1.4) and used to correct the preceding regeneration dose measurements for changes in sensitivity (L_N/T_N, L_1/T_1, etc). A graph of L_x/T_x as a function of the regeneration dose produces a dose response curve (DRC, lower panel of Figure 1.4) onto which the natural measurement (L_N/T_N, Figure 1.4) is interpolated to determine the equivalent dose (D_e).

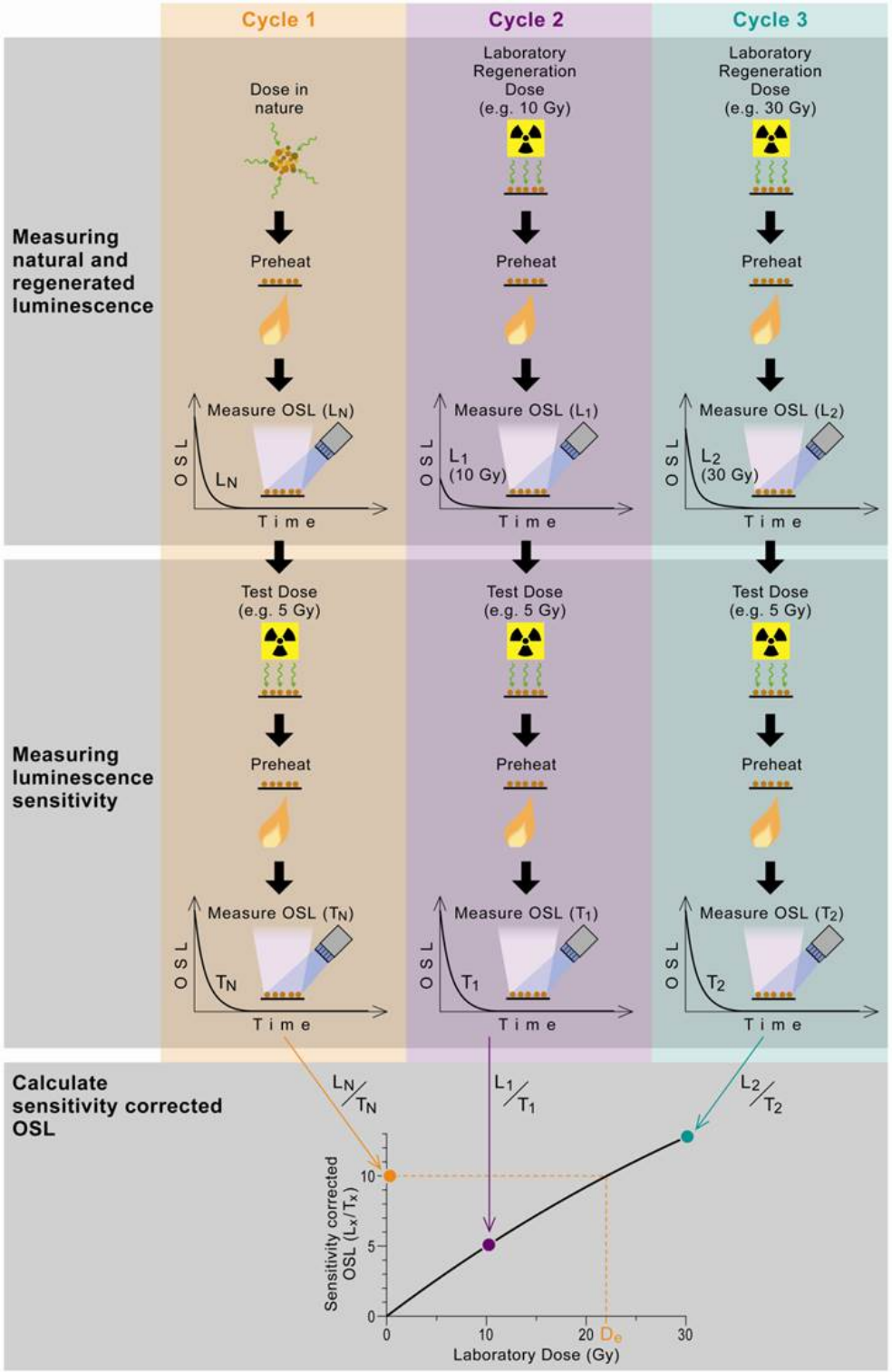

Figure 1.4: Schematic of the single aliquot regenerative (SAR) dose protocol applied to quartz (Duller, 2008a).

Since the early 2000s emphasis has been placed on the development of methods utilising quartz for OSL dating, and quartz has subsequently been shown to be a sensitive, reliable dosimeter (e.g. Wintle and Murray, 2006). Quartz does, however, have several limitations. In certain geological settings it is completely absent (e.g. selected volcanic terrains) and in others it may suffer from low sensitivity which limits its use as a dosimeter (Preusser et al., 2009; Thomsen et al., 2008). Furthermore, because sand-sized grains of quartz produce negligible internal radioactivity, they are particularly susceptible to changes in the environmental dose rate brought on by conditions such as fluctuating water content within a fluvial environment (Wintle, 2008). Yet the most pertinent limiting factor in terms of this study is that the fast component from the OSL signal, which bleaches rapidly and is used in the SAR protocol, saturates at a relatively low dose (Thomsen et al., 2008; Wintle, 2008), limiting the age range over which it can be used.

1.3.2 Saturation of the quartz OSL signal

The maximum age range of quartz OSL is determined by saturation of the electron traps, i.e. the point at which no additional charge can be stored within the crystal lattice. Also, because the age equation involves both D_e and $\dot{D}$, the calculated age is dependent on the dose rate. For example, if all electron traps available for dating are saturated with electrons after absorbing 200 Gy of radiation, the associated maximum age could lie anywhere between 50 ka and 400 ka depending on the environmental dose rate (typical dose rates ranging between ~0.5 Gy/ka and ~4 Gy/ka). Therefore, when considering the maximum limit of a luminescence dating

technique, it is more practical to consider the saturation dose as opposed to the maximum age.

Saturation of the quartz OSL signal can be determined from the DRC. In the simplest instance, where the OSL signal arises from a single trap, the DRC should be best fit by a single saturating exponential (SSE, Figure 1.5 (a)) function (Aitken, 1998). However, numerous studies have reported DRCs that are better described by the sum of a saturating exponential component and an additional component, such as a single saturating exponential plus linear (SEPL, Figure 1.5 (b)) function (e.g. Kim et al., 2009; Lowick and Preusser, 2011; Murray et al., 2008; Pawley et al., 2008; Roberts and Duller, 2004) and a double saturating exponential (DSE) function (e.g. Timar-Gabor et al., 2012). Thus, laboratory derived DRCs are typically described by either a SSE function (Equation 1.2), a SEPL function (Equation 1.3) or a DSE function (Equation 1.4)

$$I = I_{max}(1 - e^{-\frac{D+c}{D_0}}) \tag{1.2}$$

$$I = I_{max}(1 - e^{-\frac{D+c}{D_0}}) + gD \tag{1.3}$$

$$I = I_{max1}(1 - e^{-\frac{D+c}{D_{01}}}) + I_{max2}(1 - e^{-\frac{D+c}{D_{02}}}) + c \tag{1.4}$$

where I is the intensity of the luminescence signal for a given dose (D), I_{max} is the luminescence signal at saturation, D_0 is the characteristic saturation dose of the DRC and c is the signal intensity when no radiation energy has been absorbed. For the SEPL function, g describes an indefinite increase in luminescence signal with radiation dose that never saturates. For DSE functions, the two components may have different characteristic saturation doses (D_{01} and D_{02}).

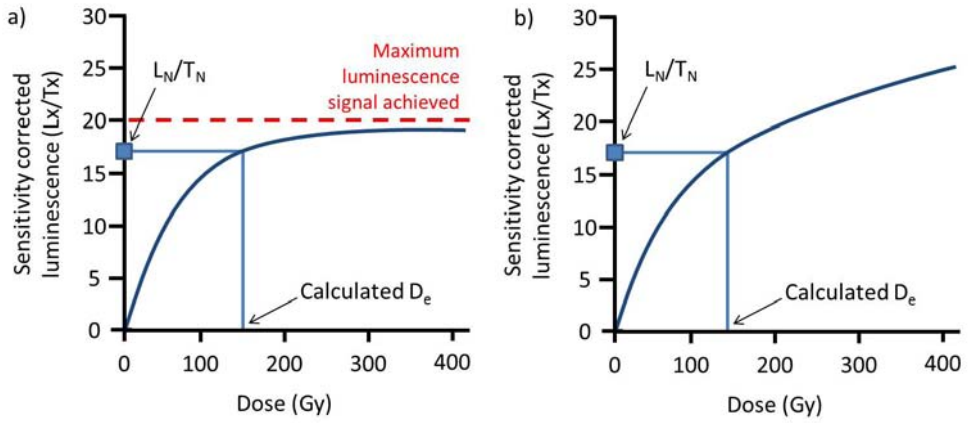

Figure 1.5: Schematic diagram showing dose response curves fit with a) a single saturating exponential (SSE) function and b) a single saturating exponential plus linear (SEPL) function (redrawn from Duller, 2008a).

A potential explanation for SEPL dose response is that the linear component is an early expression of the second saturating exponential, which has yet to begin saturating. This theory is supported by the observation of the SEPL function beginning to saturate at very high doses (~1 kGy Lowick et al., 2010b). DSE dose response could be explained by a second set of charge traps with a different saturation level (Berger and Chen, 2011; Lai et al., 2008) or grain specific saturation levels, which are averaged during multiple grain measurements and sufficiently well described by a DSE function (Roberts et al., 1999). Alternatively, the second saturating exponential could be a laboratory-induced component that does not exist in the natural signal (Lai, 2010). DSE dose response could also be a combination of these various factors.

Murray and Funder (2003) showed that on a non-linear growth curve the uncertainties associated with D_e values in the high dose region became increasing large and asymmetrical (Figure 1.6). This lead Wintle and Murray (2006) to suggest a maximum reliability threshold of $2D_0$ for dating (i.e. D_e

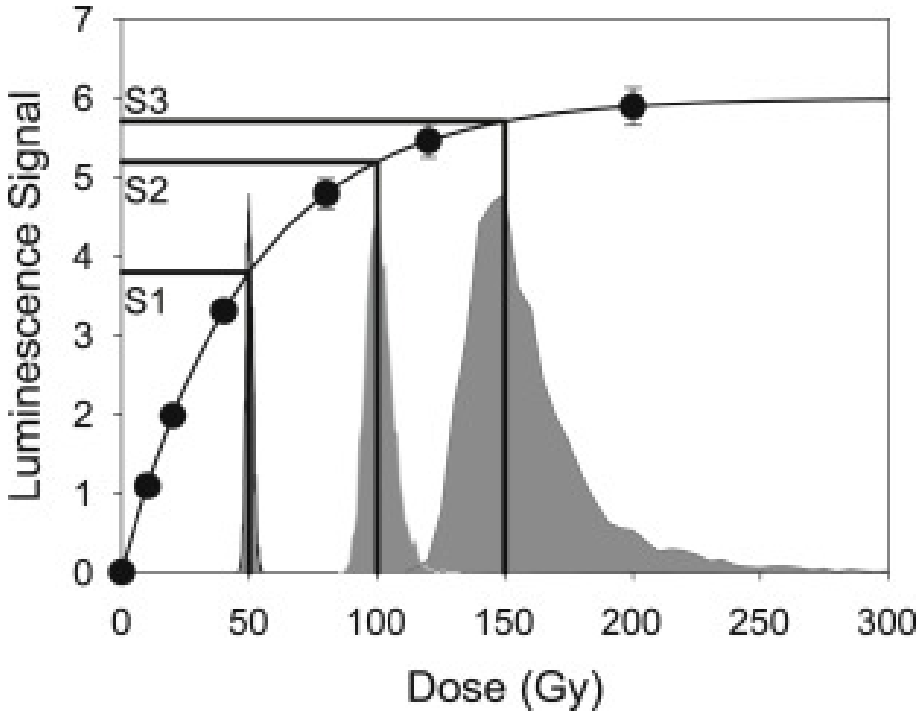

Figure 1.6: Simulation showing the impact of saturation upon the variability in D_e, and thus age, for a sample (Duller, 2016). Three different luminescence signal levels were simulated (S1, S2 and S3), which generated D_e values equal to D_0 (S1), $2D_0$ (S2) and $3D_0$ (S3). D_e distributions (4000 D_e values for each signal level) were simulated using a Monte Carlo process and are shown by the shaded areas. At $3D_0$ the scatter in D_e values becomes very large, and the distribution becomes asymmetric because of the shape of the dose response curve.

$< 2D_0$), when using the quartz OSL signal. The $2D_0$ limit corresponds to the amount of absorbed radiation necessary to fill ~85 % of the electron traps available for dating. Various D_0 values have been published for the fast component, ranging from 55 – 190 Gy (Wintle and Murray, 2006). This would equate to a maximum D_e of 110 – 380 Gy and a maximum age of 220 – 760 ka for a low dose rate (e.g. 0.5 Gy/ka) and 27.5 – 95 ka for a high dose rate (e.g. 4.0 Gy/ka). More recently, Chapot et al. (2012) observed a divergence between natural and laboratory DRCs at ~150 Gy

and cautioned that D_e estimates above this value should be considered as potential underestimations.

Our understanding of saturation of the quartz OSL signal is incomplete, and the resultant maximum age limit is therefore difficult to define. However, this is important because the majority of published luminescence ages for southern Africa are based on quartz OSL, for both geoproxy records (e.g. Carr et al., 2007; Chase, 2009) and archaeological sites (e.g. Feathers and Migliorini, 2001; Feathers and Pagonis, 2015; Jacobs et al., 2006b). Furthermore, the oldest ages for some of these sites coincide with the last interglacial (~130 – 115 ka), leading to uncertainty over whether this represents a climatic control on formation of these geoproxies or a maximum limit to quartz OSL.

1.4 K-feldspar as a luminescence dosimeter

Potassium-rich feldspar is a valuable alternative to quartz as a luminescence dosimeter because it offers an extended maximum age range. This is because the infrared stimulated luminescence signal (IRSL) for K-feldspar grows to larger doses than the quartz OSL signal (Figure 1.7), e.g. ~300 Gy (Porat et al., 2010), ~500 – 600 Gy (Li et al., 2014). K-feldspar also displays higher intrinsic luminescence sensitivity and thus offers an improved minimum detection limit (Thomsen et al., 2008). Unlike quartz, K-feldspar is sensitive to IR stimulation (~850 – 1000 nm), which allows for the direct targeting of feldspar during stimulation (i.e. without the need to consider quartz contamination) and the centring of the detection window over the main luminescence emission at ~400 nm (Huntley et al., 1991). Unfortunately,

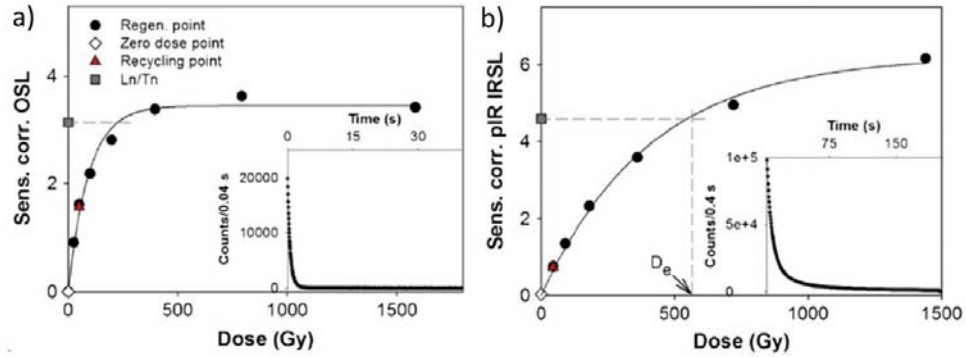

Figure 1.7: Dose response curves for a) quartz OSL and b) K-feldspar post-IR $IRSL_{290}$ (modified from Thiel et al., 2012).

K-feldspar has one major limitation, anomalous fading. Anomalous fading is defined as the decrease of the luminescence signal with storage time faster than expected based on trap depth and ambient temperature (Spooner, 1994; Thomsen et al., 2008; Wintle, 1973), and if uncorrected it can lead to age underestimation.

1.4.1 Anomalous fading

Anomalous fading occurs when electrons do not remain in the relevant defects even though kinetic studies show that they should be stable over geological time scales (Huntley and Lamothe, 2001). Thus, a signal which should be stable (based on the mean lifetime of electrons in the defect) for over 10^2 – 10^4 years at environmental temperatures, may be seen to fade over laboratory time scales (as electrons leave the defects within days or weeks). Anomalous fading is typically ascribed to quantum mechanical tunnelling, whereby electrons travel from traps to recombination centres without moving through the conduction band (Jain and Ankjærgaard, 2011; Kars et al., 2008; Spooner, 1994; Thomsen et al., 2008). To understand

anomalous fading, knowledge of the charge distribution and luminescence generation in K-feldspars is necessary.

The basic mechanics of quartz OSL (see Section 1.3) are broadly applicable to K-feldspar grains, but the key difference is that electrons trapped within the K-feldspar crystal lattice can recombine with luminescence centres via a number of different recombination routes. Poolton et al. (2002a,b) suggested that the IRSL signal was the result of electrons moving to a recombination centre via (i) localised tunnelling or (ii) transfer into a low-mobility band tail state beneath the conduction band. Jain and Ankjærgaard (2011) have developed a model for feldspar luminescence (Figure 1.8) in which a single dosimetric trap exists and where the localised donor-acceptor pairs are less stable and subject to different recombination routes (e.g. ground-state tunnelling) than the more stable, distant donor-acceptor pairs (which use more energetic band tail states). In this model, K-feldspar luminescence is dependent on the distance between the trap and the recombination centre (the donor-acceptor pairs).

1.4.2 The post-IR IRSL protocol

Two signals are typically used in luminescence dating of K-feldspar. The infrared stimulated luminescence (IRSL) signal uses a typical SAR protocol (see Section 1.3.1) to measure D_e, usually with the sample held at a low (50 °C) temperature during IR stimulation (e.g. Duller, 1991; Hütt et al., 1988). However, this signal is affected by anomalous fading. An alternative post-IR IRSL signal was established by Thomsen et al. (2008) in an attempt to address the issue of anomalous fading. They used a two-step stimulation approach, with a first IR stimulation at a temperature of 50 °C and a second

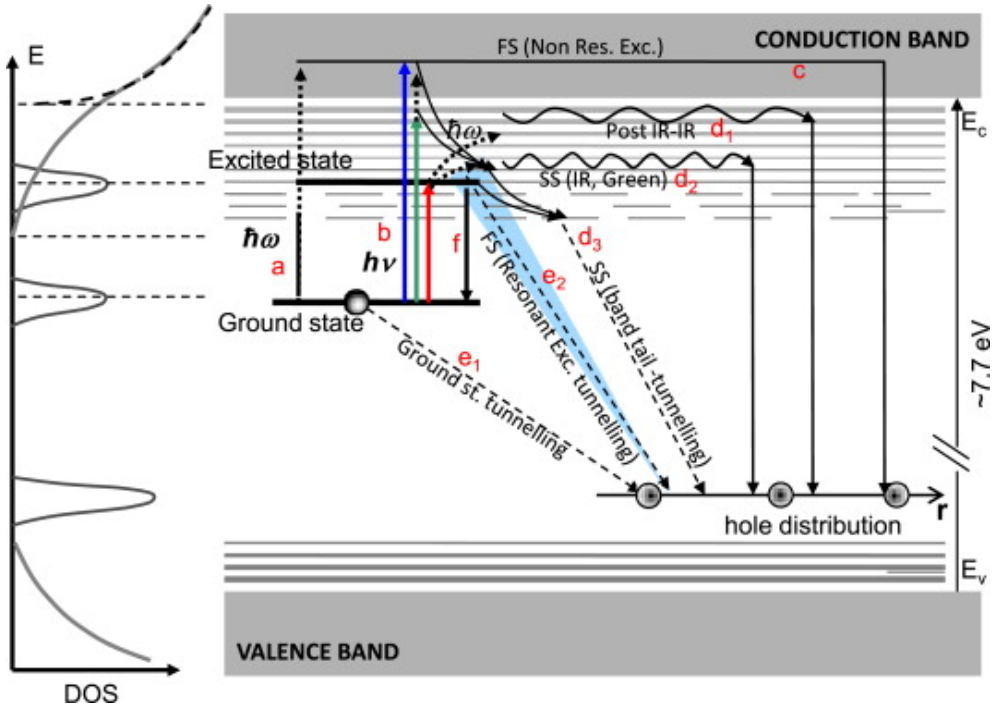

Figure 1.8: The schematic model of Jain and Ankjærgaard (2011) for feldspar luminescence. The distribution of the density of states (DOS, Poolton et al., 2002a, left) is shown alongside the band model with different transitions inferred from time-resolved OSL measurements (right). The various recombination routes are shown via thermal excitation (a), optical excitation (b), recombination through the conduction band (c), transitions through the band tail states (d), ground state tunnelling (e) and retrapping (f).

IR stimulation at a higher temperature (typically 225 °C to 290 °C) to access more stable traps, thereby reducing the apparent fading rate. Successful application of the post-IR IRSL protocol was reported by Buylaert et al. (2009) using a stimulation temperature of 225 °C (post-IR $IRSL_{225}$) and subsequently by Thiel et al. (2011) using 290 °C (post-IR $IRSL_{290}$). The post-IR IRSL protocol has been applied to a wide range of environments, from water-borne (e.g. Lowick et al., 2012) to aeolian (e.g. Roskosch et al., 2012) and will be used in this study to explore the dating of K-feldspars

from semi-arid environments to extend the age range beyond that available from quartz OSL.

1.5 Research aim and objectives

The aim of this research project is to explore and develop luminescence chronometers to establish the timing of colluvial/alluvial sedimentation during the late Quaternary in South Africa. This will be achieved by addressing the following objectives:

1. Investigate multiple luminescence chronometers (specifically quartz OSL and K-feldspar post-IR IRSL) and using paired ages to assess the ability of each chronometer to successfully date geoproxy records.

2. Extend the maximum age limit of K-feldspar post-IR IRSL dating by determining the measurement parameters which provide access to the most stable IRSL signal.

3. Obtain reliable chronologies using OSL and post-IR IRSL for four sites (Moopetsi tributary, Voordrag, St Paul's and Goedgedacht) across interior South Africa that represent a range of geological, climatic and vegetative conditions. The chronologies will be used to:

   (a) establish the timing of the initiation of sedimentation;

   (b) constrain the timing of intervening phases of erosion and sedimentation (cut-and-fill) and pedogenesis; and

   (c) constrain the timing of the cessation of the most recent phase of deposition and the onset of the current phase of deep incision, which has resulted in extensive donga formation.

4. Construct a revised time scale for late Quaternary landscape dynamics within South Africa and assess the possible driving factors (i.e. natural vs anthropogenic drivers).

1.6 Thesis layout

Chapters 1 to 3 will provide the context for this study. Chapters 4 to 7 will address objectives 1 and 2 (Section 1.5) and Chapters 8 and 9 will synthesise and summarise the results to address objectives 3 and 4 (Section 1.5).

Chapter 1 has outlined the need for accurate dating techniques in order to exploit the wealth of geoproxy records available within the interior of southern Africa. The basic mechanics of luminescence dating, using both quartz and K-feldspar, have been explained with particular attention paid to the determination of saturation of the quartz signal and the associated maximum age limit. A statement of the research aim and objectives has been made.

Chapter 2 will outline the sampling sites visited during this research project, including an explanation for their selection and a description of their geographical location, geology, geomorphology, climate and land use histories. A description and justification of the sampling strategy adopted at each site will be presented, as well as location data for each luminescence sample collected in this study.

Chapter 3 will describe sample collection in the field and the subsequent laboratory processing procedures, for both luminescence and dosimetry measurements. This will be followed by an explanation of the instrumentation and measurement parameters used during the luminescence measurements. The chapter will also explore the various techniques used to measure the dose rate, followed by an explanation of the calculation used to determine the total environmental dose rate.

Chapter 4 will outline the development of a K-feldspar chronology for the Moopetsi tributary site. It will investigate the bleaching rates of various signals, selection of an appropriate post-IR IRSL signal, and the effect of averaging of luminescence signals during multiple grain measurements to illustrate the value of using single grain measurements for heterogeneously-bleached sediments.

Chapter 5 will focus on the construction of a paired quartz-feldspar chronology for the Voordrag site using single grain measurements. The effect of saturation on the quartz OSL signal will also be investigated with respect to the paired K-feldspar ages and an extensive existing radiocarbon chronology.

Chapter 6 will focus on further refining the post-IR IRSL protocol for use in single grain dating. The development and application of a 'modified' post-IR IRSL protocol will be investigated.

Chapter 7 will present the single grain quartz and K-feldspar ages for both the St Paul's and Goedgedacht sites, based on the dating approach outlined at the end of the previous chapter.

Chapter 8 will examine the landscape development of the four sites investigated within the context of the paired single grain chronologies. A conceptual model for the timing of events will be presented for each site.

Chapter 9 will place the single grain chronologies obtained during this study into a wider geomorphological context through (i) an inter-site comparison and (ii) a broader comparison with other locations across South Africa.

Chapter 10 will summarise the main findings of this study as they relate to the aim and objectives presented in Chapter 1.

Chapter 2

Field sites and sampling strategy

2.1 Introduction

This chapter will introduce the sampling sites visited during this study, justifying their selection and providing context in terms of their geographical location, regional geology, geomorphology, climate and land use features (Section 2.2). This will be followed by an explanation of the sampling strategy employed to collect samples for luminescence dating at each site, within the context of any existing stratigraphy (Section 2.3).

2.2 Details of field sites

A typical feature of many fluvial (water-borne) and colluvial (hillslope) Quaternary sedimentary successions in South Africa is discrete layering. These layers typically differ in colour and grain size and locally may be separated by dark palaeosol units. In areas where dongas have formed,

these thick sedimentary successions are highly visible, which provides access to extensive records of sedimentation, pedogenesis and erosion during the mid-late Quaternary. To investigate these records, four field sites were selected from across the eastern interior of South Africa (Figure 2.1), to target a range of geological, geomorphological, climatic, vegetative and land use conditions. One of the objectives of this research project, as outlined in Chapter 1, is to establish the timing of sedimentation during the late Quaternary with particular focus on the initial pulse of sedimentation, the rate and timing of cut-and-fill sequences, and the timing of the most recent phase of incision. Therefore, during the site selection process, sites were prioritised based on a set of criteria, specifically: (i) an observable contact with the underlying bedrock; (ii) a stratigraphy characterised by multiple horizontal layers; and (iii) observable cut-and-fill sequences within the stratigraphy. Each of the selected sites offers access to individual donga systems with varied attributes, including their overall extent, length, surface geomorphology and complexity of preserved sediments.

2.2.1 Moopetsi tributary site, Limpopo

The Moopetsi River catchment is located in the Steelpoort region in the south of Limpopo Province. The catchment covers an area of ~228 km^2 and forms part of the Limpopo River catchment (Figure 2.2). Rivers within the catchment are typically deeply incised, many into bedrock, and dongas are commonly observed in alluvial and colluvial sediments. The underlying geology is comprised of the sedimentary Proterozoic Transvaal Supergroup (~2500 Ma) and the mafic Bushveld Complex (~2050 Ma). Extensive donga incision is visible in the sediments atop the Bushveld lithologies, with fewer

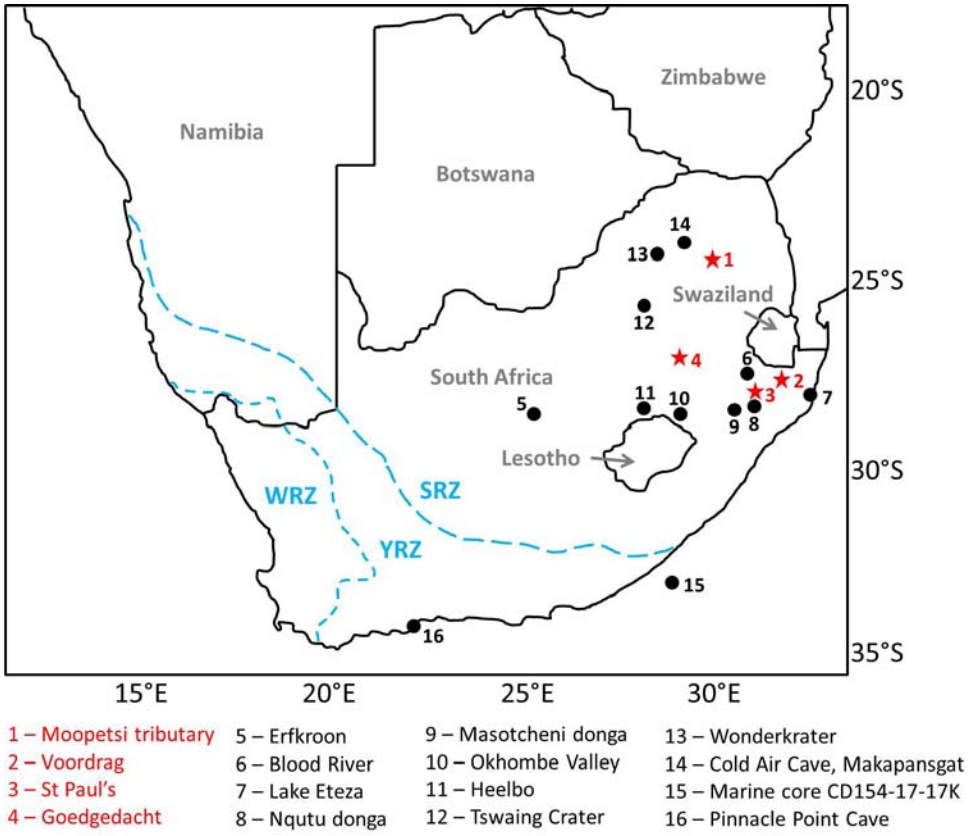

Figure 2.1: Map of southern Africa showing the location of the sample sites from this study (red) and other sites (black) used for comparative purposes in later chapters. The map also shows the present location of the winter rainfall zone (WRZ), the summer rainfall zone (SRZ) and the year-round rainfall zone (YRZ).

dongas apparent on sediments atop the Transvaal Supergroup lithologies (see stippled zone in Figure 2.2). The mountain ranges generally trend north-south and reach elevations of ~2000 m. The climate is semi-arid with most rainfall occurring during the summer months from October through March. Total annual precipitation is ~500 mm and annual potential evaporation ~2100 mm, leading to strongly moisture deficit conditions (Schulze, 1997; Wessels et al., 2007). Vegetation is typical of the savannah biome and is mainly composed of a grassy ground layer and an upper layer of woody

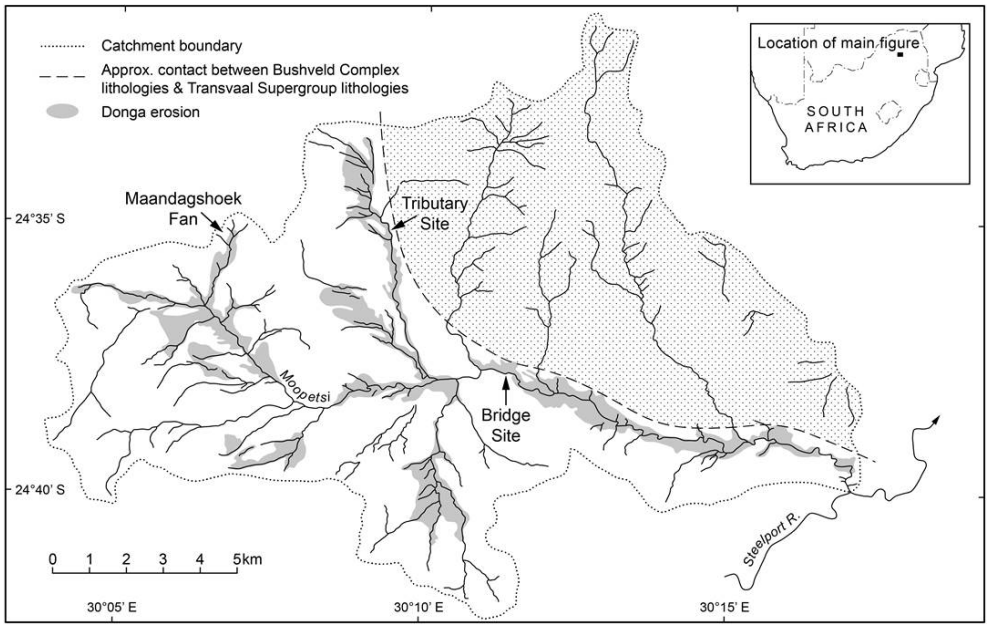

Figure 2.2: Location of the three sites within the Moopetsi River catchment, investigated by Lyons (2012). This study focused on the sampling site along the unnamed tributary of the Moopetsi River (modified from Colarossi et al., 2015).

plants (Mucina and Rutherford, 2006). Land use is split between subsistence agriculture, cattle ranching, commercial agriculture (e.g. tropical fruits, sunflowers, cotton, maize) and mining (e.g. platinum group metals, iron ore, chromium and dimension stone).

Along the Moopetsi River and its tributaries, dongas have eroded through the sedimentary succession into bedrock, thereby providing access to the basal sediments needed to ascertain the onset of sedimentation in the region. A recent quartz OSL chronology (Lyons, 2012) exists for this site, providing a basis for comparison with the K-feldspar chronology. The original samples collected and processed for quartz luminescence dating were stored at the Aberystwyth Luminescence Research Laboratory (ALRL) and thus were available for this research project. This allowed the K-feldspar fraction

used in this research to be extracted from the same sample as the quartz fraction used by Lyons (2012). This makes the Moopetsi site invaluable for paired quartz and K-feldspar luminescence dating because all other factors (e.g. dosimetry, sample collection, transportation, preparation, etc.) are constant.

Lyons (2012) identified three principal sites within the Moopetsi River catchment (see Figure 2.2). The Maandagshoek fan was subjected to detailed sedimentological and geomorphological analysis by Kendall (2000), but no chronology was determined. Unfortunately, this locality is not suited to luminescence dating as it is composed of material sourced from the Bushveld Complex. These ultramafic to mafic rocks include feldspathic pyroxenites, norites, anorthosites and associated chromitites. These lithologies are devoid of quartz, and while they have plagioclase feldspar in abundance, they contain virtually no K-feldspar (Cawthorn and Ashwal, 2009). The bridge site, located along the middle reaches of the Moopetsi River was ^{14}C dated using authigenic carbonates by Verster and van Rooyen (1999). The sediments here are derived from both the Bushveld Complex and Transvaal Supergroup, with exposures up to ~10 m visible in the succession. Samples collected by Lyons (2012) from this site, however, yielded minute (<0.05 g) quartz fractions for dating and so the site was abandoned. During the current research project, exploration for K-feldspar in the sediments from the bridge site yielded separates with such low K-contents (~1 wt% K) that the samples are also deemed unsuitable for IRSL dating. The tributary site (24°35′6″S 30°9′26″E) is located ~16 km north northwest of Steelpoort. As a consequence of its location close to the contact between the Bushveld Complex and Transvaal Supergroup, sediments are derived from

both lithologies thus giving sufficient quantities of quartz and K-feldspar for luminescence dating.

2.2.2 Voordrag, KwaZulu-Natal

The Voordrag donga site (27°44′30″S 31°19′24″E) is located in northern KwaZulu-Natal, 52 km east of Vryheid (Figure 2.3). The Mkuze River is located ~2.4 km to the north of the donga site and flows in an easterly direction, ultimately draining into Lake St Lucia on the east coast of South Africa. The ~18 m thick sedimentary succession, part of the Masotcheni Formation, sits on the lower transportational midslope of the northern face of the Ntumbane Hill (Clarke et al., 2003) and is underlain by Permian Vryheid Formation sandstone (Botha, 1996). Extensive incision has exposed a composite stratigraphy of stacked colluvial sedimentary units intercalated with palaeosols or splits of palaeosol horizons, as described by Botha (1996) and Clarke et al. (2003), but bedrock is not exposed in the central part of the donga. Of all the dongas investigated in this study, the Voordrag donga has the smallest areal extent and is located within a basin-shaped depression, giving it a unique geomorphological context.

The donga site, which used to be located on the farm Voordrag, is now located on communal land. Several homesteads are located in the immediate vicinity and the donga is being mined for building sand by the local populace. KwaZulu-Natal is located within a dry-subhumid zone and has a subtropical climate with summer rainfall. Mean annual precipitation is ~900 mm (Wessels et al., 2007) and mean annual potential evaporation is ~1900 mm (Lynch, 2004), resulting in a moisture deficit. Vegetation in KwaZulu-Natal is diverse, with subtropical indigenous forests along the

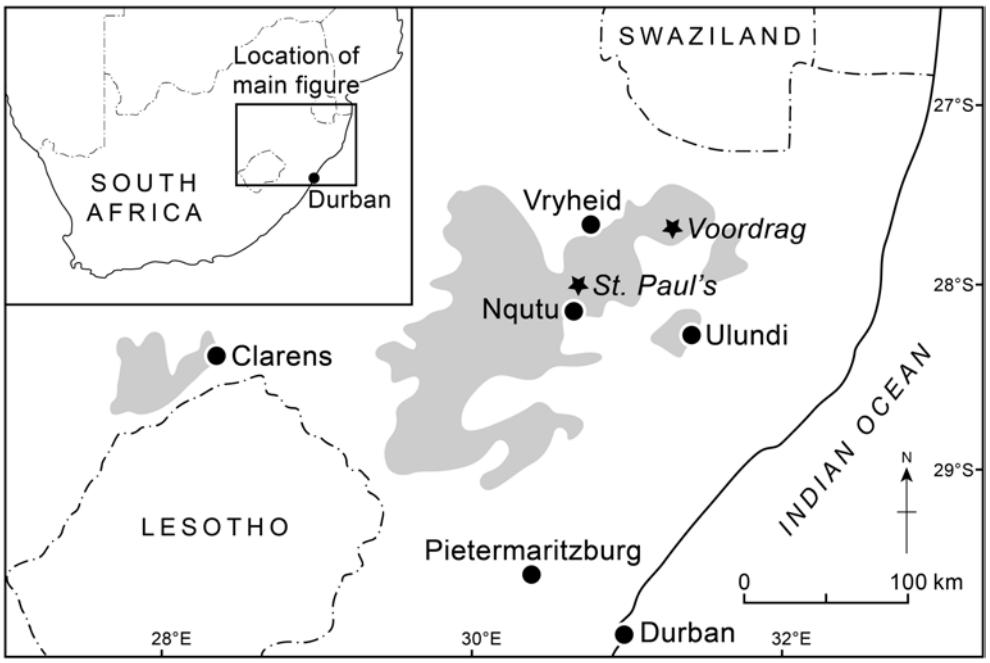

Figure 2.3: Location of the Voordrag and St Paul's donga sites in KwaZulu-Natal (redrawn from Botha et al., 1994). The shaded zone represents areas where the colluvial sediments of the Masotcheni Formation are widespread.

coastal regions and savannah and grassland covering the rest of the province. At Voordrag the vegetation tends towards the savannah biome, with a combination of low grasses and woody shrubs (Mucina and Rutherford, 2006). Land use in the north of the province is mainly given over to forestry (particularly around Vryheid) and game parks, with emphasis being placed on conservation and tourism (e.g. Hluhluwe-Imfolozi Game Park, Tembe Elephant Park) and local subsistence farming.

The Voordrag donga site was selected primarily due to existing chronologies, specifically IRSL and ^{14}C published by Botha (1996) and Clarke et al. (2003). The intercalated colluvial sediments and palaeosols allows for ^{14}C ages on the palaeosols to be used as independent age control for the luminescence ages obtained from the colluvial sediments. Furthermore,

recent advances in the measurement of luminescence ages from feldspar (i.e. the post-IR IRSL protocol) have provided a more stable signal that is less inclined to anomalous fading, and it seems prudent to test this new protocol against existing ages. Also, at the time of the original study, a reliable technique for correcting the sensitivity changes in the quartz luminescence signal had yet to be proposed, therefore quartz OSL was not considered a viable method for dating this site at that time. With the advent of the SAR protocol (Murray and Wintle, 2000), however, quartz OSL has become more reliable especially for young sediments. Hence, Voordrag is an ideal site to compare quartz OSL and feldspar post-IR IRSL methods. Finally, on a more practical note, the rapid erosion currently occurring at this site makes the collection of samples a priority if the site is to be subjected to reinvestigation.

2.2.3 St Paul's Mission, KwaZulu-Natal

The St Paul's site, which hosts the Dabekazi donga (28°5′54″S 30°40′42″E) is located in northern KwaZulu-Natal directly north of the settlement St Paul's Mission and 38 km southwest of Vryheid (Figure 2.3). The donga has formed on the east-facing slope of Telezeni hill and forms part of the Vumankala catchment, which is part of the larger Mfolozi River catchment. According to Botha (1996), the linear donga is ~1.5 km long and 5 – 150 m wide. Headward erosion over the last 13 years has increased the length of the donga by ~10 m, whilst the width across the widest part of the donga has increased to ~170 m. The sedimentary succession, named the Masotcheni Formation, overlies Permian Vryheid Formation sandstones and shales. St Paul's is located ~75 km southwest of Voordrag and so the regional climatic

conditions are similar. The only obvious difference is in vegetation type, as the St Paul's site tends toward a grassland biome dominated by a single layer of grasses and almost no trees (Mucina and Rutherford, 2006). This is likely due to the combination of grazing and annual burning of pastures.

Exposed in the sidewalls of the Dabekazi donga is one of the most complex and complete late Quaternary records of donga erosion, colluviation and palaeosol formation (Wintle et al., 1995a). For this reason, St Paul's was subjected to luminescence (IRSL) and radiocarbon dating during the 1990s (see Botha, 1996; Botha et al., 1994; Wintle et al., 1995a,b). As with Voordrag, given the advances in luminescence dating protocols over the last two decades, the St Paul's site was identified as an ideal location at which to apply the paired quartz OSL and K-feldspar post-IR IRSL dating approach. Furthermore, the Dabekazi donga has incised through the entire sedimentary succession and into bedrock. Unlike at Voordrag, there is access to the basal sediments, potentially enabling the timing of the onset of sedimentation in eastern South Africa to be determined.

2.2.4 Goedgedacht, Mpumalanga

The Goedgedacht donga site (27°11′48″S 29°20′30″E) is located on the farm Goedgedacht in Mpumalanga Province, ~29 km southeast of Standerton (Figure 2.4). The donga has formed along a right-bank tributary of the lower Klip River and is <6 km long and covers an area of ~4.5 km^2. The Klip River joins the Vaal River ~30 km downstream and forms part of the larger Orange River catchment system. The underlying geology is composed of generally flat-lying Permian sandstones and shales of the Karoo Supergroup that have

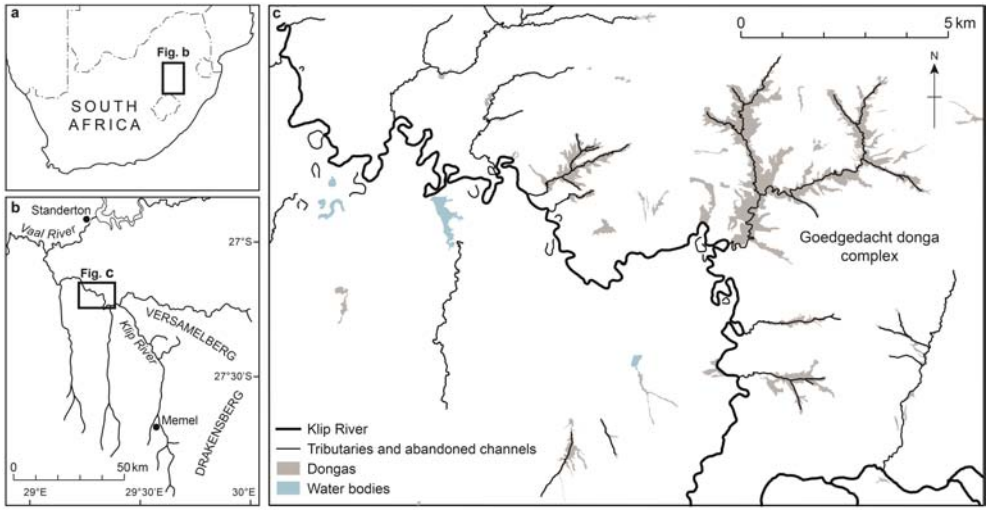

Figure 2.4: Location of the Goedgedacht donga in Mpumalanga showing the a) larger South African context and b) the lower reaches of the Klip River. Figure c) shows the extent of the Goedgedacht donga system and other nearby dongas.

been intruded by Jurassic irregular dolerite sills and dykes (typically ~5 – 20 m thick) (Rodnight et al., 2005).

Goedgedacht is located in a semi-arid region. A mean annual precipitation of ~600 mm (Wessels et al., 2007) and a mean annual potential evaporation of ~2100 mm (Lynch, 2004) results in a moisture deficit environment. Vegetation is typical grassland biome, dominated by a single layer of grasses and largely devoid of trees (Mucina and Rutherford, 2006). Land use is typically dairy and sheep farming and commercial agriculture (e.g. citrus, cotton, tobacco, wheat).

Goedgedacht is the only site investigated in this research project without an existing chronology. This previously unstudied site was investigated in order to apply the combined dating protocol determined using the Moopetsi tributary and Voordrag sites and tested at the St Paul's site. The donga has incised through a thick sedimentary succession (~14 m) and there are

several locations where the contact with the underlying bedrock is visible below cut-and-fill structures.

2.3 Sampling strategy

Each sampling site was characterised by thick sedimentary successions featuring numerous horizontal layers. During sampling, care was taken to focus sample collection to satisfy the objectives of the project, as follows:

1. To ascertain the timing of the initial pulse of sedimentation, the oldest (lowermost) sedimentary unit was sampled (Figure 2.5, Sample 1). Localities with a visible bedrock contact were prioritised and samples were collected ~30 cm above the contact between the bedrock and sediment to minimise complications arising from heterogeneous dose rates.

2. Cut-and-fill sequences were targeted by sampling on either side of the erosive contact when both units were comprised of sediment (Figure 2.5, Samples 2 and 4, and 7 and 8).

3. To determine the timing of the most recent phase of incision, the youngest sediments, (i.e. the uppermost horizon (Figure 2.5, Sample 9), and any sediment infill in the dongas (Figure 2.5, Sample 10)) were targeted for sampling. This dual approach allows the incision event to be bracketed, with the upper horizon offering a maximum age for incision and donga formation, while the sedimentary infill provides a minimum age for incision.

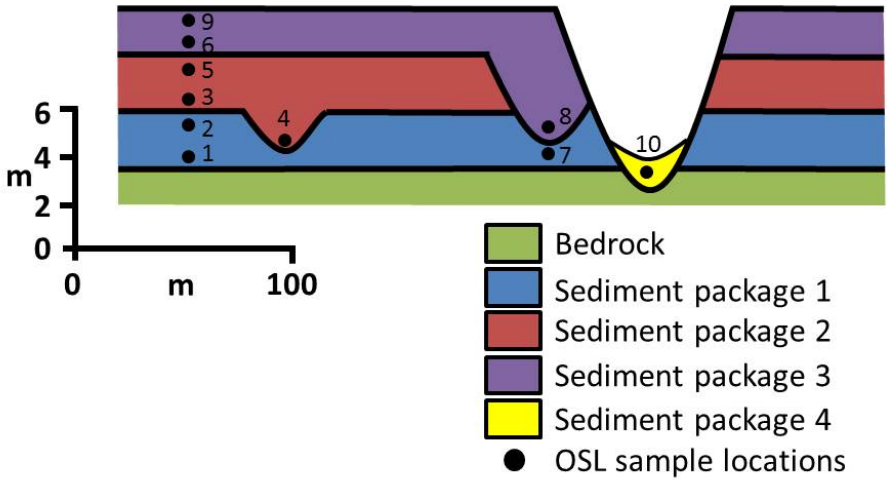

Figure 2.5: Schematic diagram depicting the general sampling strategy (modified from Tooth, 2015). Numbered samples provide the following age control: 1 = the onset of local deposition and a maximum limiting age for sediment package 1; 2 = minimum limiting age for sediment package 1 and a maximum limiting age for subsequent incision; 3,4 = maximum limiting age for locally renewed deposition (sediment package 2) and minimum limiting age for preceding incision; 5 = minimum limiting age for sediment package 2 and maximum age for subsequent incision; 6 = maximum limiting age for locally renewed deposition (sediment package 3) and minimum limiting age for preceding incision; 7 = maximum limiting age for incision; 8 = minimum limiting age for preceding incision; 9 = minimum limiting age for sediment package 3 and maximum limiting age for subsequent incision; 10 = maximum limiting age for most recent deposition and minimum limiting age for preceding incision.

2.3.1 Moopetsi tributary site, Limpopo

Sample collection at the Moopetsi tributary site was undertaken during July 2008 and 2009 and September 2010 by R. Lyons and S. Tooth from Aberystwyth University for the purpose of quartz OSL dating. The K-feldspar fractions used for this research were obtained from the sub-samples processed during the aforementioned study, therefore the following explanation of the sampling strategy is taken largely from the work of Lyons (2012).

The general stratigraphy for the Steelpoort region was established at the Maandagshoek fan and described by Kendall (2000) through the use of field reconnaissance, topographic surveys, stratigraphic logs and sampling of river bank and donga exposures. The general stratigraphy (Figure 2.6) is composed of: (i) the lower gravelly sand (LGS) unit overlying heavily weathered bedrock; (ii) the olive grey palaeosol (OGP) formed from weathered LGS sediments; (iii) the upper gravelly sand (UGS) unit; (iv) the black turf (BT) vertisol formed from weathered UGS sediments; (v) the brown silty sand (BSS) unit; and (vi) the minor channel fill (CF) unit which represents the youngest sediment within the stratigraphy. The present channel has incised through the entire succession and into bedrock, with dongas eroding headward from steepened channel banks. The CF unit is representative of a minor phase of aggradation that followed the initial incision phase (Lyons, 2012).

Lyons (2012) collected samples from each major sedimentary unit, with particular focus on the upper and lower contacts of the LGS, UGS and BSS. This sampling strategy was designed to establish the timing of the onset

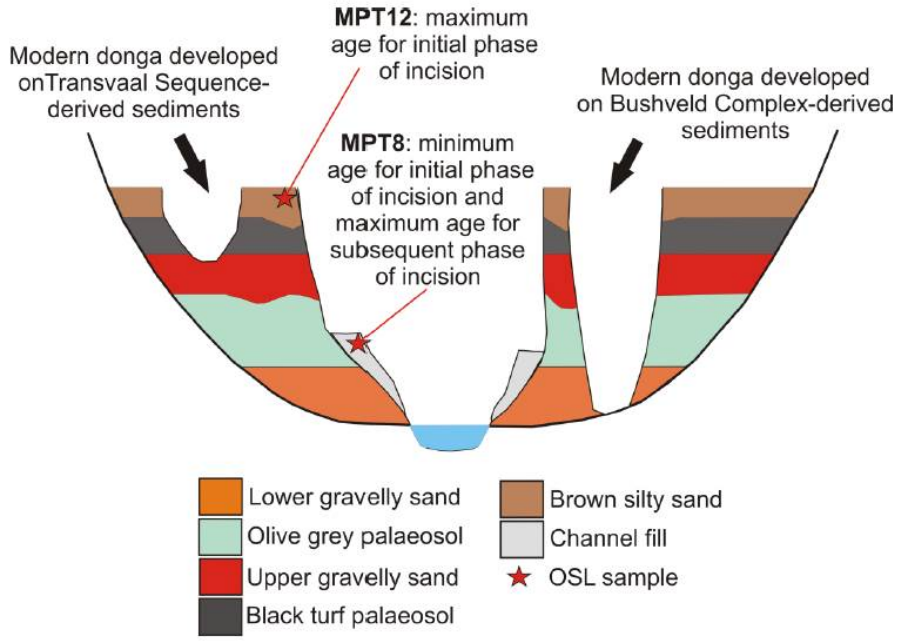

Figure 2.6: Schematic representation of the stratigraphy at the Moopetsi tributary site and the sampling strategy employed to constrain the timing of the current phase of incision (reproduced from Lyons, 2012).

and cessation of the major phases of sedimentation, to determine a time frame for palaeosol (OGP and BT) formation and to provide a maximum age for the last phase of incision. In order to gain access to all sedimentary units, which vary in thickness and preservation across the site, samples were collected from four closely-spaced points along the channel (see Figures 2.7 and 2.8). This approach provided the best opportunity to constrain the entire stratigraphy, as described by Kendall (2000) from the nearby Maandagshoek fan.

At location 1 (see Figures 2.7 and 2.8), two samples were collected from the LGS unit: (1) MPT7 from the base of the unit close to bedrock and thus indicative of the onset of sedimentation; and (2) MPT6, from directly below the contact with the young channel fill. The upper and

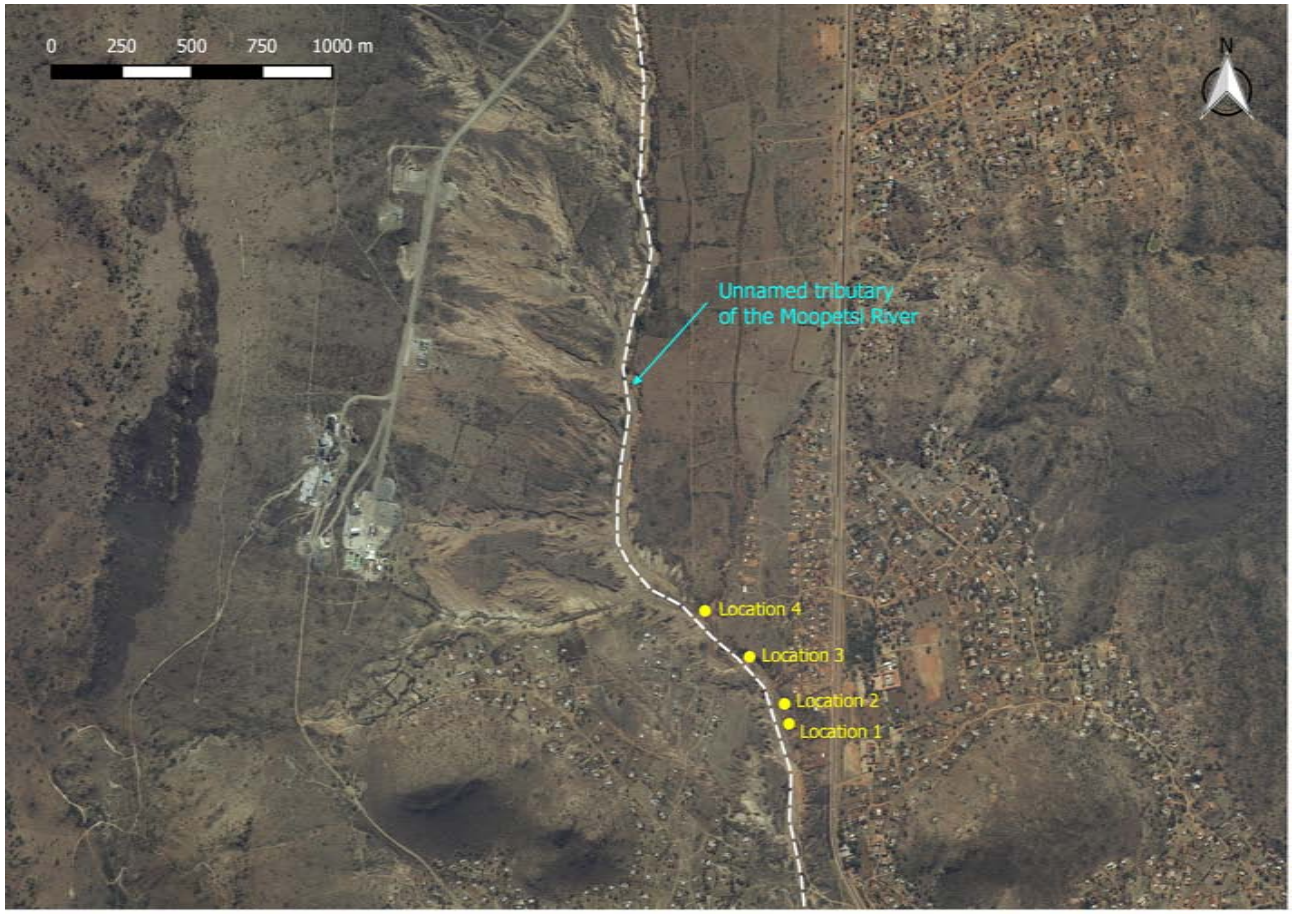

Figure 2.7: Satellite image showing the four sampling locations along the unnamed tributary of the Moopetsi River. The dashed line shows the approximate contact between the mafic Bushveld Complex in the west and the Transvaal Supergroup lithologies in the east. Satellite imagery was obtained from the South African Government Department: Rural Development and Land Reform, National Geospatial Information.

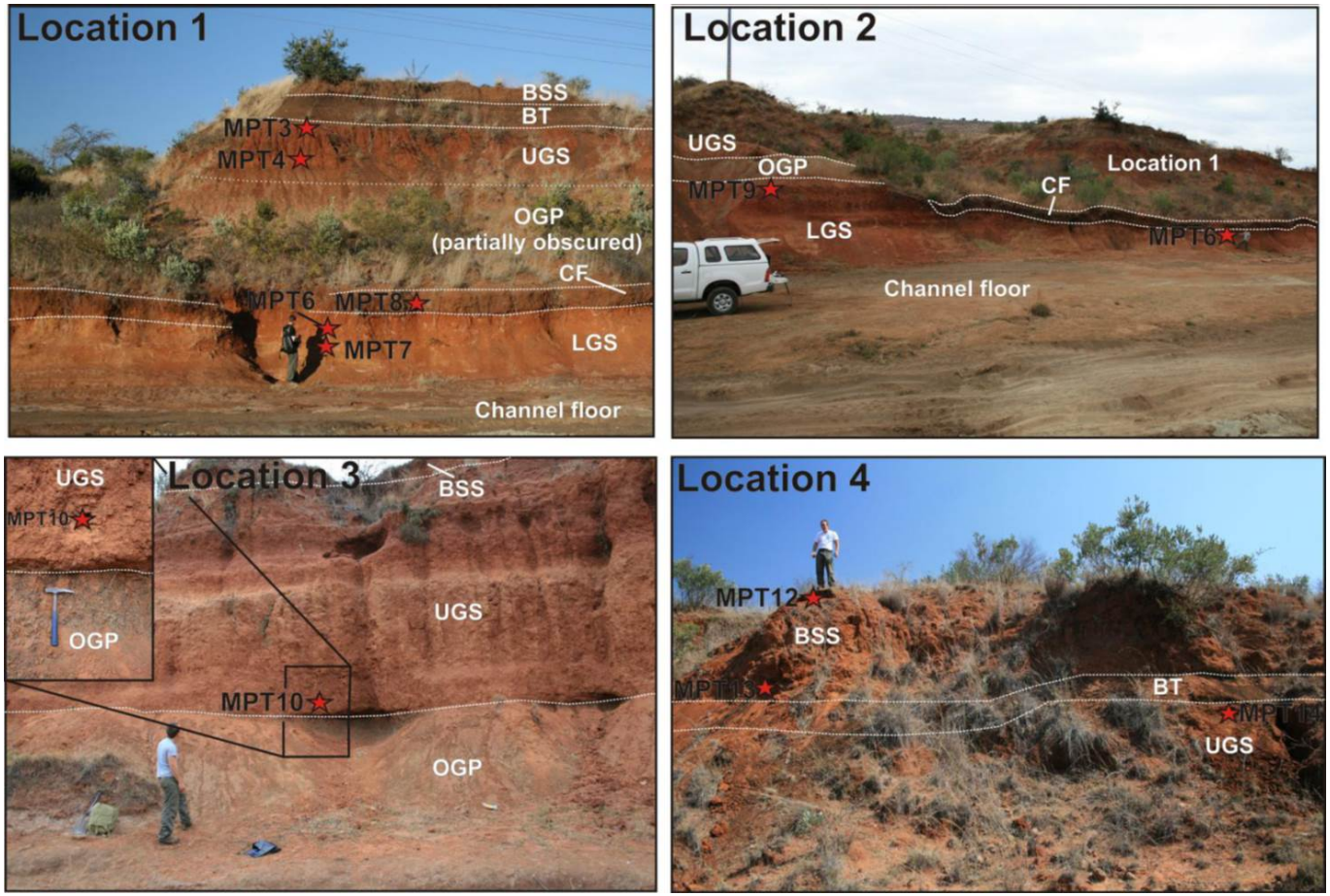

Figure 2.8: Photographs depicting the sampled sections and the location of the OSL samples at the Moopetsi tributary site (reproduced from Lyons, 2012).

lower contacts for the OGP were not clear at this location and so sample MPT9 was collected ~29 m upstream at ~2.4 m vertical height above MPT6 (see Figures 2.7 and 2.8, location 2) below a well-defined contact with the OGP in order to provide a maximum age for the cessation of LGS sedimentation and a maximum age for the onset of the OGP pedogenesis. Further upstream, sample MPT10 was collected from the base of the UGS, just above the well-defined, erosive lower contact with the OGP (Figures 2.7 and 2.8, location 3). This sample provides a minimum age for the formation of the OGP and indicates the timing of the onset of UGS sedimentation. To provide a minimum age for the cessation of UGS sedimentation and a maximum age for BT formation, sample MPT14 was collected (Figures 2.7 and 2.8, location 4) from just below the contact with the overlying BSS. An additional two samples were collected from the UGS, identified as MPT3 and MPT4 (Figures 2.7 and 2.8, location 1). The other two samples collected were MPT13 and MPT12 (Figures 2.7 and 2.8, location 4) from the lower and upper section of the BSS respectively; the former sample provided the timing for the onset of BSS sedimentation and a minimum age for BT formation, and the latter sample provides the timing of the cessation of sedimentation and a maximum age for subsequent channel and donga incision. The minor channel fill was sampled (MPT8, Figures 2.7 and 2.8, location 1) to determine a minimum age for the onset of the initial phase of incision and donga formation (see Figure 2.6). Sample location details are summarised in Table 2.1.

Table 2.1: Location details of samples collected at the Moopetsi tributary site (Lyons, 2012).

Sample ID	Sample type	Location	Latitude (S)	Longitude (E)	Elevation (m)	Depth (m)[a]
162/MPT3	Fluvial	1	24°35′6.1″	30°9′26.5″	925	2.60
162/MPT4	Fluvial	1	24°35′6.1″	30°9′26.5″	925	4.20
162/MPT6	Fluvial	1	24°35′6.1″	30°9′26.5″	925	7.65
170/MPT7	Fluvial	1	24°35′6.1″	30°9′26.5″	925	8.05
170/MPT8	Channel fill	1	24°35′6.1″	30°9′26.5″	925	0.30
170/MPT9	Fluvial	2	24°35′4.8″	30°9′26.4″	925	5.25
170/MPT10	Fluvial	3	24°34′59.7″	30°9′22.8″	925	3.70
170/MPT12	Fluvial	4	24°34′53.2″	30°9′17.8″	925	0.40
170/MPT13	Fluvial	4	24°34′53.2″	30°9′17.8″	925	2.80
170/MPT14	Fluvial	4	24°34′53.2″	30°9′17.8″	925	4.00

[a] Depth below projected land surface

2.3.2 Voordrag, KwaZulu-Natal

The extensive colluvial deposits of the Masotcheni Formation are found across northern KwaZulu-Natal. This sedimentary succession is comprised of a series of dominantly sandy colluvial sediments, interspersed with a number of buried palaeosols, as described by Botha (1992). The Voordrag sequence is grouped as the Voordrag Pedocomplex and roughly correlated with the St Paul's Alloformation, due to difficulties with mapping and correlating this site with the other sedimentological or pedostratigraphical units in northern KwaZulu-Natal (Botha, 1996).

Sample collection at Voordrag was undertaken in the company of G.A. Botha during July 2014 and samples were collected from as close as possible to the original locations used by Clarke et al. (2003). Samples were generally collected along the west-facing central wall of the donga or from a stack that could be associated stratigraphically to the centre wall (Figures 2.9,

2.10 and 2.11). The sedimentary layers have varying dips based on their location within the sedimentary succession. This is because sedimentation occurred in a bowl-shaped depression on the side of a hill with active sediment transport occurring over different parts of the hillslope at different times. The basal sediments dip 'upslope' at an angle of 23° with subsequent layers dipping at shallower angles until reaching the angle of the current 4° hillslope. Minor faulting within the sedimentary succession (Clarke et al., 2003) may also have altered some of the original dips.

Given that there is no visible contact with the bedrock in the central wall of the donga, the basal sample (VRD01, equivalent to sample R in Clarke et al. (2003), see Figure 2.10) was collected from the lowest sedimentary unit exposed within the donga. This unit is exposed in a stack at the foot of the central wall due to the 23° dip of the unit. The stack was connected to the central wall during the original sampling trip by Clarke et al. (2003), with the adjoining section having eroded since. Therefore, it was not possible to collect a sample equivalent to sample Q during July 2014. Other samples were collected from each of the major colluvial units exposed within the central wall (refer to Figure 2.10 for sample locations). To this end, samples (VRD02 - VRD08) were collected near the base of each colluvial unit, which provides a maximum limiting age for the onset of sedimentation of the targeted unit and also provides a minimum limiting age for the underlying palaeosol unit. Thus sample VRD02 (equivalent sample P) provides a minimum age for the cessation of pedogenesis in the Palaeosol 5 (P5) unit, while the same can be said of sample VRD03 (equivalent sample O) and the P4U (palaeosol 4 upper) unit, VRD05 (equivalent sample M) and the P3 unit, VRD06 (equivalent sample E) and the P2 unit and VRD07 (equivalent

Figure 2.9: Satellite image of Voordrag donga showing individual sample locations. All samples at this site have the sample ID code 215/VRD, e.g. 215/VRD01. Satellite imagery was obtained from the South African Government Department: Rural Development and Land Reform, National Geospatial Information.

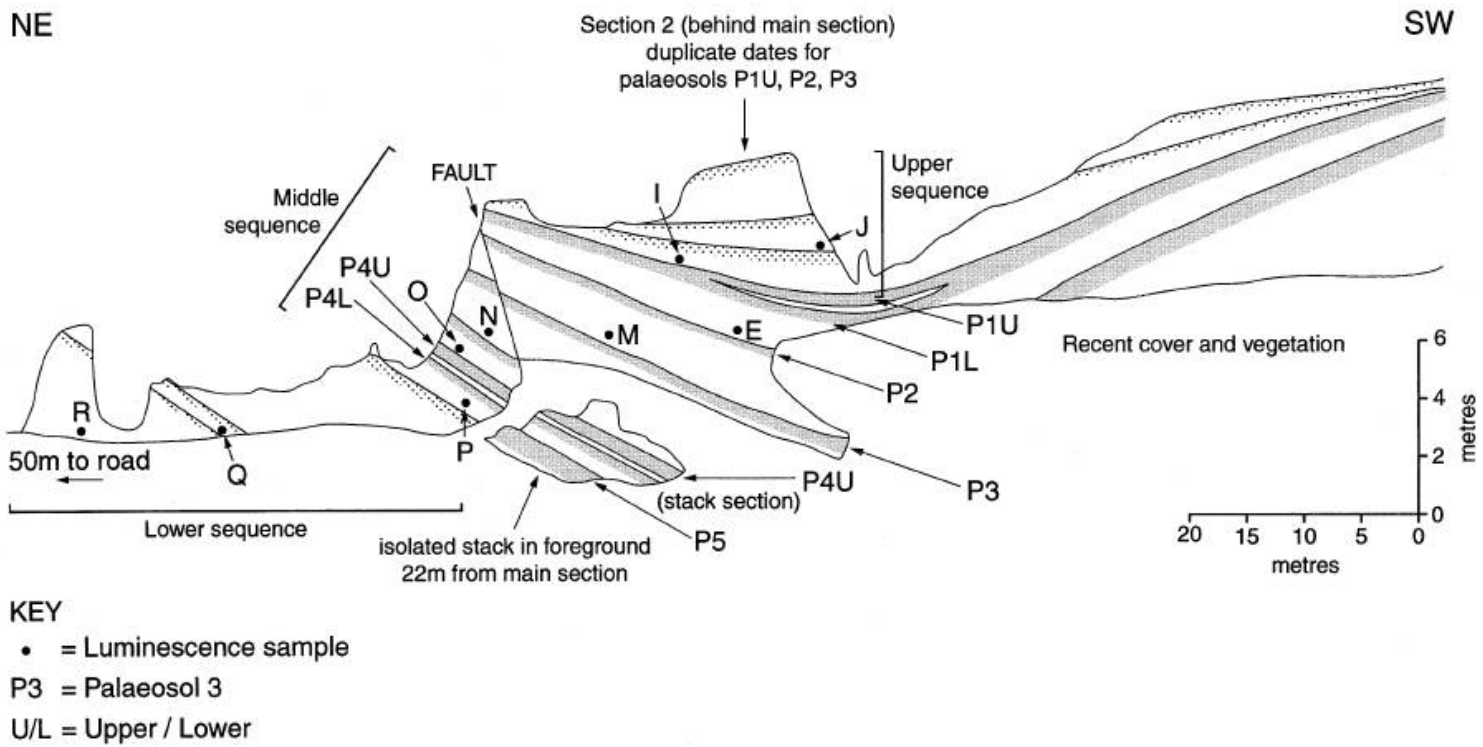

Figure 2.10: Schematic cross section of the colluvial succession exposed in the Voordrag donga side walls (Clarke et al., 2003). Palaeosol 5 (P5) is not preserved within the central wall, and the colluvial unit from which Q was collected has been eroded. Samples for this study were collected from the same locations as the samples of Clarke et al. (2003) and equivalent samples ID codes are as follows: R = VRD01, Q = no equivalent, P = VRD02, O = VRD03, N = VRD04, M = VRD05, E = VRD06, I = VRD07, J = VRD08. VRD09 and VRD10 have no equivalent and are not shown on the section.

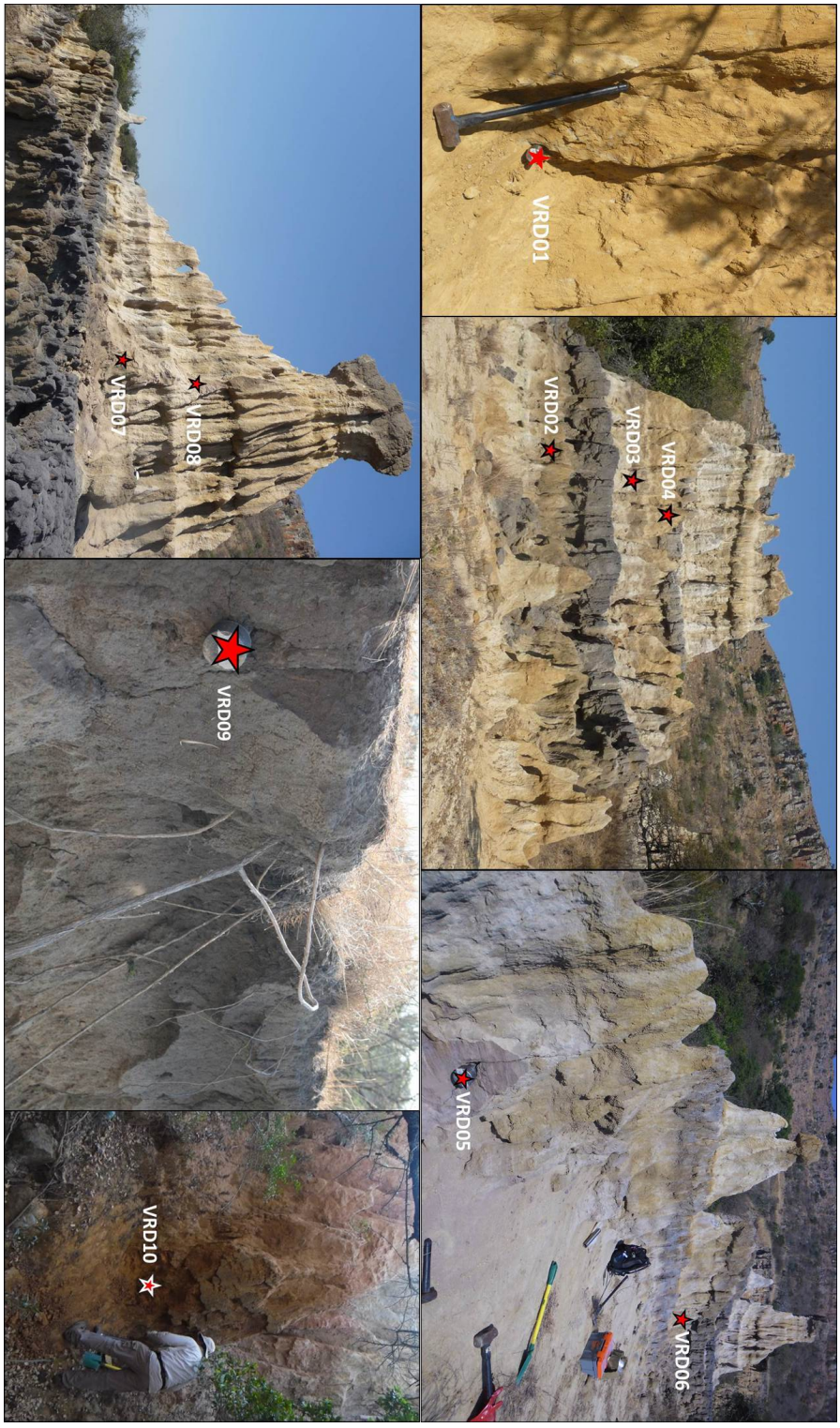

Figure 2.11: Photographs showing sample locations within the Voordrag donga.

Table 2.2: Location details of samples collected at Voordrag.

Sample ID	Sample type	Latitude (S)	Longitude (E)	Elevation (m)	Depth (m)[a]
215/VRD00	Colluvium	27°44′32.3″	31°19′27.7″	942	0.05
215/VRD01	Colluvium	27°44′30.5″	31°19′30.3″	933	12.0
215/VRD02	Colluvium	27°44′31.3″	31°19′29.6″	938	10.0
215/VRD03	Colluvium	27°44′31.3″	31°19′29.6″	938	8.7
215/VRD04	Colluvium	27°44′31.8″	31°19′29.6″	938	8.1
215/VRD05	Colluvium	27°44′31.8″	31°19′29.3″	941	7.3
215/VRD06	Colluvium	27°44′31.8″	31°19′29.0″	945	5.7
215/VRD07	Colluvium	27°44′32.2″	31°19′28.8″	945	4.1
215/VRD08	Colluvium	27°44′32.2″	31°19′28.8″	945	3.4
215/VRD09	Colluvium	27°44′32.3″	31°19′27.7″	952	0.3
215/VRD10	Colluvium	27°44′33.2″	31°19′28.9″	948	14.5

[a] Depth below projected land surface

sample I) and the P1U unit. Sample VRD04 (equivalent sample N) provides a minimum age for a minor undeveloped unit marked by an unconformity that was not designated as a palaeosol by Clarke et al. (2003). In order to obtain a maximum age for the initiation of the current phase of incision, sample VRD09 was collected from the top wall of the donga, 30 cm below the present day land surface.

There were no obvious sediment infills in the donga floor and so a sample to provide a minimum age for donga formation could not be acquired. However, a sample was collected to act as a modern process analogue, namely VRD00 which was scooped from the floor of the donga, up to ∼5 cm below the present surface.

One final sample, VRD10, was collected from an incised channel to the east of the central wall of the donga (see Figures 2.9 and 2.11). Here, a dark red (10R 4/8) sediment is exposed beneath the layered succession exposed by the donga. The red sediment sits atop heavily weathered shale

bedrock and contains boulders of locally-derived bedrock. This sample was collected because it was thought that it might provide an age for the onset of sedimentation at the site. Sample location details are summarised in Table 2.2.

2.3.3 St Paul's Mission, KwaZulu-Natal

Sample collection at St Paul's was undertaken in the company of G.A. Botha during July 2014 and so samples were collected from similar locations as those published in Botha (1996) and Wintle et al. (1995a). The existing stratigraphy of the Masotcheni Formation was described in detail by Botha (1992) (see Table 2.3) and is based on pedogenic characteristics (e.g. colour, structure, texture and relative stratigraphic position). These characteristics were used to correlate sedimentary units and associated palaeosols, with the chronological history based on radiocarbon and IRSL ages. In July 2014 samples were collected from the side-walls of the donga (Figures 2.12, 2.13 and 2.14), focusing on the basal sediments just above the contact with bedrock. Other samples focused on constraining the timing of cut-and-fill structures (palaeodongas), with samples being collected above and below observable unconformities. The most recent sediments and donga infills were sampled to ascertain the timing of the most recent phase of incision.

The Dabekazi donga has incised through the entire sedimentary succession and bedrock is visible as a series of local knickpoints. STP01 and STP02 were collected from the base of the Dingaanstad Alloformation from opposite side walls of the donga (Figures 2.12 and 2.14). STP02 was collected from ~30 cm above the visible bedrock contact and STP01 from ~1 m vertical height above STP02. STP03 was taken from the top of the Dingaanstad

Table 2.3: Description of allostratigraphic subdivisions of the Masotcheni Formation (reproduced from Wintle et al., 1995a).

Allostratigraphy (Alloformation/Allomember)		Allo-unit characteristics
Batsche Formation		Colluvial fan deposited prior to the incision of current dongas
Telezeni Alloformation		Debris flow/talus deposits fining downslope
St Paul's Alloformation (comprises the thin, stacked colluvial units which infill palaeodongas incised into the Dingaanstad Alloformation sediment)	Malonjeni Allomember	Yellow-brown sediment ubiquitous in donga exposures. Thickness variable and generally present even where older/younger units are not present
	Kwa Vundla Allomember	Leached, sandy colluvium sometimes found overlying the Hazeldene Pedoderm but may overlap onto the adjacent, truncated Ndhlamadoda Pedoderm hard plinthite
	Nqutu Allomember	Red stratified colluvium deposited in steep-sided palaeodongas incised into Dingaanstad Alloformation sediments. The distinctive Hazeldene Pedoderm forms in the top of these sediments
Dingaanstad Alloformation		Reddish-brown stratified colluvium containing petroplinthite gravel
St Augustine's Alloformation		Stratified colluvium preserved in bedrock hollows

Figure 2.12: Satellite image of St Paul's donga showing individual sample locations. All samples at this site have the sample ID code 215/STP, e.g. 215/STP01. Satellite imagery was obtained from the South African Government Department: Rural Development and Land Reform, National Geospatial Information.

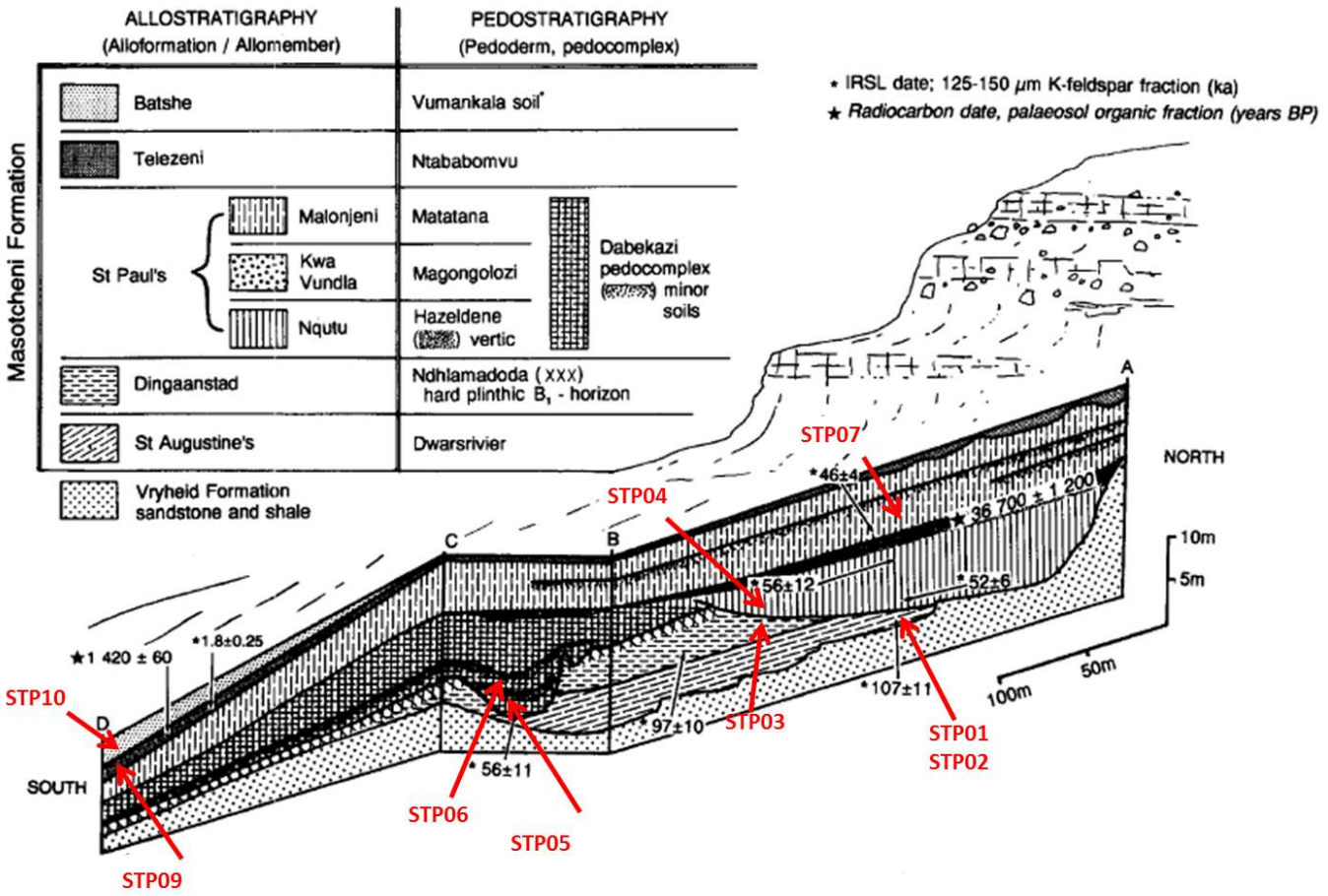

Figure 2.13: Schematic cross section of the St Paul's donga (Botha and Fedoroff, 1995) showing the relative location of samples within the context of the stratigraphy.

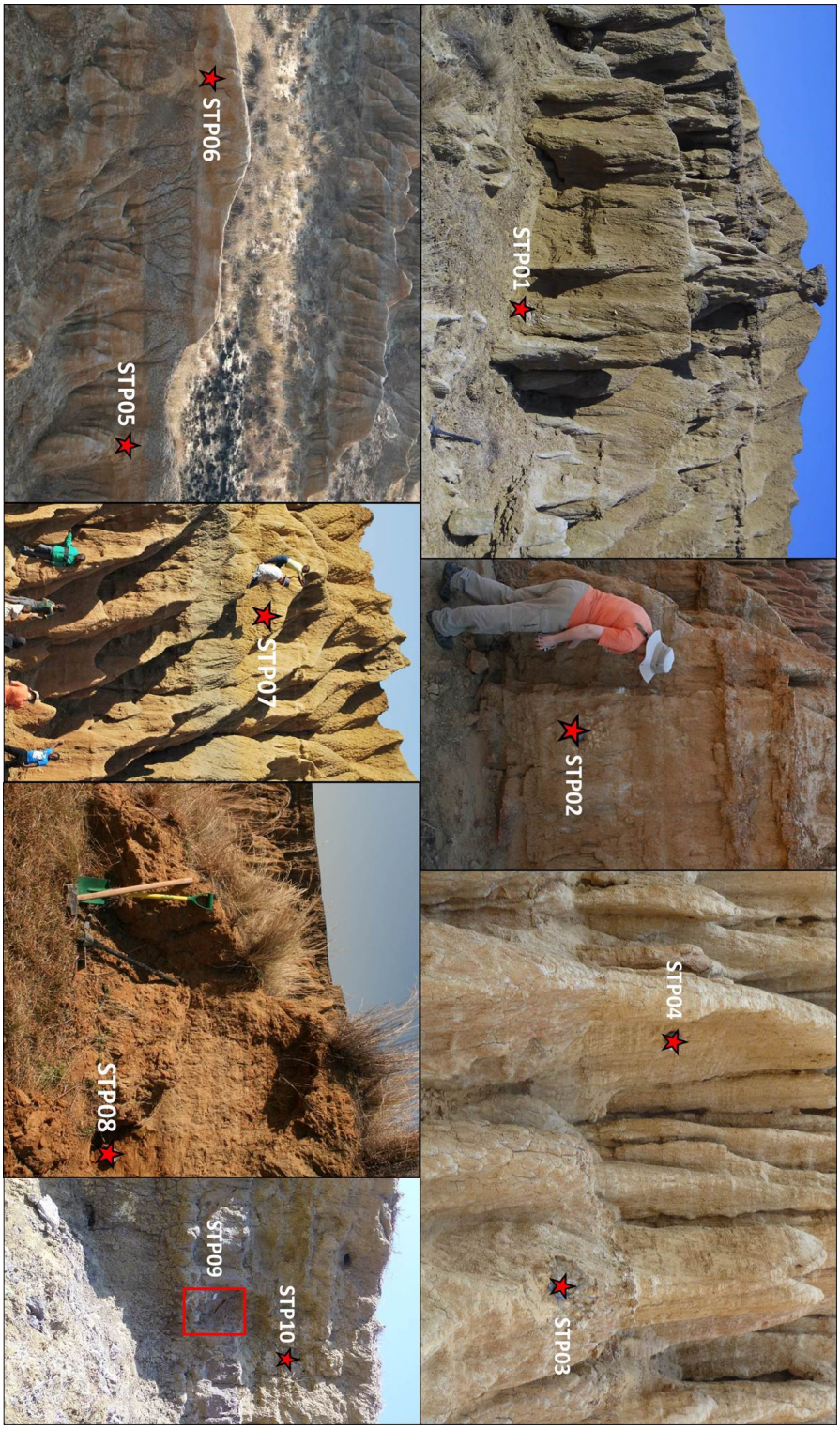

Figure 2.14: Photographs showing sample locations within the St Paul's donga.

Alloformation (Figures 2.13 and 2.14), 30 cm below an unconformity marked by reworked ferricrete which represents a previous cut-and-fill episode. These three samples provide a time frame for sedimentation of the Dingaanstad Alloformation; STP01 and STP02 provide a maximum age for the onset of sedimentation and STP03 provides a minimum age for the cessation of sedimentation and a maximum limiting age for the subsequent erosive phase. STP04 was collected ~30 cm above the unconformity, from the base of the Nqutu Allomember. This provides a maximum limiting age for the onset of sedimentation, which can be used with existing radiocarbon ages from the Hazeldene Pedoderm formed in the top of this Allomember, to bracket sedimentation of the Nqutu Allomember. STP05 and STP06 were collected from inside another palaeodonga, below and above a well-defined palaeosol unit respectively (Figures 2.13 and 2.14). STP05 provides a minimum limiting age for the cessation of sedimentation and a maximum limiting age for the onset of pedogenesis which formed the palaeosol, whilst STP06 provides a minimum limiting age for the cessation of pedogenesis and a maximum limiting age for the onset of subsequent episode of sedimentation. STP07 was collected from the base of the Malonjeni Allomember (Figure 2.13), which lies above the Hazeldene Pedoderm and provides a maximum limiting age for the onset of sedimentation for the Malonjeni Allomember and a minimum limiting age for cessation of pedogenesis for the Hazeldene Pedoderm.

Overlying the St Paul's Alloformation is the Telezeni Alloformation. STP09 was collected from the Ntababomvu Pedoderm near the top of the Telezeni Alloformation. STP10 was collected from the overlying Batshe Alloformation which provides a maximum age for the onset of the current

Table 2.4: Location details of samples collected at St Paul's.

Sample ID	Sample type	Latitude (S)	Longitude (E)	Elevation (m)	Depth (m)[a]
215/STP01	Colluvium	28°5′55.9″	30°40′46.9″	1228	18.0
215/STP02	Colluvium	28°5′55.0″	30°40′46.7″	1230	18.0
215/STP03	Colluvium	28°5′54.9″	30°40′46.4″	1232	13.6
215/STP04	Colluvium	28°5′54.9″	30°40′46.4″	1232	12.9
215/STP05	Colluvium	28°5′56.8″	30°40′49.2″	1227	16.4
215/STP06	Colluvium	28°5′56.6″	30°40′49.4″	1191	14.7
215/STP07	Colluvium	28°5′56.9″	30°40′42.9″	1242	7.3
215/STP08	Colluvial fill	28°5′58.5″	30°40′37.9″	1256	1.5
215/STP09	Palaeosol	28°5′53.9″	30°40′53.6″	1226	1.2
215/STP10	Colluvial fan	28°5′53.9″	30°40′53.6″	1226	0.8

[a] Depth below projected land surface

phase of donga incision. A channel fill deposit near the head of the donga was sampled (STP08) to provide a minimum age for the current phase of incision. Sample location details are summarised in Table 2.4.

2.3.4 Goedgedacht, Mpumalanga

Unlike the other three sampling sites, Goedgedacht did not have a pre-existing stratigraphic framework to guide sample collection, nor an existing chronology. Samples were collected during August 2014, and although it was the dry winter season when sampling was undertaken, the surrounding area experienced rainfall during the week of sample collection. Samples were collected from the central portion of the extensive donga system (Figures 2.15, 2.16 and 2.17), focusing on the basal sediments to ascertain the timing of the initiation of sedimentation, and on near-surface sediments to constrain the timing of the most recent episode of incision. Few cut-and-fill structures were visible in the exposed sediments.

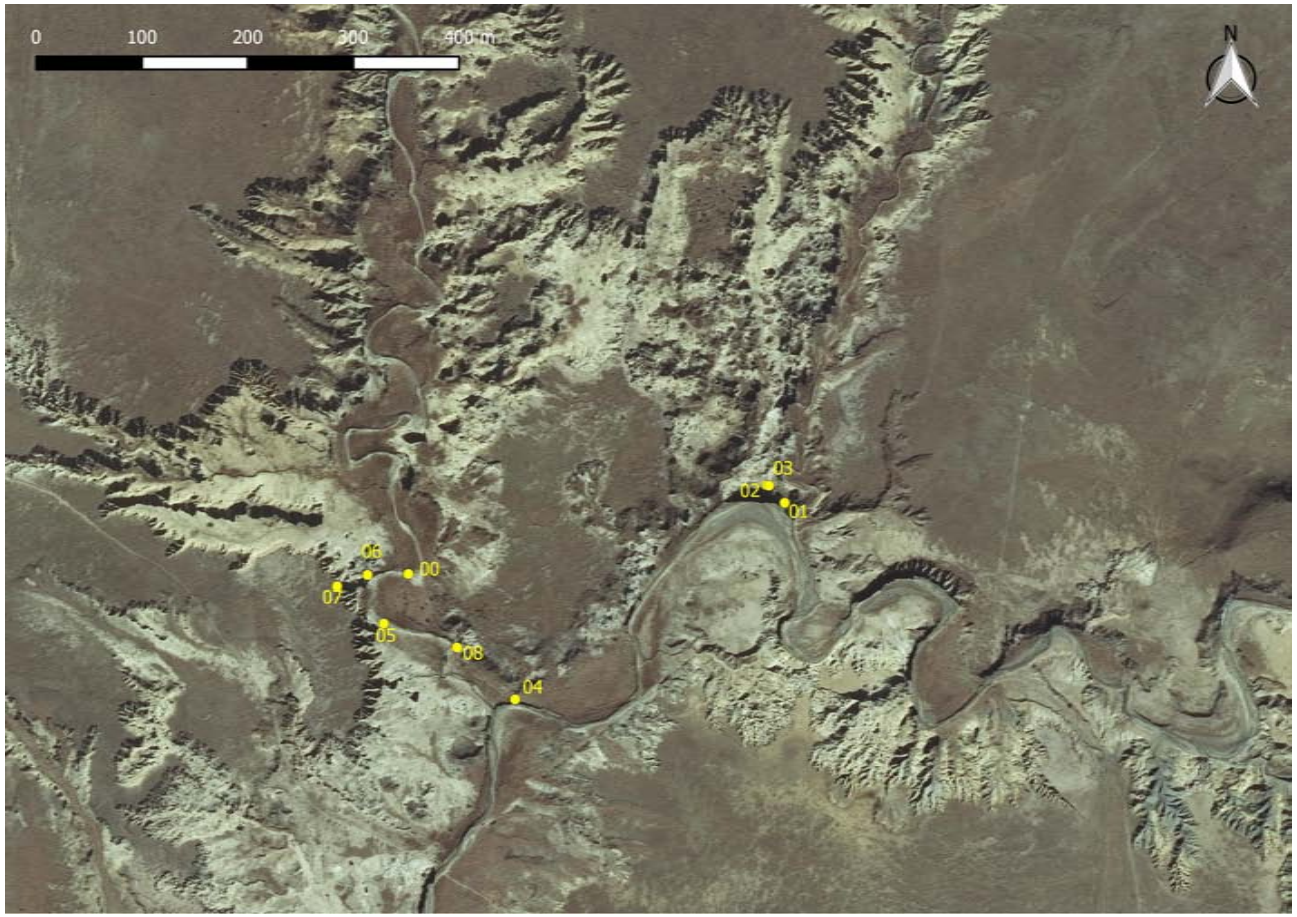

Figure 2.15: Satellite image of the Goedgedacht donga showing individual sample locations. All samples at this site have the sample ID code 218/GGD, e.g. 218/GGD01. Satellite imagery was obtained from the South African Government Department: Rural Development and Land Reform, National Geospatial Information.

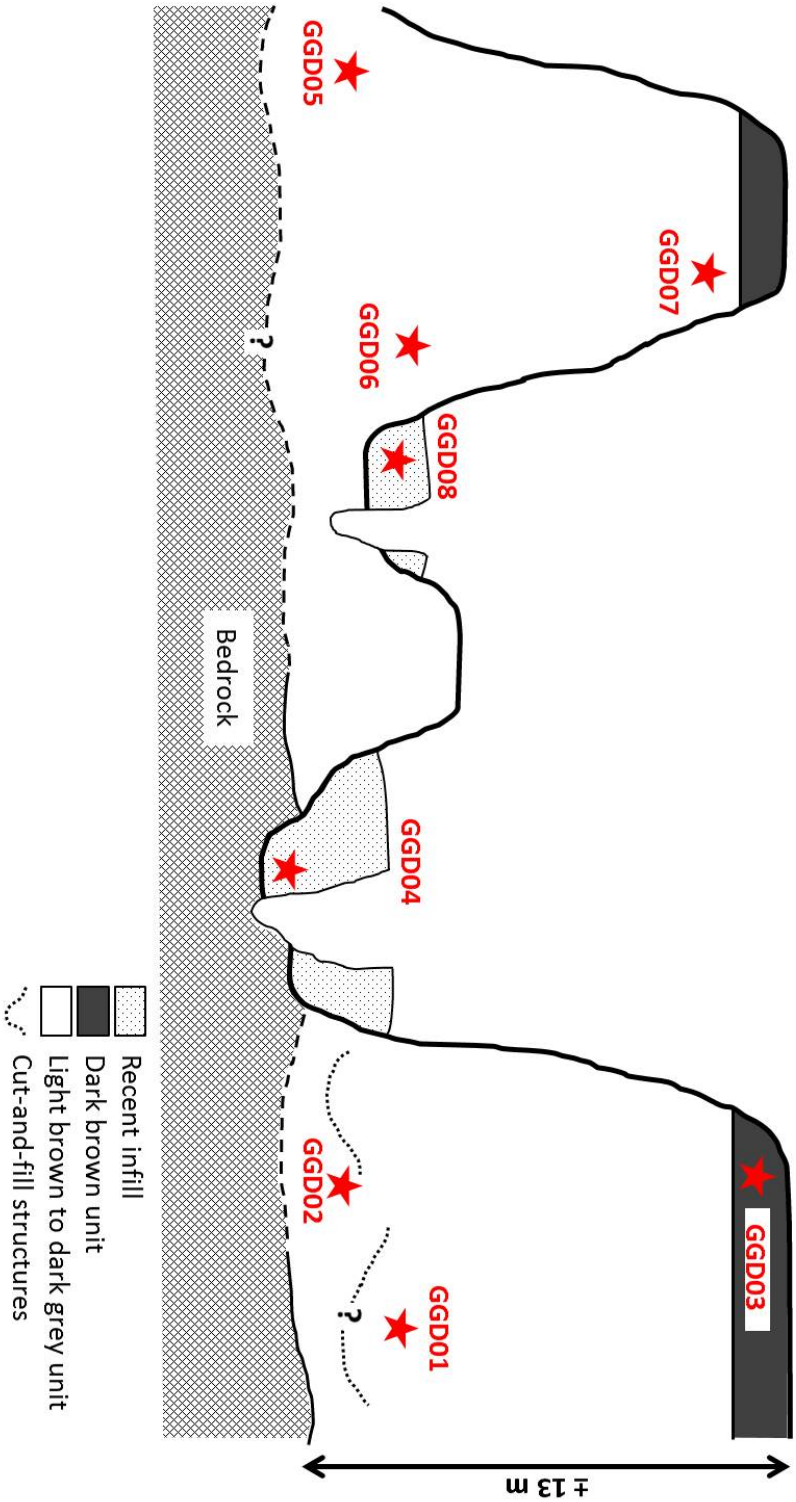

Figure 2.16: Schematic cross section of Goedgedacht donga system showing sample locations.

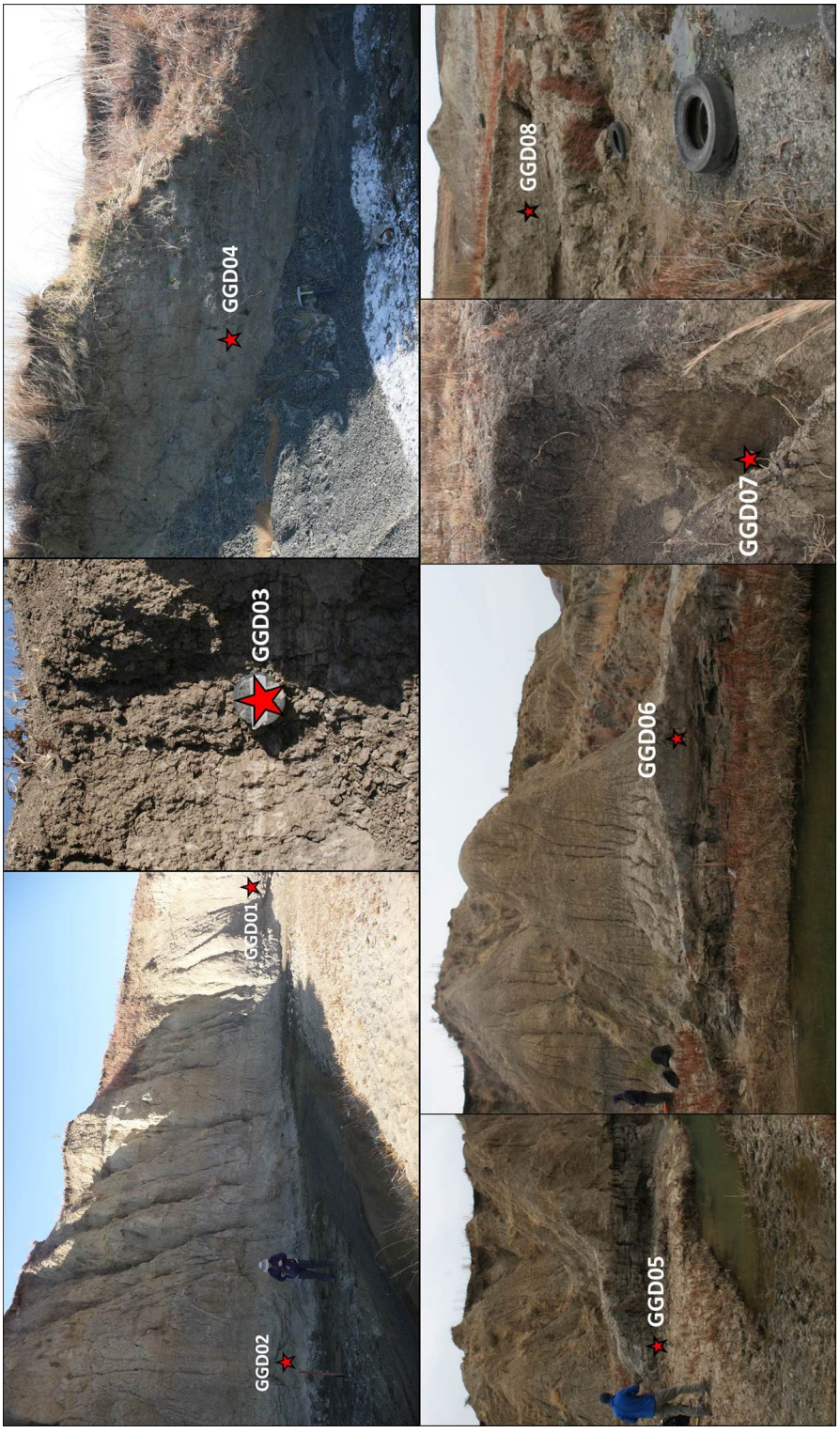

Figure 2.17: Photographs showing sample locations within the Goedgedacht donga.

GGD01 and GGD02 were collected from a light brown (10YR 5/3), predominantly sandy unit with local patches of clay and matrix-supported gravels that overlay weathered shale bedrock (Figures 2.15 and 2.16). The unit displays crude horizontal laminations and minor (∼0.5 m) scour structures which were later infilled, and is deemed to represent basal, fluvially-reworked sediments. GGD01 was collected ∼1 m above the bedrock contact. GGD02 was collected along the same exposure (Figure 2.17), ∼15 m downstream and at least ∼1 m vertical height below GGD01, where the bedrock contact was not visible. These two samples provide maximum ages for the onset of the initial pulse of sedimentation. GGD05 and GGD06 were collected from a dark grey (10YR 4/1) layer dominated by fine sand and silt featuring horizontal laminations and cm-scale interbedded sands and silts. This layer dips towards the main donga floor, which supports the assertion that these are colluvial sediments derived from nearby low-lying ridges. The bedrock contact is not visible at this location, so GGD05 was collected from the base of the exposed layer and GGD06 was collected ∼40 m upstream and ∼1.8 m vertical height above GGD05 (Figures 2.16 and 2.17).

GGD07 was collected from a light brown layer which features laminated mud and clay through fine sand at mm- to cm-scales. This layer is located directly below the dark brown topsoil (Figures 2.16 and 2.17) with which it has a gradational upper contact. GGD03 was collected from the topsoil layer directly above GGD02, ∼30 cm below the modern land surface (Figures 2.16 and 2.17). The layer is dark brown (10YR 4/3) with a developed soil structure and hosts blocky peds and mm- to cm-scale laminations of clay, silt and sand. Roots are disseminated through the top 20 – 30 cm of the

Table 2.5: Location details of samples collected from Goedgedacht.

Sample ID	Sample type	Latitude (S)	Longitude (E)	Elevation (m)	Depth (m)[a]
218/GGD01	Fluvial	27°11′46.6″	29°20′45.3″	1542	9.6
218/GGD02	Fluvial	27°11′46.1″	29°20′44.7″	1532	10.0
218/GGD03	Topsoil	27°11′46.1″	29°20′44.8″	1545	0.3
218/GGD04	Donga fill	27°11′52.7″	29°20′36.1″	1539	0.8
218/GGD05	Colluvium	27°11′50.4″	29°20′31.5″	1546	12.5
218/GGD06	Colluvium	27°11′48.9″	29°20′31.0″	1543	10.5
218/GGD07	Colluvium	27°11′49.3″	29°20′29.9″	1556	1.2
218/GGD08	Donga fill	27°11′51.1″	29°20′34.0″	1541	0.8

[a] Depth below projected land surface

topsoil layer. This sample will provide a maximum limiting age for donga formation. GGD08 was collected from a fine- to medium sand package, with a maximum thickness of 1.35 m, lying within an uneven basal scour into older sediments (Figures 2.16 and 2.17). Horizontal layers (<10 cm thick) comprised of fine- to coarse sand, sandy silt and silt are the only structures present within this layer. However, there is a weak blocky structure towards the top of the layer and a maximum rooting zone of 30 cm. GGD04 was collected from a dominantly sandy package overlying fresh shale bedrock (Figures 2.16 and 2.17). The shale has been scoured unevenly, with sandy gravels (~20 – 30 cm thick) near the base overlain by fine grained through silty sand layers (up to ~3 cm thick) with minimal soil development. Both GGD08 and GGD04 are representative of recent donga infill and will provide minimum ages for donga formation. Sample location details are summarised in Table 2.5.

2.4 Summary

In this chapter, the regional and local geology, geomorphology, climate and land use of the four sites selected for luminescence dating was outlined. Site selection was based on the ability to provide access to thick sedimentary successions with observable bedrock contacts, and in three of the four instances, a pre-existing chronology. This is of particular importance to the formulation of a combined quartz OSL and K-feldspar post-IR IRSL dating approach. The Moopetsi tributary and Voordrag sites will be used to determine the optimal protocol, which will then be tested on samples collected from the St Paul's site, and finally applied to samples from the Goedgedacht site. The detailed sampling strategy and location data was outlined for every sample presented in this study, within the context of the existing stratigraphy (where available). The following chapters will outline the process of obtaining luminescence ages by describing the sample preparation techniques for luminescence dating (Chapter 3), the dosimetry measurements and dose rate calculations (Chapter 3) and the optimisation of measurement protocols to be utilised in equivalent dose determination (Chapters 4 to 6).

Chapter 3

Sample preparation and dosimetry

3.1 Introduction

The determination of luminescence ages requires the accurate measurement of two parameters, namely the laboratory dose equivalent to the dose received in nature (equivalent dose, D_e), and the rate at which the sediments were irradiated during burial (environmental dose rate, $\dot{D}$). Thus, there are two main components to sample preparation for luminescence dating. In this study, one of the objectives is to develop the use of multiple luminescence chronometers within a single stratigraphic section, and so both quartz and K-feldspar separates were required from each sample. The first part of this chapter will deal with sample preparation for equivalent dose measurements, outlining the collection and preparation of samples in the field for transport to the laboratory and the procedure followed during the laboratory processing of samples (Section 3.2). This will be followed by a

brief explanation of the instrumentation and measurement parameters used during the measurement of the equivalent dose (Section 3.3). The second part of the chapter will explore the dose rate preparation and measurement techniques (Section 3.4) and the calculation of the total environmental dose rate (Section 3.5).

3.2 Luminescence sample preparation

3.2.1 Collection and preparation in the field

In most instances, samples were collected by hammering light-tight metal tubes horizontally into layers within thick sedimentary successions that had been exposed by donga formation. The end of each tube was stuffed with bubble wrap and taped shut and the tube was wrapped in two layers of black plastic. This packaging approach minimises sediment movement within the tube and water loss from the tube, and prevents light exposure during transport to the laboratory. Where sediments proved too hard for the tubes to be hammered in, a block was excavated from the exposure. The outside edges of the block were removed at night under red-light conditions and the block was then wrapped in light-tight black plastic bags for transport to the laboratory.

3.2.2 Opening samples in the laboratory

All samples collected for OSL analysis were opened and prepared under controlled red-light conditions in the ALRL. In order to remove any sample potentially exposed to light during the collection process, the outer sediment portion in every tube (between 3 cm and 5 cm) was removed and used for

dosimetry measurements and determination of the water content. Unexposed sediment from the centre of each sample tube was placed into a labelled beaker for further treatment. For samples collected as a block, material was chiselled off and placed in a beaker for further treatment. Samples deemed to have a large proportion of fine grains were wet sieved prior to chemical treatment using a sieve with mesh size of 90 μm. The aim of sample preparation from this point onwards was to isolate quartz and K-feldspar material from each sample so that they could be measured independently of one another.

3.2.3 Chemical treatment of samples

Samples were washed in 10 % v.v. dilution of concentrated (37%) hydrochloric acid (HCl) to remove any carbonate material present. Repeated washes were used to ensure all carbonate was removed and once reaction ceased, the samples were washed in distilled water three times. Subsequently, samples were washed in 20 vols hydrogen peroxide (H_2O_2) to remove organic material. The reaction of H_2O_2 is dependent on the pH level of the solution, therefore carbonate is removed prior to the addition of H_2O_2 to reduce the alkalinity and prevent the protection of organic material by carbonate coatings (Mikutta et al., 2005). Once visible effervescence had ceased, samples were rinsed in distilled water three times.

3.2.4 Dry sieving

Following the chemical treatment, samples were dried overnight in the oven at 50 °C. Once dry, samples were sieved using a combination of sieves with mesh sizes ranging from 90 μm to 355 μm. A maximum of 40 g of sample

was placed into the sieve stack, which was secured on a sieve shaker for 20 mins to allow the particle size fractions to separate. The 180-212 μm size fraction was retained for all further preparation and measurement steps.

3.2.5 Separation of mineral fractions

Mineral fractions were separated on the basis of density using sodium polytungstate (SPT) solutions with densities of 2.62 g/cm^3 and 2.70 g/cm^3 for quartz, and 2.53 g/cm^3 and 2.58 g/cm^3 for K-rich feldspar (Figure 3.1). Typically the <2.58 g/cm^3 fraction is isolated for IRSL dating of K-feldspars (see Barr and Lamothe, 2010; Buylaert et al., 2015; Lamothe et al., 1994; Li et al., 2013; Mejdahl, 1983). However, measurements of the K-content using GM-beta counting for the separates obtained from this research showed variable increases with the additional density separation step at 2.53 g/cm^3 (Table 3.1). For samples in the <2.58 g/cm^3 fraction with a high K-content the increase was negligible; for example 170/MPT12 increased from 11.00 %K to 11.81 %K. Alternatively, for some of the samples with a low K-content the increase was substantial, such as 162/MPT4 which increased from 5.47 %K to 12.56 %K. Unfortunately, some samples with a low K-content displayed only a marginal increase (particularly 170/MPT9 and 170/MPT7). Any increase is due to the removal of low density minerals, such as clays and micas and thus is sample dependent. Given the overall increase in K-content observed in the Moopetsi tributary samples (see Table 3.1) it was decided to use both a 2.58 g/cm^3 and 2.53 g/cm^3 density separation step for the standard processing of K-feldspar samples in this research.

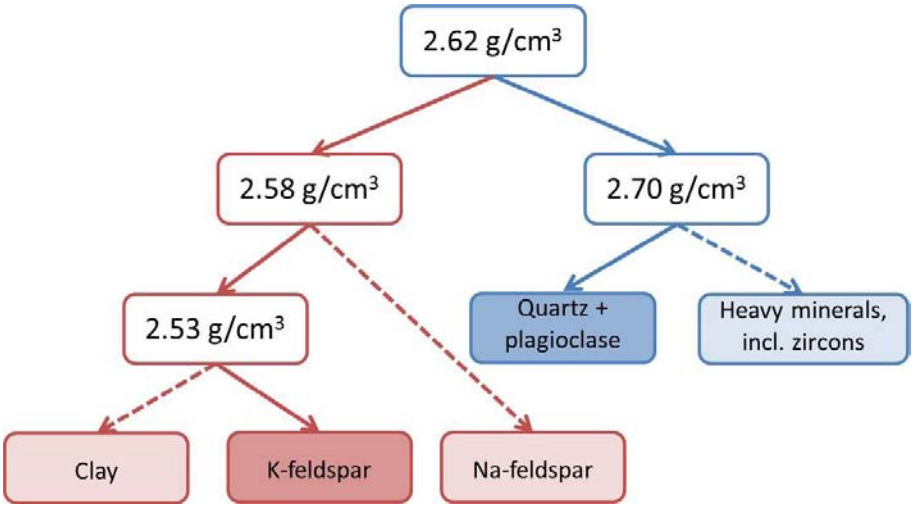

Figure 3.1: Schematic diagram showing the density separation process to isolate quartz and K-feldspar for luminescence dating (redrawn from Aitken (1998)). Arrows pointing towards the left denote the mineral fraction that floats and arrows pointing to the right denote the fraction that sinks. Solid lines denote the separation process followed to obtain K-feldspar (red) and quartz (blue), while dashed lines show mineral fractions that were discarded from the bulk sample.

Table 3.1: Measured K-contents (%wt) for K-feldspar separates obtained from SPT density separation on samples collected from the Moopetsi tributary site (samples are ordered in stratigraphic succession from top to bottom of the section).

Sample ID	Density (g/cm^3)		
	< 2.58	2.53 - 2.58	< 2.53
170/MPT8	4.33	6.21	3.97
170/MPT12	11.00	11.81	10.52
170/MPT13	11.20	11.98	11.23
170/MPT14	6.11	9.41	4.37
162/MPT3	4.84	12.33	2.44
162/MPT4	5.47	12.56	2.54
170/MPT10	3.40	5.25	3.07
170/MPT9	2.72	3.97	2.43
162/MPT6	3.07	7.26	3.14
170/MPT7	3.65	4.32	3.63

3.2.6 Etching of samples

Etching of grains in hydrofluoric (HF) acid is standard practice during the preparation of samples for luminescence dating. Etching removes the alpha-irradiated skin, thereby removing the contribution of external alpha particles from the dosimetry calculation (Aitken, 1998; Brennan, 2006; Wintle, 1997). The etching process is based on the assumption that a uniform thickness is removed from the outer surface of the grain. Whilst this assumption may be valid for quartz grains, it is problematic when considering feldspar grains due to the crystal structure of the grains. Both quartz and feldspar are tectosilicates, but feldspar grains contain well-defined cleavage (planes of weakness) which allows for the preferential etching of material along these crystal planes. Scanning electron microscopy (SEM) images taken by Duller (1992) of unetched and etched K-feldspars showed deep etch pits and accentuation of cleavage planes on the latter. The contribution from external alpha irradiation (which is also dependent on soil water content) will be dwarfed by the internal beta contribution for these samples, due to their high K-contents. Therefore, in this research K-feldspar grains were not etched in HF acid due to concern about the anisotropic removal of the surface. However, quartz grains were etched in 40% HF acid for 45 min in order to remove the alpha-irradiated surface of the grains and any remaining feldspars prior to resieving.

3.2.7 Water content measurements

Knowledge of the water content (WC) is necessary for calculation of the dose rate for luminescence dating. The modern WC was measured for each

sample collected, using the sediment in the outer end of the metal tube that was removed during sample preparation (Section 3.2.2). This sediment was placed in a beaker and weighed, before being placed in the oven to dry for several days. The beaker was weighed again after drying and the weight of the water calculated. The sample WC was calculated using Equation 3.1, where WC is the water content, weight_{wet} is the weight of the wet sediment and weight_{dry} the weight of the dry sediment.

$$WC\,(\%) = \frac{weight_{wet}(g) - weight_{dry}(g)}{weight_{dry}(g)} \times 100 \tag{3.1}$$

Additionally, saturated WC was measured for several samples from the Voordrag, St Paul's and Goedgedacht sites. Sediment was packed into tights, weighed and then placed in a beaker of distilled water and left to stand until completely saturated. The tights were then suspended from a clamp stand and the excess water allowed to drain away. The sample was deemed to be saturated once a timed interval of 1 minute was recorded between individual drops of water. The wet samples were then weighed again and placed into the oven to dry over several days. Once completely dried, the sample was re-weighed to determine the wet weight, and the WC calculated using Equation 3.1. The modern WC ranged from 0.5 – 4.1 % at Voordrag, 1.0 – 8.0 % at St Paul's and 5.2 – 16.5 % at Goedgedacht. Saturated WC ranged from 41 – 48 % at Voordrag, 47 – 53 % at St Paul's and 48 – 61 % at Goedgedacht. WC measurements at Moopetsi were undertaken by Lyons (2012); modern WC ranged from 0.4 – 2.0 % and saturated WC was assumed to be ~30 %.

3.3 Instrumentation and measurement parameters

All D_e measurements in this study were undertaken on a Risø TL/OSL-DA-10, -15 or -20 automated reader (see Table 3.2 for technical specifications of each reader). Laboratory irradiations were made using a calibrated $^{90}Sr/^{90}Y$ beta source and the dose rate for each reader is recorded in Table 3.2. Multiple grain measurements (hereafter referred to as small aliquot measurements) were made by mounting a mono-layer of grains onto the surface of a 9.7 mm diameter aluminium disc, using Silkospray silicone oil and a small (~2 mm diameter) mask. This produced small aliquots with ~30 grains mounted on each disc. A small mask was used to obtain the lowest number of grains per disc, due to the high intensity luminescence signal produced by both quartz and K-feldspar separates in this study. Single grain measurements were made by mounting individual grains onto a 9.7 mm diameter single grain disc, with a 10 x 10 grid of holes (diameter and depth ~300 μm) drilled into the surface. D_e measurements were run on the 180 – 212 μm grain size fraction whenever possible, to prevent multiple grains from occupying a single hole on the disc.

3.3.1 Quartz D_e measurements

Quartz stimulation for multiple grain measurements used blue LEDs (470 nm; 80 mW/cm^2 Bøtter-Jensen et al. (2010)) and detection used a photo-multiplier fitted with 7.5 mm thickness of Hoya U-340 filter. Stimulation for single grain measurements used the green laser fitted in the single grain

Table 3.2: Technical specifications of the Risø automated readers used during this study.

	Risø 1	Risø 3	Risø 4	Risø 7
System type	DA-10	DA-15	DA-15	DA-20
Photo-multiplier type	EMI 9635 QA	EMI 9235 QA	EMI 9235 QA	EMI 9635 QA
Coarse grain dose rate (Gy/s)[a]	0.0384	0.0744	0.0339	0.0962
Single grain dose rate (Gy/s)[a]	-	0.0867	0.0389	-
Multiple grain measurements				
Blue LED type	NISHIA (NSPB-500AS)	NISHIA (NSPB-500S)	NISHIA (NSPB-500S)	NISHIA (NSPB-500S)
Number of diodes	28	28	28	28
Emission wavelength (nm)	470	470	470	470
Stimulation power (mW)	83	54	34	80
IR LED type	Vishay (TSFF5210)	Vishay (TSFF5200)	Vishay (TSFF5200)	Vishay (TSFF5210)
Number of diodes	22	24	24	21
Emission wavelength (nm)	870	870	870	870
Stimulation power (mW)	161	146	122	145
Single grain measurements				
Green laser type	-	$Nd:YVO_4$	$Nd:YVO_4$	-
Emission wavelength (nm)	-	532	532	-
Stimulation power (mW)	-	10	10	-
IR laser type	-	-	IR laser diode	-
Emission wavelength (nm)	-	-	830	-
Stimulation power (mW)	-	-	150	-

[a] Dose rate calculated on 11/02/2014

attachment (532 nm; 50 W/cm^2 Bøtter-Jensen et al. (2010)) and detection used a photo-multiplier fitted with 2.5 mm thickness of Hoya U-340 filter. Quartz D_e values were determined in Analyst Ver 4.31 (Duller, 2015), by integrating the initial signal from the decay curve after subtraction of a late background. Multiple grain measurements integrated the initial 0.8 s and the last 8 s of the decay curve, whilst single grain measurements integrated the initial 0.165 s and the last 0.17 s of the decay curve.

3.3.2 K-feldspar D_e measurements

Infrared (IR) stimulation of K-feldspar used an IR LED array (875 nm; 135 mW/cm^2; Bøtter-Jensen et al., 2010) for multiple grain measurements and a 150 mW IR laser (830 nm; 500 W/cm^2; Bøtter-Jensen et al., 2010) for single grain measurements. Detection was in the blue region of the spectrum using a combination of 2 mm BG-39 and 2 mm Corning 7-59 glass filters. Multiple grain D_e values were determined by integrating the initial 4 s of the decay curve after subtraction of a late background, taken from the final 20 s. Single grain D_e values were determined by integrating the initial 0.165 s of the decay curve after subtraction of a late background taken from the final 0.33 s of the decay curve.

3.3.3 Construction of dose response curves

In this study, optical dating of quartz used the SAR protocol of Murray and Wintle (2000) (see Section 1.3.1). Three routine tests are typically used to assess the suitability of the SAR protocol to date samples. The first test ensures that the SAR protocol is correcting for sensitivity change by making a repeat measurement (the recycling dose) on one of the regeneration doses

used to build the DRC. The *recycling ratio* is defined as the ratio of the original regeneration dose to the recycled dose and should equal unity; typically a ratio between 0.90 and 1.10 is deemed acceptable (Murray and Wintle, 2000). The second test measures the luminescence signal from a zero dose; termed *recuperation*, this signal is typically presented as a percentage of the natural dose and should be <5 % (Murray and Wintle, 2000). The third test assesses the ability of the chosen protocol to recover a known given dose by bleaching the sample, administering a fixed given dose and treating it as an unknown dose during measurement. The *dose recovery ratio*, i.e. the ratio of the measured dose to the given dose, should equal unity if the SAR protocol is functioning properly (Wintle and Murray, 2006). The post-IR IRSL protocol (see Section 1.4.2) used to date K-feldspar in this study is based on the same principle of repeated measurement cycles, with sensitivity correction made by administering a test dose used in the SAR protocol.

DRCs for both small aliquot and single grain measurements were constructed using a minimum of five regeneration doses, one recycled dose, one recuperation dose and an IR/OSL depletion ratio (Duller, 2003) in the case of quartz OSL to asses for feldspar contamination. Quartz DRCs were fit using either a SSE or DSE function (see Section 1.3.2). This was to avoid the inclusion of anomalously large D_e values into the dose distribution, as seen when fitting a SEPL function (this was of concern when measuring quartz grains very near to saturation). K-feldspar DRCs were fit using a best fit approach, i.e. either a SSE, DSE or SEPL functions were applied based on the visual fit and reduced Chi squared parameter. This was

because the resultant D_e values were not unreasonably large and none of the K-feldspar samples were close to saturation.

Acceptance criteria for quartz and K-feldspar D_e values required a (i) recycling ratio within 10% of unity; (ii) recuperation ratio less than 5% of the natural signal for all samples, except near-modern samples which required an absolute recuperation < 2 Gy; (iii) IR/OSL depletion ratio within 10% of unity; (iv) maximum test dose error within 10%; and (v) T_n signal more than 3 sigma above background. An additional acceptance criteria (vi) was applied to the single grain data and excluded grains whereby the shape of the DRC precluded the return of a meaningful D_e value (e.g. Figure 3.2). These grains produce very low D_0 values probably because their radiation storage capacity is much lower than that of other grains, and if included in the dose distribution would produce a phantom population of very low D_e values, which would bias the age models to produce lower burial doses.

3.3.4 Determining the burial dose using appropriate age models

Luminescence dating of sediments relies on the exposure of the constituent grains to sunlight during weathering, erosion and deposition (see Section 1.2). In certain environments (e.g. fluvial, glacial) not all grains are exposed to sunlight, which results in some grains being completely reset and others being partially reset. This is referred to in luminescence dating as partial bleaching. In an attempt to deal with this problem a number of statistical models have been proposed to determine the burial dose by identifying the D_e value that best records the dose acquired since the last exposure

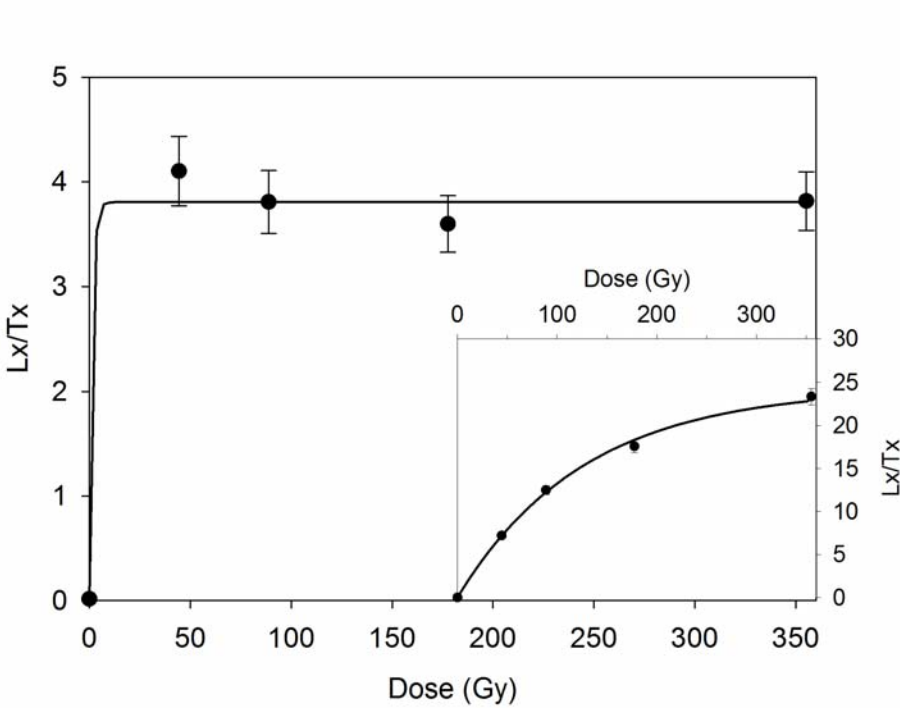

Figure 3.2: Example of early saturation in quartz used as a screening criterion for single grain D_e measurements. Inset shows a typical DRC for the same sample.

to daylight (e.g. Galbraith et al., 1999; Olley et al., 1998; Thomsen et al., 2003, 2007).

The D_e distribution for each sample is subjected to statistical analysis to determine the burial dose (D_b, Figure 3.3), which is used to calculate the luminescence age. A variety of statistical age models have been suggested, including models which target (i) the most well-bleached proportion of grains, e.g. lowest 5 % of D_e values (Olley et al., 1998), the minimum age model (MAM, Galbraith et al., 1999) and the Internal-External Consistency Criterion (IEU, Thomsen et al., 2003, 2007); (ii) a measure of central tendency e.g. arithmetic mean and the central age model (CAM, Galbraith et al., 1999); and (iii) the identification of multiple populations within a single distribution e.g. the finite mixture model (FMM, Galbraith and

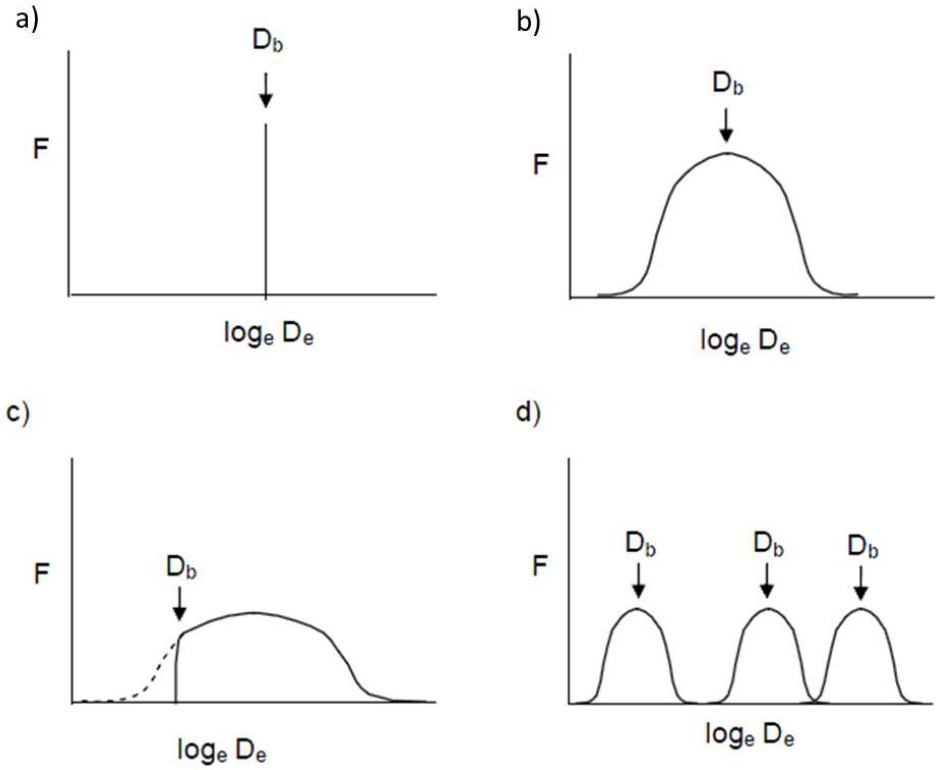

Figure 3.3: Schematic of D_e distributions in various statistical age models: a) the common age model; b) the central age model; c) the minimum age model and d) the finite mixture model. The curves indicate the distribution of the D_e values, F represents the frequency and D_b represents the burial dose that would be calculated using the relevant age model (Rodnight, 2006).

Green, 1990). Fluvially- and colluvially-derived sediments, such as those dealt with in this study, may have been poorly bleached and the most well-bleached proportion of grains is generally targeted (Rittenour, 2008). It is worth noting at this point that a useful statistical value, overdispersion (OD), is generated when applying the CAM to a D_e distribution. OD represents the amount of variation within the D_e distribution that cannot be accounted for by measurement uncertainties, such as photon counting statistics and curve-fitting uncertainties (Galbraith and Roberts, 2012).

Numerous attempts have been made to define objective criteria which can be used to select an appropriate age model. Olley et al. (2004b) analysed fourteen single grain D_e distributions from Holocene samples and suggested that the degree of OD could be applied as a diagnostic property in order to distinguish between the application of the MAM and CAM and suggested a threshold value of 20 %. However, they caution that the MAM may not be appropriate for samples where the scatter in the D_e data may be due to reasons other than partial bleaching (particularly relevant for Pleistocene aged sediments), nor for samples which have undergone post-depositional mixing (e.g. bioturbation). An analysis of single grain OSL data by Guérin et al. (2015a) led them to conclude that a well bleached sample does not necessarily have an OD $<$ 20 %, showing OD values as high as 62 % for well-bleached samples with no post-depositional mixing.

Bailey and Arnold (2006) thought that the use of a threshold OD value was insufficient on its own to distinguish between fully and incompletely bleached samples. Instead they presented a 'decision tree' approach based on values of OD, skewness and kurtosis derived from their replicate D_e values. However, several studies have reported that application of the decision tree protocol resulted in both overestimation and underestimation of single grain ages based on independent age control (e.g. Medialdea et al., 2014; Thomsen et al., 2016). Galbraith and Roberts (2012) question whether skewness and kurtosis are valid parameters on which to base the selection of an appropriate age model and caution against relying solely on statistical criteria to select an age model, as do Murray et al. (2012). In this study, selection of an appropriate age model was considered on a site-by-site basis and will be discussed in detail in the relevant chapter.

3.4 Dose rates and measurement techniques

The total environmental dose rate ($\dot{D}$) originates from a combination of internal and external radiation together with a relatively small cosmic dose (Aitken, 1985; Ankjærgaard and Murray, 2007; Duller, 2008a; Guérin et al., 2012). The internal dose rate is produced by alpha (α) and beta (β) emissions from uranium (U), thorium (Th) and potassium (K), and typically accounts for a smaller contribution to the environmental dose rate than the external dose rate. The external dose rate is the direct result of the interaction of α, β and gamma (γ) radiation (emitted by U, Th and K) with silt- and sand-sized grains within the sediment (Figure 3.4).

Potassium-40 (^{40}K) undergoes direct decay into its stable daughter isotopes argon-40 (^{40}Ar) and calcium-40 (^{40}Ca) through γ emission and β decay respectively (Aitken, 1985). The parent isotopes of the Th and U decay series, specifically ^{232}Th, ^{238}U and ^{235}U, decay via a decay chain (Figure 3.5) into various daughter isotopes, some of which are themselves radioactive, until they reach a stable isotope form. For example, ^{232}Th decays into radium-228 (^{228}Ra), which is itself a beta-emitter that decays into actinium-228 (^{228}Ac), another beta emitter. The final product of ^{232}Th is ^{208}Pb, a stable lead isotope. It is this series of successive radioactive decays that results in the trapped charge necessary for the luminescence dating technique to be utilised effectively.

In addition to K, U and Th decay, the decay of rubidium-87 (^{87}Rb) to strontium-87 (^{87}Sr) produces a contribution to the external dose rate, but this is small due to the low energy β particles that are emitted (Warren, 1978). In luminescence dating, when not directly measured,

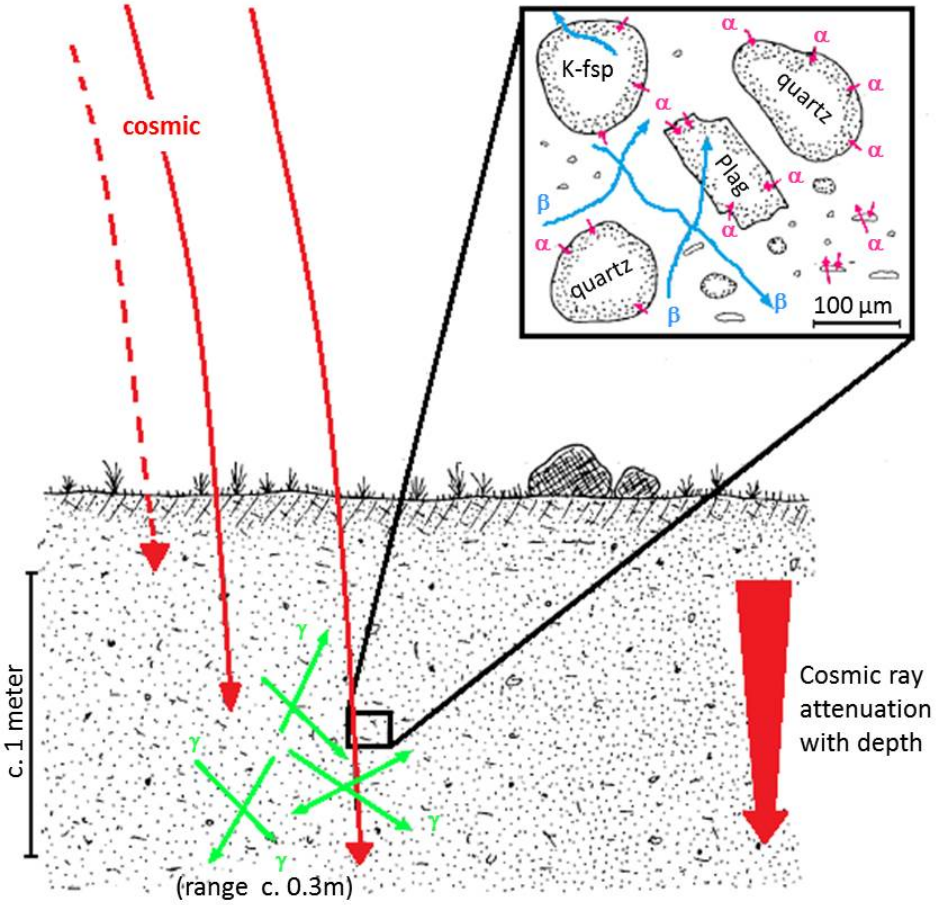

Figure 3.4: Natural radiation travelling through soil (redrawn from Aitken, 1998). A maximum travel distance exists for radioactive α (pink) and β (blue) particles and gamma rays (green), ~3 μm, ~3 mm and ~30 cm, respectively (Aitken, 1998). In contrast, cosmic rays (red) are highly penetrating but dependent on latitude, altitude and the depth (overburden) of the sample from the surface (Aitken, 1998; Prescott and Hutton, 1994).

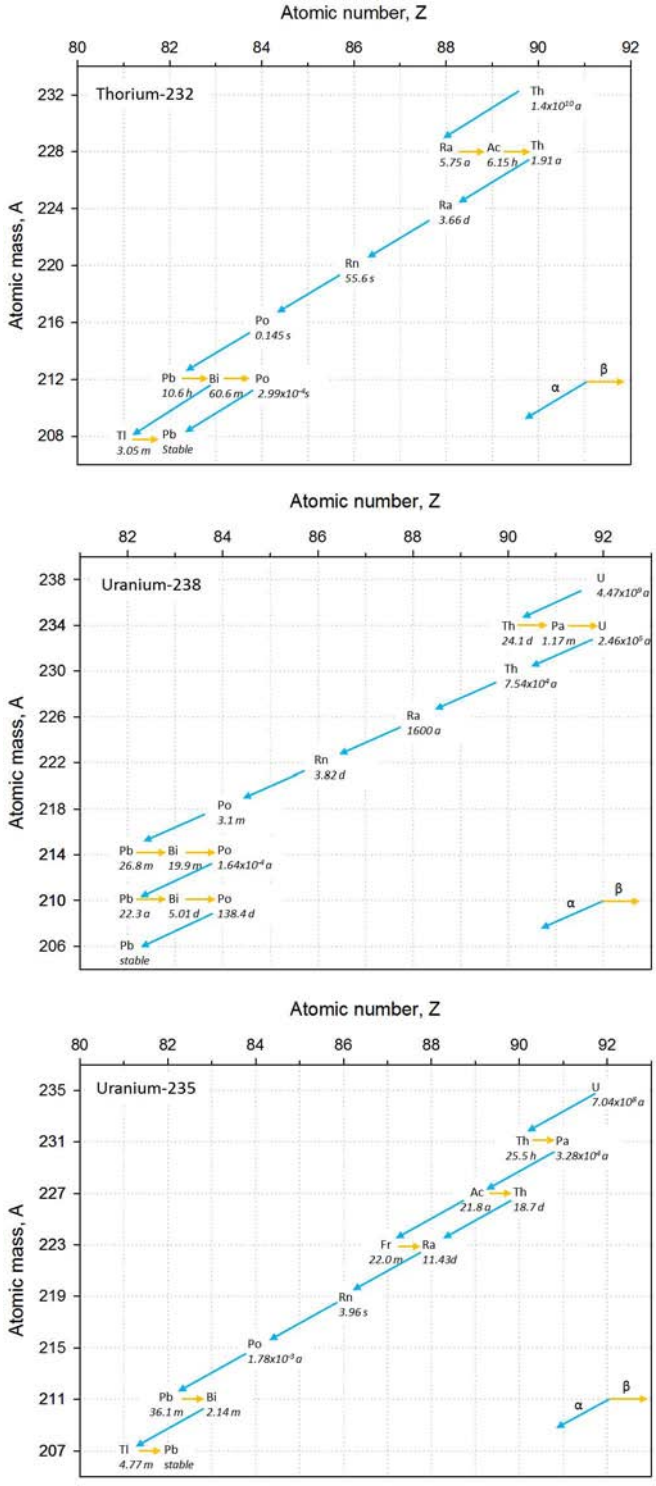

Figure 3.5: Decay chains for the parent isotopes (a) ^{232}Th, (b) ^{238}U and (c) ^{235}U. The time below the isotope represents the half-life (s = second, m = minutes, d = days, a = years). Alpha decay is represented by diagonal (blue) arrows and beta decay by horizontal (orange) arrows (redrawn from Aitken (1985)).

the Rb concentration in sediments is typically estimated on the basis of the K-concentration using a ratio of 200:1 (Huntley and Hancock, 2001; Warren, 1978). Thus, the contribution of Rb to the dose rate for K-feldspar can be incorporated into the dose rate calculation using a ratio of 200:1 in conjunction with the dose rate conversion factors. However, given the negligible concentrations of K within quartz grains, the Rb contribution to the dose rate can be safely disregarded when working with quartz (Aitken, 1985; Warren, 1978). In this study, the contribution of Rb to the dose rate is disregarded for quartz but is incorporated into the dose rates for the K-feldspar samples because of the high measured K-contents.

External radiation is produced in roughly equal amounts by potassium-40 (^{40}K) and the uranium-238 (^{238}U) and thorium-232 (^{232}Th) decay chains, with a smaller contribution from uranium-235 (^{235}U) and rubidium-87 (^{87}Rb) (Aitken, 1985; De Corte et al., 2007). Beta (β) and γ radiation from these sources is by far the dominant contributor to the external dose rate compared with α and cosmic radiation (Aitken, 1985; Ankjærgaard and Murray, 2007; Guérin et al., 2012).

3.4.1 Emission counting methods

Dosimetry analyses for this research were undertaken using emission counting methods, which measure the α and β particles, and γ ray emissions, and then use these when necessary to calculate the parent radionuclide concentrations. This approach to dosimetry relies on the assumption of an infinite matrix, where the dosimeter in question is located within a sphere with a radius greater than the distance travelled by the relevant radioactive particle/ray, and the sphere is composed of a homogeneous

sediment with evenly dispersed radioisotopes (Aitken, 1985; Guérin et al., 2012; Nathan and Mauz, 2008). This assumption allows the conversion of radioisotope concentrations into α, β and γ dose rates and vice versa using conversion factors (e.g. Adamiec and Aitken, 1998; Guérin et al., 2011; Liritzis et al., 2013). The assumption of a homogeneous matrix is most likely to be violated for the γ dose since this originates from a sphere ~30 cm in radius. One means of overcoming any heterogeneity on this scale is to make in-situ measurements.

In this study, in-situ field gamma spectroscopy (FGS) measurements were used in conjunction with laboratory thick source alpha counting (TSAC) and Geiger-Muller beta counting (GMBC) measurements to determine the γ, α and β dose rates, respectively. The cosmic dose rate was calculated as described in Prescott and Hutton (1994). Table 3.3 includes the measured alpha, beta and gamma activities and the radioisotope concentrations determined from TSAC and GMBC for each sample.

3.4.2 Thick source alpha counting (TSAC)

The radioactive decay of Th and U results in the emission of alpha particles, which can be measured via thick source alpha counting (TSAC) and used to estimate the Th and U concentration within a sample. The pairs counting method outlined in Appendix J of Aitken (1985) was used in this study, and all TSAC measurements were undertaken on Daybreak 582 and 583 alpha counters.

Table 3.3: Uncorrected in-situ field and laboratory dosimetry measurements.

Sample ID	Field WC (%)	Field γ activity (Gy/ka)	Infinite matrix β activity (Gy/ka)	α count rate (cts/ks/cm^2)	Sealed/ Unsealed ratio	U conc. (ppm)	Th conc. (ppm)	Internal K content (wt%)
162/MPT3	1.9	-	1.31 ± 0.05	0.30 ± 0.01	0.92 ± 0.03	1.21 ± 0.16	4.34 ± 0.51	12.33 ± 0.57
162/MPT4	1.3	-	1.92 ± 0.06	0.25 ± 0.01	0.95 ± 0.04	0.82 ± 0.15	4.20 ± 0.48	12.56 ± 0.81
162/MPT6	1.2	-	1.48 ± 0.05	0.25 ± 0.01	1.02 ± 0.04	0.63 ± 0.16	4.84 ± 0.51	7.26 ± 1.07
170/MPT7	1.4	-	1.21 ± 0.04	0.19 ± 0.01	1.01 ± 0.03	0.77 ± 0.10	2.69 ± 0.32	4.32 ± 0.06
170/MPT8	1.2	-	1.29 ± 0.04	0.46 ± 0.01	0.92 ± 0.03	1.67 ± 0.27	7.50 ± 0.88	6.21 ± 0.39
170/MPT9	1.4	-	1.18 ± 0.04	0.25 ± 0.01	1.01 ± 0.04	0.89 ± 0.13	4.04 ± 0.42	3.97 ± 0.07
170/MPT10	20.0	-	1.67 ± 0.06	0.32 ± 0.01	1.03 ± 0.03	1.68 ± 0.14	3.43 ± 0.47	5.25 ± 0.03
170/MPT12	0.4	-	1.95 ± 0.06	0.31 ± 0.01	1.02 ± 0.03	1.49 ± 0.16	3.83 ± 0.51	11.81 ± 0.86
170/MPT13	0.4	-	1.81 ± 0.06	0.34 ± 0.01	0.94 ± 0.03	1.49 ± 0.17	4.47 ± 0.56	11.98 ± 0.56
170/MPT14	0.5	-	1.27 ± 0.04	0.30 ± 0.01	0.96 ± 0.03	1.34 ± 0.15	3.83 ± 0.49	9.41 ± 0.55
215/VRD01	3.2	1.15 ± 0.06	2.35 ± 0.09	0.54 ± 0.01	1.00 ± 0.03	2.57 ± 0.26	6.62 ± 0.86	11.40 ± 0.60
215/VRD02	2.0	1.07 ± 0.05	2.09 ± 0.03	0.46 ± 0.01	1.07 ± 0.04	2.31 ± 0.22	5.15 ± 0.73	10.66 ± 0.20
215/VRD03	0.9	1.06 ± 0.05	2.52 ± 0.13	0.43 ± 0.01	0.99 ± 0.04	2.11 ± 0.20	5.04 ± 0.67	15.13 ± 1.13
215/VRD04	1.7	1.03 ± 0.05	2.47 ± 0.09	0.46 ± 0.01	1.03 ± 0.04	2.25 ± 0.22	5.27 ± 0.73	14.57 ± 0.71
215/VRD05	1.3	1.28 ± 0.06	2.72 ± 0.11	0.50 ± 0.01	0.93 ± 0.03	2.07 ± 0.27	7.17 ± 0.88	15.47 ± 0.24
215/VRD06	1.0	1.07 ± 0.05	2.41 ± 0.11	0.45 ± 0.01	1.00 ± 0.03	1.97 ± 0.22	6.14 ± 0.74	11.15 ± 0.61
215/VRD07	1.7	1.08 ± 0.05	2.90 ± 0.14	0.45 ± 0.01	1.04 ± 0.04	1.91 ± 0.23	6.23 ± 0.74	14.24 ± 0.46
215/VRD08	0.5	1.12 ± 0.05	2.40 ± 0.02	0.42 ± 0.01	0.99 ± 0.03	1.84 ± 0.22	5.67 ± 0.71	14.25 ± 0.68
215/VRD09	1.9	1.15 ± 0.05	2.74 ± 0.09	0.56 ± 0.01	1.06 ± 0.04	2.99 ± 0.27	5.77 ± 0.87	14.50 ± 1.15
215/VRD10	4.1	1.66 ± 0.08	3.19 ± 0.12	0.85 ± 0.01	1.00 ± 0.03	3.61 ± 0.40	11.85 ± 1.31	10.11 ± 0.44

Continued on next page

Table 3.3 (cont.): Uncorrected in-situ field and laboratory dosimetry measurements.

Sample ID	Field WC (%)	Field γ activity (Gy/ka)	Infinite matrix β activity (Gy/ka)	α count rate (cts/ks/cm^2)	Sealed/ Unsealed ratio	U conc. (ppm)	Th conc. (ppm)	Internal K content (wt%)
215/STP01	2.9	2.03 ± 0.10	2.48 ± 0.08	1.67 ± 0.03	1.02 ± 0.03	8.02 ± 0.80	20.16 ± 2.66	8.81 ± 0.25
215/STP02	3.6	2.50 ± 0.12	3.09 ± 0.13	1.64 ± 0.03	1.03 ± 0.03	7.14 ± 0.82	22.38 ± 2.75	10.92 ± 0.51
215/STP03	4.8	1.40 ± 0.07	2.43 ± 0.02	0.95 ± 0.01	1.01 ± 0.03	4.83 ± 0.39	10.63 ± 1.29	10.65 ± 0.45
215/STP04	1.3	-	2.89 ± 0.06	1.76 ± 0.03	0.96 ± 0.03	7.90 ± 0.86	23.29 ± 2.87	11.29 ± 0.80
215/STP05	2.2	1.19 ± 0.06	1.66 ± 0.03	0.68 ± 0.01	1.03 ± 0.04	3.42 ± 0.32	7.75 ± 1.06	12.92 ± 0.57
215/STP06	2.8	1.36 ± 0.07	2.10 ± 0.09	0.80 ± 0.01	1.01 ± 0.04	4.07 ± 0.31	8.81 ± 1.03	9.47 ± 0.74
215/STP07	1.8	-	2.10 ± 0.06	0.85 ± 0.02	0.98 ± 0.03	4.79 ± 0.40	7.90 ± 1.29	9.18 ± 0.24
215/STP08	8.0	2.59 ± 0.13	4.02 ± 0.01	2.81 ± 0.05	1.05 ± 0.04	13.40 ± 1.74	34.27 ± 5.82	11.58 ± 1.01
215/STP09	1.0	1.61 ± 0.08	2.08 ± 0.07	1.20 ± 0.02	0.99 ± 0.02	5.28 ± 0.67	16.05 ± 2.21	14.33 ± 0.11
215/STP10	3.0	1.30 ± 0.07	1.97 ± 0.08	0.88 ± 0.02	0.92 ± 0.03	3.82 ± 0.46	11.95 ± 1.51	11.34 ± 0.90
218/GGD01	5.6	-	2.16 ± 0.10	0.73 ± 0.01	1.02 ± 0.04	3.09 ± 0.40	10.32 ± 1.33	10.77 ± 0.45
218/GGD02	16.5	-	2.46 ± 0.07	0.74 ± 0.01	0.99 ± 0.03	3.68 ± 0.38	8.58 ± 1.24	6.61 ± 0.17
218/GGD03	9.6	1.54 ± 0.08	2.47 ± 0.02	0.85 ± 0.02	1.01 ± 0.03	4.35 ± 0.42	9.26 ± 1.37	5.19 ± 0.11
218/GGD04	10.1	1.58 ± 0.08	2.66 ± 0.05	0.99 ± 0.02	1.02 ± 0.03	5.89 ± 0.46	7.96 ± 1.49	9.10 ± 0.43
218/GGD05	9.0	1.35 ± 0.07	2.37 ± 0.07	0.68 ± 0.01	1.00 ± 0.04	3.21 ± 0.31	8.37 ± 1.03	10.11 ± 0.41
218/GGD06	6.7	1.41 ± 0.07	2.65 ± 0.02	0.79 ± 0.01	0.97 ± 0.03	4.04 ± 0.40	8.74 ± 1.31	7.82 ± 0.51
218/GGD07	12.2	1.54 ± 0.08	2.78 ± 0.06	0.89 ± 0.02	1.01 ± 0.04	5.05 ± 0.40	8.05 ± 1.31	10.17 ± 0.62
218/GGD08	5.2	1.41 ± 0.07	2.37 ± 0.03	0.67 ± 0.01	1.00 ± 0.04	3.34 ± 0.30	7.60 ± 0.99	10.26 ± 0.43

The pairs counting method compares the number of pairs counted to the total number of alpha particles detected, to determine the radionuclide concentrations. Emitted alpha particles produce scintillations of light when they collide with a zinc sulphide (ZnS) screen, which are measured by a photomultiplier (Aitken, 1985). In the ^{232}Th decay series (see Figure 3.5), the successive alpha decays of ^{220}Rn ($t_{1/2}$ = 55.6 s) and ^{216}Po ($t_{1/2}$ = 0.145 s) produce two scintillations observed in quick succession (termed 'slow pairs'), which account for ~3 % of the counts emitted by the Th decay chain. By contrast, in the ^{235}U series (see Figure 3.5), ^{219}Rn ($t_{1/2}$ = 3.96 s) decays into ^{215}Po ($t_{1/2}$ = 0.002 s) and these two scintillations are termed 'fast pairs'. The Daybreak counters are set up to count slow and fast pairs separately, with slow pairs being able to be used to determine the concentration of Th.

Prior to counting samples, the background counts for two ZnS screens were measured by placing two screens face to face in the holder. A glass screen covered them to prevent any contribution of atmospheric radon (Rn) in the count. Each background measurement was monitored hourly during the first 8 hours to ensure a linear count rate, with a minimum counting time of 24 hours.

Samples were dried and milled in a TEMA mill to obtain a homogeneous powder. The powdered sample was placed in a Perspex holder, spread evenly to a thickness > 1 mm over a ZnS screen held in place by a retaining ring. This produces an α thick layer of sample, contained within a well-defined counting area. Individual samples were counted twice to assess the possibility of disequilibrium in the decay chain, whereby gaseous daughter products (particularly ^{222}Rn which has a half-life ($t_{1/2}$) of 3.82 days in the ^{238}U decay series) have the potential to diffuse out of the sediment sample

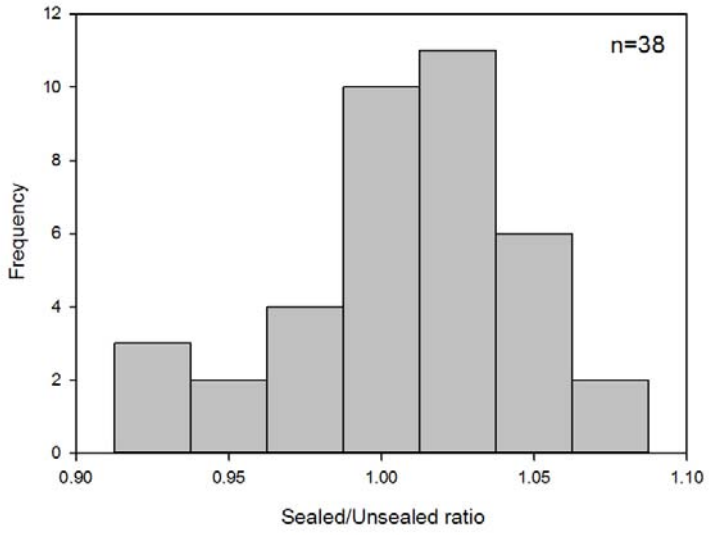

Figure 3.6: Sealed/unsealed ratios for TSAC measurements.

during preparation and storage. If this process occurs, the amount of parent activity will be higher than the activity of Rn and all subsequent daughter radioisotopes. Thus, an 'unsealed' alpha count was recorded by placing wooden spacers between the pot and lid and counting for a minimum of 3000 counts, followed by a 'sealed' alpha count for a minimum of 1000 counts, during which the spacers were removed and the pot sealed. The sealed/unsealed ratio should be within 10 % of unity for samples that are in equilibrium where no Rn loss has occurred (Aitken, 1985). Figure 3.6 shows the sealed/unsealed ratios measured for all samples during this research. The distribution of values is broadly symmetrical about unity and all samples fall within the optimum range of 0.90 to 1.10. Therefore, there is no need for further investigation into the possibility of radioactive disequilibrium.

3.4.3 GM beta counting (GMBC)

The α and β counting techniques used during this study were non-destructive, so the same powdered, homogenised sub-sample was used for both TSAC and GMBC methods. Thick source beta counting measures the total β emission from U, Th and K in a homogenised sample. All β counting for this research was carried out on a low level Risø GM-25-5 beta counter (Figure 3.7). The system comprises five individual Geiger-Mueller (GM) cylindrical counter elements with a common guard counter, all of which are gas flow type counters designed for use with 99 % argon and 1 % isobutane (Bøtter-Jensen and Mejdahl, 1988). External radiation in the form of cosmic rays is reduced by the guard counter, which detects and rejects coincident counts between the guard counter and the GM detectors, and by the 10 cm thick lead shield surrounding the instrument. Sample pots are placed on a slide below the GM detectors allowing five samples to be loaded simultaneously, and are raised by a lift slide to minimise the sample-to-window distance. This ensures accurate and reproducible sample positioning.

The dried and milled sample was packed into a Perspex pot, with internal dimensions of 21 mm diameter and 7 mm depth (and thus β thick). The top of the sample was levelled and the pot covered with cling film in order to prevent contamination of the instrument. Individual samples were counted in triplicate, with the remaining positions in the instrument used to measure two standards of known radioactivity. Counting continued until ~3000 counts were obtained for each sample. The two standards used are Shap granite and magnesium oxide (MgO) powder standards, with dose

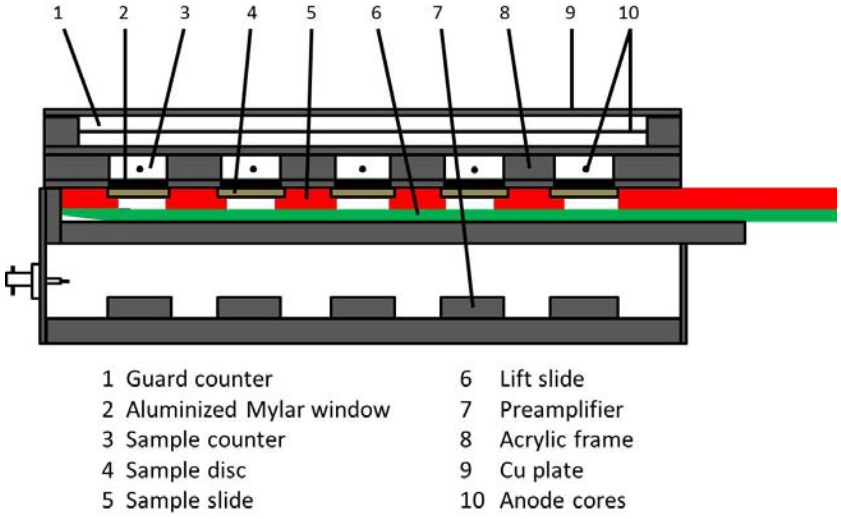

Figure 3.7: Schematic diagram of the GM-25-5 beta counter illustrating the various components, specifically the (1) guard counter, (2) Mylar window, (3) sample counter, (4) sample pot, (5) sample slide, (6) lift slide, (7) preamplifier, (8) acrylic frame, (9) copper plate and (10) anode cores (redrawn from Bøtter-Jensen and Mejdahl (1988)).

rates of 6.07 Gy/ka and 0.00 Gy/ka respectively. The raw counts were position corrected for minor variations in the GM detector efficiency, using values calculated from analyses of a ^{36}Cl standard. The resulting corrected counts were converted into β dose rates for each sample position using the known dose rates of the standard materials. The calculated dose rates from each position were averaged to determine the infinite matrix β dose rate for the sample, with uncertainty cited as the standard deviation (see Table 3.3).

Additional GMBC measurements were made to determine the K-content (see Table 3.3) of the density-separated K-feldspar material (2.53 – 2.58 g/cm^3) using the process described above. However, in these measurements three replicate sample pots containing 0.1 g of sample were counted with two standards of known K concentration, specifically MgO (0.00 %K) and

70a (9.794 %K). Once again, the raw counts were position corrected and K concentrations calculated using the same method as the beta dose rates.

3.4.4 Field gamma spectrometry (FGS)

In-situ gamma spectrometry measurements were made using an Ortec DigiDart portable field spectrometer with a 2″ x 2″ NaI(Tl) detector. The spectrometer was calibrated using the set of radioactive doped blocks at the Research Laboratory for Archaeology and the History of Art at Oxford (see Murray et al., 1978; Rhodes and Schwenninger, 2007). The blocks are made of concrete mixed with pitchblende (U), monazite sand (Th) and sulphate of potash (K) to increase their radioactivity, and have a known gamma dose rate and chemical composition; with one block each for U, Th and K and a non-doped block for use as a background.

In-situ measurements were made in the field directly following sample collection, using the hole left by the removal of the metal sampling tube. The diameter of the hole was increased using a hand auger to allow the detection crystal to fit tightly. Measurements were usually recorded for a minimum of 60 minutes, but several samples were counted 40 minutes or 30 minutes due to inclement weather and time constraints.

Analysis of the γ spectrometry data using the 'threshold' technique described by Mercier and Falgures (2007), which identifies a threshold value (or triple point) where the count rate of the detector is independent of the individual U, Th and K contributions to the gamma dose rate. This was done by measuring the gamma spectrum from U, Th and K (using the Oxford doped blocks) and subtracting the background signal from the non-doped block to obtain a pure spectrum. The individual spectra were

then normalised by the dose rate of each block and plotted as cumulative spectra as a function of energy (in cts/ks/Gy/ka). Finally the standard deviation of the three curves was computed, allowing the threshold value (or triple point) to be defined. The threshold value is usually in the region of 350 – 450 keV (see Løvborg and Kirke, 1974; Murray et al., 1978). The threshold approach integrates the total counts above a fixed energy, which uses a larger portion of the spectrum than the window approach, which identifies specific high-energy gamma peaks centred on the ^{40}K, ^{214}Bi and ^{208}Tl radioisotopes. This significantly reduces the counting time, which limits the effect of temperature changes during measurement. The overall error on the measurement is estimated to be ~5 % (Mercier and Falgures, 2007).

3.5 Deriving the environmental dose rate

The environmental dose rate comprises one half of the luminescence age equation (Equation 1.1). The parameters included in the calculation of the environmental dose rate are determined by the dosimeter (i.e. quartz or K-feldspar) used in the luminescence measurements as well as the laboratory preparation procedure. Parameters to be considered include the contribution from external and internal alpha and beta radiation, external gamma radiation, and cosmic radiation. This section will outline the process followed to calculate the environmental dose rate from the TSAC, GMBC and FGS measurements undertaken during this study. All dose rate calculations were made in the ALRL database (LDB2016), written by Geoff Duller as per the method described below. The attenuated dose rates (corrected for grain

size and water content) used to calculate the total environmental dose rate are included in Table 3.4 for quartz and Table 3.5 for K-feldspar.

3.5.1 Alpha dose rate

When working with coarse grains, the effect of etching the grains in HF acid is to remove the external alpha dose rate (D_α) contribution. Thus the D_α is disregarded for all quartz samples in this research because of the etching step. Due to the fact that the K-feldspar was not HF acid etched during preparation (see Section 3.2.6) the external D_α must be included in the K-feldspar dosimetry calculations. The external D_α was calculated using the pairs counting method described in Section 3.4.2, whereby the α emissions of U and Th are counted and the total counts converted into U and Th concentrations. These concentrations were converted to dose rates using the conversion factors of Guérin et al. (2011) and summed to determine the total D_α.

The external α contribution to the total environmental dose rate is typically ~3 % for the samples from Voordrag and the Moopetsi tributary site, ~5 % for Goedgedacht and ~7 % for the St Paul's site. This illustrates that the proportion of the dose rate coming from U and Th is larger at the St Paul's site, which may explain the relatively high dose rates (see Tables 3.4 and 3.5) and different behaviour of some of these samples (see Section 3.5.4).

Table 3.4: Dose rates for quartz samples corrected for grain size and water content.

Sample ID	Depth (m)	WC (%)	External β dose rate (Gy/ka)	External γ dose rate (Gy/ka)	Cosmic dose rate (Gy/ka)	Environmental dose rate (Gy/ka)
162/MPT3	2.6	15 ± 5	0.97 ± 0.06	0.56 ± 0.04	0.15 ± 0.02	1.69 ± 0.07
162/MPT4	4.2	15 ± 5	1.42 ± 0.09	0.70 ± 0.05	0.13 ± 0.01	2.25 ± 0.10
162/MPT6	7.65	15 ± 5	1.09 ± 0.07	0.59 ± 0.04	0.09 ± 0.01	1.77 ± 0.08
170/MPT7	8.05	15 ± 5	0.89 ± 0.06	0.46 ± 0.03	0.09 ± 0.01	1.44 ± 0.06
170/MPT8	0.3	15 ± 5	0.95 ± 0.06	0.69 ± 0.06	0.20 ± 0.02	1.84 ± 0.09
170/MPT9	5.25	15 ± 5	0.87 ± 0.06	0.50 ± 0.03	0.11 ± 0.01	1.49 ± 0.07
170/MPT10	3.7	15 ± 5	1.24 ± 0.08	0.66 ± 0.04	0.14 ± 0.01	2.03 ± 0.09
170/MPT12	0.4	15 ± 5	1.44 ± 0.09	0.73 ± 0.05	0.20 ± 0.02	2.37 ± 0.10
170/MPT13	2.8	15 ± 5	1.34 ± 0.08	0.72 ± 0.05	0.15 ± 0.02	2.20 ± 0.10
170/MPT14	4.05	15 ± 5	0.94 ± 0.06	0.54 ± 0.04	0.13 ± 0.01	1.61 ± 0.07
215/VRD01	12	30 ± 5	1.52 ± 0.08	0.89 ± 0.06	0.06 ± 0.01	2.48 ± 0.10
215/VRD02	10	30 ± 5	1.36 ± 0.08	0.81 ± 0.05	0.08 ± 0.01	2.25 ± 0.09
215/VRD03	8.7	30 ± 5	1.63 ± 0.09	0.80 ± 0.05	0.09 ± 0.01	2.52 ± 0.11
215/VRD04	8.1	30 ± 5	1.60 ± 0.09	0.79 ± 0.05	0.09 ± 0.01	2.48 ± 0.10
215/VRD05	7.3	30 ± 5	1.76 ± 0.10	0.97 ± 0.06	0.10 ± 0.01	2.82 ± 0.12
215/VRD06	5.7	30 ± 5	1.56 ± 0.09	0.81 ± 0.05	0.12 ± 0.01	2.48 ± 0.10
215/VRD07	4.1	30 ± 5	1.87 ± 0.11	0.82 ± 0.05	0.14 ± 0.01	2.84 ± 0.12
215/VRD08	3.4	30 ± 5	1.56 ± 0.09	0.84 ± 0.06	0.15 ± 0.01	2.55 ± 0.10
215/VRD09	0.3	30 ± 5	1.77 ± 0.10	0.87 ± 0.06	0.22 ± 0.02	2.86 ± 0.12
215/VRD10	14.5	30 ± 5	2.07 ± 0.12	1.30 ± 0.09	0.05 ± 0.01	3.41 ± 0.14

Continued on next page

Table 3.4 (cont.): Dose rates for quartz samples corrected for grain size and water content.

Sample ID	Depth (m)	WC (%)	External β dose rate (Gy/ka)	External γ dose rate (Gy/ka)	Cosmic dose rate (Gy/ka)	Environmental dose rate (Gy/ka)
215/STP01	17	15 ± 5	1.86 ± 0.12	1.79 ± 0.13	0.05 ± 0.01	3.70 ± 0.17
215/STP02	18	15 ± 5	2.31 ± 0.14	2.22 ± 0.16	0.04 ± 0.00	4.58 ± 0.21
215/STP03	13.6	15 ± 5	1.82 ± 0.11	1.27 ± 0.09	0.06 ± 0.01	3.15 ± 0.14
215/STP04	12.9	15 ± 5	2.17 ± 0.13	2.01 ± 0.18	0.06 ± 0.01	4.24 ± 0.22
215/STP05	16.4	15 ± 5	1.25 ± 0.08	1.04 ± 0.07	0.05 ± 0.01	2.34 ± 0.11
215/STP06	14.7	15 ± 5	1.57 ± 0.10	1.20 ± 0.08	0.05 ± 0.01	2.83 ± 0.13
215/STP07	7.3	15 ± 5	1.57 ± 0.10	1.10 ± 0.09	0.11 ± 0.01	2.78 ± 0.13
215/STP08	1.52	15 ± 5	3.01 ± 0.19	2.42 ± 0.17	0.20 ± 0.02	5.63 ± 0.25
215/STP09	1.2	15 ± 5	1.56 ± 0.10	1.39 ± 0.10	0.21 ± 0.02	3.16 ± 0.14
215/STP10	0.8	15 ± 5	1.48 ± 0.09	1.15 ± 0.08	0.22 ± 0.02	2.84 ± 0.12
218/GGD01	9.6	15 ± 5	1.62 ± 0.10	1.11 ± 0.09	0.09 ± 0.01	2.81 ± 0.14
218/GGD02	10	15 ± 5	1.81 ± 0.11	1.15 ± 0.09	0.08 ± 0.01	3.04 ± 0.14
218/GGD03	0.3	15 ± 5	1.85 ± 0.12	1.34 ± 0.09	0.24 ± 0.02	3.42 ± 0.15
218/GGD04	0.8	15 ± 5	2.00 ± 0.12	1.51 ± 0.11	0.22 ± 0.02	3.73 ± 0.16
218/GGD05	12.5	15 ± 5	1.77 ± 0.11	1.15 ± 0.08	0.07 ± 0.01	2.99 ± 0.14
218/GGD06	10.5	15 ± 5	1.99 ± 0.12	1.19 ± 0.08	0.08 ± 0.01	3.26 ± 0.15
218/GGD07	1.2	15 ± 5	2.08 ± 0.13	1.40 ± 0.10	0.21 ± 0.02	3.69 ± 0.16
218/GGD08	0.75	15 ± 5	1.78 ± 0.11	1.17 ± 0.08	0.23 ± 0.02	3.17 ± 0.14

Gamma dose rates in blue were calculated using U, Th and K concentrations from TSAC and GMBC

Table 3.5: Dose rates for K-feldspar samples corrected for grain size and water content.

Sample ID	Depth (m)	WC (%)	Internal β dose rate (Gy/ka)	External α dose rate (Gy/ka)	External β dose rate (Gy/ka)	External γ dose rate (Gy/ka)	Cosmic dose rate (Gy/ka)	Environmental dose rate (Gy/ka)
162/MPT3	2.6	15 ± 5	0.67 ± 0.06	0.07 ± 0.02	0.99 ± 0.06	0.56 ± 0.04	0.15 ± 0.02	2.45 ± 0.10
162/MPT4	4.2	15 ± 5	0.67 ± 0.06	0.06 ± 0.02	1.45 ± 0.09	0.70 ± 0.05	0.13 ± 0.01	3.01 ± 0.12
162/MPT6	7.65	15 ± 5	0.67 ± 0.06	0.06 ± 0.02	1.12 ± 0.07	0.59 ± 0.04	0.09 ± 0.01	2.53 ± 0.10
170/MPT7	8.05	15 ± 5	0.67 ± 0.06	0.04 ± 0.01	0.91 ± 0.06	0.46 ± 0.03	0.09 ± 0.01	2.17 ± 0.09
170/MPT8	0.3	15 ± 5	0.67 ± 0.06	0.11 ± 0.03	0.97 ± 0.06	0.69 ± 0.06	0.20 ± 0.02	2.65 ± 0.11
170/MPT9	5.25	15 ± 5	0.67 ± 0.06	0.06 ± 0.02	0.89 ± 0.06	0.50 ± 0.03	0.11 ± 0.01	2.23 ± 0.09
170/MPT10	3.7	15 ± 5	0.67 ± 0.06	0.08 ± 0.02	1.26 ± 0.08	0.66 ± 0.04	0.14 ± 0.01	2.80 ± 0.11
170/MPT12	0.4	15 ± 5	0.67 ± 0.06	0.08 ± 0.02	1.47 ± 0.09	0.73 ± 0.05	0.20 ± 0.02	3.15 ± 0.12
170/MPT13	2.8	15 ± 5	0.67 ± 0.06	0.08 ± 0.02	1.37 ± 0.09	0.72 ± 0.05	0.15 ± 0.02	2.98 ± 0.12
170/MPT14	4.05	15 ± 5	0.67 ± 0.06	0.07 ± 0.02	0.96 ± 0.06	0.54 ± 0.04	0.13 ± 0.01	2.37 ± 0.10
215/VRD01	12	30 ± 5	0.70 ± 0.06	0.11 ± 0.03	1.55 ± 0.09	0.89 ± 0.06	0.06 ± 0.01	3.32 ± 0.13
215/VRD02	10	30 ± 5	0.70 ± 0.06	0.09 ± 0.03	1.38 ± 0.08	0.81 ± 0.05	0.08 ± 0.01	3.07 ± 0.12
215/VRD03	8.7	30 ± 5	0.70 ± 0.06	0.09 ± 0.03	1.66 ± 0.09	0.80 ± 0.05	0.09 ± 0.01	3.34 ± 0.13
215/VRD04	8.1	30 ± 5	0.70 ± 0.06	0.09 ± 0.03	1.63 ± 0.09	0.79 ± 0.05	0.09 ± 0.01	3.30 ± 0.13
215/VRD05	7.3	30 ± 5	0.70 ± 0.06	0.10 ± 0.03	1.80 ± 0.10	0.97 ± 0.06	0.10 ± 0.01	3.66 ± 0.14
215/VRD06	5.7	30 ± 5	0.70 ± 0.06	0.09 ± 0.03	1.60 ± 0.09	0.81 ± 0.05	0.12 ± 0.01	3.31 ± 0.12
215/VRD07	4.1	30 ± 5	0.70 ± 0.06	0.09 ± 0.03	1.91 ± 0.11	0.82 ± 0.05	0.14 ± 0.01	3.67 ± 0.14
215/VRD08	3.4	30 ± 5	0.70 ± 0.06	0.09 ± 0.03	1.59 ± 0.09	0.84 ± 0.06	0.15 ± 0.01	3.37 ± 0.13
215/VRD09	0.3	30 ± 5	0.70 ± 0.06	0.12 ± 0.03	1.81 ± 0.10	0.87 ± 0.06	0.22 ± 0.02	3.72 ± 0.14
215/VRD10	14.5	30 ± 5	0.70 ± 0.06	0.17 ± 0.05	2.11 ± 0.12	1.30 ± 0.09	0.05 ± 0.01	4.33 ± 0.17

Continued on next page

Table 3.5 (cont.): Dose rates for K-feldspar samples corrected for grain size and water content.

Sample ID	Depth (m)	WC (%)	Internal β dose rate (Gy/ka)	External α dose rate (Gy/ka)	External β dose rate (Gy/ka)	External γ dose rate (Gy/ka)	Cosmic dose rate (Gy/ka)	Environmental dose rate (Gy/ka)
215/STP01	17	15 ± 5	0.70 ± 0.06	0.40 ± 0.12	1.90 ± 0.12	1.79 ± 0.13	0.05 ± 0.01	4.84 ± 0.22
215/STP02	18	15 ± 5	0.70 ± 0.06	0.39 ± 0.12	2.36 ± 0.15	2.22 ± 0.16	0.04 ± 0.00	5.72 ± 0.25
215/STP03	13.6	15 ± 5	0.70 ± 0.06	0.23 ± 0.07	1.86 ± 0.12	1.27 ± 0.09	0.06 ± 0.01	4.12 ± 0.17
215/STP04	12.9	15 ± 5	0.70 ± 0.06	0.42 ± 0.13	2.21 ± 0.14	2.01 ± 0.18	0.06 ± 0.01	5.41 ± 0.27
215/STP05	16.4	15 ± 5	0.70 ± 0.06	0.17 ± 0.05	1.27 ± 0.08	1.04 ± 0.07	0.05 ± 0.01	3.23 ± 0.13
215/STP06	14.7	15 ± 5	0.70 ± 0.06	0.19 ± 0.06	1.61 ± 0.10	1.20 ± 0.08	0.05 ± 0.01	3.76 ± 0.16
215/STP07	7.3	15 ± 5	0.70 ± 0.06	0.21 ± 0.06	1.61 ± 0.10	1.10 ± 0.09	0.11 ± 0.01	3.72 ± 0.16
215/STP08	1.52	15 ± 5	0.70 ± 0.06	0.68 ± 0.21	3.07 ± 0.19	2.42 ± 0.17	0.20 ± 0.02	7.07 ± 0.33
215/STP09	1.2	15 ± 5	0.70 ± 0.06	0.29 ± 0.09	1.59 ± 0.10	1.39 ± 0.10	0.21 ± 0.02	4.18 ± 0.18
215/STP10	0.8	15 ± 5	0.70 ± 0.06	0.21 ± 0.06	1.51 ± 0.09	1.15 ± 0.08	0.22 ± 0.02	3.79 ± 0.15
218/GGD01	9.6	15 ± 5	0.70 ± 0.06	0.18 ± 0.05	1.66 ± 0.10	1.11 ± 0.09	0.09 ± 0.01	3.72 ± 0.16
218/GGD02	10	15 ± 5	0.70 ± 0.06	0.18 ± 0.05	1.85 ± 0.12	1.15 ± 0.09	0.08 ± 0.01	3.96 ± 0.17
218/GGD03	0.3	15 ± 5	0.70 ± 0.06	0.21 ± 0.06	1.89 ± 0.12	1.34 ± 0.09	0.24 ± 0.02	4.37 ± 0.18
218/GGD04	0.8	15 ± 5	0.70 ± 0.06	0.24 ± 0.07	2.04 ± 0.13	1.51 ± 0.11	0.22 ± 0.02	4.71 ± 0.19
218/GGD05	12.5	15 ± 5	0.70 ± 0.06	0.16 ± 0.05	1.81 ± 0.11	1.15 ± 0.08	0.07 ± 0.01	3.90 ± 0.16
218/GGD06	10.5	15 ± 5	0.70 ± 0.06	0.19 ± 0.06	2.03 ± 0.13	1.19 ± 0.08	0.08 ± 0.01	4.20 ± 0.17
218/GGD07	1.2	15 ± 5	0.70 ± 0.06	0.22 ± 0.06	2.13 ± 0.13	1.40 ± 0.10	0.21 ± 0.02	4.66 ± 0.19
218/GGD08	0.75	15 ± 5	0.70 ± 0.06	0.16 ± 0.05	1.81 ± 0.11	1.17 ± 0.08	0.23 ± 0.02	4.07 ± 0.16

Gamma dose rates in blue were calculated using U, Th and K concentrations from TSAC and GMBC

Alpha particles have a very short travel distance (~3 μm), thus when working with coarse grains ~200 μm in size, it is possible to have an internal α dose contribution. Quartz typically has very low U and Th concentrations. Thus, whilst a small amount of α activity may be produced within the individual grain, it is commonly assumed that the internal dose rate of quartz grains is negligible (Aitken, 1998). In situations where external dose rates are very low, it would be prudent to ascertain the internal dose rate via α counting. Jacobs (2004) measured an attenuated internal alpha dose rate of 0.029 $\pm$ 0.002 Gy/ka for quartz from Blombos Cave in South Africa, which contributed < 3 % to the total dose rate of the sample with the lowest environmental dose rate. For this research, a dose rate of 0.029 Gy/ka (Jacobs, 2004) would contribute < 1 % to the overall environmental dose rate, thus it was deemed that the internal alpha contribution from quartz was negligible (as suggested by Aitken (1998)) and the contribution was omitted.

Naturally occurring K-feldspar typically contains low concentrations of U and Th, making the effective internal alpha dose rate contribution to the environmental dose rate minimal (Duller, 1992; Mejdahl, 1987). Two approaches are generally taken when considering the internal alpha dose contribution for K-feldspar. Either a negligible contribution is assumed (e.g. Duller, 1992; Reimann et al., 2012; Rhodes, 2015) or an internal dose rate of 0.10 $\pm$ 0.05 Gy/ka is applied after Mejdahl (1987) (e.g. Buylaert et al., 2011a; Sohbati et al., 2012; Wallinga et al., 2001). Smedley and Pearce (2016) measured the concentration of U and Th in single grains of feldspar using LA-ICP-MS and determined that grain-to-grain variability in the U and Th concentration was linked to mineral composition, and K-rich

feldspars displayed characteristically low ($\sim$ 0.1 Gy/ka) internal alpha dose rates. Based on the high K-contents measured for the K-feldspar samples, and the minor contribution the internal D_α will make to the total dose rate when compared to the internal β dose rate, the first approach has been adopted in this study. The internal α component was assumed to be negligible and the contribution omitted from the total dose rate calculation.

3.5.2 Beta rose rates

The external beta dose rate (D_β) is measured directly using the GMBC procedure described in Section 3.4.3 and only requires correction for grain size and water content to give the effective D_β for the samples (Tables 3.4 and 3.5).

K-feldspar grains have high concentrations of potassium, and thus the internal beta dose rate makes up a large proportion ($\sim$15 – 20 % in this study) of the total environmental dose rate. The average K-content measured for the separated feldspar grains is 11.7 % with the majority of these values clustered around 12 %K (Figure 3.8). There are several samples with low K contents, particularly from the Moopetsi tributary site, which represent the oldest samples stratigraphically. It is conceivable that these low K-contents may be due to weathering processes, since this can result in leaching of K from the feldspar and the formation of clay minerals (Parish, 1994). Alternatively, the low K-contents could be due to the nature of the bedrock material. The K-content varies across each site and there is no clear correlation between decreasing K-content and depth.

Measurements are seldom made of the internal K-content, and for the purposes of calculating the internal beta dose rate an assumed value is

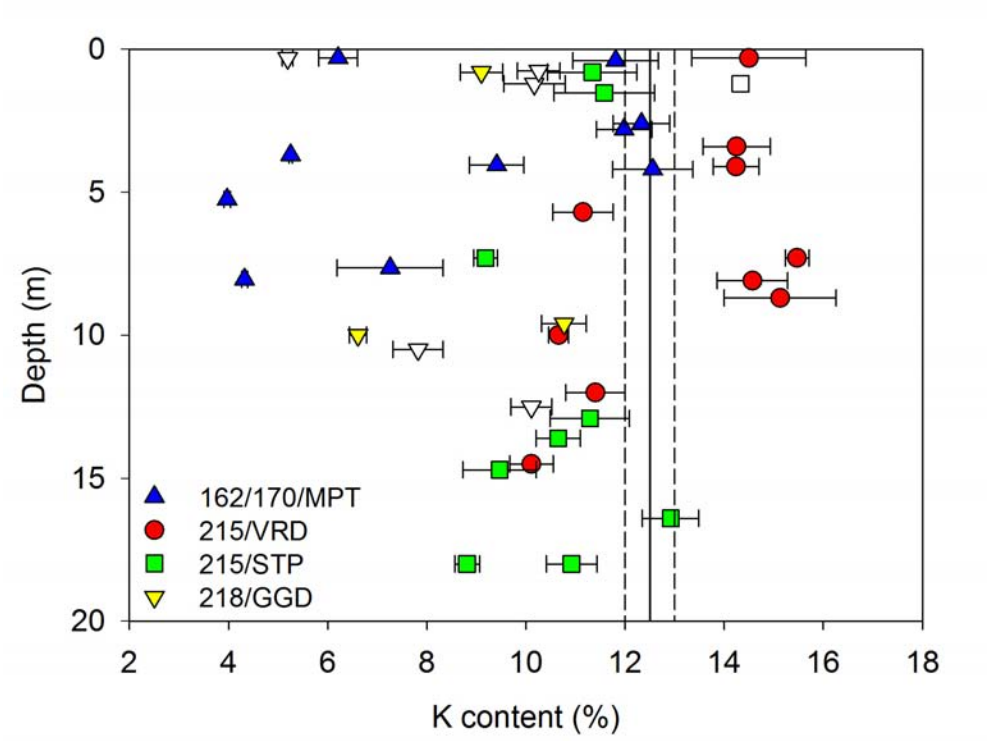

Figure 3.8: Measured K-contents for all K-feldspar samples processed during this study. Open symbols denote the samples that were ultimately not used for dating.

generally applied. The value of 12.5 ± 0.5 % was determined by Huntley and Baril (1997) (based on 21 samples from 7 distinct geographical areas) as a suitably conservative estimate for the K-content of K-feldspar, given that the maximum concentration of K in a feldspar lattice is 14 %. Smedley et al. (2012) proposed an assumed internal K-content of 10 ± 2 % for single grains of K-feldspar based on a single sample. They also analysed the K-content with depth in 12 grains and identified a sub-set that had lower K-content on the surface of the grain compared to the centre, which they attributed to the possibility of weathering and the lack of an HF etch during the laboratory preparation of samples. Given the overall high K-contents measured for these samples, and considering the three lower K-contents

at the Moopetsi tributary site which may be due to weathering, for the purposes of internal beta dose rate determination in this study, the internal K-content was assumed to be 12.5 ± 0.5 %.

In order to obtain the internal D_β, the K-content was multiplied by the conversion factors of Guérin et al. (2011). The contribution of Rb to the beta dose rate must be considered due to the high measured K-contents. Mejdahl (1987) calculated that the beta dose contribution from Rb is ~3 % of the contribution from K for grain size between 100 μm and 300 μm. Therefore, the Rb content was inferred from the K-content based on a ratio of 200:1 and converted to a dose rate using the conversion factors.

3.5.3 Gamma dose rate

Gamma dose rates (D_γ) were determined directly from in-situ measurements using a portable field gamma spectrometer, as discussed in Section 3.4.4. In-situ measurements made in this way take into account the modern water content. Thus the measured D_γ was corrected for modern water content measured during the sample preparation stage (see Section 3.2.7) to obtain a dry dose rate that can be used in the environmental dose rate calculation. The estimated water content during burial (which is almost always larger than the water content measured during sampling) can then be applied.

In the few instances where in-situ FGS was unable to be measured, the U and Th concentrations calculated from TSAC and the K concentration for the bulk sediment calculated from GMBC were used in conjunction with conversion factors (Guérin et al., 2011) to calculate the gamma dose rate. These D_γ are highlighted in blue in Tables 3.4 and 3.5. In-situ FGS measurements were not made for the Moopetsi samples which were collected

by R. Lyons and S. Tooth and so all of these gamma dose rates are calculated using the radioisotope concentrations and conversion factors.

3.5.4 Assessing the internal consistency of dose rate measurements

The availability of multiple dosimetry methods makes it possible to assess the internal consistency of the dose rate measurements made during this study. As FGS data was not available for every sample, it was of paramount importance to show that the two techniques of determining the D_γ were comparable. Figure 3.9 shows the unattenuated D_γ calculated using FGS (corrected for the modern water content) plotted against the D_γ calculated using the radioisotope concentrations determined by TSAC with GMBC. All three sites show a good correlation, with average ratios of 0.97 ± 0.07, 1.02 ± 0.09 and 1.07 ± 0.09 measured for the Voordrag, St Paul's and Goedgedacht sites respectively. The only obvious outlier within this dataset is the value for 215/STP08. This sample gave a value of D_γ consistently higher than all other samples. No reasons were found to exclude this sample.

An additional check for internal consistency within the dose rate measurements can be undertaken by comparing the unattenuated infinite matrix D_β with the D_γ. Ankjærgaard and Murray (2007) reported a γ to β dose rate ratio of 0.496 for 3700 samples, based on GMBC and gamma spectrometry. A similar ratio of 0.59 with a standard deviation of 0.13 was reported by Roberts et al. (2009), based on 427 samples measured at the ALRL using GMBC and TSAC. Figure 3.10 shows the relationship between the unattenuated dry β and γ dose rates measured for each sample in this study, as grouped by sampling site. Also plotted is the γ to β dose rate

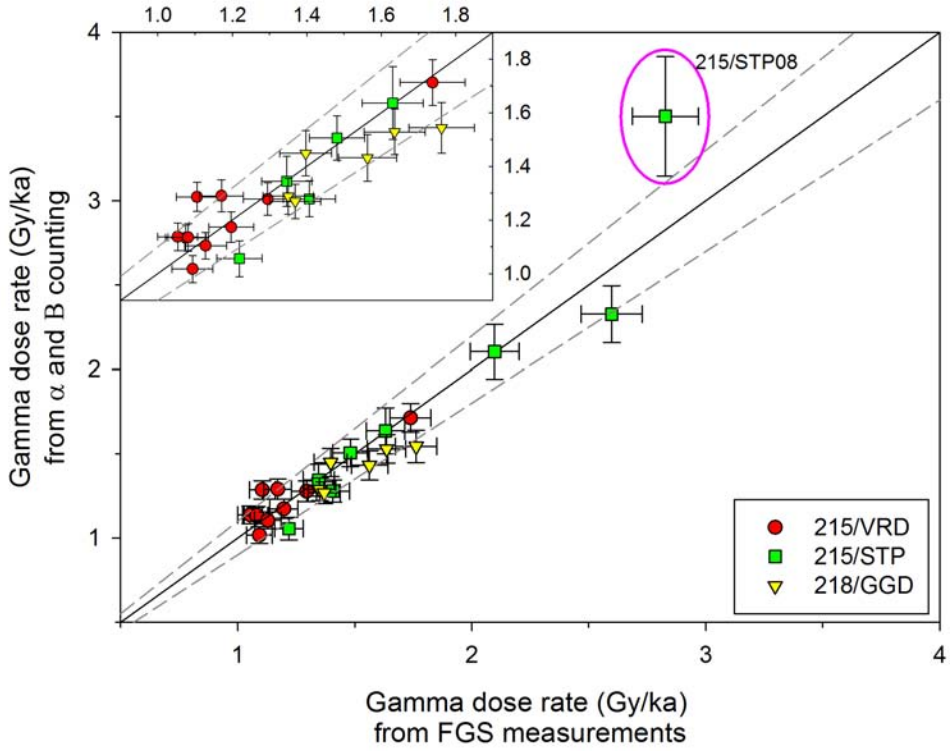

Figure 3.9: Comparison of dry, unattenuated gamma dose rates calculated from in-situ field gamma spectrometry measurements (corrected for measured water content) and laboratory alpha and beta counting. Inset shows enlarged region between 1 Gy/ka and 2 Gy/ka.

ratio of Roberts et al. (2009), as these measurements were made in the ALRL using the same equipment. Samples from each field site form separate trends, albeit with some overlap. This can most likely be ascribed to the different source materials at various site locations, resulting in different relative concentrations of U, Th and K and hence dose rate ratios.

3.5.5 Corrections applied to dose rates

To derive the dose rate received during burial by the grains used for luminescence dating several factors need to be taken into account. These

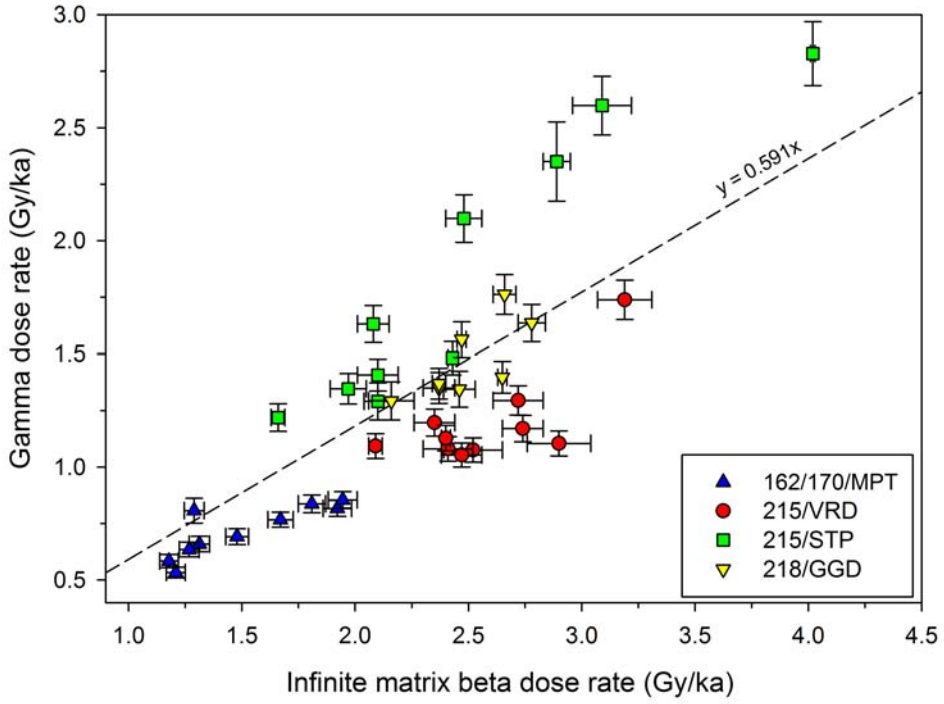

Figure 3.10: Comparison of unattenuated, dry beta and gamma dose rates measured for all four sites, using GM-beta counting, FGS, and TSAC where FGS was unavailable. The dashed line shows the ratio between gamma and beta dose rates reported by Roberts et al. (2009).

include (i) the efficiency of α particles relative to β particles and γ rays, (ii) the effect of attenuation due to grain size on α and β particles, (iii) the effect of etching on α and β dose rates, and (iv) the effect of the moisture content of the surrounding sediment on the dose rates.

3.5.5.1 Efficiency of alpha radiation

Alpha radiation has a lower efficiency than β and γ radiation (Brennan, 2006; De Corte et al., 2007), therefore a correction in the form of an a-value is applied to the D_α. Several published a-values for feldspar have been reported (see Aitken, 1998; Balescu and Lamothe, 1994; Balescu et al., 2007;

Kolstrup and Mejdahl, 1986; Kreutzer et al., 2014). However, the only measured a-value for coarse grain feldspars available is 0.11 ± 0.03 cited by Balescu and Lamothe (1993). Therefore, this a-value is applied to all external α dose rates calculated for K-feldspar samples.

3.5.5.2 Attenuation for grain size

The effects of attenuation can be seen on both α particles (Aitken, 1985; Bell, 1980) and β particles (Aitken, 1985; Bell, 1979; Brennan, 2003; Fain et al., 1999; Mejdahl, 1979) with the degree of attenuation directly dependent on grain size and the energy of emission, which differs for U, Th and K. Due to their large mass, α particles have a limited range, and so the average D_α received by a grain decreases rapidly with grain size. Bell (1980) determined alpha attenuation factors for quartz grains ranging from 1 μm to 1000 μm in diameter for both the U and Th decay series individually. Where the chemical composition of the sediment is unknown, it is assumed that both decay series are contributing equally to the dose rate and a mean of the two values is used as the attenuation factor. Alpha attenuation factors for K-feldspar are presumed to be 7 % less than those for quartz, based on measurements made on 100 μm K-feldspar grains by Bell (1980). Also, because α particles have a greater range in feldspars than in quartz, the attenuation of dose is smaller in the former.

Beta particles have less mass than α particles and are more penetrating. Thus, the attenuation of β particles within a grain is smaller than that for α particles. Mejdahl (1979) determined β attenuation factors for spherical quartz grains of diameter 5 μm to 10 000 μm for the K, Th and U decay series. Updated values were published by Brennan (2003), with adjustments

of up to 3 % of the infinite matrix dose, while Fain et al. (1999) published updated values for non-spherical grains. When the chemical composition of the sediment is unknown, the attenuation factor is calculated based on a proportional contribution of 70 % from K, 20 % from Th and 10 % from U. In this study the attenuation factors of Mejdahl (1979) and Bell (1979) are used when correcting the infinite matrix D_β. For the internal β dose contribution in K-feldspar, the amount of β dose absorbed by the grain is determined using β absorption factors, given by one minus the β attenuation factor.

3.5.5.3 Effect of etching

Due to the limited penetration of α particles, the α dose is significantly reduced when grains are etched using HF acid. However, by etching quartz in HF acid, a small modification to the β dose is induced because the distribution of the β dose within the grain is non-uniform. Bell (1979) calculated values to quantify the effect of etching on the α and β attenuation factors, for 100 μm grains with 9 μm removed during the HF etching procedure.

In this study, the 180 – 212 μm quartz grains were etched in HF acid to remove the outer 10 μm, and the correction values for attenuation of the β dose rate due to grain size and the effect of HF etching were based on the values of Mejdahl (1979) and Bell (1979). The K-feldspars in this study were not etched in HF acid and therefore no correction is necessary for the etching process. The only correction applied was for α and β dose rate attenuation of the grain size.

3.5.5.4 Water content correction

Water present within the pore spaces of a sediment absorbs radiation which would otherwise be stored within the individual grains. Thus, a correction must be applied to the measured dose rates to prevent systematic underestimation (Aitken, 1998). For a dose rate that has been measured using dry material, the correction is applied using Equation 3.2 from Aitken and Xie (1990), based on the work of Zimmerman (1971);

$$D_w = \frac{D_d}{1 + xWF} \tag{3.2}$$

where D_w is the dose rate of the sediment when wet, D_d is the sediment dose rate when dry, W is the saturation water content (expressed as weight of water/dry weight), F is the fraction of pore space occupied by water, and x the ratio of effective mass absorption coefficients for water and burial medium. Zimmerman (1971) proposed x values of 1.50, 1.25 and 1.14 for the α, β and γ correction respectively, based on the ratios of the coefficients of water to aluminium (which has absorption properties similar to that of soil) for α and β particles and γ rays of 1 MeV.

Field water contents (expressed as the percentage of the weight of water in terms of the weight of the dry sediment) ranged from 0.5 - 4.1 % at Voordrag, 1.0 - 8.0 % at St Paul's, 5.2 - 16.5 % at Goedgedacht and 0.4 - 2.0 % at the Moopetsi tributary site (see Table 3.3). Although it is possible to measure field water content, the uncertainty over the change in water content during the burial period hampers accuracy. Typically, an increase of ~1 % in the water content will result in an age increase of ~1 %. Dongas typically form within dryland regions and so the burial water contents

are expected to be relatively low. However, the very low measured field water contents are indicative of the winter dry period in South Africa's summer rainfall zone (SRZ). Also, the relatively higher water contents measured at Goedgedacht are most likely due to rainfall which occurred during the sample collection period. Therefore, these values cannot be deemed representative of the fluctuating water content during burial.

Saturation water contents were measured for a minimum of three samples per site to give an upper limit on the water content during burial (see Section 3.2.7). A representative water content for each site was selected based on consideration of: (i) the measured field water content; (ii) the saturated water content; (iii) the annual variations between wet and dry seasons; (iv) the long term variation in water content with climatic changes; (v) the geomorphological setting during deposition and subsequent erosion; and (vi) sedimentological evidence pertaining to sediment deposition and subsequent pedogenesis.

A burial water content of 15 ± 5 % was selected for the Moopetsi tributary, St Paul's and Goedgedacht sites and 30 ± 5 % for the Voordrag site. The geomorphic settings of the first three sites all allow for free drainage of water through the sediments; coupled with the low measured water contents and the similar upper limit given by the saturated water contents, this justifies selection of an identical burial water content across sites. This water content is the same as that used by Lyons (2012) for his OSL chronology at the Moopetsi tributary site, but higher than the 10 ± 5 % assigned by Wintle et al. (1995b) to the St Paul's site. The much higher water content selected for the Voordrag site was based on the work of Clarke et al. (2003) and Botha et al. (1992). They noted the presence

of wetland flora pollen combined with ferruginous plinthic mottling and iron-strained root channels indicative of colluvium accretion and subsequent pedogenesis in a poorly drained environment subject to fluctuating vadose zone conditions. Furthermore, the sediments were deposited in a bowl-shaped structure underlain by impermeable shale bedrock, which would have hampered drainage.

The external D_β and D_γ were corrected for water content using Equation 3.2 and the relevant x value. For the K-feldspar dose rate calculation, in addition to the external D_β and D_γ water corrections, the external D_α was also corrected for water content.

3.5.6 Cosmic dose rate contribution

Cosmic radiation consists of two components; a 'soft' component comprised mainly of electrons and a 'hard' component comprised of muons. The soft component is typically absorbed by a soil depth of ~0.5 m and so it is the more penetrating 'hard' component that is responsible for most of the cosmic ray contribution in the environmental dose rate (Aitken, 1985; Prescott and Hutton, 1988, 1994). The cosmic ray contribution to the environmental dose rate is relatively small, but not negligible. Prescott and Hutton (1994) present a method to calculate the cosmic dose rate based on the relationship between muon intensity and depth by Barbouti and Rastin (1983) that is valid at any altitude from the surface to a depth of 5 km. To calculate the dose rate (D_0) in Gy/ka delivered to a 'standard rock' at sea level at 55° geomagnetic latitude, the expression

$$D_0 = \frac{6072}{((x+11.6)^{1.68}+75)(x+212)} exp(-5.50 \times 10^{-4} x) \qquad (3.3)$$

is used, where x is the depth in hg/cm^2. The geomagnetic latitude (λ) of the sample site is determined using the equation

$$\sin\lambda = 0.203\cos\theta\cos(\phi - 291) + 0.979\sin\theta \tag{3.4}$$

where θ is the geographic latitude and ϕ the geographic longitude. Positive values indicate north and east and negative values south and west. A correction for the geomagnetic latitude of the sample site is applied to D_0 using the expression

$$D = D_0[F + Jexp(\frac{h}{H})] \tag{3.5}$$

where D is the corrected cosmic dose rate in Gy/ka, h is the altitude in km and F, J and H are read from a graph (Figure 3.11) using the calculated geomagnetic latitude value. The error on the cosmic dose rate is assumed to be 10 % of the total cosmic dose rate.

Cosmic dose rates were calculated using this procedure for each sample (Tables 3.4 and 3.5), applying their individual latitude, longitude and altitude values, which were recorded using a Garmin GPSmap 62 hand-held GPS during sample collection. The overburden at each site was deemed to be the distance of the sample from the extrapolated land surface and not the present measurement between the sample and the top of the section. This is because the incision into the Quaternary sediments occurred relatively recently and the cosmic component would be largely overestimated in relation to the total environmental dose if the present day levels were used.

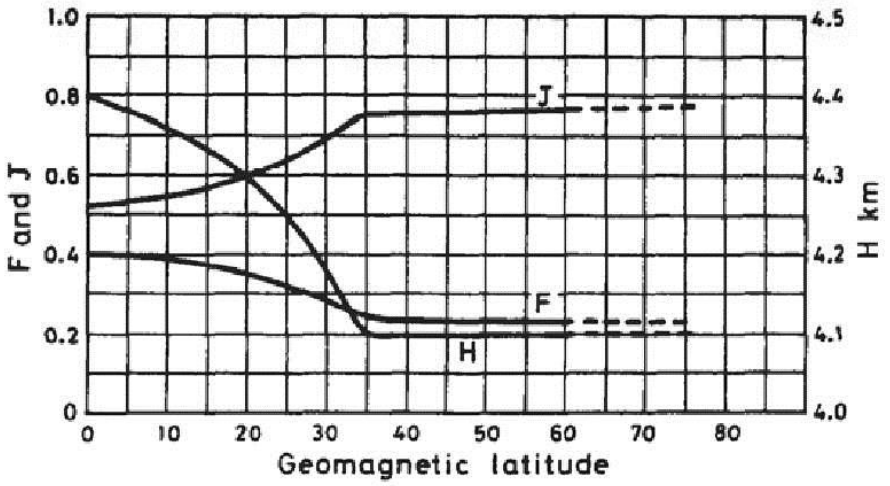

Figure 3.11: Parameters used in the determination of the cosmic dose rate shown as a function of geomagnetic latitude (Prescott and Hutton, 1994).

3.5.7 Total environmental dose rate

The components that determine the environmental dose rate ($\dot{D}$) are dependent on the dosimeter used in the luminescence measurements. The $\dot{D}$ as calculated in this study can be defined by Equation 3.6 for quartz and Equation 3.7 for K-feldspar,

$$\dot{D} = D_\beta + D_\gamma + D_c \tag{3.6}$$

$$\dot{D} = aD_\alpha + D_\beta + D_{\beta-int} + D_\gamma + D_c \tag{3.7}$$

where a is the alpha efficiency, D_α the external alpha dose rate, D_β the external beta dose rate, $D_{\beta-int}$ the internal beta dose rate, D_γ the external gamma dose rate and D_c the cosmic dose rate.

All dosimetry calculations in this project made use of the conversion factors of Guérin et al. (2011), with the exception of the Moopetsi tributary

samples. This was to avoid any confusion as dose rates for the Moopetsi tributary samples using the Adamiec and Aitken (1998) conversion factors have already been published by Colarossi et al. (2015). To facilitate a comparison, the $\dot{D}$ for the Moopetsi tributary samples were calculated using the Guérin et al. (2011) conversion factors and an increase of ~1 % and ~2 % was evident for the quartz and K-feldspar samples respectively, which is within the calculated uncertainty on the dose rates. To illustrate using sample 162/MPT4, the Adamiec and Aitken (1998) conversion factors give dose rates of 2.248 ± 0.101 Gy/ka and 3.008 ± 0.120 Gy/ka for quartz and K-feldspar respectively, whilst the Guérin et al. (2011) conversion factors increase these rates to 2.286 ± 0.106 Gy/ka and 3.061 ± 0.125 Gy/ka respectively.

3.6 Summary

This chapter has discussed the collection of samples in the field, and the subsequent laboratory preparation undertaken to separate quartz and K-feldspar from individual bulk samples. Details of the instruments and measurement parameters used in this study for equivalent dose measurements were also presented, alongside a brief review of the age models available to determine the burial dose. The basic concepts behind radioactive decay of the naturally-occurring radioisotopes ^{232}Th, ^{238}U, ^{235}U and ^{40}K were also reviewed. This was followed by an explanation of the techniques used in this study to measure the environmental α, β and γ dose rates using emission counting techniques, including TSAC, GMBC and FGS. Finally the calculation of the environmental dose rate was explained. This is a

crucial calculation as the environmental dose rate comprises half of the luminescence age equation. The following four chapters will explore the measurement and calculation of the equivalent dose, which makes up the other half of the age equation, on a site-by-site basis.

Chapter 4

Developing a K-feldspar chronology for the Moopetsi tributary site

4.1 Introduction

The Moopetsi tributary site has an existing chronology consisting of ten quartz OSL ages (see Lyons, 2012) that extend over the last ~120 ka. The ages are stratigraphically consistent throughout the section, except in the basal LGS unit where an age inversion occurs in the three lowermost samples (see Section 4.3.3). These three samples have D_e values ranging from 158 Gy to 170 Gy and are near the reliable limit of quartz OSL (see Section 1.3.2). This site provides the opportunity to investigate paired K-feldspar post-IR IRSL ages with quartz OSL ages measured independently of this study. This chapter begins with an investigation into the bleaching rates of quartz and K-feldspar signals (Section 4.2), which is followed by

an initial analysis of the post-IR IRSL signal using multiple grain (Section 4.3) and single grain (Section 4.4) measurements. Next, the effect of the test dose size on the post-IR IRSL protocol is investigated (Section 4.5). Finally, a combined quartz-feldspar chronology for the Moopetsi tributary site is presented (Section 4.6). Some of the work presented in this chapter has been published in Colarossi et al. (2015).

4.2 Bleaching experiment for multiple chronometers

K-feldspar is an alternative dosimeter to quartz in luminescence dating, and has become more viable as more stable signals have been identified e.g. post-IR IRSL and multi-elevated temperature (MET) post-IR IRSL. However, different bleaching rates have been observed for quartz and low temperature (50 °C) K-feldspar signals (e.g. Godfrey-Smith et al., 1988; Thomsen et al., 2008). Furthermore, the post-IR $IRSL_{290}$ signal has been shown to bleach more slowly than the K-feldspar IRSL signals measured at 50 °C (e.g. Buylaert et al., 2012, 2013; Murray et al., 2012). However, the bleaching rates of the post-IR IRSL signal using different second stimulation and preheat temperatures have not been investigated. Due to the nature of the sediments under investigation and the potential for heterogeneous bleaching, the bleaching rate of quartz OSL and two potential post-IR IRSL signals were investigated. Sample 162/MPT4 was selected for initial tests because of its high measured K-content (12.6 ± 0.8 wt%), increasing the confidence that the signal observed is from K-rich feldspar.

Table 4.1: The quartz OSL protocol used during the bleaching experiment on sample 162/MPT4.

Step	Treatment	Measured
1	Dose	
2	Bleach in SOL-2 for time (t)	
3	Preheat at 260 °C for 10 s	
4	OSL at 125 °C for 40 s	L_x
5	Test dose (5 Gy)	
6	Preheat at 160 °C for 10 s	
7	OSL at 125 °C for 40 s	T_x
8	Return to step 1	

A bleaching experiment was conducted to assess the rate at which different luminescence signals from quartz and K-feldspar decrease due to light exposure. A total of nine small aliquots were prepared and divided into subsets of three, one for each signal to be investigated, specifically quartz OSL and feldspar post-IR IRSL using a first stimulation temperature of 50 °C and second stimulation temperature of 225 °C and 290 °C. To reduce sensitivity change between the measurement steps and to ensure the reproducibility of the signal, aliquots were measured repeatedly prior to commencing the bleaching experiment using either the quartz protocol shown in Table 4.1 or the K-feldspar protocol shown in Table 4.2. Once sensitised, the aliquots were irradiated with a β dose of ~45 Gy and the luminescence signal remaining after exposure to light in a Honlë SOL-2 solar simulator was measured. The irradiation and measurement process was repeated for varying amounts of exposure time in the SOL-2 and all measurements were normalised to the measurement where no exposure to the SOL-2 had occurred (Figure 4.1).

As expected based on previous studies, the quartz OSL signal bleached more rapidly than both the feldspar $IRSL_{50}$ and post-IR IRSL signals. After

Table 4.2: The post-IR IRSL protocol used during the bleaching experiment on sample 162/MPT4.

Step	Treatment	Measured
1	Dose	
2	Bleach in SOL-2 for time (t)	
3	Preheat at 250 or 320 °C for 60 s	
4	IRSL at 50 °C for 200 s	
5	IRSL at 225 or 290 °C for 200 s	L_x
6	Test dose (5 Gy)	
7	Preheat at 250 or 320 °C for 60 s	
8	IRSL at 50 °C for 200 s	
9	IRSL at 225 or 290 °C for 200 s	T_x
10	IRSL at 290 or 325 °C for 100 s	
11	Return to step 1	

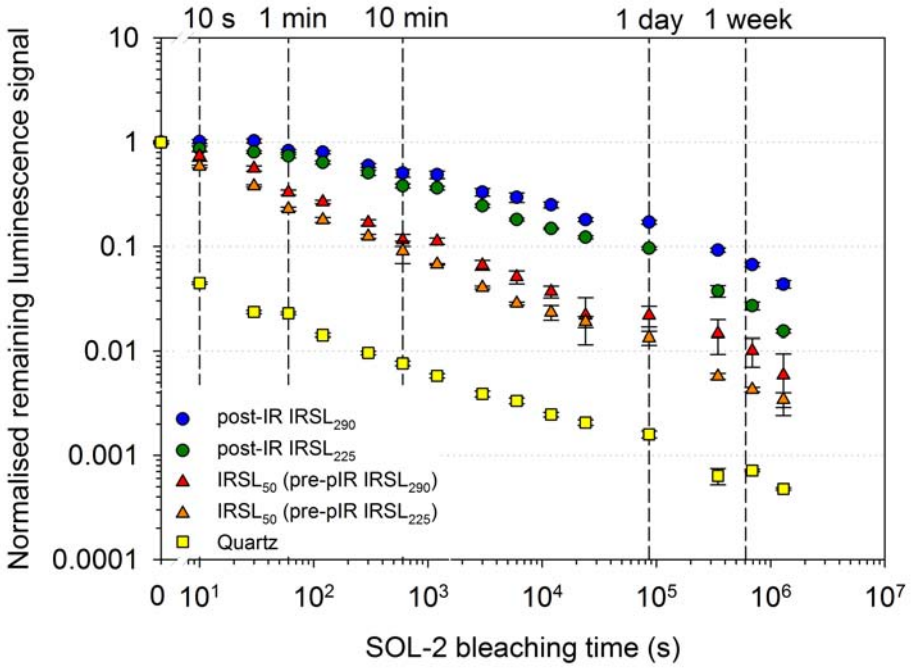

Figure 4.1: Bleaching rates of the quartz OSL and feldspar post-IR $IRSL_{225}$, post-IR $IRSL_{290}$ and associated $IRSL_{50}$ signals by exposure to the Honlë SOL-2 solar simulator. Data are normalised to the response when no exposure has occurred (Colarossi et al., 2015).

10 s of bleaching, the quartz OSL signal was reduced to 5 % of the original signal whilst the post-IR $IRSL_{225}$ signal was reduced to ~86 %, and the post-IR $IRSL_{290}$ showed negligible reduction. The post-IR $IRSL_{225}$ signal required 4 days (96 hr) in the SOL-2 to reduce the signal to 5 % of the original signal, whilst the post-IR $IRSL_{290}$ signal took 14 days (336 hr) to reach this level. The $IRSL_{50}$ signals are reduced to 5 % after ~3 hr 20 min and show slightly different bleaching rates due to the difference in their respective preheat temperatures.

It is interesting to note that over a period of exposure in the SOL-2 in excess of 1 million seconds (14 days), the post-IR IRSL signals show a monotonic decrease; there is no indication of a residual post-IR IRSL signal that cannot be removed by exposure to the light source. Figure 4.1 emphasises the very slow rate at which the post-IR IRSL signals bleach in the laboratory in comparison to the quartz OSL signal.

4.3 Initial K-feldspar investigations

A chronology for the Moopetsi site has been produced by Lyons (2012) using small aliquot quartz OSL measurements. To enable direct comparison with the post-IR IRSL ages from this study, initial K-feldspar investigations were undertaken on small aliquots. It has been suggested that low post-IR IRSL stimulation temperatures are more appropriate for dating young sediments because such signals bleach more quickly (e.g. Madsen et al., 2011; Reimann and Tsukamoto, 2012; Reimann et al., 2011). However, Thomsen et al. (2008) observed a systematic decrease in fading rate with increased stimulation temperature, implying the higher temperature protocols access

more stable signals. Thus the post-IR IRSL signals at 225 °C and above will potentially provide more accurate ages by minimising the influence of fading, which is particularly important when targeting old samples.

In order to determine the most suitable post-IR IRSL temperature regime for these sediments, a series of tests were conducted to ascertain the magnitude of the residual signal, the extent of anomalous fading and the ability to recover a given dose. These tests were undertaken on sample 162/MPT4 for the reason expressed in Section 4.2 and because of the low OD (17 %) for the quartz small aliquot D_e distribution implying that quartz has been well-bleached, which offers the best chance for a well-bleached K-feldspar sample.

4.3.1 Using a dose recovery test to assess the residual signal

A total of 20 small aliquots were prepared and bleached in a Honlë SOL-2 solar simulator for 48 hours to remove the stored charge accrued during burial. This process simulates consistent bleaching within the sample, i.e. all grains are bleached to the same extent, representing a well-bleached sample. The 20 aliquots were divided into four sets, each numbering five aliquots. Within each set, 2 aliquots were given no dose (i.e. 0 Gy) and 3 aliquots were irradiated with a β dose of ~45 Gy (equivalent to the average expected D_e for the sample). Each of the four sets was assigned a different combination of preheat and post-IR stimulation temperature for the post-IR IRSL protocol shown in Table 4.3. Second stimulation temperatures (steps 5 and 9, Table 4.3) were 225 °C, 250 °C, 270 °C and 290 °C, with a corresponding preheat temperature (steps 3 and 7, Table 4.3)

Table 4.3: The post-IR IRSL protocol used during the initial K-feldspar investigations on sample 162/MPT4.

Step	Treatment	Measured
1	Bleach in SOL-2 for 48 hours	
2	Dose (45 Gy)	
3	Preheat at 250, 270, 290 or 320 °C for 60 s	
4	IRSL at 50 °C for 200 s	
5	IRSL at 225, 250, 270 or 290 °C for 200 s	L_x
6	Test dose (5 Gy)	
7	Preheat at 250, 270, 290 or 320 °C for 60 s	
8	IRSL at 50 °C for 200 s	
9	IRSL at 225, 250, 270 or 290 °C for 200 s	T_x
10	IRSL at 290, 300, 310 or 325 °C) for 100 s	
11	Return to step 1	

20 – 30 °C higher than the stimulation temperature, so as to be consistent with published literature (e.g. Buylaert et al., 2009).

Standard rejection criteria (see Section 3.3.3) were applied to the individual D_e values and the mean D_e of the two aliquots which received a 0 Gy β irradiation was calculated. This D_e value represents the residual dose i.e. the signal that was not removed after 48 hours of continual bleaching in the SOL-2. The residual was subtracted from the D_e values measured for the three aliquots that received a 45 Gy β dose and the measured to given dose ratio calculated for each aliquot. The measured residuals increase with preheat temperature (Figure 4.2 (a)) from 1 Gy to 5 Gy. The measured to given dose ratio (after subtraction of the residual dose) lies within 10 % of unity for the post-IR $IRSL_{225-270}$ signals (Figure 4.2 (b)) and all four signals are able to recover a dose within uncertainty. This suggests that any of the four signals could be used to date this material.

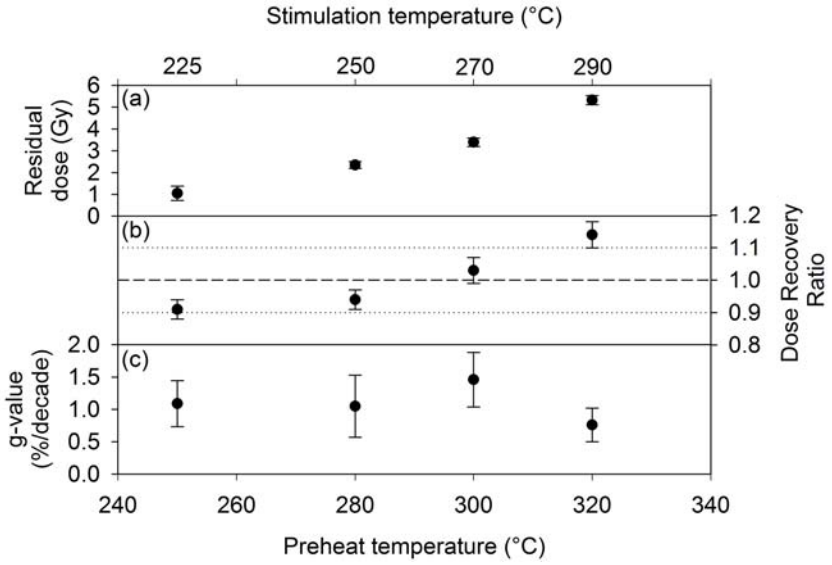

Figure 4.2: Initial tests run on 162/MPT4 (Colarossi et al., 2015). Results of the dose recovery test (given dose ~45 Gy) show a) the measured residual signals after a 48 hour bleach in the Honlë SOL-2 and b) the measured to given dose ratios. Shown in c) are the fading rates calculated using Eq. 4 of Huntley and Lamothe (2001) and normalised to 2 days.

4.3.2 Extent of anomalous fading

A major issue affecting the use of feldspars in luminescence dating is anomalous fading of the IRSL signal, whereby electron tunnelling causes the signal to decrease more rapidly over time than expected based on thermal stability measurements (see Section 1.4.1). Thus fading typically results in age underestimation if it is not corrected for. A fading test was conducted using the same four post-IR IRSL signals used in the dose recovery test (Table 4.3). Twenty small aliquots were prepared, five for each signal, and dose response curves (DRCs) were constructed to measure the D_e values. Following this step, the aliquots were irradiated with a known β dose (~45 Gy) similar to the expected average D_e, preheated immediately following irradiation as per Auclair et al. (2003) and stored for

varying periods of time before measurement. The delay between irradiation and measurement ranged from 10 min to 47 days and all g-values are < 1.5%/decade, irrespective of the stimulation temperature (Figure 4.2 (c)). It was suggested by Thiel et al. (2011) that very low fading rates may be a laboratory artefact. In support of this argument, they presented a g-value of 1.3 ± 0.3 %/decade that they measured for quartz, which is thought not to suffer from anomalous fading.

Low g-values imply minimal fading of the post-IR IRSL signal across the four temperature regimes (Figure 4.2 (c)). Furthermore, each protocol displays the ability to recover a laboratory-given dose within uncertainty (Figure 4.2 (b)), to recycle within errors and to show recuperation < 5 % of the natural signal. Therefore, any of the four temperature-based protocols could be applied to date the K-feldspars from the Moopetsi tributary site. The post-IR IRSL protocol with a second stimulation temperature of 225 °C and a preheat of 250 °C for 60 s, hereafter referred to as the post-IR $IRSL_{225}$ protocol, was selected because it displayed the lowest residual signal (Figure 4.2 (a)) consistent with the bleaching experiment in Section 4.2.

4.3.3 Small aliquot post-IR $IRSL_{225}$ D_e distributions

D_e values were measured for all ten samples from the Moopetsi tributary site using the post-IR $IRSL_{225}$ protocol on small aliquots of K-feldspar. The number of replicate D_e measurements was higher for the seven uppermost samples (n = 31 to 39) than the three lowermost samples (n = 4 to 15) due to the limited amount of material available for the latter. Standard acceptance criteria (Section 3.3.3) were applied to individual D_e values and D_e distributions compared to those obtained from quartz OSL. The D_e

distributions for 170/MPT8 and 170/MPT7 (the top and bottom samples respectively) are shown in Figure 4.3. Radial plots for all Moopetsi samples are included in Appendix A and the two datasets are summarised in Table 4.4. Luminescence dating does not use an agreed datum when reporting ages (Duller, 2011), therefore all luminescence ages determined during this study are reported as thousand of years (ka) before the year of sample collection (i.e. AD 2014).

The overdispersion (OD) values for both quartz and feldspar are generally lower for the older samples (Table 4.4). Where OD was > 20 % (for K-feldspar) the minimum age model (MAM) was applied to extract the population of D_e values with the most completely bleached signal at deposition. For the five oldest samples the OD was less than 20 % and the CAM was applied. Lyons (2012) used an OD threshold of 30 % to distinguish between the CAM and MAM for their quartz OSL data. Sample 162/MPT3 is interesting because whilst the feldspar post-IR IRSL signal is poorly bleached (OD = 33 %), the quartz OSL signal is well-bleached (OD = 19 %). This implies a significant difference between the bleaching rates of the two signals as expected (see Section 4.2).

Comparison of the D_e distributions from the two minerals (Figure 4.3, Appendix A and Table 4.4) shows that the feldspar post-IR IRSL signal consistently produced higher D_e values. This results in consistently older feldspar ages with respect to the quartz ages (Figure 4.4, blue circles and red triangles). The offset between the paired ages could be due to the difference in the bleaching rate of the two signals (see Figure 4.1). Assuming that the quartz OSL age calculated for the youngest sample (170/MPT8) using the MAM is accurate, and both minerals are in fact dating the same depositional

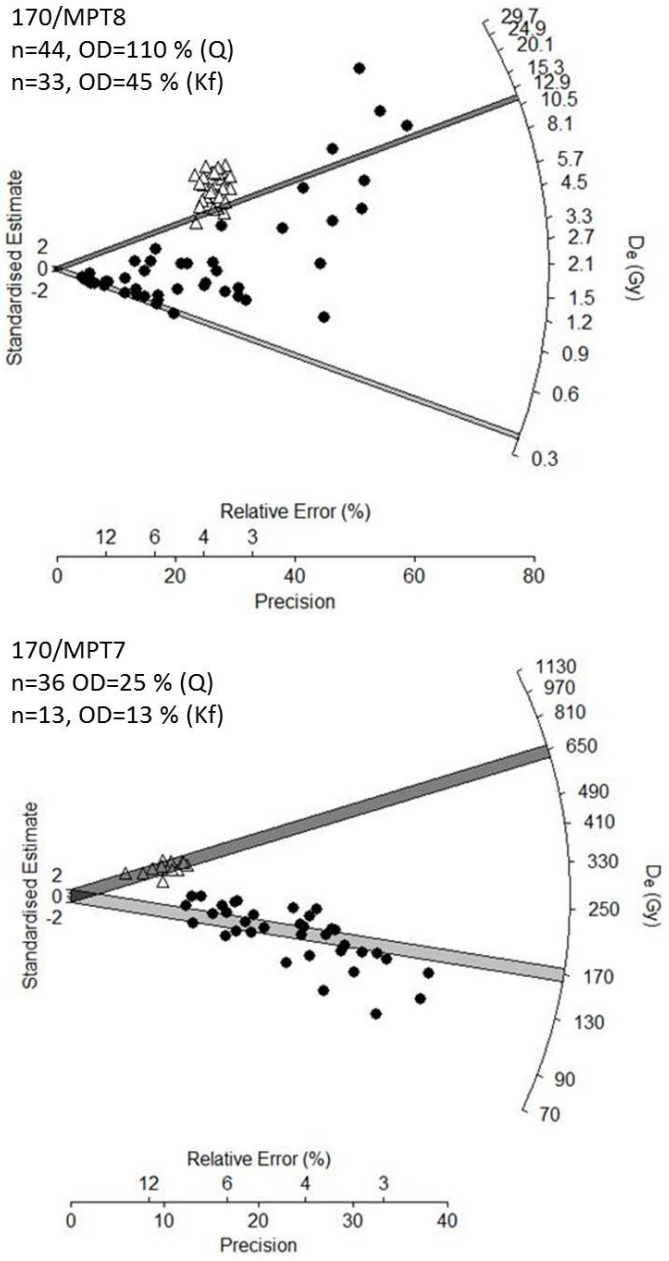

Figure 4.3: Small aliquot quartz OSL (black circles) and K-feldspar post-IR $IRSL_{225}$ (white triangles) D_e distributions for the youngest (170/MPT8) and oldest (170/MPT7) samples. The light and dark grey bars for 170/MPT8 represent the MAM D_e values for quartz and K-feldspar, 0.37 Gy and 11.5 Gy respectively. For 170/MPT7, the bars represent the CAM D_e values, 170 Gy and 643 Gy respectively.

Table 4.4: D_e distribution data and ages for small aliquot quartz OSL and K-feldspar post-IR $IRSL_{225}$ measurements for ten samples from the Moopetsi tributary site. Also shown is the number of aliquots used in the D_e estimate (n), the overdispersion (OD) of the D_e distribution and the age model used to derive the burial D_e value (Colarossi et al., 2015).

Sample ID	Quartz OSL [a]					K-feldspar post-IR $IRSL_{225}$				
	n	OD (%)	Age model[b]	D_e (Gy)	Age (ka)	n	OD (%)	Age model[b]	D_e (Gy)	Age[c] (ka)
170/MPT8	44	110	MAM	0.37 ± 0.04	0.20 ± 0.02	33	45	MAM	11.5 ± 1.3	0.20 ± 0.68
170/MPT12	48	31	MAM	8.18 ± 0.62	3.45 ± 0.30	31	37	MAM	32.2 ± 1.3	6.72 ± 0.62
170/MPT13	43	59	MAM	9.05 ± 0.51	4.11 ± 0.30	39	30	MAM	22.6 ± 1.9	3.88 ± 0.78
170/MPT14	42	59	MAM	7.29 ± 0.31	4.53 ± 0.28	39	27	MAM	18.4 ± 2.6	3.10 ± 1.24
162/MPT3	47	19	CAM	11.3 ± 0.3	6.72 ± 0.35	39	33	MAM	29.1 ± 1.0	7.38 ± 0.71
162/MPT4	48	17	CAM	20.6 ± 0.5	9.15 ± 0.47	31	11	CAM	46.1 ± 1.0	11.7 ± 0.9
170/MPT10	38	24	CAM	103 ± 4	50.6 ± 3.0	37	15	CAM	257 ± 7	88.2 ± 4.4
170/MPT9	42	25	CAM	158 ± 6	106 ± 6	4	10	CAM	608 ± 45	268 ± 23
170/MPT6	49	16	CAM	161 ± 4	90.8 ± 4.7	4	0	CAM	664 ± 34	258 ± 17
170/MPT7	36	25	CAM	170 ± 8	119 ± 7	15	13	CAM	643 ± 29	292 ± 18

[a] Quartz data are based on Lyons (2012)

[b] A sigma-b value of 0.15 was used for the MAM calculations for both quartz and K-feldspar measurements

[c] Ages using K-feldspar post-IR $IRSL_{225}$ measurements were calculated after subtracting a residual dose of 11.0 ± 1.3 Gy from the D_e as described in the text

event (as they were taken from the same physical sample), the magnitude of the feldspar post-IR IRSL residual signal at the time of deposition can be calculated as 11.0 ± 1.3 Gy. Based on the geomorphic context and sedimentology of the samples in this study, it seems that the depositional environment has remained similar over time and it is thus reasonable to assume that a similar residual D_e was present in all samples at the time of deposition. Subtracting the residual D_e prior to age calculation, greatly improves the agreement between the quartz OSL and feldspar post-IR IRSL ages for the six uppermost samples (see Figure 4.4, blue circles and yellow triangles; Table 4.4). With the exception of the uppermost sample, which was used to determine the residual value, the quartz and feldspar ages overlap within one sigma for three of the five samples (170/MPT13, 170/MPT14, and 162/MPT3), within two sigma for one sample (162/MPT4) and just beyond two sigma for one sample (170/MPT12). However, the subtraction of the residual D_e has introduced an additional uncertainty into the final feldspar ages, and they show consistently larger uncertainties than the quartz ages.

Ages calculated for the four lowermost samples (170/MPT10, 170/MPT9, 170/MPT6 and 170/MPT7) differ substantially, with the K-feldspar post-IR IRSL signal producing ages between 38 ka and 170 ka older than the quartz OSL ages. Several possible explanations can be suggested for this offset.

1. The underestimation of quartz ages owing to the OSL signal approaching saturation. Using samples from Chinese loess, Chapot et al. (2012) showed that natural and laboratory dose response curves for quartz OSL deviated above ~150 Gy, leading to increasingly severe age underestimation. At the Moopetsi tributary site, the three lowermost

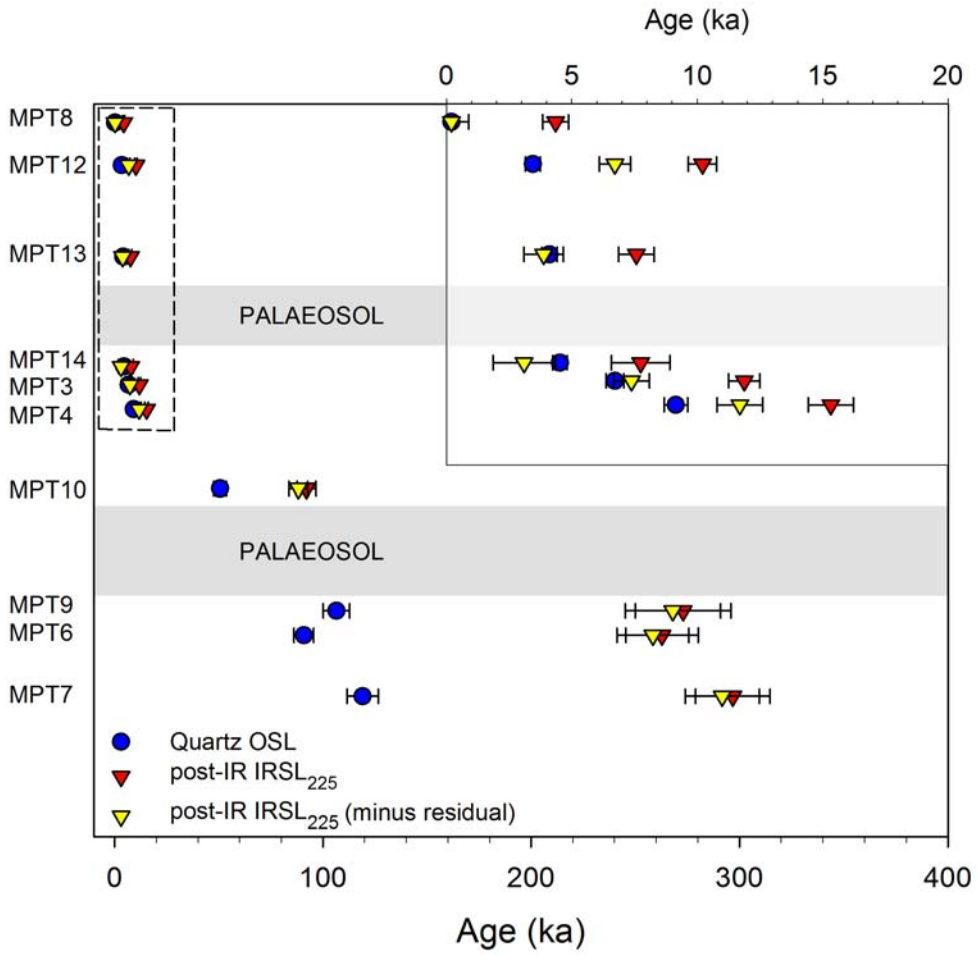

Figure 4.4: Comparison between small aliquot ages from quartz OSL (circles) and feldspar post-IR IRSL (triangles). The post-IR $IRSL_{225}$ ages were calculated without the residual subtraction (red triangles) and after the subtraction of an 11.0 $\pm$ 1.3 Gy residual (yellow triangles). Residual subtraction improved agreement between paired ages < 15 ka but had little effect on ages > 50 ka. The inset shows an enlargement of the period from 0 – 20 ka enlarged (Colarossi et al., 2015).

samples have D_e values between 158 Gy and 170 Gy (Table 4.4), all of which are above the threshold value identified by Chapot et al. (2012) but lower than $2D_0$ (see Section 1.3.2) for these samples, which is ~280 Gy. However, MPT10 which also shows an offset between ages has a D_e of 103 Gy, which should be within the datable range for quartz OSL.

2. The different bleaching rate of the two signals. Subtracting the residual should remove this effect, unless the older sediments were not reset to the same extent at deposition and the residual signal was of the order of ~450 Gy instead of the ~11 Gy on the younger samples. A residual of this magnitude could be explained if the lowermost sediments were dominantly sourced from local bedrock by scouring rather than being derived from reworking of older fluvial sediments. However no sedimentological evidence exists to support this theory and the offset is greater than can be explained by the different bleaching rates.

3. The overestimation of feldspar ages owing to extensive averaging of a variety of D_e values on each aliquot. The dose distributions for the post-IR IRSL signal display less variation in precision of D_e values for individual small aliquots than the OSL signal (Figure 4.3). This could result from a greater variation in the luminescence efficiency for individual grains of quartz when compared to feldspar, or a larger proportion of feldspar grains producing a luminescence signal than quartz (Duller et al., 2003)). To measure the variability in a heterogeneously bleached population, the extent of averaging needs to be minimised.

The final two explanations are manifestations of the same phenomenon, i.e. heterogeneous bleaching. Number 2 represents a sedimentological manifestation of heterogeneous bleaching, whereby a potential variation in the extent of bleaching occurs down section. In contrast, number 3 represents a technical luminescence manifestation of heterogeneously bleached sediments, whereby a large potential variation in D_e measurements occurs.

4.3.4 Extent of signal averaging

Based on the consistently lower OD values (Table 4.4) for the feldspar D_e distributions in relation to the paired quartz distributions, coupled with the higher signal intensity and better precision of the feldspar measurements, the possibility of averaging the post-IR IRSL signal on the small aliquots was investigated. To assess the possibility of averaging of the feldspar signal leading to an overestimation in the post-IR $IRSL_{225}$ ages, two samples were selected for single grain measurements. The uppermost sample, 170/MPT8 has the highest OD for both small aliquot distributions and the largest difference between OD values, i.e. 110 % for quartz and 45 % for feldspar. In contrast, sample 162/MPT4, located mid-way down the stratigraphic section, has one of the lowest OD values, 17 % for quartz and 11 % for feldspar.

The single grain K-feldspar distributions for these two samples (Figure 4.5) show significantly more scatter and higher OD values (101 % and 35 % for 170/MPT8 and 162/MPT4 respectively) than the equivalent small aliquot datasets. The variation in D_e values, likely due to heterogeneous bleaching of the grains during deposition given the short transport distances

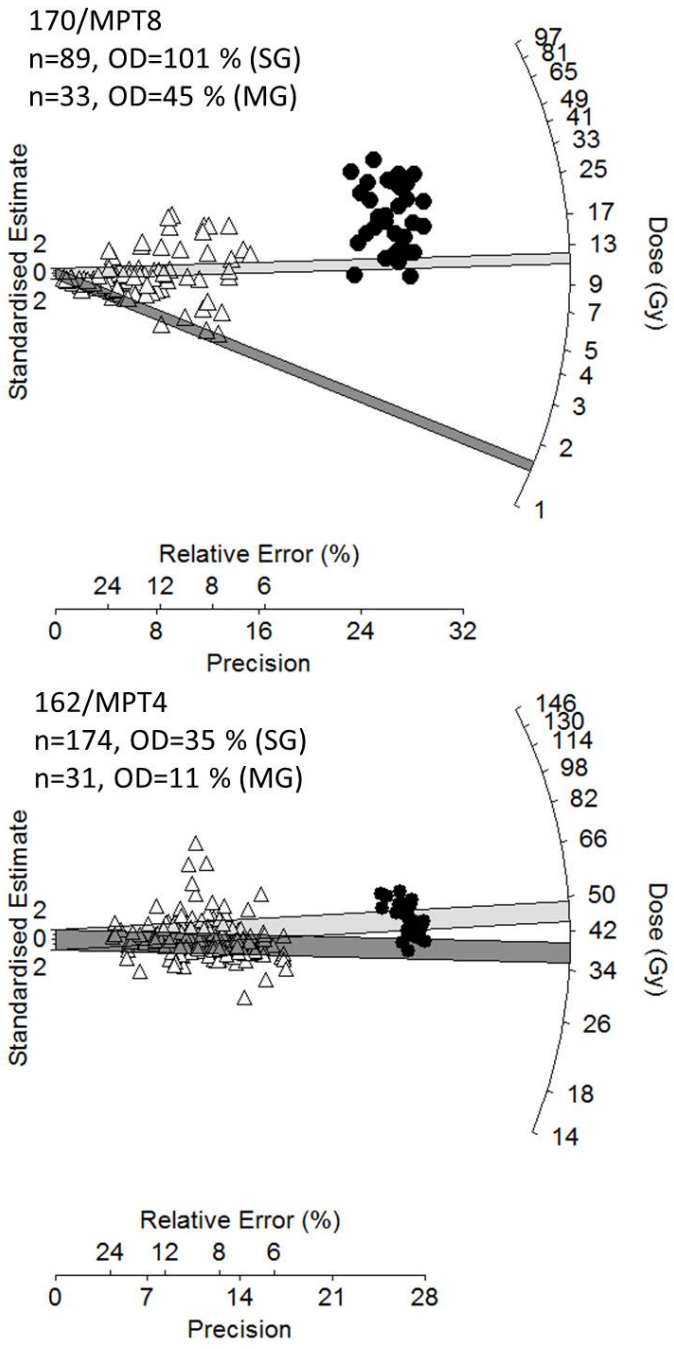

Figure 4.5: Comparison of K-feldspar small aliquot (MG, black circles) and single grain (SG, white triangles) D_e distributions for a) 170/MPT8 and b) 162/MPT4. The light and dark grey bars represents the MAM D_e value for the small aliquot and single grain distributions, respectively.

(< 5 km), would account for this OD. This is because small D_e values, obscured at the small aliquot level by averaging, become visible at the single grain level (Wallinga, 2002a). Therefore, in environments such as this where sediments are heterogeneously bleached and a large proportion of grains are contributing to the D_e population (31 % accepted grains for 170/MPT8 and 54 % for 162/MPT4), the highly variable D_e values are averaged on small aliquots. Overestimation of multiple grain measurements has been attributed to averaging effects in both quartz (Russell and Armitage, 2012) and K-feldspar (Reimann et al., 2012, 2011). In this case, single grain D_e measurements will provide a more accurate estimation of the burial dose and the apparent age.

4.4 Investigating single grains for dating K-feldspar samples

A series of D_e measurements were undertaken on single grains of K-feldspar using the post-IR $IRSL_{225}$ protocol (see Table 4.5). Standard acceptance criteria (Section 3.3.3) were applied and the number of grains that passed ranged between 8 % and 67 % (Table 4.6). The D_e distributions (Figure 4.6) show a large amount of scatter, with high OD values (> 50 %) for all samples in the stratigraphic section, except for 162/MPT4 (35 %, Table 4.6). Given the high OD values the MAM was applied throughout the section for the purposes of age calculation. As with the small aliquot ages, the MAM D_e value for 170/MPT8 was used to determine the residual signal (see discussion in Section 4.3.3), and a residual of 0.97 ± 0.23 Gy was subtracted from all D_e values prior to age calculation.

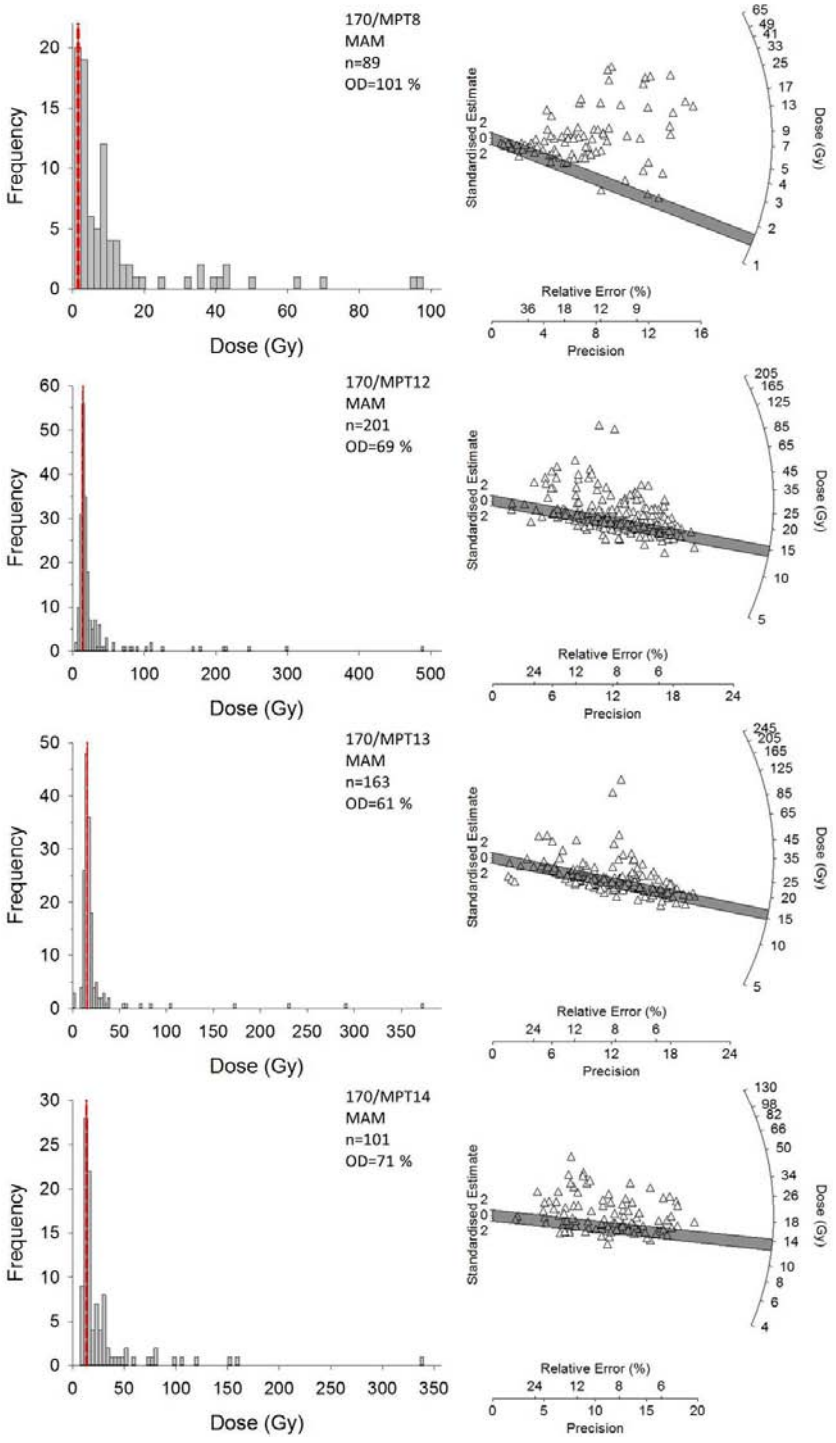

Figure 4.6: Histograms and radial plots of single grain K-feldspar D_e distributions (low test dose measurements). The solid red line denotes the MAM D_e value with uncertainties (dashed red lines) and the grey bar the 2σ region about the MAM D_e value. Data presented here are from prior to the subtraction of the residual signal (see discussion in text).

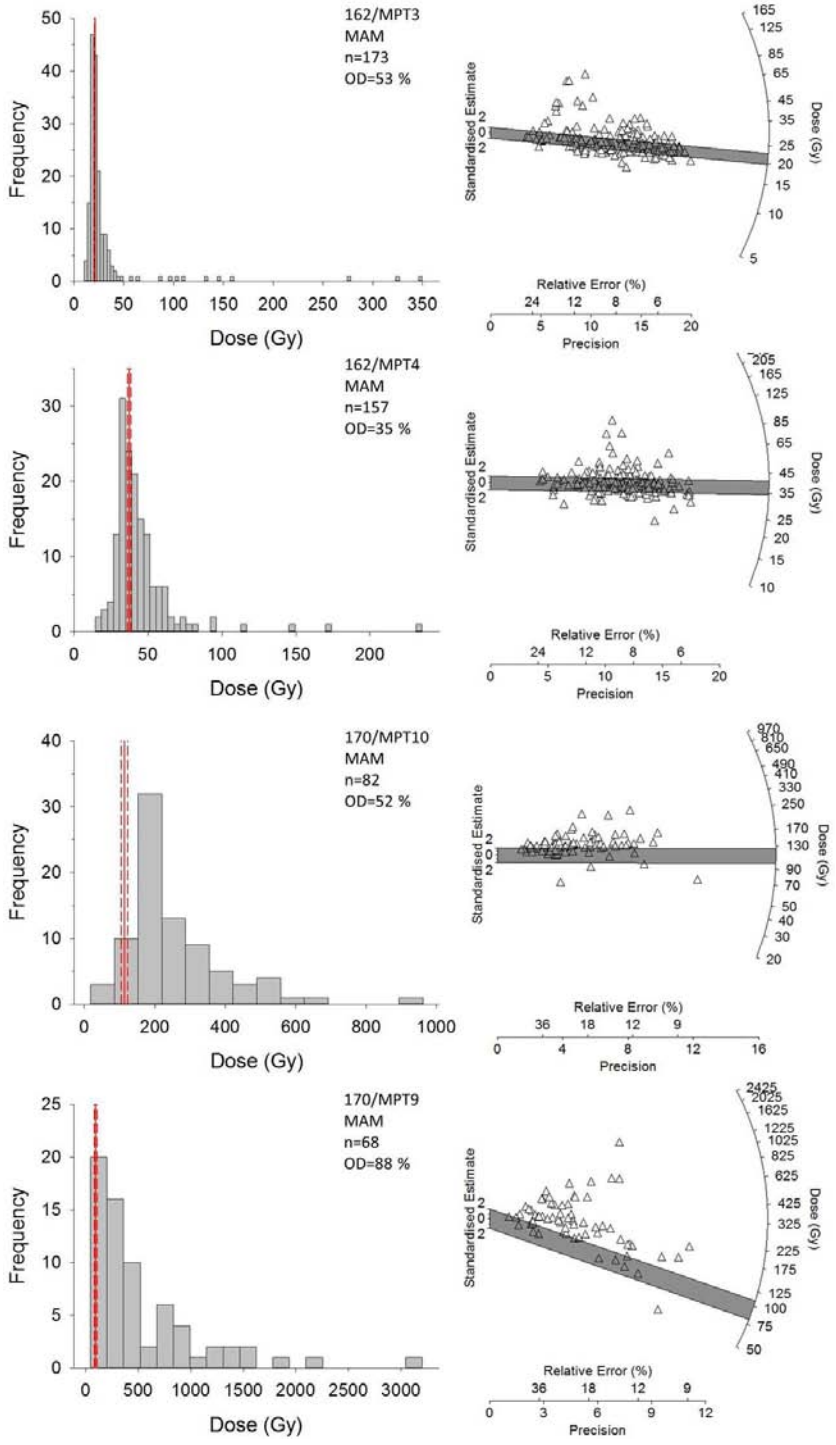

Figure 4.6: Histograms and radial plots of single grain K-feldspar D_e distributions (low test dose measurements)(continued).

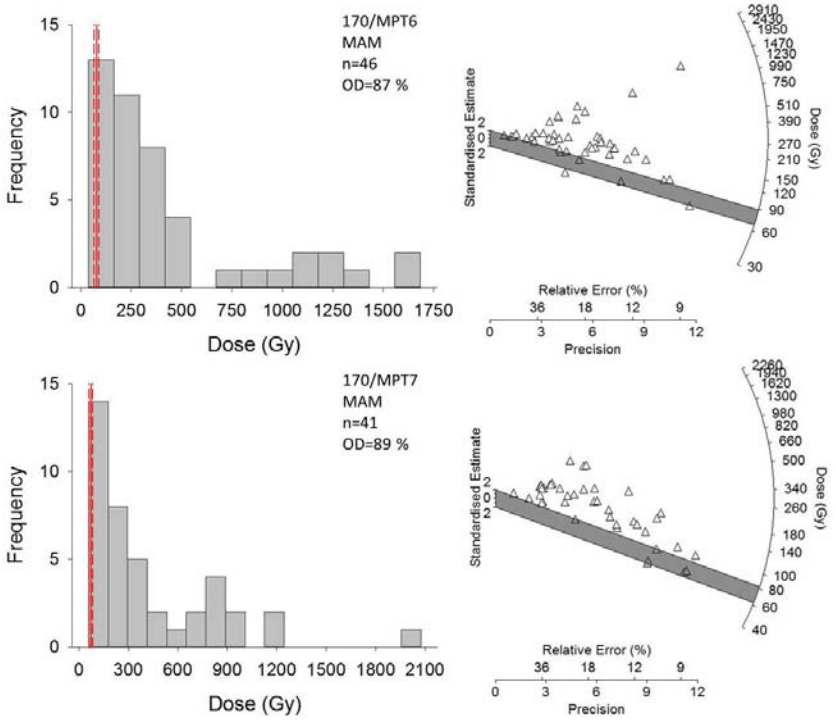

Figure 4.6: Histograms and radial plots of single grain K-feldspar D_e distributions (low test dose measurements)(continued).

Table 4.5: The post-IR $IRSL_{225}$ protocol used for single grain measurements on all K-feldspar samples from the Moopetsi tributary site.

Step	Treatment	Measured
1	Dose	
2	Preheat at 250 °C for 60 s	
3	IRSL at 50 °C for 200 s (LEDs)	
4	IRSL at 225 °C for 2 s (Laser)	L_x
5	Test dose (5 Gy)	
6	Preheat at 250 °C for 60 s	
7	IRSL at 50 °C for 200 s (LEDs)	
8	IRSL at 225 °C for 2 s (Laser)	T_x
9	IRSL at 290 °C for 100 s (LEDs)	
10	Return to step 1	

Table 4.6: Single grain K-feldspar D_e measurements and ages using the post-IR $IRSL_{225}$ protocol with a low test dose (5 Gy) on the 180 – 212 μm grain size fraction. Both MAM and CAM D_e values are included for the lowermost four samples (see discussion in text).

Sample ID	Number of grains N_T [a]	N [b]		n_{sat} [c]		n [d]		OD (%)	Skewness	Kurtosis	Age model[e]	D_e(Gy)[f]	Age (ka)
170/MPT8	300	92	(31%)	3	(3%)	89	(97%)	101	2.76	10.95	MAM	0.53 ± 0.36	0.20 ± 0.12
170/MPT12	300	201	(67%)	0	(0%)	201	(100%)	69	5.57	41.36	MAM	13.6 ± 0.4	4.32 ± 0.19
170/MPT13	300	167	(56%)	4	(2%)	163	(98%)	61	6.13	43.71	MAM	14.7 ± 0.4	4.92 ± 0.22
170/MPT14	300	101	(34%)	0	(0%)	101	(100%)	71	4.74	31.61	MAM	12.3 ± 0.6	5.17 ± 0.31
162/MPT3	300	173	(58%)	0	(0%)	173	(100%)	53	5.40	34.85	MAM	20.0 ± 0.5	8.15 ± 0.37
162/MPT4	300	161	(54%)	4	(2%)	157	(98%)	35	4.42	29.06	CAM	36.3 ± 1.1	12.1 ± 0.6
170/MPT10	600	87	(15%)	5	(6%)	82	(94%)	52	1.88	8.09	CAM	214 ± 14	76.0 ± 5.8
											MAM	113 ± 11	40.1 ± 4.1
170/MPT9	600	71	(12%)	3	(4%)	68	(96%)	88	2.19	8.88	CAM	358 ± 40	160 ± 19
											MAM	94.9 ± 12.4	42.1 ± 5.8
162/MPT6	600	49	(8%)	3	(6%)	46	(94%)	87	1.47	3.96	CAM	283 ± 38	111 ± 16
											MAM	78.4 ± 12.1	30.6 ± 5.0
170/MPT7	300	61	(20%)	20	(33%)	41	(67%)	89	1.83	6.92	CAM	269 ± 39	123 ± 19
											MAM	72.2 ± 11.0	32.8 ± 5.2

[a] Total number of grains measured

[b] Number of grains that passed acceptance criteria

[c] Number of grains in saturation (as % of N)

[d] Number of grains in D_e distribution (as % of N)

[e] A sigma-b value of 0.20 was used in the MAM calculation

[f] D_e values reported have had a residual dose of 0.97 ± 0.23 Gy subtracted

At the single grain level, the feldspar ages compare well with the quartz ages in the upper stratigraphy (Figure 4.7), where five ages (170/MPT12 – 162/MPT4) are within one sigma of each other. The behaviour of the paired ages for the four lowermost samples is surprising since there was concern that the quartz OSL ages may underestimate due to their proximity to the level of saturation for the OSL signal. The K-feldspar single grain MAM ages (pink triangles, Figure 4.7) of these samples are significantly younger (up to 80 ka) than the quartz ages (blue circles, Figure 4.7) and cannot be explained by depositional processes. Alternatively, the CAM ages (white triangles, Figure 4.7) are in better agreement with the quartz ages, albeit with larger uncertainties and an age inversion. However, application of the CAM is difficult to support considering the very large OD values (52 – 89 %) for these samples.

A possible explanation for this conundrum is offered by recent findings which suggest that the post-IR IRSL signal is dependent on the size of the test dose (e.g. Buylaert et al., 2013; Li et al., 2014; Nian et al., 2012). Therefore, in order to better constrain the D_e values for the four lowermost samples, the behaviour of the post-IR $IRSL_{225}$ signal at high doses was examined to determine its ability to successfully recover a dose when using a test dose of varying sizes.

4.5 Influence of the test dose magnitude

Recent literature has highlighted the importance of the test dose magnitude when dating K-feldspar. Qin and Zhou (2012) looked at the effect of test dose size on D_e estimation (using a given dose of 240 Gy) and suggested

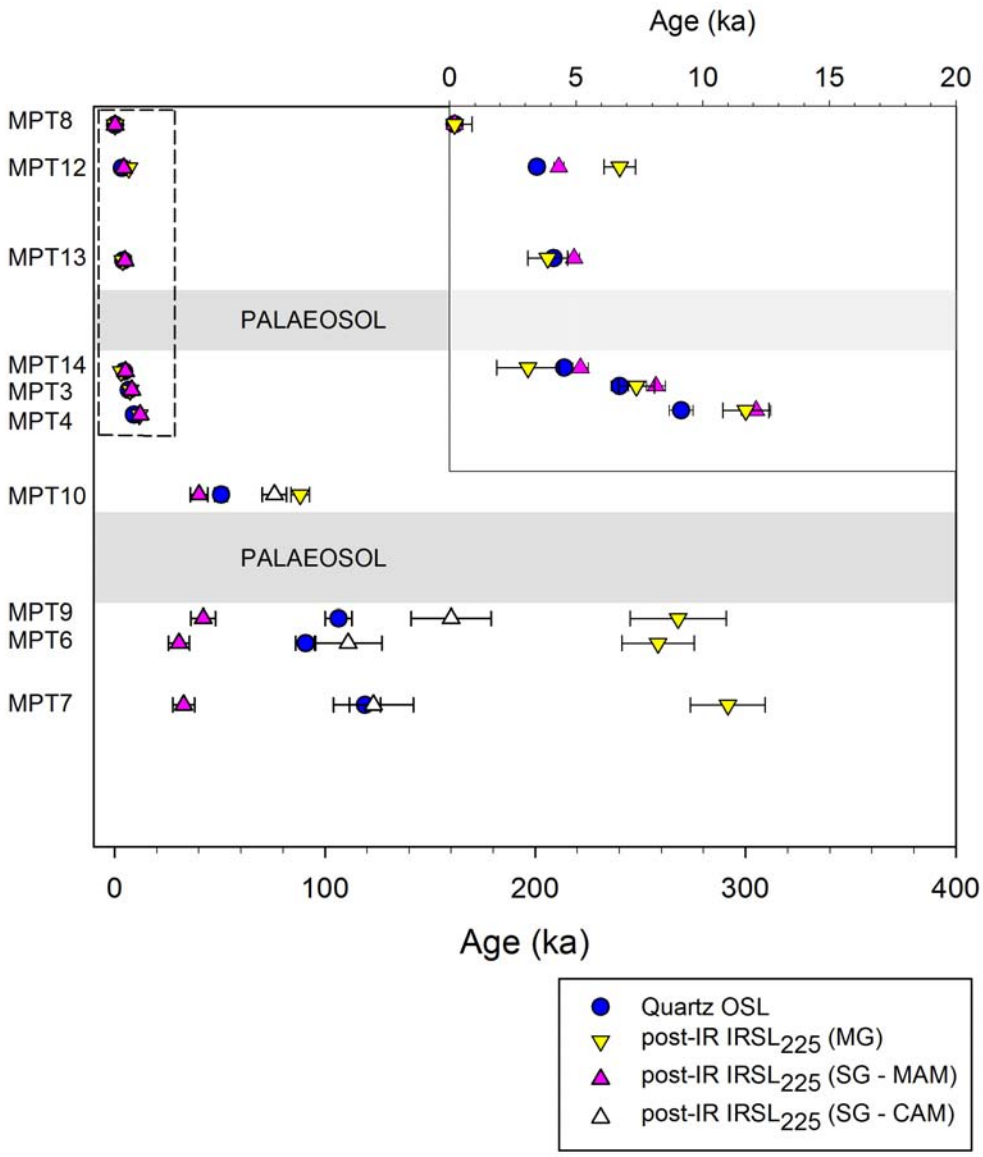

Figure 4.7: Comparison of small aliquot quartz OSL ages (blue circles) with small aliquot (yellow triangles) and single grain (red triangles) feldspar post-IR $IRSL_{225}$ ages. Single grain K-feldspar ages show improved agreement with small aliquot quartz OSL ages, however poor agreement between the four lowermost paired ages warrants further investigation of the post-IR IRSL protocol (see explanation in text). Single grain K-feldspar ages for the four lowermost samples calculated from the CAM D_e (white triangles) are plotted for comparison purposes.

using a large magnitude test dose, of the order of 50 – 80 Gy to reduce the effect of thermal transfer. In contrast, Buylaert et al. (2012) found no correlation between test dose size and the measured to expected dose ratio for a given dose of 149 Gy, which may be due to the 325 °C IRSL clean-out applied in their protocol. Subsequent publications have reported the use of a large test dose (100 Gy, Nian et al., 2012) or the test dose as a proportion of the expected D_e (e.g. 25 % (Sohbati et al., 2012); 30% (Buylaert et al., 2013; Fu et al., 2015; Yi et al., 2015); and 50% (Buylaert et al., 2015)). Yi et al. (2016) presented a series of dose recovery experiments, adding a beta dose between 99 Gy and 1593 Gy onto a sample with a D_e value of ~100 Gy. They used a range of test dose values for the post-IR $IRSL_{290}$ protocol and suggested a test dose magnitude of 15 – 80 % of the D_e was most likely to produce a satisfactory dose estimate. However, no study has explored the effect of test dose magnitude on the post-IR IRSL elevated temperature signal at the single grain level. To explore this effect, a series of dose recovery tests were initiated using the post-IR $IRSL_{225}$ protocol on sample 162/MPT4.

4.5.1 Dose recovery experiment 1: Recovery of various given doses using a fixed test dose

Individual grains of K-feldspar were mounted on single grain discs, bleached for 48 hr in the Honlë SOL-2 solar simulator and irradiated with a β dose ranging between 0 Gy and ~400 Gy. Three discs were measured for each given dose (GD) using the post-IR $IRSL_{225}$ protocol with a fixed test dose of 5.1 Gy, similar to the value used in the measurements presented earlier in this chapter. The mean value calculated from the D_e distribution for the

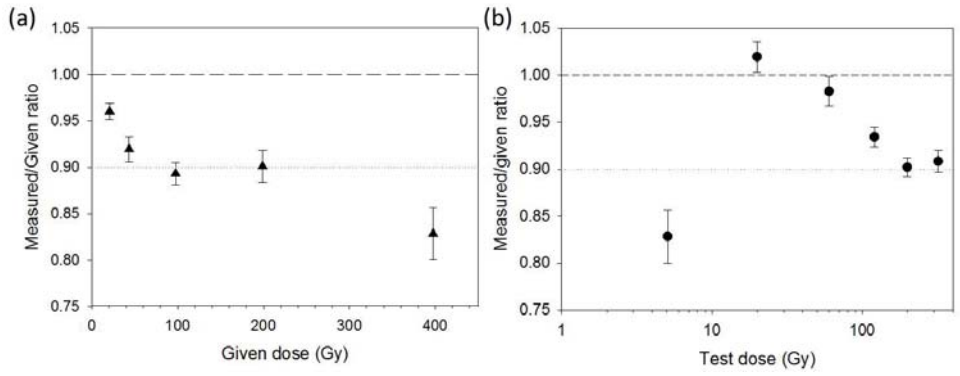

Figure 4.8: Results from dose recovery experiments 1 and 2 showing the measured to given dose ratios for the post-IR $IRSL_{225}$ signal for a) given doses ranging between 0 Gy and ~400 Gy with a fixed test dose of ~5 Gy and b) a given dose of ~400 Gy with a test dose varying between ~5 Gy and ~320 Gy (i.e. 1 % – 80 % of the corresponding given dose). Note the logarithmic scale of the x-axis in b).

0 Gy given dose was 1.20 ± 0.08 Gy and was used to represent the residual signal remaining within the population of grains after uniform bleaching. This value was subtracted from the individual D_e values measured for all other given doses. The average measured to given dose ratios range from 0.83 ± 0.03 to 0.96 ± 0.01 (see Table 4.7 and Figure 4.8(a)) and are within 10 % of unity except the ratio at 400 Gy. Figure 4.8(a) shows consistent underestimation of the measured to given dose ratio when using a low test dose that becomes more severe as the size of the given dose increases. Thus, based on this experiment, it is not possible to successfully recover a large given dose with the post-IR $IRSL_{225}$ protocol when using a small test dose. This may explain the age underestimation observed in the four lowermost samples in Section 4.4.

To look at single grain D_e values, individual D_e values were normalised to the given dose and plotted in a histogram (Figure 4.9) to facilitate comparison of the D_e distributions for each of the five given doses. At lower

Table 4.7: Results for dose recovery experiment 1 using variable given doses with a fixed test dose (~5 Gy). Measurements were undertaken on single grains of K-feldspar using the post-IR $IRSL_{225}$ protocol on the 180 – 212 μm grain size fraction of sample 162/MPT4.

Given dose (Gy)	0	21	43	98	199	398
Test dose (Gy)	5.1	5.1	5.1	5.1	5.1	5.1
Test dose (% of GD)	-	25	12	5	3	1
Total grains measured (N_T)	200	300	300	300	300	300
Number of grains accepted (N)	135	214	189	218	198	145
Number of saturated grains (n_{sat})	0	0	1	8	34	40
Number of grains giving D_e (n)	135	214	188	210	164	105
OD (%)	46	9	13	15	23	34
Apparent sensitivity change (%)	135	39	71	56	70	85
Skewness	3.48	0.76	3.31	0.44	0.40	0.40
Kurtosis	21.99	5.51	26.54	3.43	2.86	2.41
D_0 (Gy)[a]	46 ± 1	42 ± 1	49 ± 1	58 ± 1	72 ± 2	88 ± 7
D_{01} (Gy)[a]	-	-	-	-	22 ± 1	33 ± 2
D_{02} (Gy)[a]	-	-	-	-	203 ± 16	408 ± 146
Average (Gy)[b]	1.20 ± 0.08	21.0 ± 0.2	41.1 ± 0.6	88.3 ± 1.2	180 ± 3	330 ± 11
M/G ratio [c]	-	0.96 ± 0.01	0.92 ± 0.01	0.89 ± 0.01	0.90 ± 0.02	0.83 ± 0.03

[a] Multiple D_0 values due to best fit approach to DRC construction. D_0 is the average of all DRCs fit with a single exponential, while D_{01} and D_{02} are from DRCs fit with a double exponential function.

[b] Uncertainty reported as one standard error

[c] Ratio calculated after subtracting a residual of 1.20 ± 0.08 Gy from individual D_e values

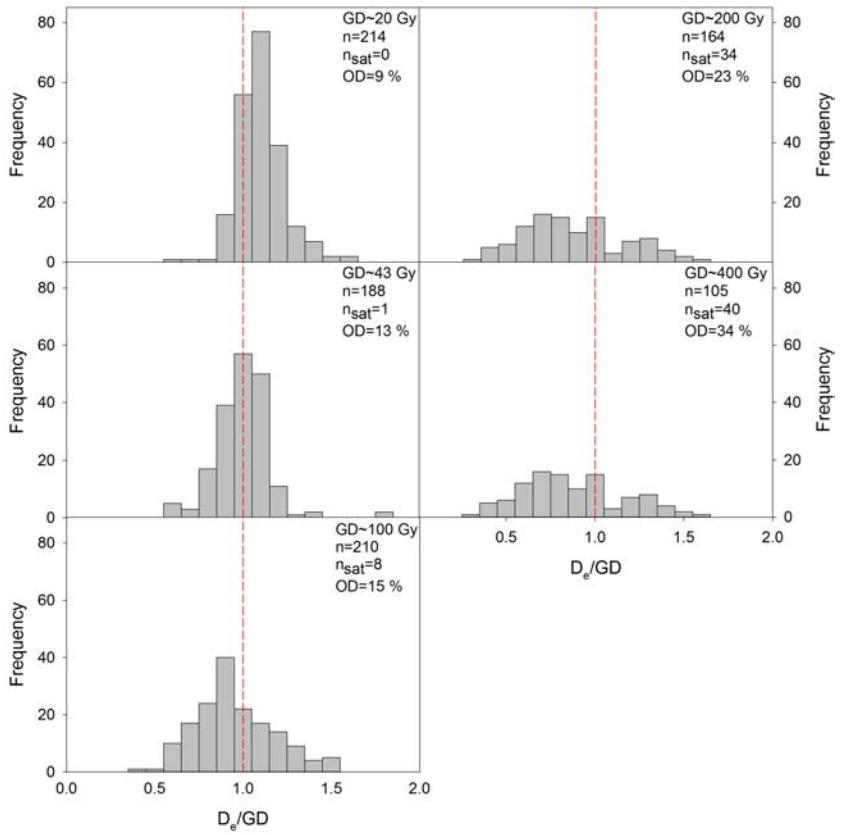

Figure 4.9: D_e distributions for dose recovery experiment 1 with variable given doses (GD) and a fixed test dose of 5.1 Gy; n represents the number of grains included in the D_e distribution excluding the saturated grains (n_{sat} and the dashed line indicates the given dose normalised to 1.

given doses (~20 Gy and ~43 Gy) D_e distributions are positively skewed (0.76 and 3.31, Table 4.7) and become broader and more symmetrical (0.40, Table 4.7) as the given dose increases. As well as becoming broader, the OD increases with given dose, from 9 % (GD ~20 Gy) to 34 % (GD ~400 Gy). It is also interesting to note that the number of saturated grains (i.e. $L_n/T_n >$ DRC) in each distribution (n_{sat}, Table 4.7) increases as the given dose increases. A high number of saturated grains may bias the distribution towards lower D_e values, which will underestimate the burial dose due to the exclusion of the oldest grains (Thomsen et al., 2016; Trauerstein et al.,

2014). This may explain the systematic underestimation of the measured to given dose ratio observed in Figure 4.8(a).

4.5.2 Dose recovery experiment 2: Recovery of a fixed given dose using various test doses

In this experiment a fixed given dose of ~400 Gy was applied to bleached grains and the size of the test dose was varied to represent test dose values used in recent publications as mentioned in Section 4.5. The test doses applied were 5.1 Gy (~1 % of the given dose), 20 Gy (~5 %), 60 Gy (~15 %), 120 Gy (~30 %), 199 Gy (~50 %) and 319 Gy (~80 %). Results (see Table 4.8 and Figure 4.8(b)) show a sharp increase in the measured to given dose ratio when increasing the test dose from 5 Gy (~1 %) to 20 Gy (~5 %) followed by a steady decline in the ratio as the test dose increases to 199 Gy (~50 %). These results show it is possible to use the post-IR $IRSL_{225}$ signal to recover a large given dose (400 Gy), within 10 % uncertainty, when a large test dose (5 – 80 %) is applied. This is similar to the findings of Yi et al. (2016) who recommend a test dose 15 – 80 % of the D_e but in contrast to the findings of Fu et al. (2015) who showed that the high temperature MET post-IR IRSL protocol could only recover a dose if the test dose was < 40 % of the given dose (126.9 Gy).

However, the size of the test dose cannot be selected solely on the basis of a percentage of the expected dose. Consider the measured to given dose ratios for the following combinations of given dose (GD) to test dose (Td): GD ~100 Gy, Td ~5 Gy and GD ~400 Gy, Td ~20 Gy. Both test doses represent 5 % of the given dose and yet the measured/given dose ratios are 0.89 ± 0.01 and 1.02 ± 0.02 respectively (see Tables 4.7 and 4.8, Figure

Table 4.8: Results for dose recovery experiment 2 using a fixed given dose (~400 Gy) with variable test doses. Measurements were undertaken on single grains of K-feldspar using the post-IR $IRSL_{225}$ protocol on the 180 – 212 μm grain size fraction of sample 162/MPT4.

Given dose (Gy)	398	400	400	398	398	398
Test dose (Gy)	5.1	20	60	120	199	319
Test dose (% of GD)	1	5	15	30	50	80
Total grains measured (N_T)	300	300	200	200	300	200
Number of grains accepted (N)	145	185	113	146	219	148
Number of saturated grains (n_{sat})	40	26	11	2	2	3
Number of grains giving D_e (n)	105	159	102	144	217	145
OD (%)	34	16	12	10	12	12
Apparent sensitivity change (%)	85	48	37	21	18	18
Skewness	0.40	0.69	0.23	0.77	1.04	0.96
Kurtosis	2.41	3.47	4.47	4.71	4.75	4.69
D_0 (Gy)[a]	88 ± 7	168 ± 6	255 ± 11	384 ± 23	429 ± 16	465 ± 18
D_{01} (Gy)[a]	33 ± 2	46 ± 3	40 ± 4	43 ± 4	48 ± 6	43 ± 3
D_{02} (Gy)[a]	408 ± 146	797 ± 144	628 ± 91	659 ± 96	632 ± 59	665 ± 87
Average (Gy) [b]	330 ± 11	409 ± 7	394 ± 6	372 ± 4	360 ± 4	362 ± 5
M/G ratio [c]	0.83 ± 0.03	1.02 ± 0.02	0.98 ± 0.02	0.93 ± 0.01	0.90 ± 0.01	0.91 ± 0.01

[a] Multiple D_0 values due to best fit approach to DRC construction. D_0 is the average of all DRCs fit with a single exponential, while D_{01} and D_{02} are from DRCs fit with a double exponential function.

[b] Uncertainty reported as one standard error

[c] Ratio calculated after subtracting a residual of 1.20 ± 0.08 Gy from individual D_e values

4.8). The 20 Gy test dose recovers a dose with better accuracy than the 5 Gy test dose, which may imply that a test dose of 5 Gy is too small for any but the youngest of K-feldspar samples.

The single grain D_e distributions (Figure 4.10) at low test doses (5 Gy and 20 Gy) are broad and slightly positively skewed (0.40 and 0.69, Table 4.8). At a test dose of 60 Gy (15 % of the given dose) the D_e distribution becomes symmetrical (0.23, Table 4.8), reverting to positive skewness (0.77 - 1.04, Table 4.8) at higher test doses. The OD shows a clear decrease at higher test doses, i.e. the OD is halved from 34 % (5 Gy) to 16 % (20 Gy) and becomes constant at ~12 %. The lowest OD is recorded for a test dose of 120 Gy (30 % of the given dose). Nian et al. (2012) observed a similar decrease in OD (~14 to 21 %) when increasing the size of their test dose from 25 Gy to 100 Gy.

For a test dose of 200 Gy (50 % of the given dose) and above, the measured D_e values begin systematically underestimating the given dose (see Figures 4.8 (b) and 4.10). The number of saturated grains decreases as the test dose increases, from 40 grains at the 5.1 Gy (1 %) test dose to 3 grains at the ~320 Gy (80 %) test dose. Thus, in this experiment D_e underestimation at high test doses is not due to the biasing effect of excluding saturated grains. Based on this experiment, there appears to be an optimum test dose at 30 % of the given dose where a slightly skewed distribution is coupled with the lowest OD, the lowest number of saturated grains and a recovered dose within 1 standard deviation of unity that is not systematically underestimating the given dose.

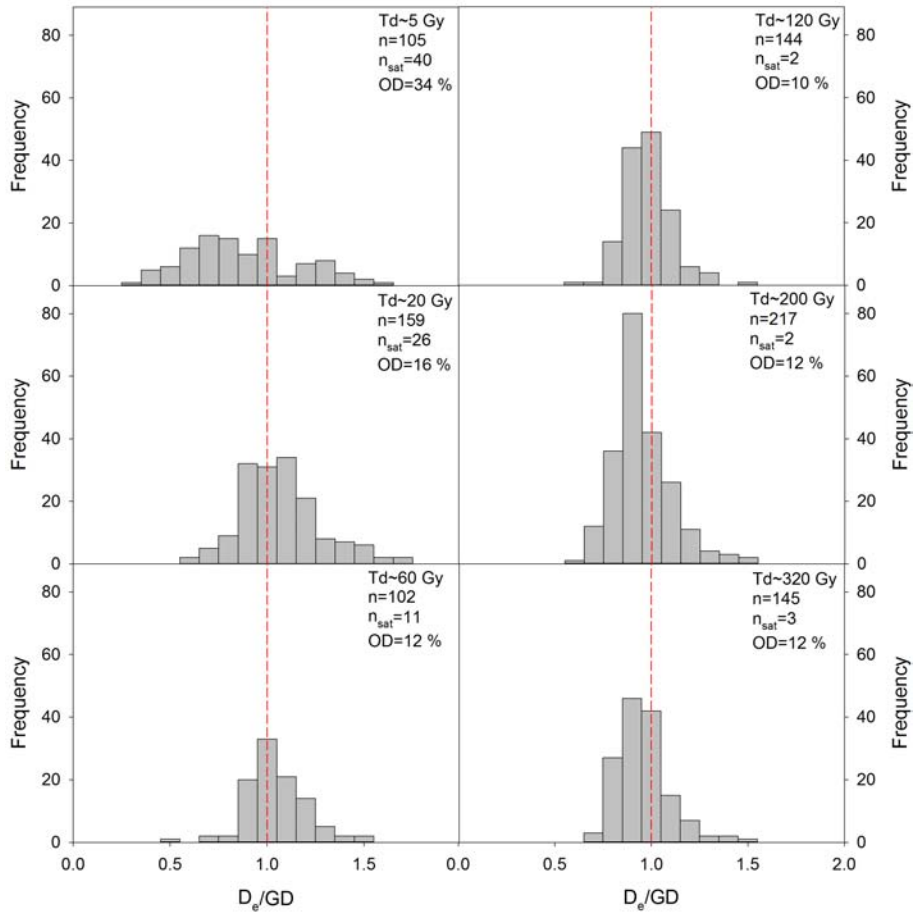

Figure 4.10: D_e distributions for dose recovery experiment 2 with a fixed given dose (~400 Gy) and a variable test dose; n represents the number of grains included in the D_e distribution excluding the saturated grains (n_{sat}) and the dashed line indicates the given dose normalised to 1.

4.5.2.1 Changes to the shape of the DRC

The dose response curves (DRCs) obtained by averaging the signals from the single grains measured using different test doses show a systematic change in the shape of the DRC as the size of the test dose increases (Figure 4.11) . The largest change is observed between the lowest test dose (5.1 Gy, ~1 %) and the 60 Gy (~15 %) test dose. Beyond this (i.e. for test doses above 120 Gy (~30 %) the change is limited. The signal arising from the 400 Gy given

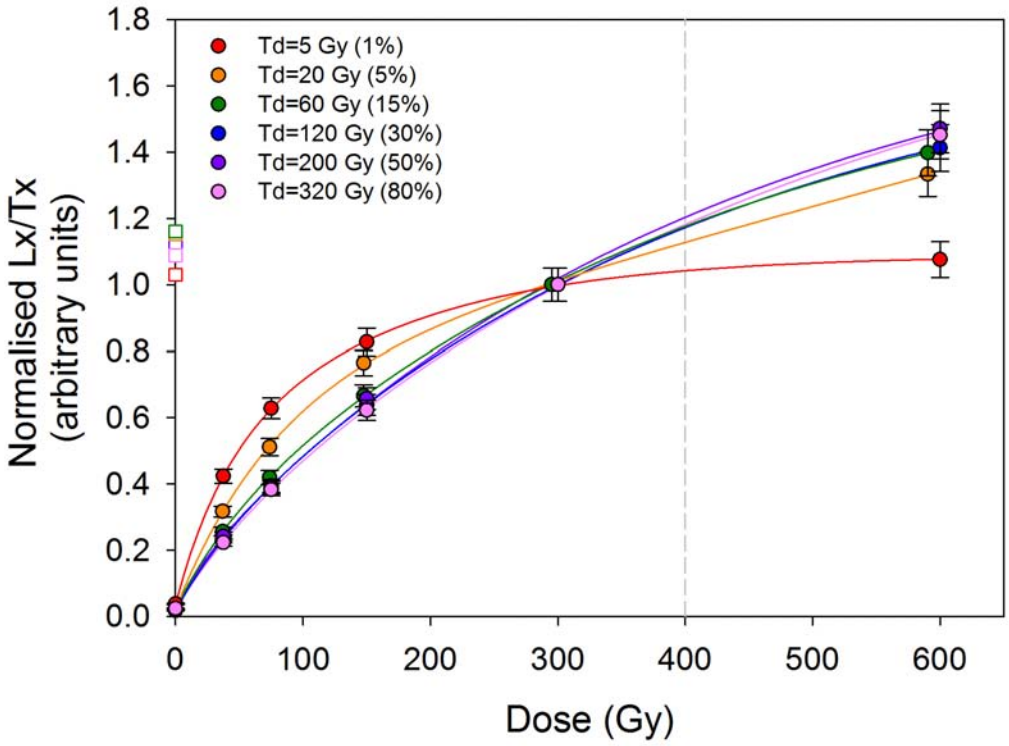

Figure 4.11: Dose response curves (from dose recovery experiment 2) normalised to the 300 Gy regeneration dose point. All dose response curves are fit with a DSE function, with the exception of the 20 Gy curve which is fit with a SEPL function. The vertical dashed line represents the given dose of 400 Gy. Curves are plotted from synthetic aliquot data, produced mathematically by summing the luminescence signals from individual grains.

dose, for the 5.1 Gy test dose curve (Figure 4.11, red), is located higher in the non-linear region of the DRC, much nearer saturation, which results in a large number of saturated grains unable to produce D_e values, and the observed underestimation of the D_e in Figure 4.8(a). Increasing the test dose changes the shape of the DRC, and the natural signal plots below the level of saturation, as seen for the curve built with a 20 Gy test dose (Figure 4.11, orange) and all subsequent larger test doses. However, it is

worth noting that from a test dose of 60 Gy all of the DRCs display the same shape and similar intensity natural signals.

4.5.2.2 Effect on the D_0

D_0 is a convenient measure to characterise the curvature of the DRC, and has an impact on the maximum age that can be reliably dated using luminescence dating protocols (see Section 1.3.2). Wintle and Murray (2006) recommended that $D_e < 2D_0$ for quartz because above this level any uncertainty in the natural measurement (L_n/T_n) may result in large asymmetric uncertainties on the D_e value. Mean D_0 values (Table 4.8) for dose response curves from dose recovery experiment 2 fitted with a SSE (Equation 1.2) show a monotonic increase in D_0 as the size of the test dose is increased, from 88 ± 7 Gy to 465 ± 18 Gy. For curves fit with a DSE (Equation 1.4), D_{01} ranges from 33 ± 2 Gy to 48 ± 6 Gy whilst D_{02} lies between 408 ± 146 Gy (5 Gy, 1 %) to 797 ± 141 Gy (20 Gy, 5 %). It should be noted at this point that D_{01} is not well characterised by the DRCs and should be treated with caution.

D_0 values for the post-IR $IRSL_{225}$ protocol vary greatly, with reported values of 335 Gy and 1000 Gy (Sohbati et al., 2012), 200 Gy (Lowick et al., 2012) and 950 Gy (Buylaert et al., 2011b). Recent studies have attempted to use D_0 as a measure of saturation (e.g. Thomsen et al., 2016; Trauerstein et al., 2014). The data from dose recovery experiment 2 shows that D_0 can vary substantially when calculated using a single or double saturating exponential function (Figure 4.12). In this instance, the DSE achieves a better fit to the data, resulting in a more precise measure of D_e. In their review paper, Li et al. (2014) concluded that whilst the dating limit of the

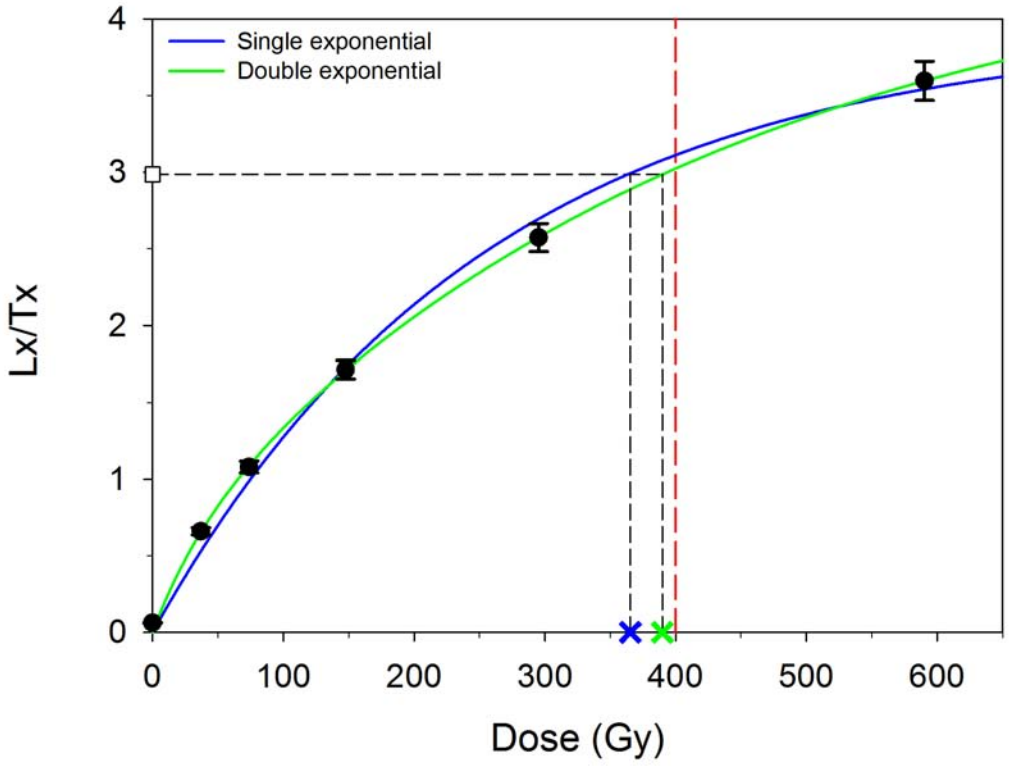

Figure 4.12: The DRC for the 60 Gy test dose data from dose recovery experiment 2 fit with both a SSE and DSE function. The blue and green crosses denote the D_e values derived via interpolation, of the signal arising from the given dose of 400 Gy, onto their respective DRCs. The dashed, red line indicates the given dose of 400 Gy.

post-IR IRSL protocol varies on a sample and regional scale, the saturation dose level is dependent on the experimental conditions applied during the measurement process, which is in agreement with the results of this study.

4.5.2.3 Effect on overall apparent sensitivity change recorded during the post-IR $IRSL_{225}$ protocol

Apparent sensitivity change is monitored by normalising the T_x measurement to the T_n measurement (e.g. Armitage et al., 2000). One impact of increasing

the size of the test dose is to significantly reduce the amount of apparent sensitivity change recorded during the post-IR $IRSL_{225}$ measurement cycle (Figure 4.13, Table 4.8), from 85 % (5 Gy, 1 %) to 18 % (320 Gy, 80 %). Notably there appears to be a plateau effect, where apparent sensitivity change is generally constant, at ~20 %, for the test doses of 120 Gy and above. It is interesting to note that most of the reduction in sensitivity change occurs between cycles 1 and 2 and cycles 7 and 8; these represent the progression from a large regeneration dose (e.g. cycle 1 ~400 Gy) to a small regeneration dose (e.g. cycle 2 = 0 Gy). This apparent sensitivity change may be due to the incomplete removal of charge during the regeneration measurement (L_x) which is then carried over into the test dose measurement (T_x). The impact of the signal transferred to the test dose measurement is diluted by using a larger test dose, therefore reducing the apparent sensitivity change recorded during the measurement protocol as seen in Figure 4.13.

4.6 A paired quartz-feldspar chronology for the Moopetsi tributary site

Systematic D_e underestimation was observed in both low test dose measurements (Section 4.4) and dose recovery experiments (Section 4.5.1). Subsequently, it was shown that using a higher test dose improves the ability of the post-IR $IRSL_{225}$ protocol to recover a known given dose (Section 4.5.2), and the effect of test dose size on the DRC (Section 4.5.2.1), D_0 (Section 4.5.2.2) and apparent sensitivity change (Section 4.5.2.3) was investigated. Thus an additional series of D_e measurements were undertaken

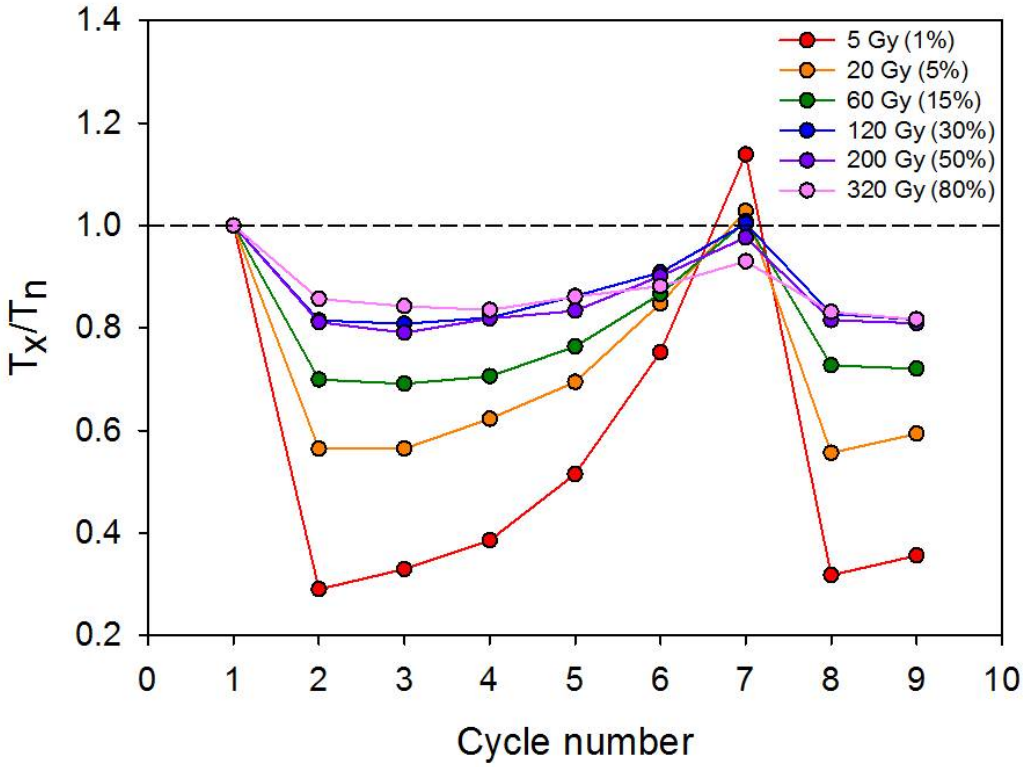

Figure 4.13: Apparent sensitivity change recorded during the post-IR $IRSL_{225}$ measurement in dose recovery experiment 2. Increasing the size of the test dose decreases the overall sensitivity change.

on the four lowermost samples from the Moopetsi tributary site, using the post-IR $IRSL_{225}$ protocol with a test dose 30 % of the expected mean D_e.

4.6.1 Single grain D_e distributions

Revised single grain dose distributions using the post-IR IRSL signal for the four lowermost samples (Figure 4.14 and Table 4.9) are substantially different to the dose distributions measured previously with a small test dose (see Figure 4.6 and Table 4.6). Not only has the proportion of grains passing the acceptance criteria increased, thus increasing the number of D_e values in the dose distribution (N and n, Table 4.9), but the proportion

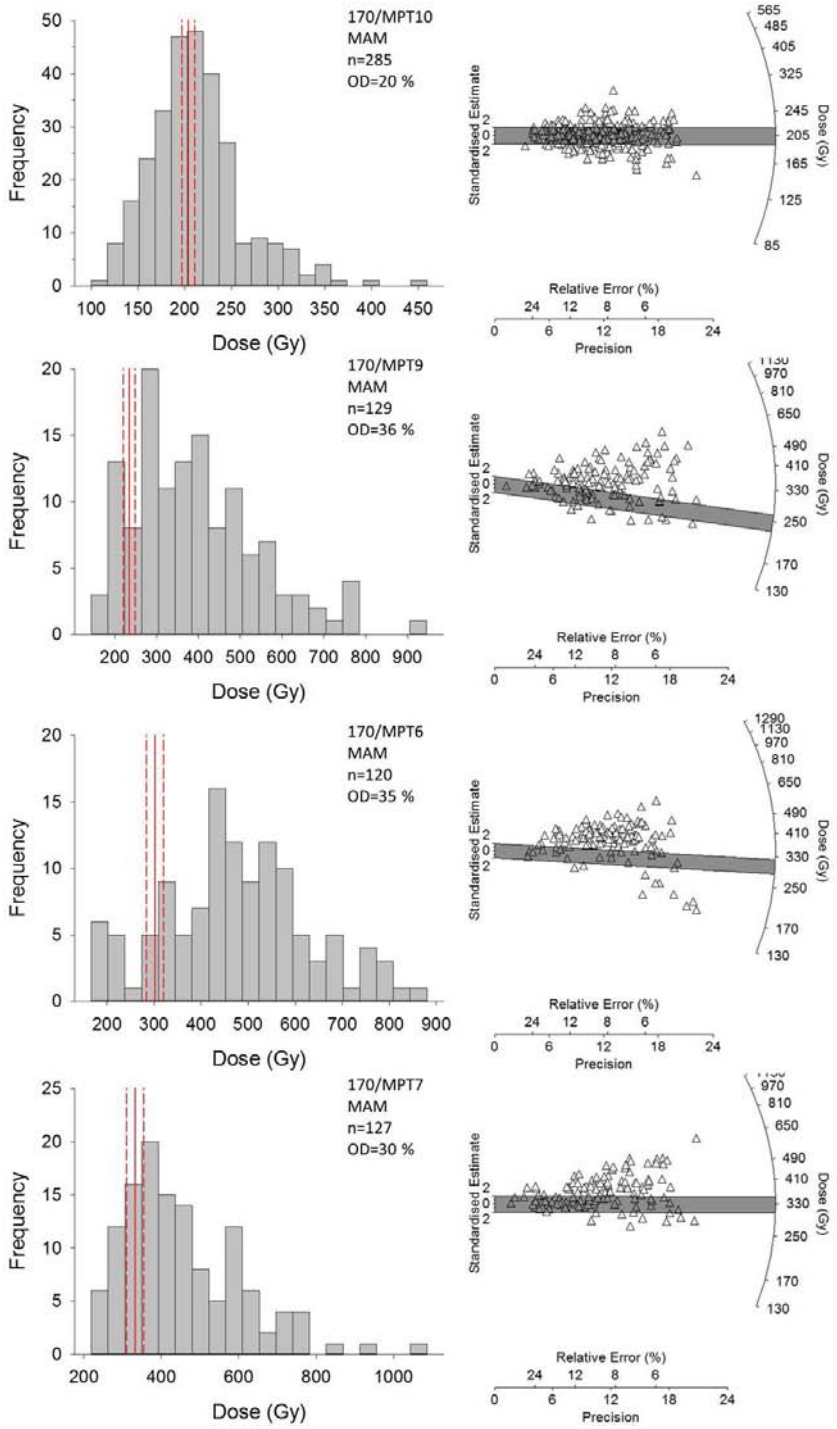

Figure 4.14: Histograms and radial plots of single grain K-feldspar D_e distributions for the four lowermost samples measured with a high (30 % of the D_e) test dose. The solid red line denotes the MAM D_e value with uncertainties (dashed red lines) and the grey bar the 2σ region about the MAM D_e value. Data presented here are prior to the subtraction of the residual signal (see discussion in text).

Table 4.9: Single grain K-feldspar D_e measurements made using the post-IR $IRSL_{225}$ protocol on the 180 – 212 μm grain size fraction. The four lowermost samples were measured with a test dose ~30 % of the average D_e (see discussion in text). D_e values were calculated using the MAM and are reported after subtraction of a 0.97 ± 0.23 Gy residual.

Sample ID	Number of grains							OD (%)	Skewness	Kurtosis	D_0 (Gy)[e]	D_e(Gy)[f]	Age (ka)
	N_T [a]	N[b]		n_{sat} [c]		n[d]							
170/MPT8	300	92	(31%)	3	(3%)	89	(97%)	101	2.76	10.95		0.53 ± 0.36	0.20 ± 0.12
170/MPT12	300	201	(67%)	0	(0%)	201	(100%)	69	5.57	41.36		13.6 ± 0.4	4.32 ± 0.19
170/MPT13	300	167	(56%)	4	(2%)	163	(98%)	61	6.13	43.71		14.7 ± 0.4	4.92 ± 0.22
170/MPT14	300	101	(34%)	0	(0%)	101	(100%)	71	4.74	31.61		12.3 ± 0.6	5.17 ± 0.31
162/MPT3	300	173	(58%)	0	(0%)	173	(100%)	53	5.40	34.85		20.0 ± 0.5	8.15 ± 0.37
162/MPT4	300	161	(54%)	4	(2%)	157	(98%)	35	4.42	29.06		36.3 ± 1.1	12.1 ± 0.6
170/MPT10	400	286	(72%)	1	(0%)	285	(100%)	20	1.04	5.29	373 ± 15	204 ± 7	72.7 ± 3.7
170/MPT9	300	131	(44%)	2	(2%)	129	(98%)	36	0.84	3.57	490 ± 22	246 ± 16	110 ± 8
162/MPT6	400	121	(30%)	1	(1%)	120	(99%)	35	0.15	2.77	431 ± 22	301 ± 18	119 ± 9
170/MPT7	400	141	(35%)	14	(10%)	127	(90%)	30	1.08	4.37	386 ± 15	331 ± 22	153 ± 12

[a] Total number of grains measured

[b] Number of grains that passed acceptance criteria

[c] Number of grains in saturation (as % of N)

[d] Number of grains in D_e distribution (as % of N)

[e] Reported only for DRCs fit with a SSE function

[f] A sigma-b value of 0.20 was used in the MAM calculation

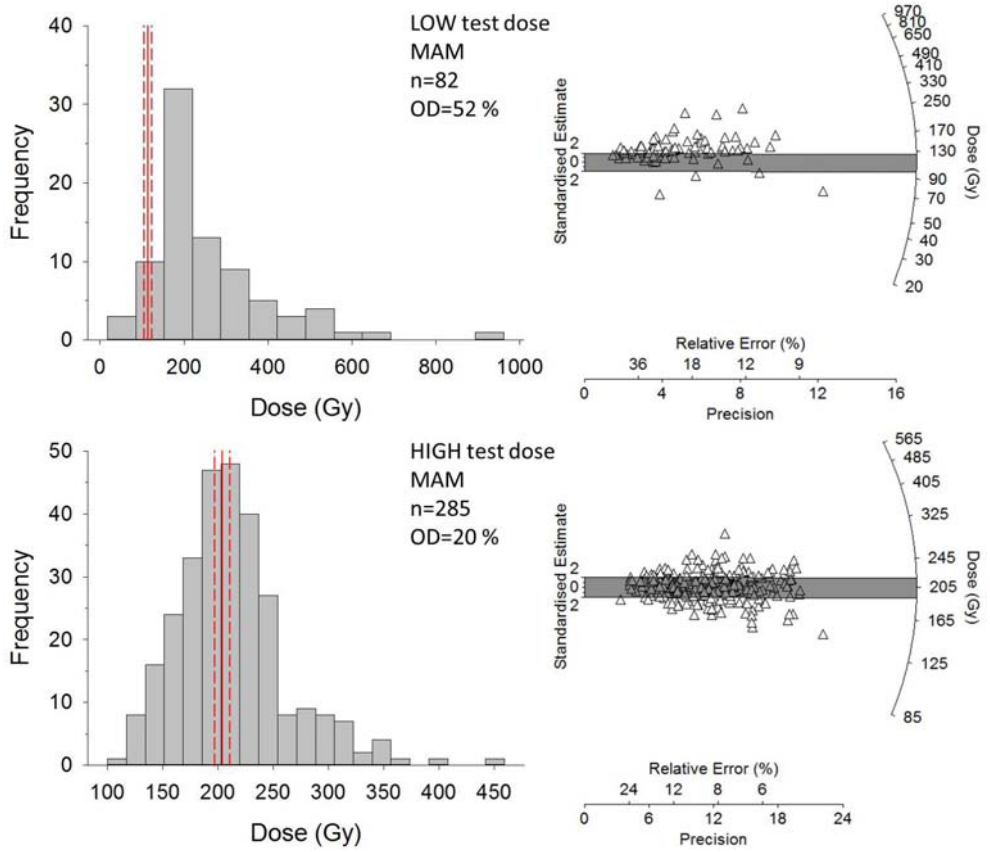

Figure 4.15: A comparison of the single grain K-feldspar D_e distributions for sample 170/MPT10 measured with a low test dose (top) and a high (30 % of the D_e) test dose (bottom). Note the different scales used on the dose (Gy) axis. The solid red line denotes the MAM D_e value with uncertainties (dashed red lines) and the grey bar the 2σ region about the MAM D_e value.

of saturated grains (n_{sat}, Table 4.9) has decreased. The highest D_e values measured with a low test dose have been removed from the high test dose distributions, making the distributions narrower. This is reflected in the lower skewness and kurtosis values and the much reduced (by up to 59 %) OD values. The D_e distributions for sample 170/MPT10, measured using both a low and high test dose, are shown in Figure 4.15 to facilitate comparison.

4.6.2 Single grain K-feldspar ages

Fluvial sediments, such as those collected from the Moopetsi tributary, are typically poorly bleached. The effect of heterogeneous bleaching was observed in the dose distributions for the upper six samples and the MAM of Galbraith et al. (1999) was selected to identify the most well-bleached proportion of grains within the distributions. Depositional processes are assumed to be the same for all ten samples, thus the most well-bleached proportion of grains is of interest in the four lowermost samples as well. This is of particular importance given the broad distributions for these samples (see Figure 4.14) as applying a measure of central tendency will result in an age ~44 ka older for sample 170/MPT7. Applying the MAM to all ten samples produces single grain K-feldspar ages (Table 4.10) consistent with depth throughout the section.

The final chronology for the Moopetsi tributary site is based on ten paired quartz and K-feldspar ages (see Table 4.10 and Figure 4.16) and the overall agreement between the paired ages is encouraging. Excluding one sample (170/MPT8, which was forced to match the quartz ages to calculate the residual signal to be subtracted from the K-feldspar measurements) seven of nine samples are within 2 sigma of each other. The remaining two samples (162/MPT4 and 170/MPT10) show a distinct offset between the quartz and K-feldspar ages.

Few studies have compared OSL and post-IR IRSL ages over extensive sequences. Reimann et al. (2011) and Sohbati et al. (2012) reported a handful of young samples in good agreement ($< \sim$20 ka). Buylaert et al. (2009) reported two fading-corrected post-IR $IRSL_{225}$ ages in exceptionally

Table 4.10: Final paired chronology based on small aliquot quartz OSL and single grain K-feldspar post-IR IRSL ages for ten samples from the Moopetsi tributary site. Also shown is the number of aliquots used in the D_e estimate (n), the overdispersion (OD) of the D_e distribution and the age model used to derive each D_e value. Ages in red have been excluded from the final paired chronology (see discussion in text) and **bold** type denotes the preferred ages.

Sample ID	Quartz OSL [a]					K-feldspar post-IR $IRSL_{225}$				
	n	OD (%)	Age model[b]	D_e (Gy)	Age (ka)	n	OD (%)	Age model[b]	D_e (Gy)	Age[c] (ka)
170/MPT8	44	110	MAM	0.37 ± 0.04	**0.20 ± 0.02**	89	101	MAM	0.53 ± 0.36	0.20 ± 0.03
170/MPT12	48	31	MAM	8.18 ± 0.62	**3.45 ± 0.30**	201	69	MAM	13.6 ± 0.4	4.32 ± 0.19
170/MPT13	43	59	MAM	9.05 ± 0.51	**4.11 ± 0.30**	163	61	MAM	14.7 ± 0.4	4.92 ± 0.22
170/MPT14	42	59	MAM	7.29 ± 0.31	**4.53 ± 0.28**	101	71	MAM	12.3 ± 0.6	5.17 ± 0.31
162/MPT3	47	19	CAM	11.3 ± 0.3	**6.72 ± 0.35**	173	53	MAM	20.0 ± 0.5	8.15 ± 0.37
162/MPT4	48	17	CAM	20.6 ± 0.5	**9.15 ± 0.47**	157	35	MAM	36.3 ± 1.1	12.1 ± 0.6
170/MPT10	38	24	CAM	103 ± 4	**50.6 ± 3.0**	285	20	MAM	203 ± 7	**72.7 ± 3.7**
170/MPT9	42	25	CAM	158 ± 6	106 ± 6	129	36	MAM	246 ± 16	**110 ± 8**
170/MPT6	49	16	CAM	161 ± 4	90.8 ± 4.7	120	35	MAM	301 ± 18	**119 ± 9**
170/MPT7	36	25	CAM	170 ± 8	119 ± 7	127	30	MAM	331 ± 22	**153 ± 12**

[a] Quartz data are based on Lyons (2012)

[b] The MAM calculation used a sigma-b value of 0.15 for quartz small aliquot measurements and 0.20 for K-feldspar single grain measurements

[c] Ages using K-feldspar post-IR $IRSL_{225}$ measurements were calculated after subtracting a residual dose of 0.97 ± 0.23 Gy from the D_e as described in the text

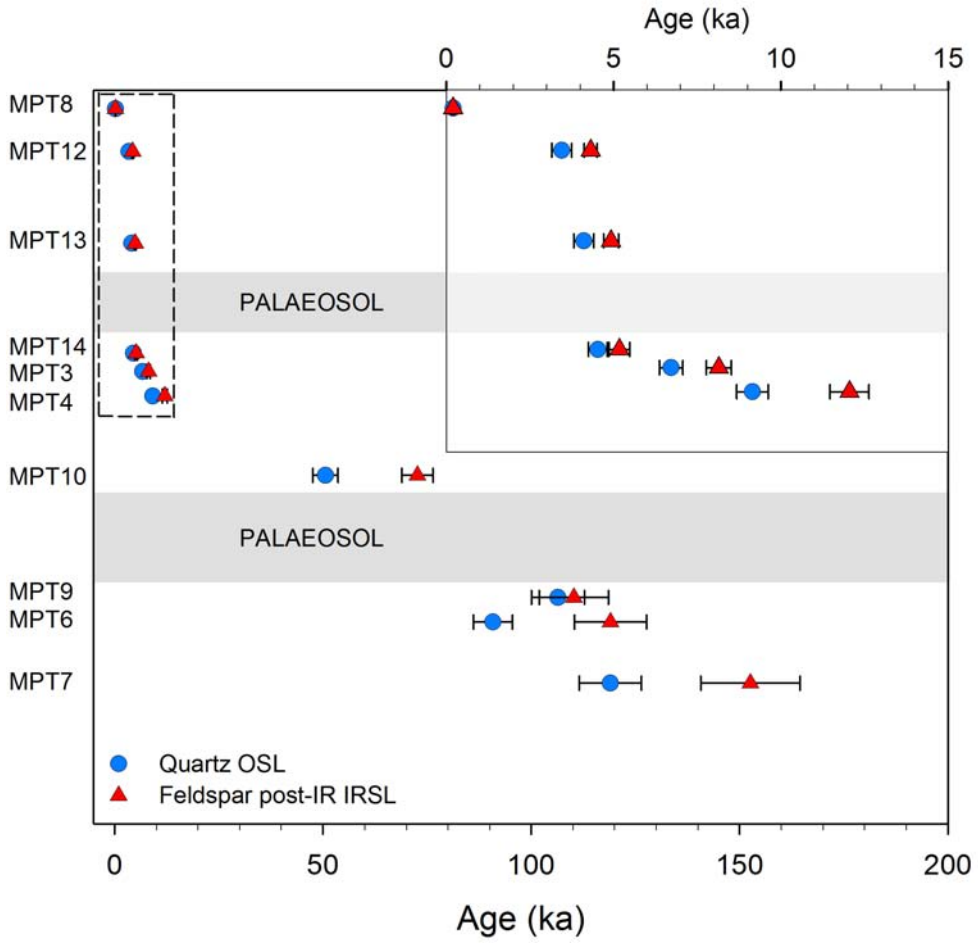

Figure 4.16: Comparison of paired quartz small aliquot (blue circles) and K-feldspar single grain (red triangles) ages from the Moopetsi tributary site. K-feldspar ages were calculated after the subtraction of a 0.97 ± 0.23 Gy residual (see discussion in text).

good agreement with quartz OSL at ~110 ka. Yi et al. (2015) presented 41 quartz and K-feldspar ages that showed good agreement up to ~40 ka (quartz D_e ~107 Gy) but beyond this age the two chronometers began to diverge. Thus the agreement between the three lowermost ages at the Moopetsi tributary site is more surprising than the offset between the two overlying ages.

Quartz is a more reliable dosimeter for young samples than K-feldspar due to rapid bleaching of the OSL signal (see Figure 4.1), which is of

particular importance in an environment where heterogeneous bleaching is expected. Thus, the quartz OSL ages are thought to be more accurate for the upper stratigraphy (170/MPT8 - 162/MPT4, see Table 4.10). However, to date environments past the Last Interglacial another dosimeter is required and K-feldspar is more reliable when the quartz OSL signal nears saturation. Thus, the K-feldspar ages are thought to be more accurate for the lower stratigraphy (170/MPT9 - 170/MPT7, see Table 4.10). This is because the lowermost three quartz samples have D_e values between 158 Gy and 170 Gy, which are above the threshold found by Chapot et al. (2012), even though they are below $2D_0$ (~280 Gy) for these samples. The K-feldspar ages are also in stratigraphic agreement, whereas the quartz ages are not. Determining the age of sample 170/MPT10 is more difficult, as both the quartz and K-feldspar ages are equally valid, and there is no definitive way to discern which age is accurate without independent age control.

4.7 Summary

This chapter outlined the development of a K-feldspar chronology for the Moopetsi tributary site, which will be applied to the Voordrag site in the next chapter. Initial investigations identified the post-IR $IRSL_{225}$ protocol as the most suitable post-IR IRSL signal for dating heterogeneously bleached fluvial sediments with very short transport distances (Section 4.3), due to the more rapid bleaching rate when compared to higher stimulation temperature protocols (Section 4.2). Furthermore, it was shown that in this environment, given the large proportion of grains producing a bright luminescence signal, it is necessary to use single grains of K-feldspar for D_e measurements to

avoid averaging a variety of D_e values and thus overestimating the apparent age (Section 4.3.4).

Small aliquot D_e distributions for quartz and feldspar from the same sample are offset, with the post-IR $IRSL_{225}$ D_e values consistently larger than those from quartz OSL (Section 4.4). Analysis of a young feldspar sample (170/MPT8) suggests that even when applying the MAM to the D_e data a residual signal of 11.0 ± 1.3 Gy remained at deposition; the measured residual signal from single grain measurements was reduced to 0.97 ± 0.23 Gy. At the single grain level, feldspar ages calculated after subtraction of the residual dose are in very good agreement with the small aliquot quartz OSL ages for the six uppermost samples. However, the four lowermost samples were in poor agreement with the quartz ages, underestimating and overestimating depending on the age model used to determine the burial dose. This lead to a series of experiments exploring the effect of the test dose size on the ability of the post-IR $IRSL_{225}$ signal to successfully recover a large known dose, which culminated in the identification of an optimal test dose, ~30 % of the D_e value (Section 4.5).

Finally, a complete feldspar post-IR $IRSL_{225}$ chronology was presented for the Moopetsi tributary site (Section 4.6). Overall, there was very good agreement between the quartz and feldspar ages up to ~10 ka, with an offset between ages older than ~10 ka and surprisingly good agreement between paired ages for the three lowermost samples >100 ka. Unfortunately, the period between 15 ka and 50 ka, where the switch between quartz and K-feldspar occurs, was not represented by the samples collected at this site, partly owing to a history of cut-and-fill events. However, at the Voordrag site there is a record of semi-continuous deposition back to ~100 ka,

with independent age control for the last ~40 ka thereby providing a rare opportunity to compare luminescence chronometers within the context of independent age control, which is the topic of the next chapter.

Chapter 5

Investigating single grain quartz and K-feldspar chronologies at Voordrag

5.1 Introduction

Voordrag is a key late Quaternary terrestrial archive which features a near-continuous succession (~18 m composite thickness) of colluvium and interbedded palaeosols that have been exposed through donga incision. The existing chronology, undertaken during the 1990s, is comprised of 9 K-feldspar IRSL ages and 11 radiocarbon ages (see Clarke et al., 2003), and suggests that the record covers the last ~100 ka. No quartz OSL measurements have previously been reported for the site.

This chapter will begin with an overview of the reasons behind revisiting the Voordrag site (Section 5.2). Initial measurements using small aliquots of quartz (Section 5.3) and subsequent equivalent dose measurements

undertaken using single grains of quartz (Section 5.4) and single grains of K-feldspar (Section 5.5) will be discussed. This will be followed by an explanation of how the two chronometers were combined to produce a single paired chronology for the site (Section 5.6).

5.2 Why revisit Voordrag?

Over the last two decades there have been major advances made within the field of luminescence dating. Three key advances are of particular interest to this study:

1. The development of the SAR protocol for quartz OSL dating (Murray and Wintle, 2000) which utilises the response to a measured test dose to correct for sensitivity change. Clarke et al. (2003) did not explore quartz OSL because a reliable procedure for OSL sensitivity correction was unavailable at the time of their original study in the early 1990s. Instead they used the single aliquot additive dose (SAAD) protocol of Duller (1994) with the dose-correction approach to measure the IRSL from large aliquots of K-feldspar. The SAAD protocol does not include a mechanism to correct for sensitivity change and assumes a linear response to luminescence dose, thus for older samples located in the non-linear portion of the DRC a correction is required to prevent systematic underestimation of the D_e value (Duller, 1994; Zhao et al., 2003). The SAAD protocol was shown to have limited applicability for a variety of samples by Stokes et al. (2000) who cautioned against its use without prior testing of the validity of the protocols underlying assumptions. Thus, the SAR protocol has become the preferred

approach due to its ability to correct for sensitivity change, the determination of the D_e by interpolation (rather than extrapolation) thereby providing better precision and accuracy and the reduced dependence of results on the equations used to fit the DRC (Zhao et al., 2003).

2. The greater signal stability offered by the post-IR IRSL protocol for feldspars (Thomsen et al., 2008). The most challenging part of dating feldspars is dealing with anomalous fading and numerous attempts have been made to accurately measure and correct for fading of the IRSL signal (e.g. Guérin and Visocekas, 2015; Kars and Wallinga, 2009; Kars et al., 2008; Lamothe and Auclair, 2000; Lamothe et al., 2003, 2012; Li and Li, 2008; Spooner, 1994). Subsequent to the measurement of the Voordrag IRSL chronology, a new approach to fading measurements was presented by Huntley and Lamothe (2001) and extended by Auclair et al. (2003), along with a proposed technique to correct IRSL ages for the effect of anomalous fading, however they are inapplicable at large doses i.e. as the DRC approaches saturation. Subsequently, Thomsen et al. (2008) determined that IR stimulation at elevated temperatures significantly reduced the apparent fading rate and Thiel et al. (2011) showed that low measured g-values (similar to those measured for the post-IR IRSL protocol in later work) may in fact be a laboratory artefact when they measured a g-value of 1.3 $\pm$ 0.3 %/decade for quartz.

3. The ability to measure single grains (Bøtter-Jensen et al., 2000; Duller et al., 2003) and to investigate distributions of equivalent dose. Many studies have been published on single grain dating of both quartz

and feldspar across a wide range of environments, but particularly in archaeological settings (e.g. Armitage et al., 2011; Feathers and Pagonis, 2015; Galbraith et al., 1999; Jacobs et al., 2003, 2013, 2008a; Murray and Roberts, 1997; Olley et al., 2004a; Reimann et al., 2012; Smedley et al., 2016). Numerous analyses of the very large dose distributions provided by single grain measurements have also been completed (e.g. Arnold et al., 2007, 2012; Bailey and Arnold, 2006; Jacobs et al., 2006a, 2008b; Neudorf et al., 2012). These studies, and others, have highlighted a need for single grain measurements to supplement multiple grain measurements, particularly in environments where poor bleaching is observed.

These advances are significant because of the very short transport distance (<1 km) of colluvial material by sheet wash within the Voordrag system, which implies a high likelihood of heterogeneous bleaching. Given the geomorphological and geochronological importance of the site, and based on the key advances made in the luminescence dating field outlined above, it is timely to re-examine the chronology for Voordrag using updated luminescence techniques.

Additionally the relatively high dose rates at the site leave the lower portion of the stratigraphic section beyond the range of quartz OSL and hence dating K-feldspar is required to constrain the timing of initial sedimentation. A positive aspect of the high dose rates is that saturation of the quartz OSL signal occurs within the range of radiocarbon. Thus, the true value of Voordrag lies in the opportunity to compare single grain quartz OSL and K-feldspar post-IR IRSL ages against one another, and also with an independent chronometer (in the form of an extensive radiocarbon

chronology) in an environment subject to heterogeneous bleaching. A comparison of this nature has not been previously reported in the literature, therefore Voordrag affords a rare opportunity to explore these three dating protocols at a single locality.

5.3 Initial quartz OSL investigations

Initial luminescence investigations were undertaken on quartz due to the very short (<1 km) transport distance within the colluvial system. Heterogeneous bleaching was expected, therefore the quartz OSL signal should provide a more accurate measure of D_e than the K-feldspar post-IR IRSL signal given the faster rate of bleaching of the quartz OSL signal compared with the K-feldspar post-IR IRSL signal as discussed in Section 4.2 (see Figure 4.1).

To determine the measurement parameters for the SAR protocol, small aliquots were used instead of single grains because the results were more reproducible. A preheat-dose recovery test was run on three samples, selected based on their location within the stratigraphic section, i.e. at the top (representative of a process analogue, 215/VRD00), middle (215/VRD06) and bottom (215/VRD01) of the sequence. A set of twenty four small aliquots were prepared for each sample, with a subset of three discs for each preheat temperature between 160 °C and 300 °C at 20 °C intervals. Each disc was irradiated with a β dose similar to the expected natural dose for the relevant sample (determined by initial signal tests run on three aliquots each). Optimal preheat temperatures were identified at 200 °C – 260 °C for 215/VRD00, 180 °C – 260 °C for 215/VRD06 and 220 °C – 240 °C for 215/VRD01 (Figure 5.1). A preheat temperature of 220°C for 10 s was

deemed most suitable for further measurements (hereafter referred to as Ph_{regen}). To avoid the issue of thermal lag and to ensure that the sample is heated to the desired temperature the test dose preheat, hereafter referred to as the Ph_{test}, was set at 160°C for 10 s rather than employing a typical cutheat (i.e. 160°C for 0 s).

5.3.1 Comparing D_e distributions from multiple and single grain measurements

In order to determine whether heterogeneous bleaching would produce an overestimation of the natural dose similar to the effect observed in the Moopetsi feldspar D_e measurements, D_e values were measured using both small aliquots (~30 – 40 grains) and single grains of quartz from the process analogue sample, 215/VRD00 (Figure 5.2). D_e values measured using small aliquots display greater precision, as expected due to their higher signal intensity. The small aliquots also have a lower (albeit relatively large) OD of 68 %, compared to 110 % for the single grains. This relationship between precision and overdispersion was also observed in the Moopetsi tributary samples between the small aliquot and single grain D_e distributions for K-feldspar, and was determined to be directly related to the averaging of a large number of variable D_e values on small aliquots which contained ~30 grains.

A relatively large difference is observed in the age model estimates for the two distributions, where the small aliquot D_e distribution gives a MAM estimate ~7 Gy larger than the corresponding single grain distribution (see Figure 5.2). This translates into an effective age difference of 2.94 ka, assuming an average dose rate of 2.59 Gy/ka for the colluvial sediments

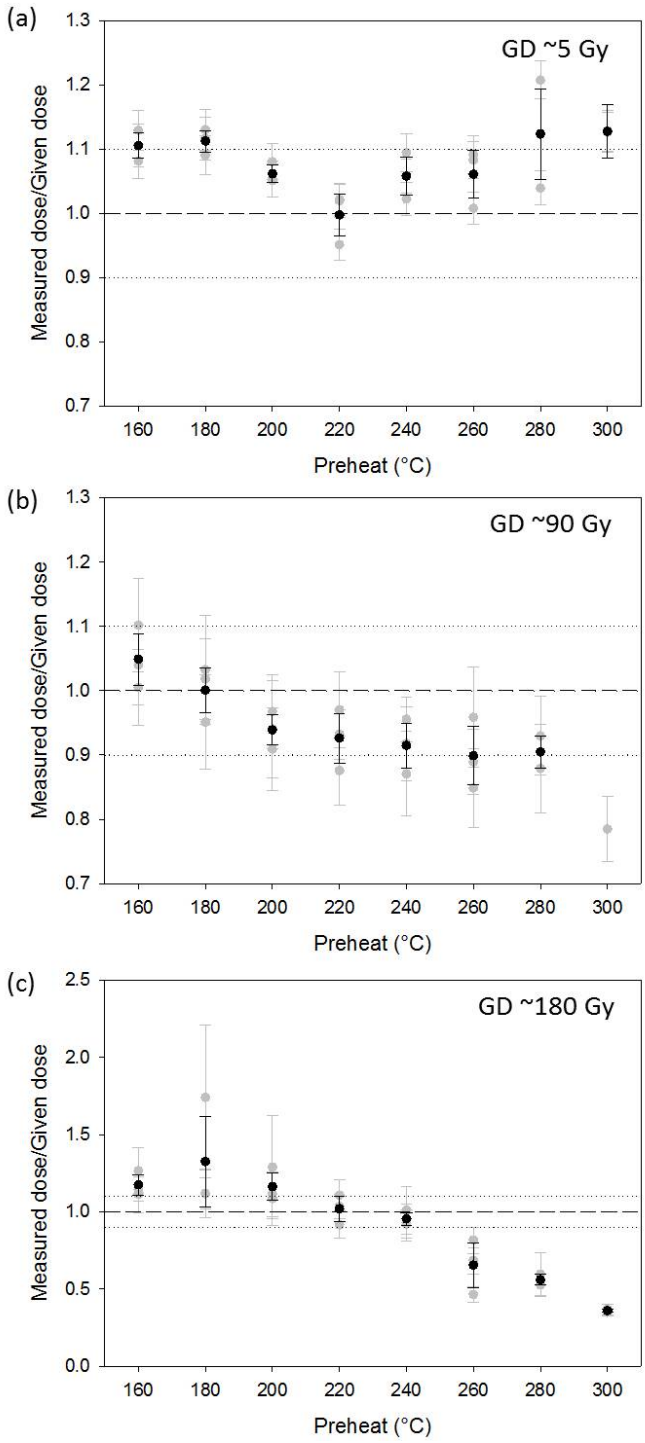

Figure 5.1: Preheat-dose recovery tests for small aliquots of quartz from three samples at Voordrag, located at the (a) top (215/VRD00), (b) middle (215/VRD06) and (c) bottom (215/VRD01) of the stratigraphic section. Grey circles represent the measurements from individual aliquots and black circles represent the mean of the three measurements. A standard test dose of ~5 Gy and a Ph_{test} of 160 °C for 10 s were used during the SAR measurement.

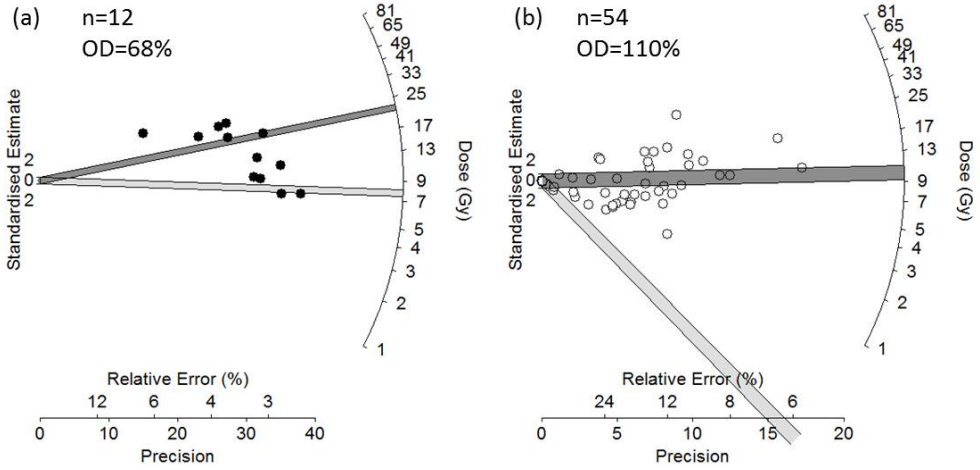

Figure 5.2: The (a) small aliquot D_e distribution and (b) single grain D_e distribution (excluding six negative values, which cannot be plotted on a radial plot) for the modern process analogue, 215/VRD00. The dark grey bar represents the mean D_e for the distribution and the light grey bar the D_e value calculated using the MAM.

at Voordrag. Thus, small aliquot quartz OSL measurements would result in an age overestimation due to the natural dose distribution being biased towards higher $D_e$values; a similar overestimation was reported by Geach et al. (2015) and Russell and Armitage (2012). Therefore, in modern donga environments where sediments were deposited by colluvial processes under very short transport distances resulting in heterogeneous bleaching of the sediments, single grain quartz measurements should prove more effective than small aliquots, both in determining the degree to which sediments have been heterogeneously bleached and in calculating accurate ages.

5.4 Single grain quartz OSL

Upon consideration of the existing IRSL D_e values and the relatively high dose rates, it seems unlikely that quartz OSL will be a reliable dosimeter for the entire length of the stratigraphic section exposed at the Voordrag donga

site. However, this provides the opportunity to explore the behaviour of the quartz OSL signal near saturation by comparing the quartz D_e distributions to the paired K-feldspar post-IR IRSL D_e distributions. Furthermore, the direct comparison of paired quartz-feldspar single grain ages, within the framework of independent radiocarbon ages, will determine whether multiple luminescence chronometers can be combined to date separate portions within a stratigraphic section.

A series of measurements were undertaken on single grains of quartz using the SAR protocol outlined in Table 5.1, to determine the D_e distribution characteristics of each sample through the entire section. The IR-OSL depletion ratio of Duller (2003) was used to assess the samples for feldspar contamination. DRCs for this site were routinely built to doses of ~350 Gy for samples in the mid-stratigraphy and ~550 Gy in the lower stratigraphy in an effort to characterise the shape of the DRC and to observe the effect of saturation on the OSL signal. Considerable variability has been reported between single grain DRCs and the dose saturation point (I_{max}) (e.g. Duller, 2012b; Duller et al., 2000; Jacobs et al., 2003; Roberts et al., 1999); this variability was also observed in the Voordrag samples (Figure 5.3). The quartz OSL signal was dominated by the fast component, seen in the rapid initial decay of the signal, confirming the suitability of the SAR protocol.

5.4.1 Proportion of grains producing an OSL signal

Typically, the number of quartz grains producing a luminescence signal is < 5 % of the total number of measured grains (e.g. Armitage et al., 2011; Carr et al., 2007; Duller, 2008b; Medialdea et al., 2014; Ou et al., 2015), however higher values have been reported including ~12 % by Jacobs

Table 5.1: SAR protocol used for single grain quartz D_e measurement.

Step	Treatment	Measured
1	Dose (Natural/regeneration)	
2	Preheat at 220 °C for 10 s	
3	OSL at 125 °C for 1 s	L_x
4	Test dose (5 Gy)	
5	Preheat at 160 °C for 10 s	
6	OSL at 125 °C for 1 s	T_x

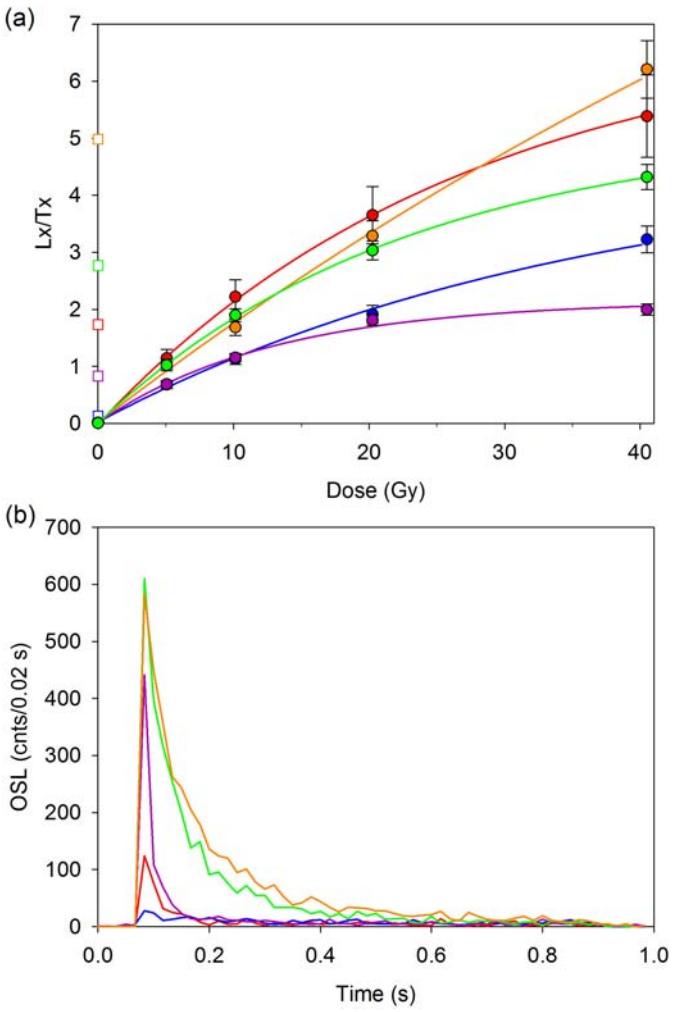

Figure 5.3: Five single grain (a) DRCs and their (b) natural luminescence signals from sample 215/VRD09.

et al. (2006b) and 21 – 94 % by Olley et al. (2004a). When determining single grain $D_e$values for Voordrag, the percentage of grains which pass the acceptance criteria is between 10 % and 15 %. Although this is relatively high, the number of grains actually producing a luminescence signal is much higher, with 95 % of the total luminescence signal coming from 45 – 50 % of the grains (Figure 5.4). This is similar to the value published for calibration quartz (65 %) by Duller et al. (2000) and implies that these samples have an even distribution of light from their grain populations. This provides reproducible multiple grain measurements where the grain-to-grain variability is averaged out and masked, as observed in the comparison of small aliquot and single grain quartz D_e distributions for 215/VRD00 in Section 5.3.1. Duller et al. (2000) also showed distributions with a low proportion of very bright grains; here the multiple grain measurements were dominated by a few grains and the grain-to-grain variability was still observable even at the multiple grain scale. The general shape of the plots in Figure 5.4 imply a smaller proportion of very bright grains (visible in the initial sharp increase) and a larger proportion of bright grains (visible in the continuous gradual increase); if all grains were equally bright the curve would appear smoother and less asymmetrical. The fact that as many as half of the grains on every disc may be contributing to the small aliquot D_e value, supports the assertion that the small aliquot data is overestimating when compared with the single grain data (Section 5.3.1).

5.4.2 Quartz D_e distributions

The single grain D_e distributions display a large amount of scatter and high OD values typical of single grain D_e measurements (e.g. Arnold et al., 2007;

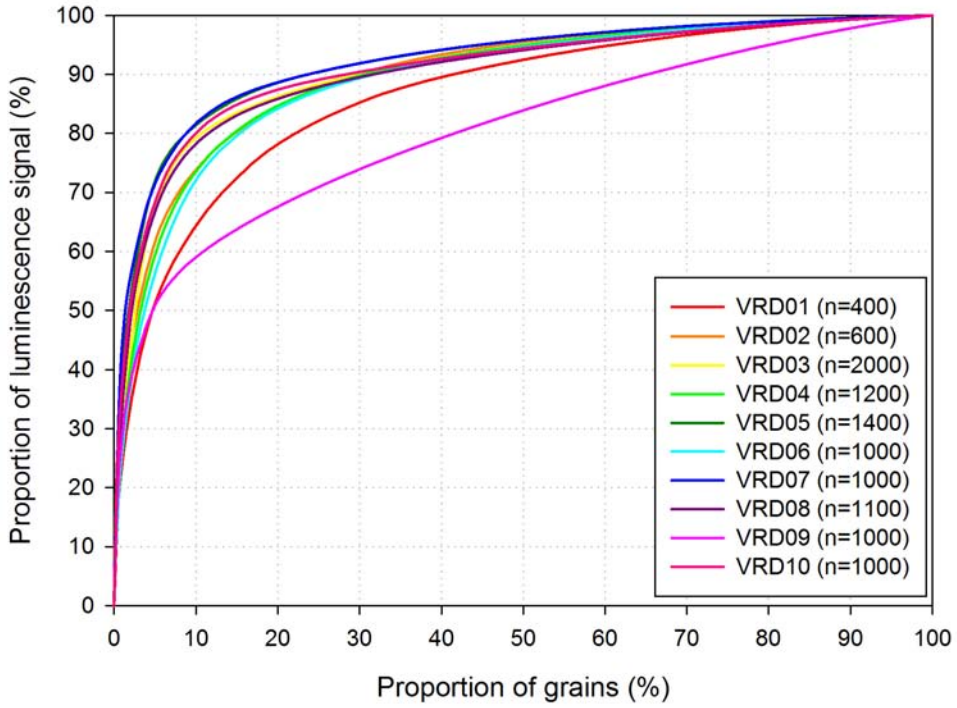

Figure 5.4: Total OSL signal produced by all measured grains for each sample. The majority of grains in all samples are producing a luminescence signal, which leads to signal averaging and overestimation of the burial dose when measuring small aliquots.

Carr et al., 2007; Jacobs et al., 2008b; Thomas et al., 2005). Histograms and radial plots of the natural dose distributions (Figure 5.5) show a large spread in the D_e data for all samples, with a maximum range as high as ~160 Gy recorded for younger samples (stratigraphically above 215/VRD05) and ~430 Gy recorded for the older samples (stratigraphically below 215/VRD05). OD values range from 23 % (215/VRD06) to 110 % (215/VRD09) but there is no clear trend with depth. The highest OD values are located at the top (215/VRD09) and the bottom (215/VRD01) of the stratigraphic section, however the dominant influence on the distribution producing the scatter is different for each of these samples. At the top of the stratigraphy

(i.e. 215/VRD09) the effect of heterogeneous bleaching is apparent in the skewed distribution and large difference (~60 Gy) between the minimum and maximum D_e values (Figure 5.5). The large proportion of well-bleached grains in this distribution implies that the sample was heterogeneously bleached as opposed to poorly or incompletely bleached, i.e. there are two subsets of grains within the sample, one where the OSL signal was reset (~84 % of the population) and another where the signal was not completely reset (~16 % of the population seen as a 'tail' in the distribution). This 'tail' spreads over ~50 Gy, which is significant at very low doses but less so at higher doses. The effect of heterogeneous bleaching on the individual D_e distributions can be seen diminishing with increasing depth, as the proportion of D_e values within the tail is reduced.

As the effect of heterogeneous bleaching decreases with depth, the effect of saturation of the OSL signal increases. This is observed in the number of grains within each distribution deemed to be in saturation, which increases with depth from 4 % for 215/VRD09 to 85 % for 215/VRD10 (Table 5.2). In this study, a sample is deemed to be in saturation when L_n/T_n is (i) equal to or (ii) larger than the signal from the maximum regeneration dose measured (Figure 5.6). As saturation of the OSL signal becomes the dominant influence, the D_e distribution should be truncated at higher doses. Thomsen et al. (2016) argue that a sample in true saturation (where 50 % of the measured L_n/T_n values lie above saturation) would produce a highly positively skewed dose distribution. This does seem to be the case for 215/VRD03, however the three lowermost samples are only slightly skewed and no longer display an obvious 'tail'. This is partly due to the small size of the dataset and also an effect of the DRC fitting approach

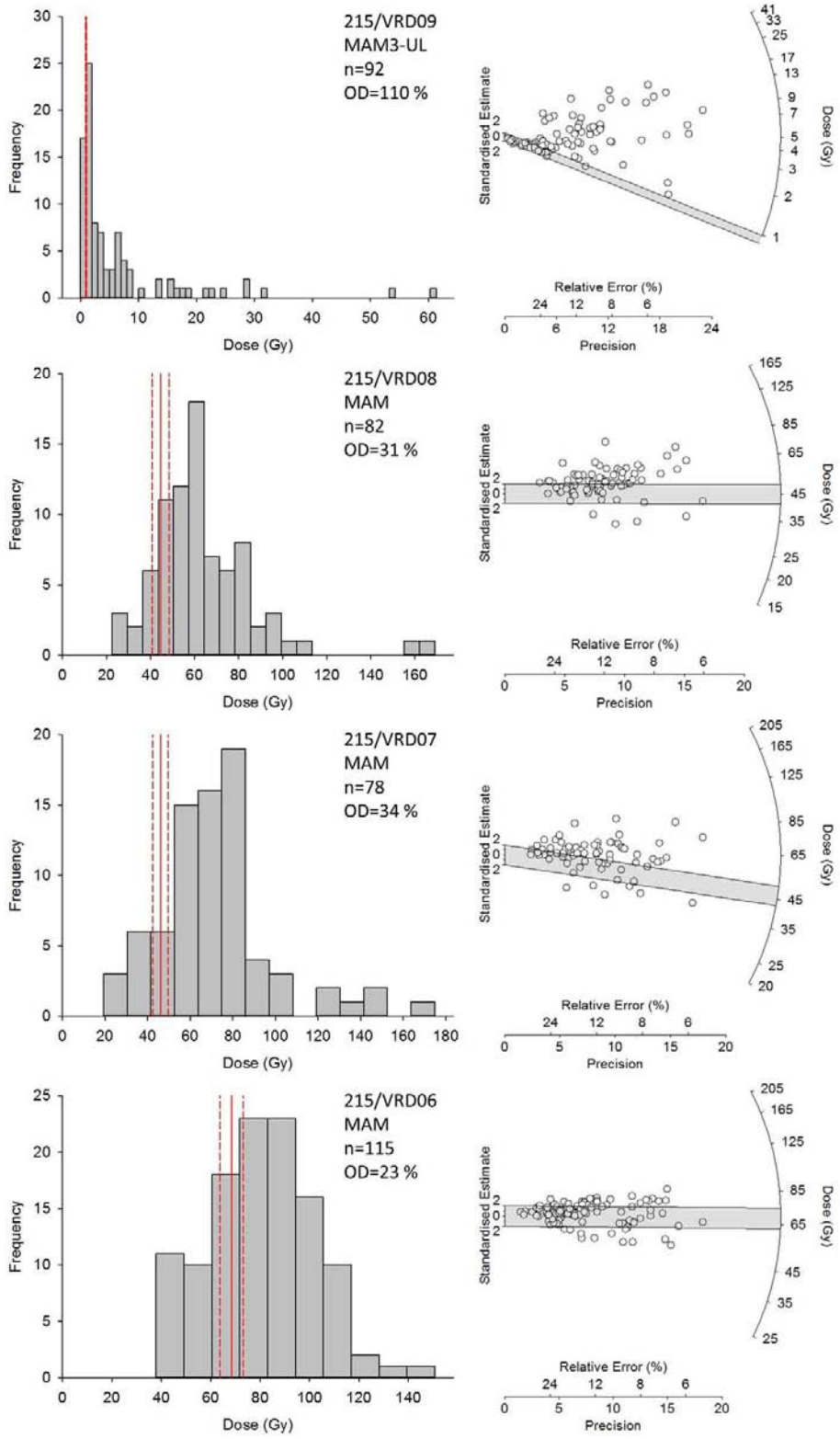

Figure 5.5: Histograms and radial plots of single grain quartz D_e distributions at Voordrag. The solid red line denotes the MAM D_e value with uncertainies (dashed red lines) and the grey bar on the radial plot shows the 2σ region about the MAM D_e value.

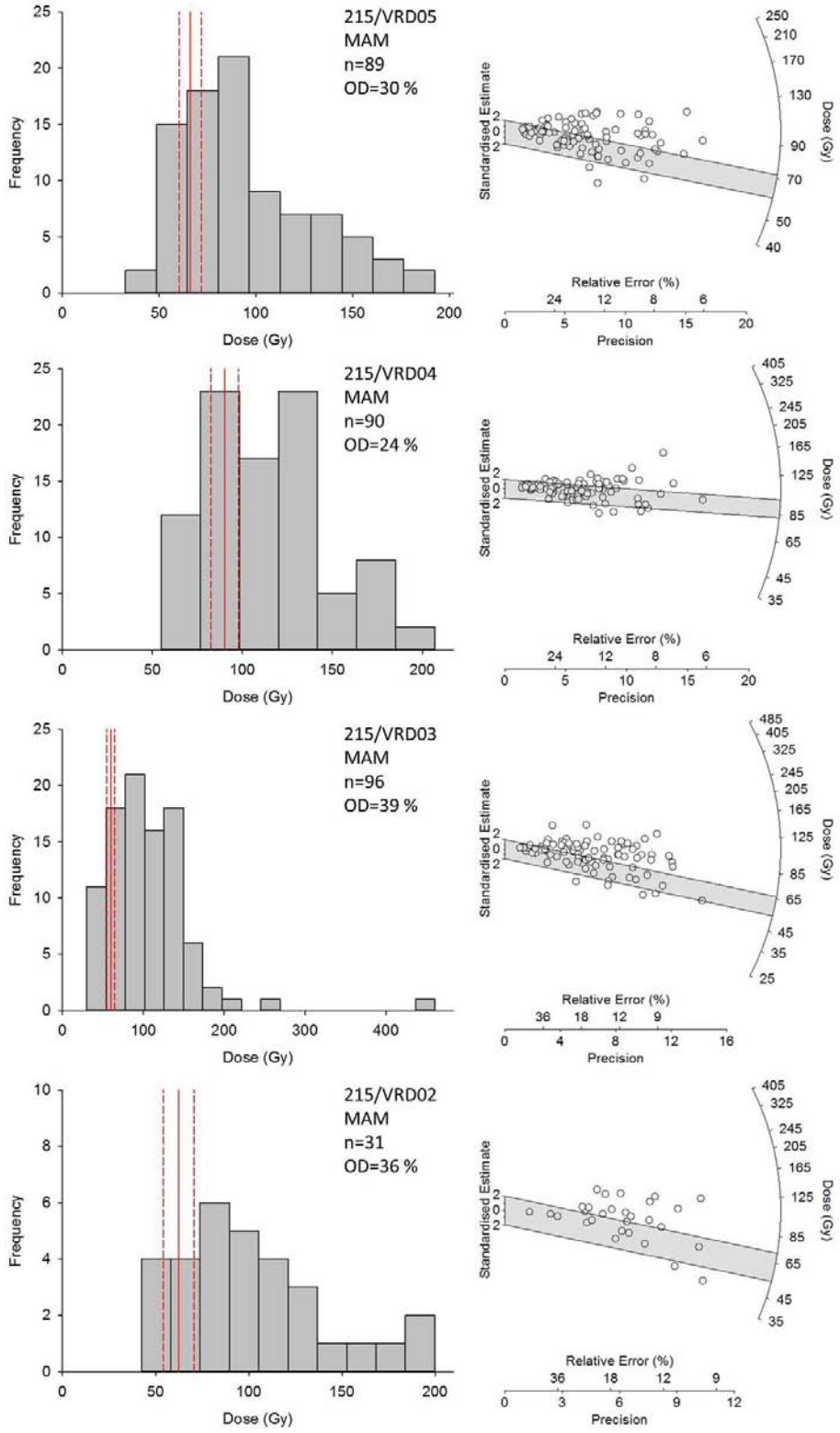

Figure 5.5: Histograms and radial plots of single grain quartz D_e distributions at Voordrag (continued).

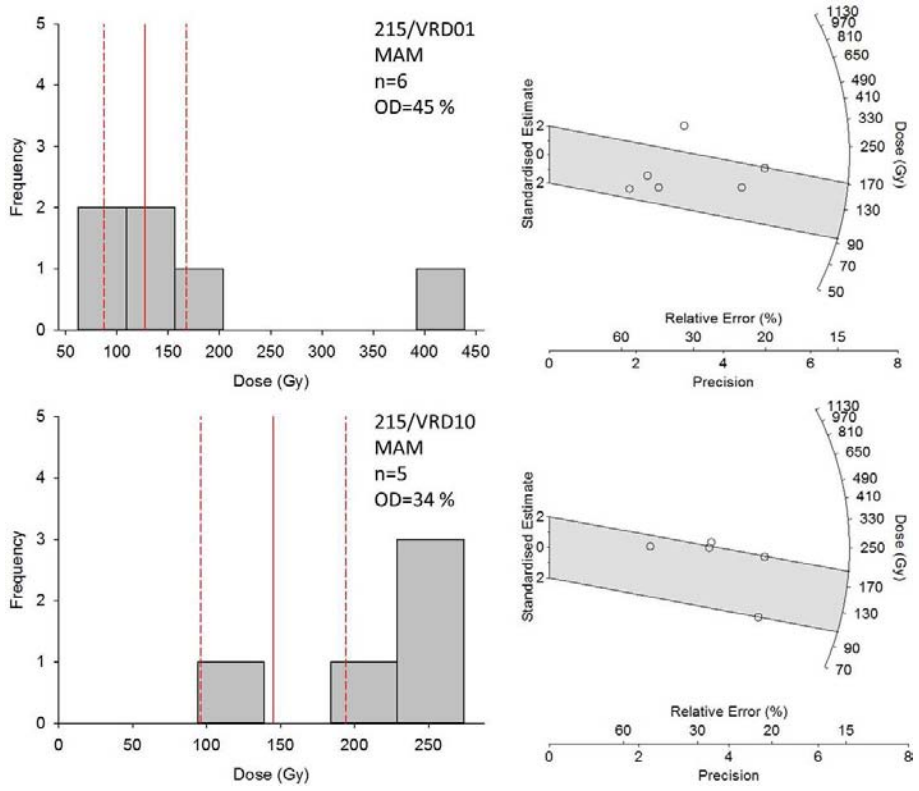

Figure 5.5: Histograms and radial plots of single grain quartz D_e distributions at Voordrag (continued).

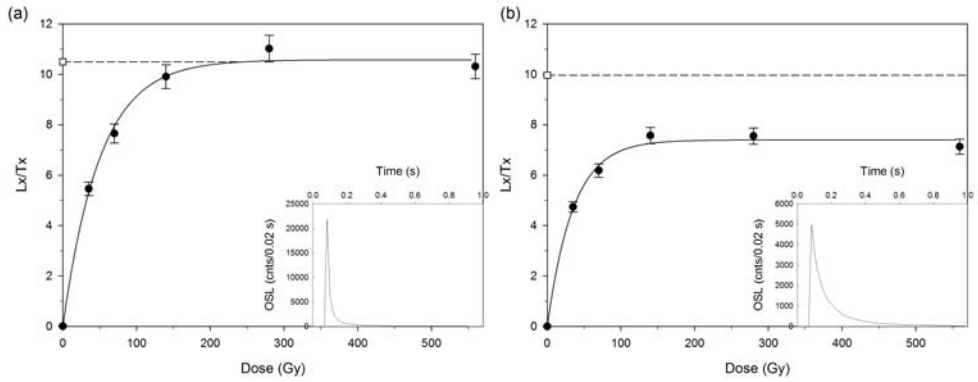

Figure 5.6: Example of single grains in saturation, where (a) L_n/T_n is equal to the signal from the maximum regeneration dose measured and (b) L_n/T_n is greater than the signal from the maximum regeneration dose during DRC construction.

used in this study. Quartz DRCs were fit with either single (SSE) or double (DSE) saturating exponential functions to prevent the inclusion of unrealistically large D_e values into the dose distribution (seen when fitting a single exponential plus linear (SEPL) function for a sample near saturation). Fitting the same data with a SSE or DSE function (instead of a SEPL function) would result in a saturated DRC and no D_e value would be obtained. The effect of having a large number of saturated grains within a population, is to potentially unfairly bias the distribution towards lower D_e values thereby underestimating the luminescence age (e.g. Thomsen et al., 2016; Trauerstein et al., 2014). Therefore, using quartz OSL to date the lower portion of this stratigraphic section would provide a minimum burial age for these sediments.

5.4.3 The effect of saturation of the quartz OSL signal

The main benefit of Voordrag's relatively high dose rates was the opportunity to look at the effect of signal saturation on OSL ages within the time frame of radiocarbon ages. A clear increase in the proportion of saturated grains with depth can be seen (Table 5.2). This is accompanied by a general decrease in the skewness of the D_e distributions from the uppermost sample 215/VRD09 to 215/VRD04 (3.10 to 0.49, Table 5.2), with a sudden increase in skewness for 215/VRD03 (3.01, Table 5.2) and then decreasing values (to -0.09, Table 5.2) for the older samples. The kurtosis values follow the same pattern as the skewness values.

Wintle and Murray (2006) suggested $2D_0$ as a maximum reliability threshold for quartz OSL dating (see Section 1.3.2). Due to the DRC fitting approach adopted in this study (see Section 3.3.3), multiple D_0 values can be calculated for the DRCs fit with either a SSE or DSE function. DRCs fit with a single exponential function produce D_0 values ranging between 33 ± 2 Gy and 63 ± 2 Gy (Table 5.2). The only sample to be fit with a double exponential function was 215/VRD03 which produced values of 23.3 ± 2.7 Gy and 142 ± 12 Gy for D_{01} and D_{02}, respectively. For the eight uppermost samples (215/VRD09 – 215/VRD02) the D_e value calculated with the MAM is below $2D_0$. For the two lowermost samples (215/VRD01 and 215/VRD10) the D_e value is larger than the $2D_0$ value.

Thomsen et al. (2016) presented alternative acceptance criteria for single grain quartz measurements, which improved their agreement with independent age control at the expense of reducing their accepted grain

Table 5.2: Single grain quartz D_e measurements at Voordrag. Measurements were made using a SAR protocol on 180 – 212 μm grain size for all samples, except 215/VRD06, VRD04, VRD02 and VRD10 where the 150 – 180 μm fraction was used. The minimum age model (MAM) was used to determine the D_e values for all samples.

Sample ID	Number of grains							OD (%)	Skewness	Kurtosis	D_0 (Gy)[e]	D_e (Gy)[f]	Age (ka)
	N_T [a]	N[b]		n_{sat} [c]		n[d]							
215/VRD09	1000	97	(10%)	4	(4%)	92	(95%)	110	3.10	14.27	33 ± 2	0.93 ± 0.07	0.32 ± 0.03
215/VRD08	1100	102	(9%)	20	(20%)	82	(80%)	31	1.86	9.21	52 ± 4	44.6 ± 3.9	17.5 ± 1.7
215/VRD07	1000	95	(10%)	17	(18%)	78	(82%)	34	1.21	5.53	60 ± 3	46.1 ± 3.6	16.2 ± 1.5
215/VRD06	1000	150	(15%)	35	(23%)	115	(77%)	23	0.21	2.96	57 ± 2	68.4 ± 4.7	27.5 ± 2.2
215/VRD05	1400	151	(11%)	62	(41%)	89	(59%)	30	0.79	2.94	58 ± 2	66.1 ± 5.7	23.4 ± 2.2
215/VRD04	1200	159	(13%)	69	(43%)	90	(57%)	24	0.49	2.75	63 ± 2	90.1 ± 7.6	36.4 ± 3.4
215/VRD03	2000	225	(11%)	129	(57%)	96	(43%)	39	3.01	19.35	49 ± 2	59.7 ± 4.9	23.7 ± 2.2
215/VRD02	600	78	(13%)	47	(60%)	31	(40%)	36	0.80	3.04	51 ± 3	62.3 ± 8.3	27.7 ± 3.9
215/VRD01	400	61	(15%)	55	(90%)	6	(10%)	45	1.08	2.45	44 ± 2	127 ± 40	51.5 ± 16.4
215/VRD10	500	33	(7%)	28	(85%)	5	(15%)	34	-0.09	1.83	62 ± 4	145 ± 49	42.5 ± 14.4

[a] Total number of grains measured

[b] Number of grains that passed acceptance criteria

[c] Number of grains in saturation (as % of N)

[d] Number of grains in D_e distribution (as % of N)

[e] Reported for DRCs fit with a single exponential function

[f] A sigma-b value of 0.2 was used in the MAM calculation

population by more than an order of magnitude. Application of their D_0 criterion excludes grains with low D_0 values (i.e. where D_0 < a sample average D_e). When applied to the Voordrag dataset, this resulted in (i) a significant decrease in n, (ii) a decrease (but not the complete elimination) of n_{sat}, (iii) an increase in OD, (iv) mean D_e and CAM D_e values within uncertainty of one another and (v) the loss of stratigraphic consistency for the resulting ages down section when the MAM was applied. An interesting outcome was the complete exclusion of every D_e value in the dose distributions for the two lowermost samples (215/VRD01 and 215/VRD10) which implies that these samples are saturated. However, several reasons to disregard the ages obtained from these two samples have already been discussed (i.e. low n, high n_{sat}, $D_e > 2D_0$) and the exclusion of these grains merely serves to reinforce the decision that these samples are beyond the range of quartz OSL. In this instance application of the D_0 criterion did not improve the agreement with the independent age control and was therefore disregarded as an acceptance criterion.

Based on the analysis of n_{sat} and $2D_0$ values (Table 5.2), the uppermost six samples are well within the limit of the quartz OSL signal and should produce reliable ages. Sample 215/VRD03 was identified as the potential point in the stratigraphy where the effect of saturation of the OSL signal becomes the dominant influence on the D_e distribution, based on the fact that the saturated grains outnumber the accepted D_e values (n_{sat}=129 and n=96, Table 5.2). Thus, whilst it is clear that the lowest two samples will not provide credible ages, the ability of 215/VRD03 and 215/VRD02 to provide reliable ages is questionable due to the large number of saturated grains within the D_e distributions.

5.4.4 Selecting an appropriate age model

The effect of heterogeneous bleaching was observed in the D_e distribution for the youngest sample (215/VRD09), which was considered to be representative of the other nine samples collected for luminescence dating in terms of depositional conditions and sediment composition. Therefore, the most well-bleached population of grains is of interest for all samples and the MAM of Galbraith et al. (1999) was applied to these distributions.

The single grain quartz OSL ages increase with depth, although there are three age inversions down stratigraphy at 215/VRD06, 215/VRD04 and 215/VRD01 respectively (see Table 5.2). Unfortunately, there is no clear indication based on dose distribution characteristics or ages of where saturation of the OSL signal becomes insurmountable without turning to another chronometer for clarification. This highlights the reason why dating a site with multiple, complementary chronometers is so attractive. Therefore, the K-feldspar post-IR IRSL protocol will be applied to the entire stratigraphic section at Voordrag in an attempt to produce a comparative chronology, with particular focus on the lower portion of the stratigraphy in an attempt to constrain the effects of saturation of the quartz signal.

5.5 Single grain K-feldspar post-IR IRSL

The post-IR $IRSL_{225}$ protocol outlined in Table 5.3 using a large magnitude test dose (30 % of the D_e) was applied to ten samples collected from the Voordrag site. Standard acceptance criteria (Section 3.3.3) were applied and a summary of the single grain post-IR $IRSL_{225}$ data are presented in Table 5.4.

Table 5.3: Post-IR $IRSL_{225}$ protocol used for single grain K-feldspar D_e measurement.

Step	Treatment	Measured
1	Dose (Natural/regeneration)	
2	Preheat at 250 °C for 60 s	
3	IRSL at 50 °C for 200 s (LEDs)	
4	IRSL at 225 °C for 2 s (laser)	L_x
5	Test dose (30 % of average D_e)	
6	Preheat at 250 °C for 60 s	
7	IRSL at 50 °C for 200 s (LEDs)	
8	IRSL at 225 °C for 2 s (laser)	T_x
9	IRSL at 290 °C for 100 s (LEDs)	
10	Return to step 1	

5.5.1 Proportion of grains producing a post-IR IRSL signal and the potential for cross talk

The proportion of accepted grains (N, Table 5.4) was generally high, ranging between 32 % and 75 % of the grains measured. The smooth curves in Figure 5.7 illustrate the even distribution of light from the individual grain populations, i.e. the population comprises a large proportion of very bright grains. Aside from the potential effect of averaging a large number of D_e values, which is negated by undertaking single grain measurements (see Section 4.3.4), the potential for cross talk between individual grains mounted on a single grain disc exists when so many grains produce a luminescence signal.

Due to the close proximity of individual grains, cross talk can occur during single grain measurements if the laser used for stimulation is poorly focused (Duller, 2012a). In this study, the effect of cross talk needs to be considered only during the laser stimulation (i.e. the IRSL at 225 °C)

Table 5.4: Single grain K-feldspar D_e measurements at Voordrag. Measurements were made using the post-IR $IRSL_{225}$ protocol on 180 – 212 μm grain size for all samples, except 215/VRD04, VRD01 and VRD10 where the 150 – 180 μm fraction was used. The MAM was used to determine the D_e values for all samples and reported D_e values have had a residual value of 0.39 ± 0.14 Gy subtracted.

Sample ID	Number of grains							OD (%)	Skewness	Kurtosis	D_0 (Gy)[e]	D_e (Gy)[f]	Age (ka)
	N_T [a]	N[b]		n_{sat} [c]		n[d]							
215/VRD09	500	365	(73%)	0	(0%)	365	(100%)	101	5.04	35.80	98 ± 1	1.21 ± 0.16	0.32 ± 0.02
215/VRD08	800	509	(64%)	10	(2%)	499	(98%)	49	2.66	12.79	200 ± 3	55.6 ± 3.1	16.5 ± 1.1
215/VRD07	600	306	(51%)	8	(3%)	298	(97%)	63	1.80	5.88	205 ± 5	37.4 ± 2.9	10.2 ± 0.9
215/VRD06	700	226	(32%)	0	(0%)	226	(100%)	45	2.53	12.99	246 ± 5	69.8 ± 4.9	21.1 ± 1.7
215/VRD05	600	381	(64%)	1	(0%)	380	(100%)	33	1.77	7.53	249 ± 3	89.1 ± 3.9	24.3 ± 1.4
215/VRD04	700	357	(51%)	1	(0%)	356	(100%)	31	1.48	6.78	238 ± 3	84.0 ± 2.9	25.4 ± 1.3
215/VRD03	600	364	(61%)	7	(2%)	357	(98%)	39	2.18	10.12	242 ± 4	81.6 ± 3.0	24.4 ± 1.3
215/VRD02	500	294	(59%)	0	(0%)	294	(100%)	28	2.19	15.44	287 ± 6	111 ± 4	36.2 ± 1.9
215/VRD01	500	365	(73%)	3	(1%)	362	(99%)	37	0.12	2.90	353 ± 6	234 ± 8	70.3 ± 3.7
215/VRD10	500	373	(75%)	8	(2%)	365	(98%)	34	0.36	2.89	377 ± 7	280 ± 9	64.6 ± 3.3

[a] Total number of grains measured

[b] Number of grains that passed acceptance criteria

[c] Number of grains in saturation (as % of N)

[d] Number of grains in D_e distribution (as % of N)

[e] Reported for DRCs fit with a single exponential function, excluding DRCs fit with a single exponential function with a linear component

[f] A sigma-b value of 0.2 was used to calculate the MAM D_e value

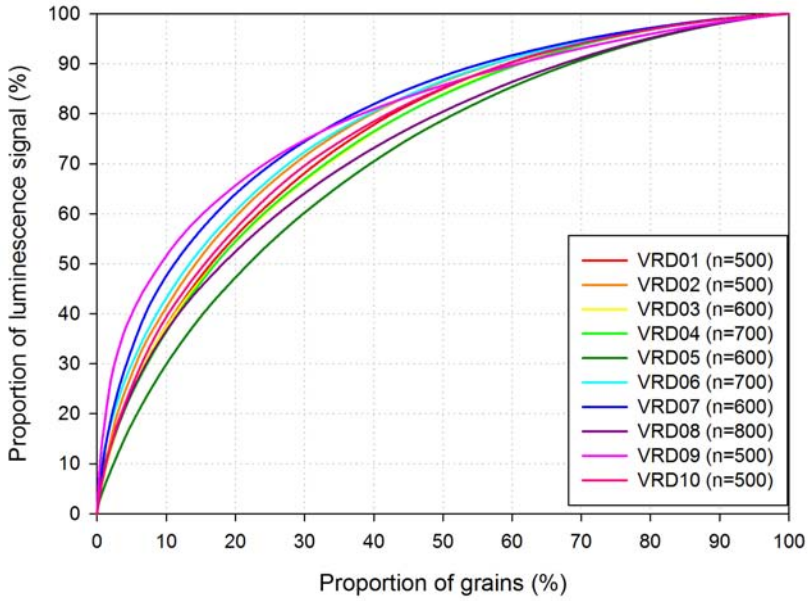

Figure 5.7: Total post-IR IRSL signal produced by all measured grains for each sample. The smooth curves show that these samples have an even distribution of light from their grain populations.

because (i) all other IRSL stimulations during the protocol were made using the IR LEDs in order to optimise the reproducibility of the measurements (see Smedley and Duller, 2013) and (ii) discs were loaded onto the carousel with an empty position between them to avoid cross talk during irradiation and LED stimulation. Duller (2012a) measured the average cross talk between adjacent positions as 0.037 – 0.079 % for the IR laser and concluded that no adverse impact should be observed on the luminescence data provided short stimulation times (1 – 2 s) are used.

5.5.2 K-feldspar D_e distributions

Histograms and radial plots of the K-feldspar post-IR IRSL D_e distributions (Figure 5.8), once again, show the effect of heterogeneous bleaching on the

samples located in the upper stratigraphy. The distributions of the four uppermost samples are strongly positively skewed (1.80 – 5.04, Table 5.4), with a large proportion of grains representing a well-bleached population and a smaller proportion of poorly-bleached grains forming a 'tail' of higher D_e values in the D_e distribution. The 'tail' observed in 215/VRD09 shows a spread of ~150 Gy and a corresponding OD of 101 %. Progressing down stratigraphy the distributions become less skewed but with a small 'tail' still in evidence (e.g. 215/VRD05, skewness 1.77, Table 5.4). From sample 215/VRD02 the majority of values within the 'tail' are removed from the D_e distribution and samples 215/VRD01 and 215/VRD10 have normal (0.12 and 0.36, Table 5.4), albeit broad, distributions. K-feldspar distributions for the three lowermost samples at the Moopetsi tributary site were also very broad (range 800 – 900 Gy), although they were more strongly skewed than the two lowermost samples at this site.

The effect of saturation of the post-IR IRSL signal is not seen to be a major influencing factor on these D_e distributions, e.g. only 2 % of the grains from the oldest sample (215/VRD10) were saturated and D_e values were less than $2D_0$ for all samples. Therefore, the spread in the D_e distribution for the oldest samples is more likely due to alternate sources of scatter.

5.5.3 Residual D_e magnitude

A residual value of 0.39 ± 0.14 Gy was determined as described in Section 4.3.3 and subtracted from the average D_e value prior to age calculation. Whilst subtracting a residual signal improved the small aliquot and single grain ages for the young (< 15 ka) Moopetsi tributary samples, applying

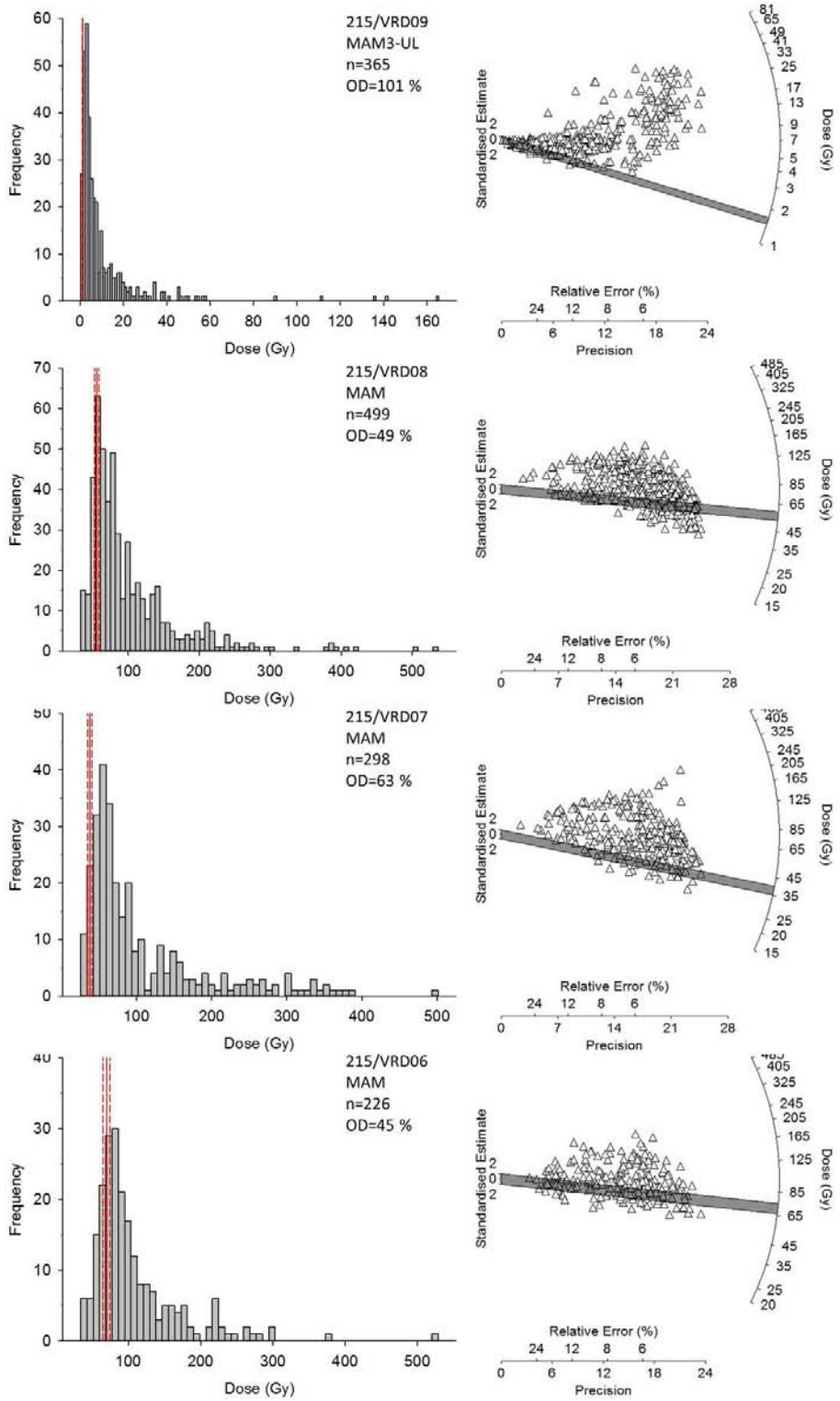

Figure 5.8: Histograms and radial plots of single grain K-feldspar D_e distributions at Voordrag. The solid red line denotes the MAM D_e value with uncertainties (dashed red lines) and the grey bar the 2σ region about the MAM D_e value. All data presented here are prior to subtraction of the calculated residual signal (see discussion in text).

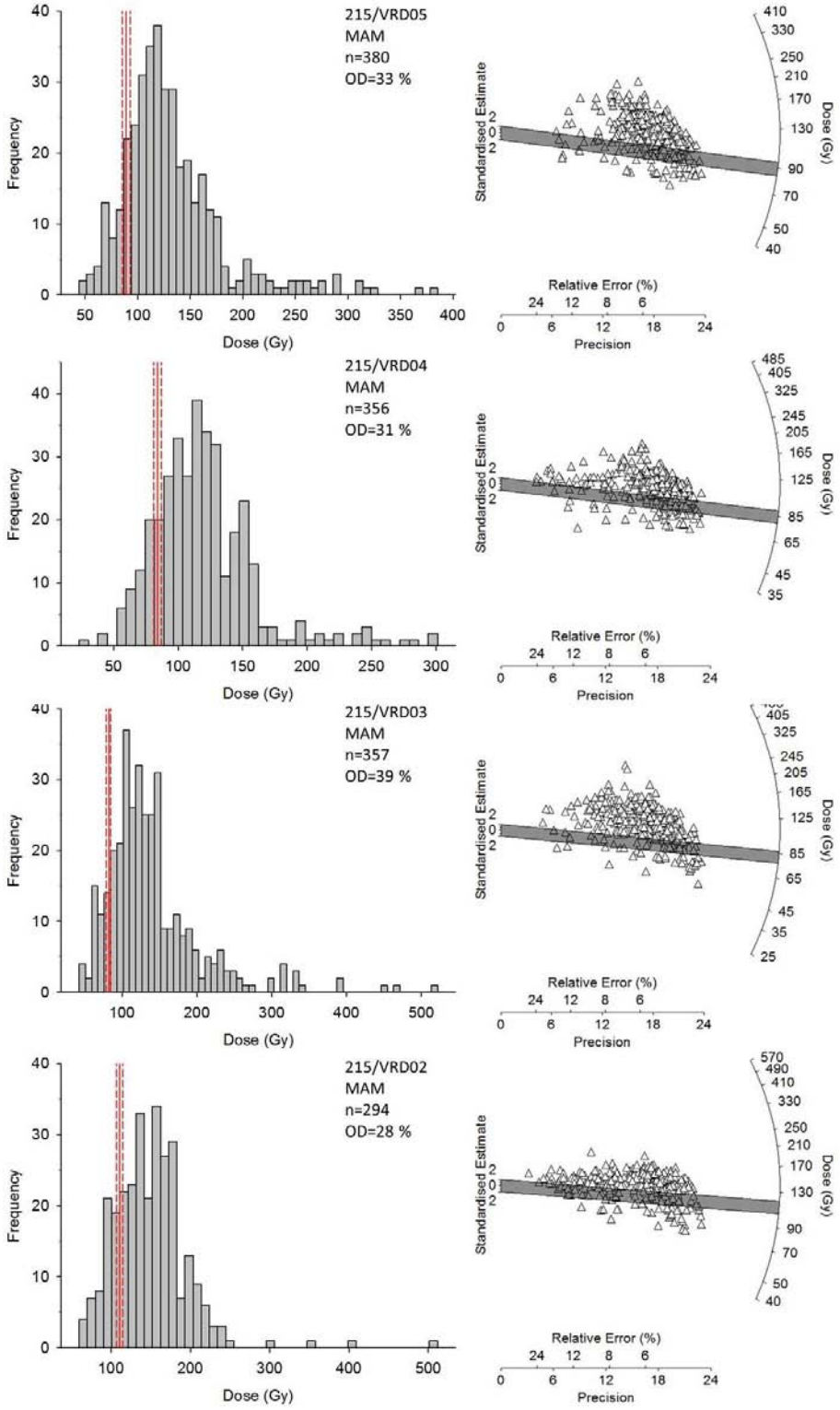

Figure 5.8: Histograms and radial plots of single grain K-feldspar D_e distributions at Voordrag (continued).

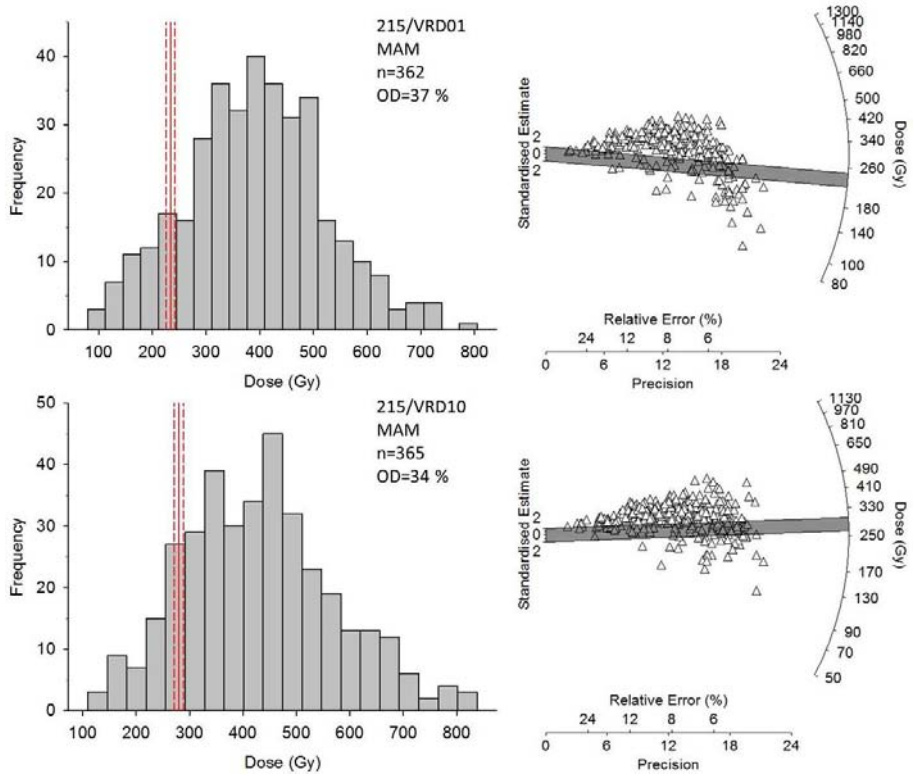

Figure 5.8: Histograms and radial plots of single grain K-feldspar D_e distributions at Voordrag (continued).

the same protocol in this instance has minimal effect on the single grain ages at Voordrag. For example, the difference between the unsubtracted and the residual subtracted age for 215/VRD08 is ~100 years. Therefore, subtracting a very small residual from a relatively large D_e value (~40 Gy) has minimal effect on the resulting age and can be safely disregarded. The residual value was subtracted from the Voordrag samples in order to be consistent across all sites dated during the study.

It is worth noting at this point that the residual value of 0.39 ± 0.14 Gy represents the amount of signal stored within the most well-bleached proportion of grains. However, the spread of D_e values in the dose distribution of 215/VRD09 suggests that a residual dose of the order of ~160 Gy could be recorded within the most poorly bleached grains. This would imply that some of the observed spread in the dose distributions for the old samples may in fact be due to heterogeneous bleaching.

5.5.4 Selecting an appropriate age model

The selection of an appropriate age model for the single grain K-feldspar D_e distributions followed the same reasoning as explained for the quartz data (Section 5.4.4). Sample 215/VRD09 is considered to be representative of the other nine luminescence samples and significant heterogeneous bleaching was observed within the dose distribution, supporting the use of the MAM to determine the proportion of grains within the distribution that have been well-bleached. It could be argued that the effect of heterogeneous bleaching is no longer of concern for the older sediments and the MAM should not be applied (Olley et al., 2004b). However, given the broad distributions of the old samples and the potentially very large (~160 Gy) residual signal stored

in the poorly-bleached grains the MAM is more appropriate. Applying the MAM to all ten samples produces single grain ages that increase consistently with depth, the only exception being an age inversion at 215/VRD07 (Table 5.4).

5.5.5 Fading corrections

Fading measurements were undertaken as discussed in Section 4.3.2 for three samples located at the top (215/VRD09), middle (215/VRD06) and bottom (215/VRD01) of the stratigraphic section. The mean measured g-value of 1.53 ± 0.22 %/decade was deemed low enough that significant fading of the post-IR $IRSL_{225}$ signal was not occurring (Thiel et al., 2011). Thus, fading corrections were not applied to these samples.

5.6 Constructing a paired quartz-feldspar chronology

This study has produced two chronologies for the stratigraphic section at Voordrag (i.e. single grain quartz OSL and single grain K-feldspar post-IR IRSL ages) in order to construct a combined chronology utilising paired ages. Quartz OSL was expected to be more accurate for the younger samples due to rapid bleaching properties and a stable, non-fading signal dominated by the fast component. Alternatively, K-feldspar post-IR IRSL can continue dating after the OSL signal has saturated, to higher doses. Numerous comparison studies have been made between quartz OSL and K-feldspar post-IR IRSL at the multiple grain level (e.g. Colarossi et al., 2015; Kars et al., 2012; Sohbati et al., 2012; Srivastava and Misra, 2012) or between

multiple grains and single grains of the same mineral (e.g. Russell and Armitage, 2012; Thomas et al., 2005; Trauerstein et al., 2014). However, very few studies have compared the two minerals at the single grain level, and of these most have focused on relatively young (<14 ka) and near-modern samples, such as Reimann et al. (2012).

5.6.1 Comparing single grain quartz OSL and K-feldspar post-IR IRSL ages

A direct comparison of the single grain OSL and post-IR $IRSL_{225}$ ages (Figure 5.9 and Table 5.5) shows good agreement between the two chronometers over the entire stratigraphic sequence, with a few exceptions. The K-feldspar age for 215/VRD09 was set equal to the quartz age in order to calculate the residual dose to be subtracted from the remaining nine ages. Three samples (215/VRD08, 215/VRD05 and 215/VRD03) have paired quartz-feldspar ages within uncertainty of one another. Three samples (215/VRD07, 215/VRD06 and 215/VRD04) have quartz ages older than the paired K-feldspar ages. For 215/VRD06 and 215/VRD04 this is most likely due to the difference in grain size of the quartz material used in the D_e measurements (i.e. 150 – 180 μm as opposed to 180 – 212 μm, Table 5.5). The smaller grain size may have led to multiple grains within each hole on the single grain disc and the effect of averaging multiple D_e values (see Section 4.3.4) would result in an age overestimation. For this reason, these two quartz ages have been excluded from the final chronology shown in Table 5.5. For sample 215/VRD07 the opposite is true and the K-feldspar age is an underestimation for unknown reasons. The K-feldspar D_e distribution for 215/VRD07 behaves differently from the other samples;

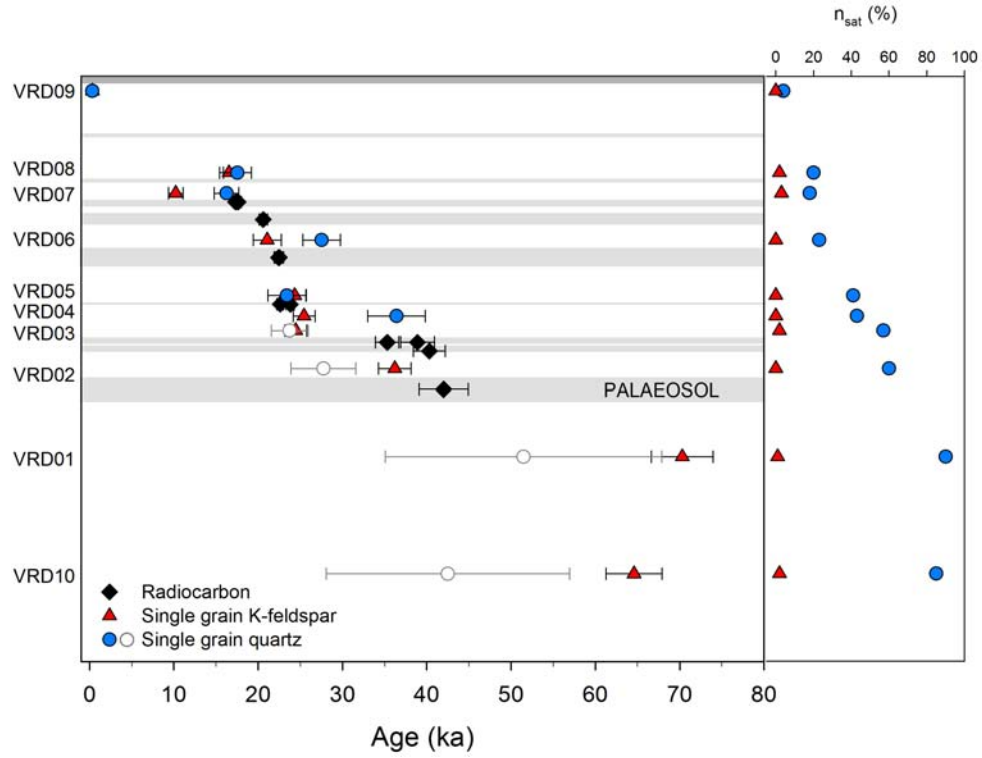

Figure 5.9: Comparison of single grain quartz OSL (blue circles) and K-feldspar post-IR IRSL (red triangles) ages. Open circles denote quartz OSL ages for samples deemed to be in saturation. The recalibrated ^{14}C ages (black diamonds) of Clarke et al. (2003) are included for comparison purposes. n_{sat} shows the percentage of grains saturated within each dose distribution.

it has the second highest OD value and lower skewness and kurtosis values than the samples immediately above and below it in the stratigraphy (Table 5.5). This K-feldspar age has been excluded on the basis of stratigraphic inconsistency.

The effect of saturation on the OSL signal becomes clearer when the quartz ages are compared to their paired K-feldspar ages and a systematic underestimation becomes apparent for samples with more than 50 % of their accepted grain population in saturation (see plot of n_{sat}, Figure 5.9). The agreement between the paired quartz-feldspar ages for 215/VRD03 is

Table 5.5: Final paired chronology based on single grain quartz and K-feldspar data for ten samples from the Voordrag site. Also shown are the number of aliquots used in the D_e estimate (n), the overdispersion (OD) of the D_e distribution and the grain size used for D_e measurements. Ages shown in red have been excluded from the final chronology (see discussion in text) and **bold** type denotes preferred ages.

Sample ID	Quartz OSL					K-feldspar post-IR $IRSL_{225}$				
	n	OD (%)	Grain size (μm)	D_e (Gy)[a]	Age (ka)	n	OD (%)	Grain size (μm)	D_e (Gy)[a]	Age (ka)[b]
215/VRD09	92	110	180-212	0.93 ± 0.07	**0.32± 0.03**	365	101	180-212	1.21 ± 0.16	0.32 ± 0.02
215/VRD08	82	31	180-212	44.6 ± 3.9	**17.5± 1.7**	499	49	180-212	55.6 ± 3.1	16.5 ± 1.1
215/VRD07	78	34	180-212	46.17± 3.6	**16.2± 1.5**	298	63	180-212	37.4 ± 2.9	10.2 ± 0.9
215/VRD06	115	23	150-180	68.4 ± 4.7	27.5 ± 2.2	226	45	180-212	69.8 ± 4.9	21.1 ± 1.7
215/VRD05	89	30	180-212	66.1 ± 5.7	**23.4± 2.2**	380	33	180-212	89.1 ± 3.9	24.3 ± 1.4
215/VRD04	90	24	150-180	90.1 ± 7.6	36.4 ± 3.4	356	31	150-180	84.0 ± 2.9	**25.4± 1.3**
215/VRD03	96	39	180-212	59.7 ± 4.9	23.7 ± 2.2	357	39	180-212	81.6 ± 3.0	**24.4± 1.3**
215/VRD02	31	36	150-180	62.3 ± 8.3	27.7 ± 3.9	294	28	180-212	111 ± 4	**36.2± 1.9**
215/VRD01	6	45	180-212	127 ± 40	51.5 ± 16.4	362	37	150-180	234 ± 8	**70.3± 3.7**
215/VRD10	5	34	150-180	145 ± 49	42.5 ± 14.4	365	34	150-180	280 ± 9	**64.6± 3.3**

[a] A sigma-b value of 0.20 was used for the MAM calculations for both quartz and K-feldspar measurements

[b] K-feldspar ages were calculated after subtracting a residual dose of 0.39 ± 0.14 Gy from the D_e as described in the text

thought to be coincidental because the underlying sample (215/VRD02) is not only underestimated but also has a similar proportion of saturated grains. The lowermost four samples, deemed to be in saturation, are interesting because the D_e value calculated using the MAM is lower than the potential limit of ~150 Gy for OSL proposed by Chapot et al. (2012). However, when using a measure of central tendency (e.g. mean, CAM) to determine the D_e value, the lowermost two samples are beyond the 150 Gy limit but all four samples return a $D_e > 2D_0$. There is also an observable increase of the relative uncertainty of the quartz ages deemed to be in saturation (Table 5.5). The lowermost four quartz ages have thus been excluded from the final chronology and the K-feldspar ages will be used instead.

5.6.2 Comparing luminescence and radiocarbon ages

Similar to the comparison studies between luminescence chronometers mentioned in Section 5.6, the majority of published literature comparing luminescence dates to radiocarbon dates is generally at the multiple grain level (e.g. Folz et al., 2001; Nielsen et al., 2006; Reimann et al., 2011; Shen et al., 2015; Thiel et al., 2010). The comparison study by Guérin et al. (2015b) included some single grain quartz OSL measurements (for samples deemed to be poorly bleached) in conjunction with multiple grain OSL, post-IR IRSL and radiocarbon ages.

The radiocarbon ages published by Clarke et al. (2003) were measured using disseminated organic material within clay sub-samples taken from the buried soil profiles; carbon content ranged from 0.6 to 2.9 %. The published ages were recalibrated in OxCal v4.2 (Bronk Ramsey, 2009) using the Southern Hemisphere calibration curve (ShCal13, Hogg et al., 2013) (see

Table 5.6). A good correlation is apparent between the final luminescence chronology and the published radiocarbon ages and stratigraphic consistency is maintained through the section (see Figure 5.9). The radiocarbon ages located below 215/VRD05 are of particular interest to explore the behaviour of quartz OSL ages near saturation, as discussed in Sections 5.4.3 and 5.6.1. The quartz age for sample 215/VRD03 was considered to be in saturation because >50 % of the accepted grains were saturated, and the agreement with the paired K-feldspar age is considered coincidental. However, this pair of ages remains stratigraphically consistent within the overlying and underlying radiocarbon ages. From sample 215/VRD02 down, the quartz ages were thought to systematically underestimate with respect to their paired feldspar ages. This is supported by the radiocarbon ages as the feldspar age for 215/VRD02 falls within range of the bracketing radiocarbon ages, whilst the quartz equivalent is underestimating by at least ~10 ka. The radiocarbon age underlying 215/VRD02 may represent a minimum age for the lowest palaeosol unit as it is approaching the limit of the radiocarbon technique. However, below this point in the stratigraphy the quartz ages are definitely unreliable, based on the n_{sat}, $2D_0$ and D_e criteria discussed in Section 5.4.3, whereas the K-feldspar ages pass all criteria and raise no cause for concern.

5.6.3 Comparison with published IRSL chronology

A comparison of the final single grain chronology from this study with the published IRSL chronology of Clarke et al. (2003), shows generally poor agreement. For all samples stratigraphically above 215/VRD05, the IRSL ages are younger than the single grain ages and for all samples below

Table 5.6: Radiocarbon ages originally published by Clarke et al. (2003) recalibrated using the ShCal13 curve.

Sample ID	Clarke et al. (2003) study			This study
	C content (%)	C-14 age (years BP)	Calibrated age (ka)[a]	Recalibrated age (ka)[b]
Pta-5429	0.65	14500 ± 140	17.3	17.6 ± 0.4
Pta-6169	1.7	14260 ± 100	17.0	17.3 ± 0.3
Pta-6173	1.0	17100 ± 170	20.3	20.6 ± 0.5
Pta-5440	0.85	18700 ± 210	22.1	22.5 ± 0.5
Pta-6170	1.0	18600 ± 190	22.0	22.4 ± 0.5
Pta-5438	1.3	19800 ± 220	23.1	23.8 ± 0.5
Pta-6168	2.9	18700 ± 150	22.1	22.6 ± 0.4
Pta-5420	2.4	34500 ± 810	40.7	38.9 ± 2.0
Pta-5418	0.80	35700 ± 1000	42.3	40.3 ± 1.9
Pta-6411	1.0	31200 ± 700	36.8	35.3 ± 1.4
Pta-6413	1.0	37400 ± 1500	43.6	42.0 ± 2.9

[a] The calibration curve used in the original publication is not stated, therefore it is assumed these ages were calibrated using IntCal98

[b] Radiocarbon ages were recalibrated using ShCal13 in Oxcal V4.2

215/VRD05 the IRSL ages are older. There are two potential explanations for this, (i) anomalous fading and (ii) averaging of individual D_e values.

As discussed in Section 5.2 the IRSL signal measured at 50 °C is prone to anomalous fading. During the original study, fading measurements were made by irradiating aliquots with a known β dose and stimulating the sample for 0.1 s using IRSL after repeated storage intervals of one month; no fading was detected in this manner for a total storage time of one year and thus the ages were not fading corrected (see Clarke et al., 2003). During this study, fading measurements were made following the protocol of Auclair et al. (2003) as discussed in Section 4.3.2 and the mean g-value of the first IR stimulation at 50 °C was 3.79 ± 0.20 %/decade. A g-value of this magnitude implies significant fading of the IRSL signal and the ages would typically be fading corrected. It is encouraging that the single grain IRSL

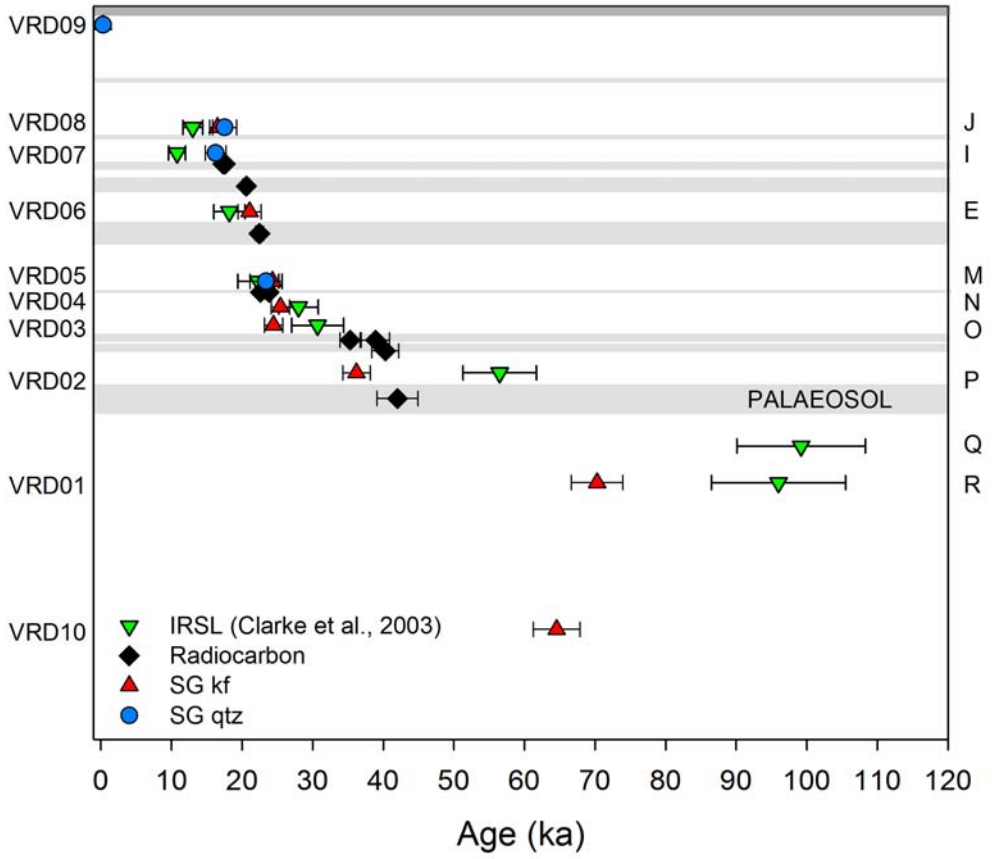

Figure 5.10: Comparison of the single grain paired quartz-feldspar chronology (blue circles and red triangles) from this study to the large aliquot IRSL ages (green triangles) and the recalibrated ^{14}C ages (black diamonds) of Clarke et al. (2003). Labels on the left give the sample IDs from this study and on the right from the Clarke et al. (2003) study.

ages calculated using the 50 °C first stimulation data from this study, are able to reproduce the published IRSL ages.

In Section 4.3.4 it was shown that multiple grain K-feldspar measurements were substantially overestimating D_e with respect to the single grain measurements. This was deemed to be the effect of averaging a large number of variable D_e values, which arise due to the heterogeneous bleaching typical in colluvial deposition systems. Given the large percentage

of K-feldspar grains producing a luminescence signal (see Figure 5.7), the relatively slow bleaching rate of the IRSL signal (see Figure 4.1) and the heterogenous bleaching observed in the single grain dose distributions (Figure 5.8), the large aliquots used by Clarke et al. (2003) were potentially averaging hundreds, possibly thousands, of D_e values on each individual aliquot. Thus it is possible that the fading of the IRSL signal has been countered to some degree by the averaging of the IRSL signal measured using large aliquots. This could explain why the three lowermost samples have a larger offset between their IRSL and post-IR $IRSL_{225}$ ages; a larger amount of stored energy resulted in more severe overestimation and fading was less able to counter the effect of averaging.

5.7 Summary

This chapter presented the measurement of a paired quartz OSL and K-feldspar post-IR $IRSL_{225}$ chronology for the entire Quaternary terrestrial archive preserved at Voordrag. It began with a brief overview of the key advancements within the field of luminescence dating made over the last two decades and their relevance to sites dated prior to 2000 (Section 5.2). Initial investigations on small aliquots of quartz from Voordrag showed the same overestimation of the burial dose due to averaging of variable D_e values produced by heterogeneous bleaching, as seen in the K-feldspar distributions from the Moopetsi tributary site. The same conclusion was drawn and all further quartz OSL measurements in this study will be made on single grains (Section 5.3).

Particular emphasis was placed on the effect of saturation of the quartz OSL signal during the single grain measurements (Section 5.4). Single grain K-feldspar post-IR $IRSL_{225}$ measurements using a high magnitude test dose (30 % of the D_e) based on the findings of Chapter 4 focused on obtaining accurate ages for the basal sediments (Section 5.5). The relatively high dose rates at Voordrag resulted in saturation of the OSL signal approximately half way down the stratigraphic section, however quartz ages below this point continued increasing with depth. Thus, in order to identify which quartz ages were unreliable, it was necessary to compare the quartz ages to their paired K-feldspar ages within the constraint provided by the radiocarbon ages.

Comparison of the paired quartz and K-feldspar ages for ten samples produced a final chronology for the site (Section 5.6). When compared with the IRSL chronology reported by Clarke et al. (2003), the single grain luminescence chronology was older in the upper stratigraphy and younger in the lower stratigraphy. This may be due to an offset between fading of the IRSL signal and D_e averaging effects on large aliquots in the former (Section 5.6.3).

Chapter 6

Developing a modified post-IR IRSL protocol

6.1 Introduction

In Chapter 4 it was shown that using a low test dose during post-IR IRSL measurements resulted in systematic underestimation of the D_e value. Subsequent investigations into the effect of the test dose size on the measurement protocol determined that a test dose of ~30 % of the expected D_e was sufficient to successfully recover large given doses. This approach was used to successfully date samples from the Moopetsi tributary (Section 4.6) and Voordrag (Section 5.5) sites. In this chapter, an alternate approach is explored, and the effect of extending the IRSL stimulation time on the post-IR IRSL protocol is investigated (Sections 6.3 and 6.4). This is followed by the development (Section 6.5) and application (Section 6.6) of a modified post-IR IRSL protocol to K-feldspar from a typical donga environment where colluvial processes were dominant during deposition.

Finally, the dating protocol to be applied to the remaining two study sites, specifically St Paul's and Goedgedacht, will be outlined (Section 6.7).

6.2 Signal transfer during post-IR IRSL measurements

In Section 4.5 it was determined that a large test dose (~30 % of the expected D_e) was required to successfully date samples using the post-IR $IRSL_{225}$ protocol. This approach was used to date the Moopetsi tributary site (Section 4.6) and the Voordrag site (Section 5.5). However, although the high test dose approach works, it does not deal with the underlying issue causing the systematic underestimation of D_e values when using a low test dose. One of the most dramatic effects of increasing the size of the test dose was to significantly reduce the apparent sensitivity change observed during the post-IR $IRSL_{225}$ measurement protocol (see Figure 4.13). This could be caused by signal transfer between the L_x and T_x measurements as evidenced by dose-dependent, 'stacked' decay curves from T_x measurements (Figure 6.1), where the signal recorded late in the measurement (e.g. from 1.0 s to 1.5 s on Figure 6.1 (a)) gets progressively higher.

The increase in overall signal intensity with subsequent irradiations, observed in Figure 6.1(a), implies that the L_x measurement is not completely removing the IRSL signal, and the remaining signal is being carried over into the following T_x measurement. The complete removal of the IRSL signal during L_x (and T_x) measurements is of particular importance because, unlike quartz, K-feldspar does not have a fast component that is rapidly reduced during IR stimulation. Increasing the size of the test dose has the

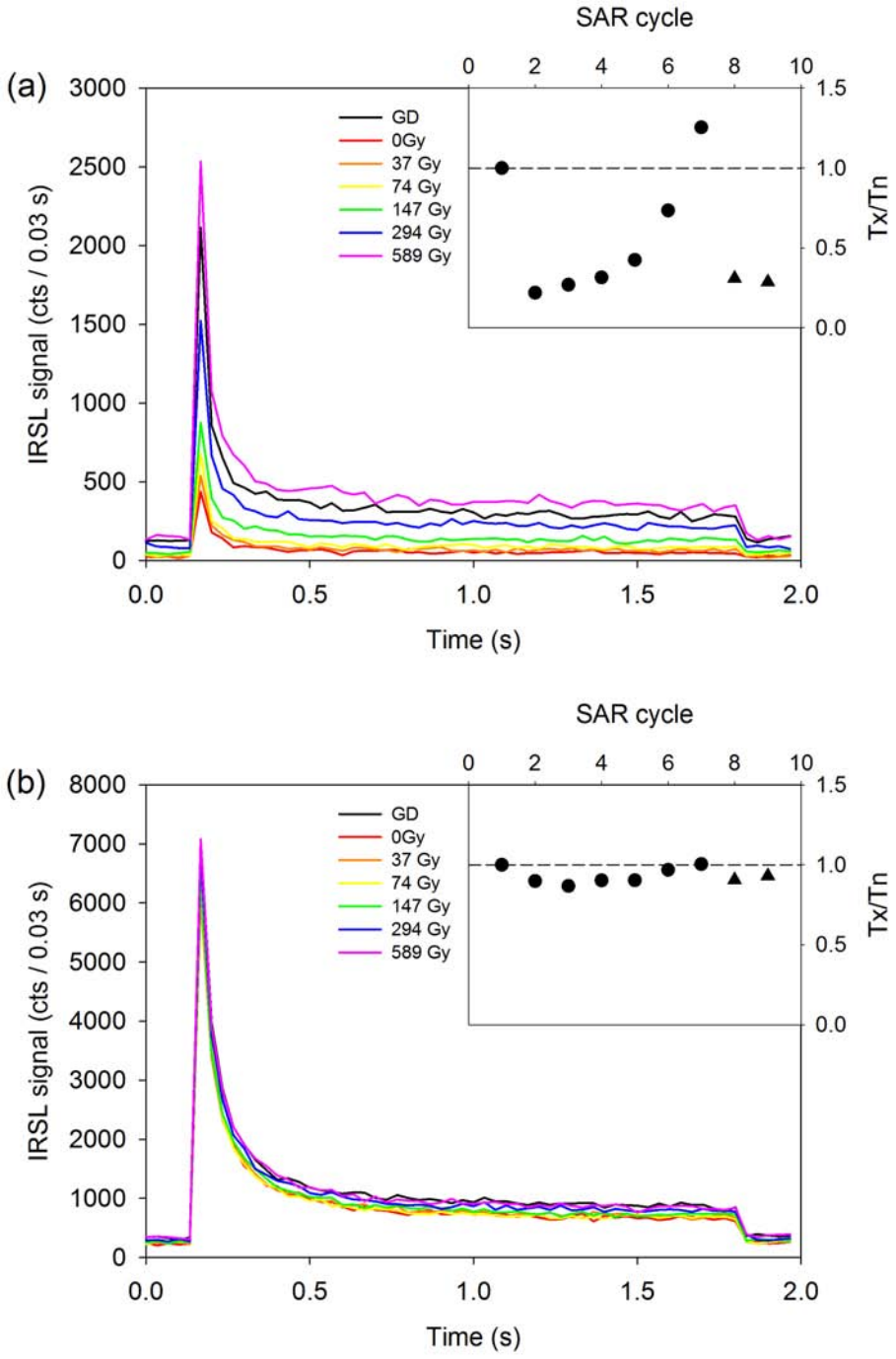

Figure 6.1: An example of 'stacked' decay curves from T_x measurements for two single grains of K-feldspar using a a) low (5 Gy) and b) high (320 Gy) test dose for sample 162/MPT4 (data from dose recovery experiment 2). In the low test dose data, with successively larger irradiations, individual decay curves preserve their shape but the overall signal intensity becomes progressively larger and the curves appear to stack on top of one another. The inset shows the sensitivity plot for each grain.

effect of masking this signal transfer as seen in Figure 6.1(b) (see Section 4.5.2).

To explore whether a relationship exists between the L_x and T_x measurement, the two signals were compared directly. Data from the IRSL stimulation (using the IR laser for 2 s) during dose recovery experiment 2 was used to plot Figure 6.2. Here the last channel from the L_x measurement (Table 4.5, step 4) was plotted against the first channel of the subsequent T_x measurement (Table 4.5, step 8). Ideally, both the L_x and T_x measurements would completely remove the IRSL signal, no excess signal would be carried over into the subsequent measurements, and the data points would plot along a straight line with a slope of zero. However, the data from dose recovery experiment 2 (Figure 6.2) fit a linear regression with a slope greater than zero. Furthermore, the slope increases with increasing test dose size and is always greater than one. Thus charge is being transferred due to (i) thermal transfer enhancing the signal or (ii) a change in the trapping probability, however it is not possible to determine which of these is the cause.

6.3 Effect of extending the post-IR IRSL stimulation time

A significant contribution from the regeneration dose was observed in the signal magnitude of the test dose during post-IR $IRSL_{225}$ D_e measurements (Figure 6.2). Buylaert et al. (2012) recommended a high temperature clean out (e.g. Table 4.5, step 9) at the end of each step in the post-IR IRSL protocol to remove excess trapped charge after each test dose measurement.

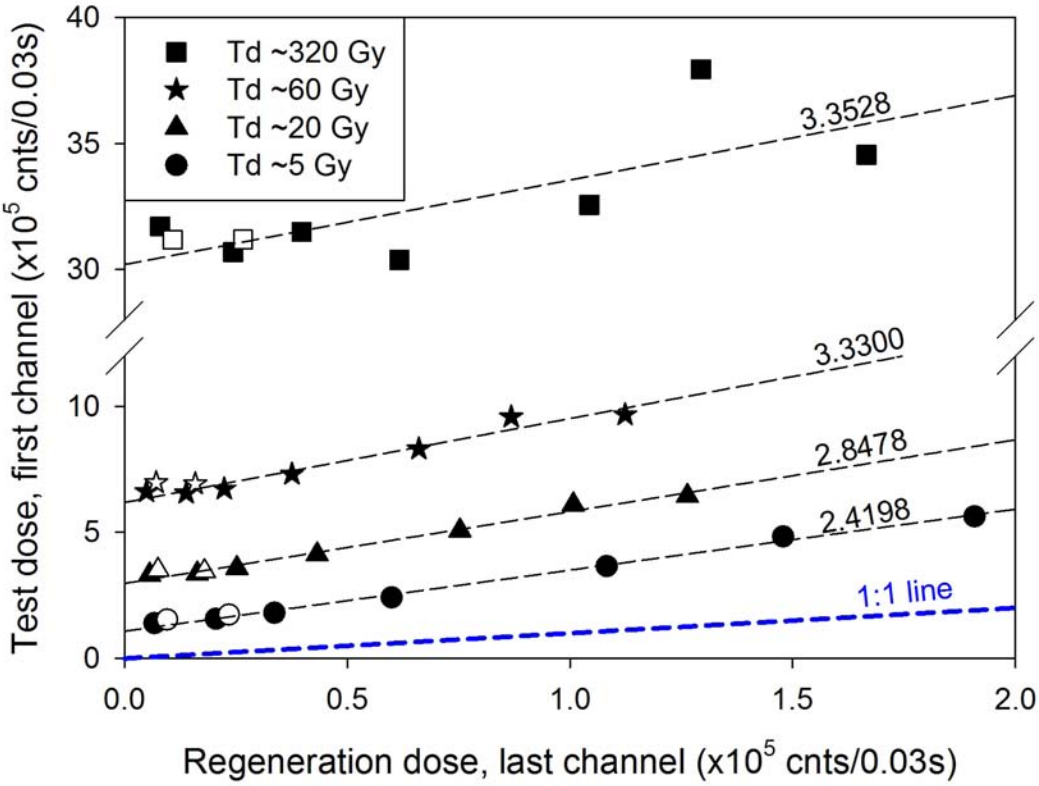

Figure 6.2: Quantifying the amount of signal transfer between the L_x and T_x measurements by directly comparing the last channel of L_x with the first channel of T_x from the IR laser stimulations for dose recovery experiment 2. Data are presented for one synthetic aliquot.

However, it has no effect on the charge transferred from the natural or regeneration dose (L_n, L_x) into the test dose (T_n, T_x) measurement. Due to the potential of the high temperature clean out to induce thermal transfer, an alternative to this approach will be explored in this chapter. In order to explore the transfer of signal between the regeneration dose measurement and the test dose measurement, a series of experiments was devised to vary the amount of signal removed during the regeneration dose measurement.

6.3.1 Signal removal experiment 1: An additional IRSL stimulation after the L_x measurement

In this experiment, in addition to the high temperature clean out at the end of each run, an additional IR stimulation using the LEDs at 225 °C for time (t_1) was added after measurement of the regeneration dose (Table 6.1, step 5). The additional stimulation used the IR LED array at 90 % of full power, as opposed to the single grain laser, to minimise the potential of cross talk during IRSL measurements (Duller, 2012a). The normalised dose response curves (Figure 6.3(a)) show a change of shape similar to that observed when increasing the test dose magnitude in dose recovery experiment 2 (see Figure 4.11), with the lower portion of the curve becoming flatter as t_1 increases. Furthermore, a comparison of the t_1=0 s and t_1=1000 s datasets shows a reduction, by up to a third, in the intensity of the initial signal, for all test dose measurements (T_x) during the protocol. Thus the additional IR stimulation is indeed removing trapped charge that would otherwise be transferred to the test dose measurement. Furthermore, the apparent sensitivity change is reduced as time (t_1) for the additional IR stimulation

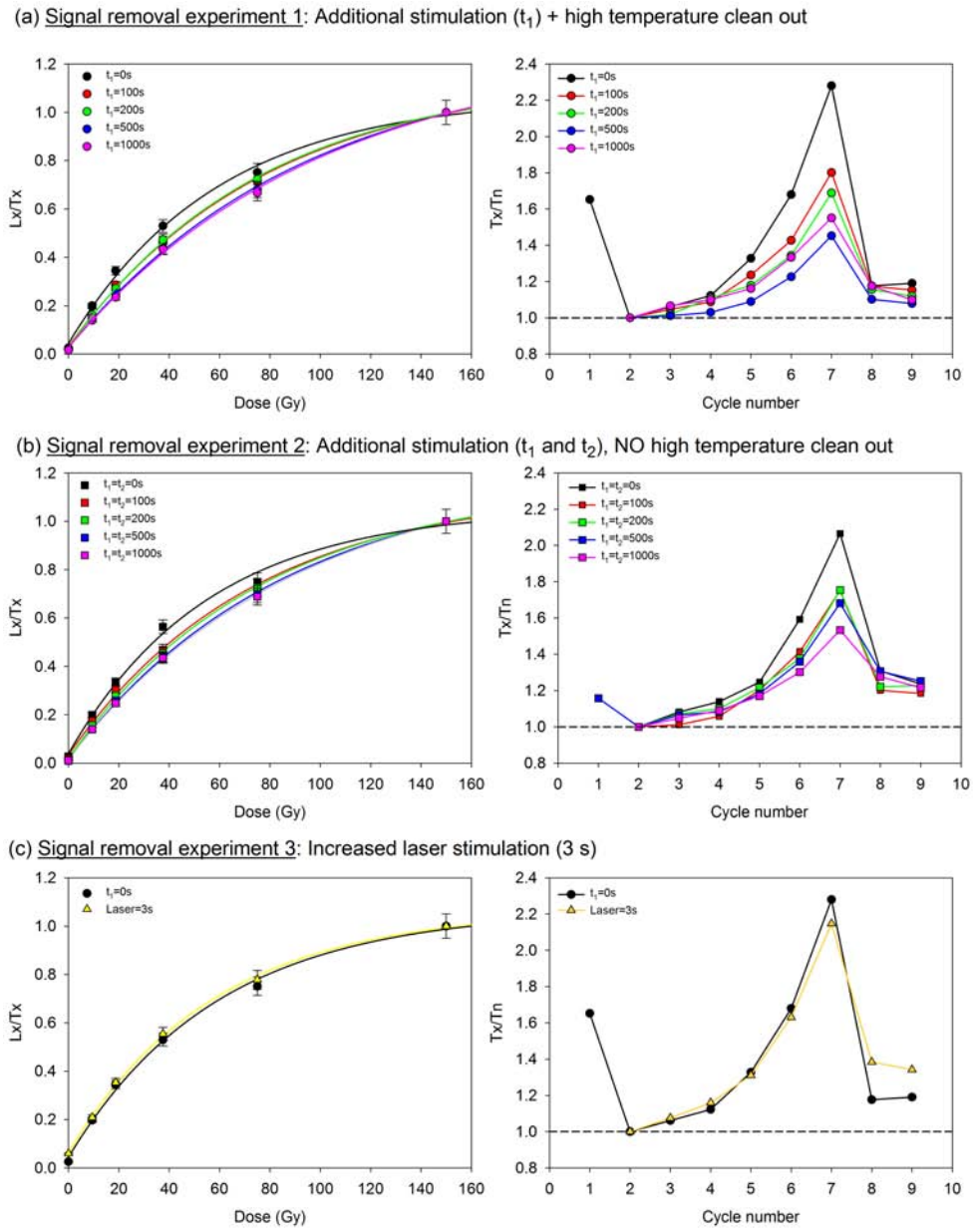

Figure 6.3: DRCs and apparent sensitivity change generated during signal removal experiments using a low test dose (5 Gy) and a) an additional IR stimulation for time (t_1) after the L_x measurement and a high temperature clean out (CO) at the end of each run; b) an additional IR stimulation for time (t_1) after the L_x measurement and for time (t_2) after the T_x measurement replacing the high temperature clean out; and c) increasing the duration of the laser stimulation. All measurements were made on an individual single grain disc and data represented here show the results of synthetic aliquots.

Table 6.1: The post-IR IRSL protocol used in the signal removal experiments, steps in **bold** represent changes made to the sequence (see discussion in text).

Step	Treatment	Measured
1	Dose	
2	Preheat 250 °C for 60 s	
3	IRSL at 50 °C for 200 s (LEDs)	
4	IRSL at 225 °C for 2 s (laser)	L_x
5	**IRSL at 225 °C for t_1 (LEDs)**	
6	Test dose	
7	Preheat 250 °C for 60 s	
8	IRSL at 50 °C for 200 s (LEDs)	
9	IRSL at 225 °C for 2 s (Laser)	T_x
10	**IRSL at 225 °C for t_2 (LEDs)**	
11	**IRSL at 290 °C for 100 s (LEDs)**	
12	Return to step 1	

is increased (reaching a minimum when t_1=500 s, Figure 6.3(a)), producing a similar relationship with cycle number as that observed during dose recovery experiment 2 (see Figure 4.13) due to increasing the test dose size.

6.3.2 Signal removal experiment 2: An additional IRSL stimulation after both the L_x and T_x measurements

In this experiment the high temperature clean out at the end of each step (Table 6.1, step 11) was replaced with an additional IR stimulation at 225 °C (Table 6.1, step 10). Time (t) was set so that $t_1 = t_2$ and the same change in dose response curve shape and decrease in overall sensitivity change with increasing time (Figure 6.3(b)) are observed. The DRCs for $t_1 = t_2 = 500$ s and $t_1 = t_2 = 1000$ s (Figure 6.3(b)) are comparable to the corresponding

curves from signal removal experiment 1 when a high temperature clean out was included (Figure 6.3(a)).

It is worth noting the effect of switching the high temperature clean out for the additional same temperature stimulation on the recuperation value. One of the motivations for including a high temperature clean out (Table 6.1, step 11) was to reduce recuperation (Buylaert et al., 2012). The mean single grain recuperation values for the t = 500 s DRC in experiment 1 is 1.19 ± 0.09 Gy and 0.54 ± 0.05 Gy for experiment 2. Thus recuperation can be minimised by using an extended IR measurement to remove the remaining charge while minimising induced sensitivity change.

6.3.3 Signal removal experiment 3: Extending the stimulation time using the single grain laser

In this experiment, the additional IR stimulations and the high temperature clean out were removed (Table 6.1, steps 5, 10 and 11) and the length of the laser stimulation increased to 3 s (Table 6.1, steps 4 and 9). The dose response curve is almost identical to the post-IR $IRSL_{225}$ protocol (i.e. $t_1 = 0$ s) when using a high temperature clean out (Figure 6.3(c)). This implies that the extra 1 s of laser stimulation time is as efficient as the high temperature clean out (IR stimulation at 290 °C for 100s) in terms of removing stored signal. The benefit of increasing the laser stimulation time is to remove a larger proportion of the signal at both the L_x and T_x measurements without introducing charge transfer due to high temperature thermal treatment. However, increasing the duration of the laser stimulation increases the potential for cross-talk between the individual grain measurements (Duller, 2012a).

Adding an additional IR stimulation at 225 °C using the LEDs for 500 s (equivalent power ~67.5 J/cm^2), or increasing the IR laser stimulation to 3 s (equivalent power ~500 J/cm^2) removes the need for a high temperature clean out and precludes excess transfer of signal between the IRSL measurements. Of these two options, the additional IR LED stimulation shows the largest reduction in overall sensitivity change (Figure 6.3(b and c)) and measured test dose luminescence signal magnitude during the post-IR IRSL measurement protocol. The measurements in all three signal removal experiments were undertaken using a low magnitude test dose (~5 Gy). Thus, given the results observed in dose recovery experiment 2, it is necessary to consider the impact of simultaneously increasing both the test dose magnitude and stimulation time on the luminescence signal to optimise the post-IR IRSL$_{225}$ protocol.

6.4 Dose recovery experiment 3: Recovery of a fixed given dose using various test doses with additional IR stimulations

The observed decrease in apparent sensitivity change and flattening of the dose response curve in signal removal experiments 1 and 2 (see Figure 6.3) agree with the results of dose recovery experiments 1 and 2 (see Figures 4.11 and 4.13). Therefore, an additional dose recovery test (dose recovery experiment 3) was undertaken to determine whether the modified post-IR IRSL sequence could successfully recover a large given dose (~400 Gy) using the same range of test doses applied previously. For this experiment the

protocol outlined in Table 6.1 was used, with $t_1 = t_2 = 500$ s (steps 5 and 10), the high temperature clean out (step 11) omitted and the same range of test doses applied as used in dose recovery experiment 2.

For dose recovery experiment 3 the average measured to given dose ratios (Table 6.2, Figure 6.4(d)) all lie within 10 % of unity, including the 5 Gy (~1 %) test dose which previously failed to recover a given dose (Figure 6.4(a); also see Table 4.8). The dose recovery ratio for the 20 Gy (~5 %) test dose remains unchanged, while the ratio for the 60 Gy (~15 %) test dose decreases and a slight improvement is observed at test doses greater than 120 Gy (~30 %)(see Figure 6.4(a and d)). OD values remain below 20 %, with the exception of the 5 Gy test dose at 29 % (Table 6.2). The same flattening of the dose response curve (Figure 6.4(b and e)) and reduction in apparent sensitivity change (Figure 6.4(c and f)) seen in dose recovery experiment 2 was observed. D_0 values (Table 6.2) are generally comparable with those in dose recovery experiment 2 (see Table 4.8). For Td $<$ 200 Gy, grains fit with a DSE function, range between 407 $\pm$ 52 Gy and 630 $\pm$ 60 Gy. For grains fit with a SSE function, irrespective of test dose size, D_0 values are consistently larger, ranging from 154 $\pm$ 6 Gy to 530 $\pm$ 43 Gy. It is also interesting to note that whilst fewer grains pass the acceptance criteria, the same decreasing pattern in the number of saturated grains is observed using the modified post-IR $IRSL_{225}$ protocol.

Table 6.2: Results for dose recovery experiment 3 using the modified post-IR $IRSL_{225}$ protocol with a fixed given dose (~400 Gy) and variable test dose. Measurements were undertaken on single grains of K-feldspar using the 180 – 212 μm grain size fraction from sample 162/MPT4.

Given dose (Gy)	406	406	406	406	406	406
Test dose (Gy)	5	20	61	120	200	320
Test dose (% of GD)	1	5	15	30	49	79
Total grains measured (N_T)	200	200	200	200	200	200
Number of grains accepted (N)	83	135	102	122	126	142
Number of saturated grains (n_{sat})	32	11	4	4	2	4
Number of grains giving D_e (n)	51	124	98	118	124	138
OD (%)	29	10	18	9	14	12
Max. sensitivity change (%)	63	27	22	12	18	6
Skewness	-0.68	0.36	-0.92	1.64	1.72	1.88
Kurtosis	3.47	4.04	5.81	7.53	8.60	8.41
D_0 (Gy)[a]	154 ± 6	282 ± 13	380 ± 18	418 ± 25	434 ± 23	530 ± 43
D_{01} (Gy)[a]	43 ± 3	43 ± 2	41 ± 3	40 ± 4	40 ± 3	51 ± 5
D_{02} (Gy)[a]	407 ± 52	462 ± 51	630 ± 60	526 ± 81	1173± 365	933 ± 277
Average (Gy)	417 ± 14	415 ± 5	373 ± 6	389 ± 5	371 ± 7	369 ± 5
M/G ratio [b]	1.02 ± 0.03	1.02 ± 0.01	0.91 ± 0.02	0.95 ± 0.01	0.92 ± 0.02	0.91 ± 0.01

[a] Multiple D_0 values due to best fit approach to DRC construction. D_0 is the average of all DRCs fit with a SSE function, while D_{01} and D_{02} are from DRCs fit with a DSE function.

[b] Ratio calculated after subtracting a residual of 1.20 ± 0.08 Gy from individual D_e values

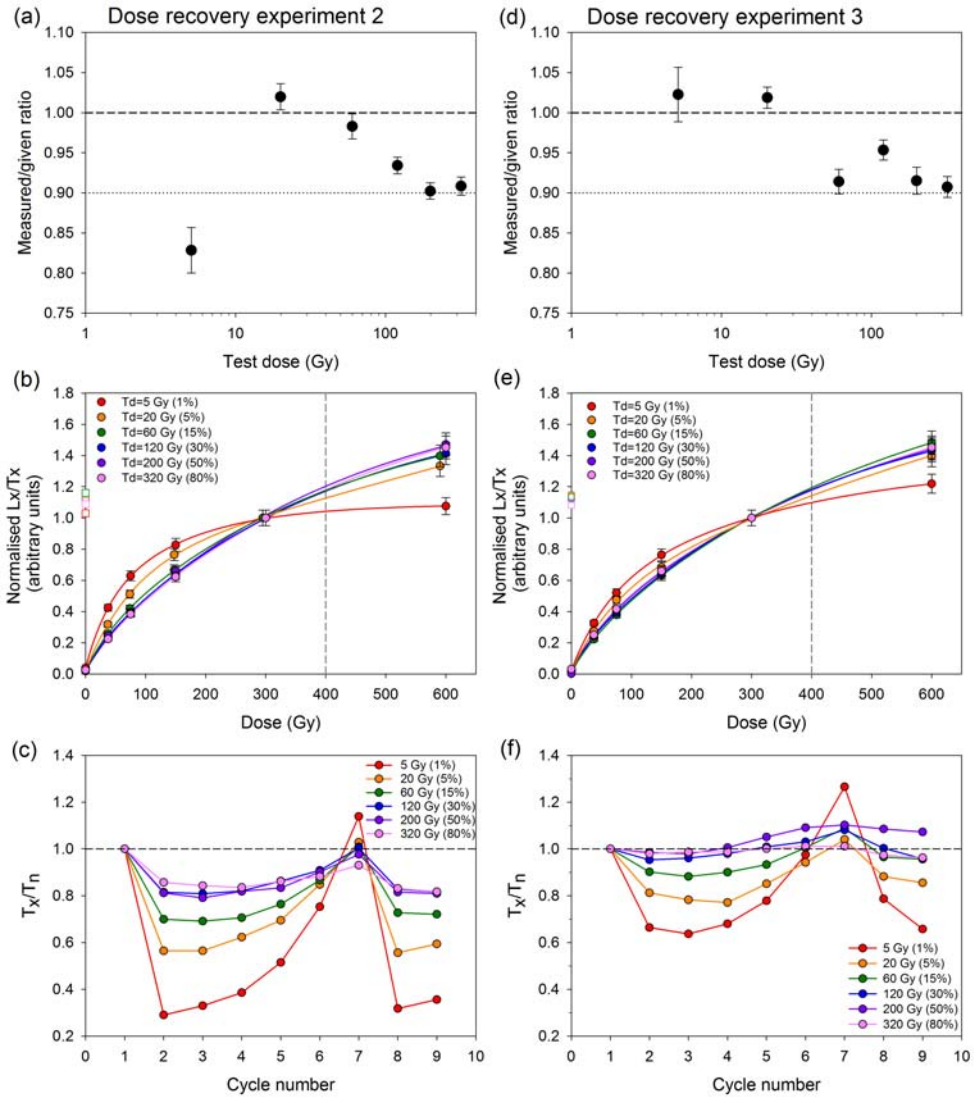

Figure 6.4: Results of dose recovery experiment 3 using the modified post-IR $IRSL_{225}$ protocol (right), figures from dose recovery experiment 2 using the standard post-IR $IRSL_{225}$ protocol are reproduced from Chapter 4 (left) for comparison purposes. Shown are the (a)(d) measured to given dose ratios (uncertainties reported as standard errors), (b)(e) DRCs fit with double saturating exponentials, and (c)(f) apparent sensitivity change.

6.5 Signal transfer during the modified post-IR $IRSL_{225}$ protocol

Using the data from dose recovery experiment 2, Figure 6.2 showed significant signal transfer occurring between the L_x measurement and subsequent T_x measurement, with the slope of the relationship varying from 2.4 to 3.4. The same analysis was undertaken on data from dose recovery experiment 3, which used a modified post-IR IRSL protocol (i.e. two additional IR LED stimulations at the same second stimulation temperature, see Section 6.4). Figure 6.5 shows a reduction in the amount of signal transferred between the two measurements. Linear regressions now have a slope of ~0.3 for all test dose sizes, which is ten times smaller than for the previous dataset, and no longer dependent upon the size of the test dose (Figure 6.2).

In Section 6.2, two possible causes for the transfer of signal were suggested, (i) thermal transfer enhancing the signal or (ii) a change in the trapping probability. Were thermal transfer the driving mechanism, more charge should be transferred at larger test doses, and an increase in slope with test dose size would be observed in Figure 6.5. However, a constant slope of 0.3 is observed across all test doses. This implies that changes in the trapping probability is the most likely cause of the signal transfer observed in this study.

The modified post-IR IRSL protocol is effectively removing the excess signal, that would otherwise be transferred between L_x and T_x measurements. This is seen in the reduction of slopes between dose recovery experiments 2 and 3 (see Figures 6.2 and 6.5), and the similar slopes for all test dose sizes in experiment 3 (Figure 6.5). This supports the hypothesis that the

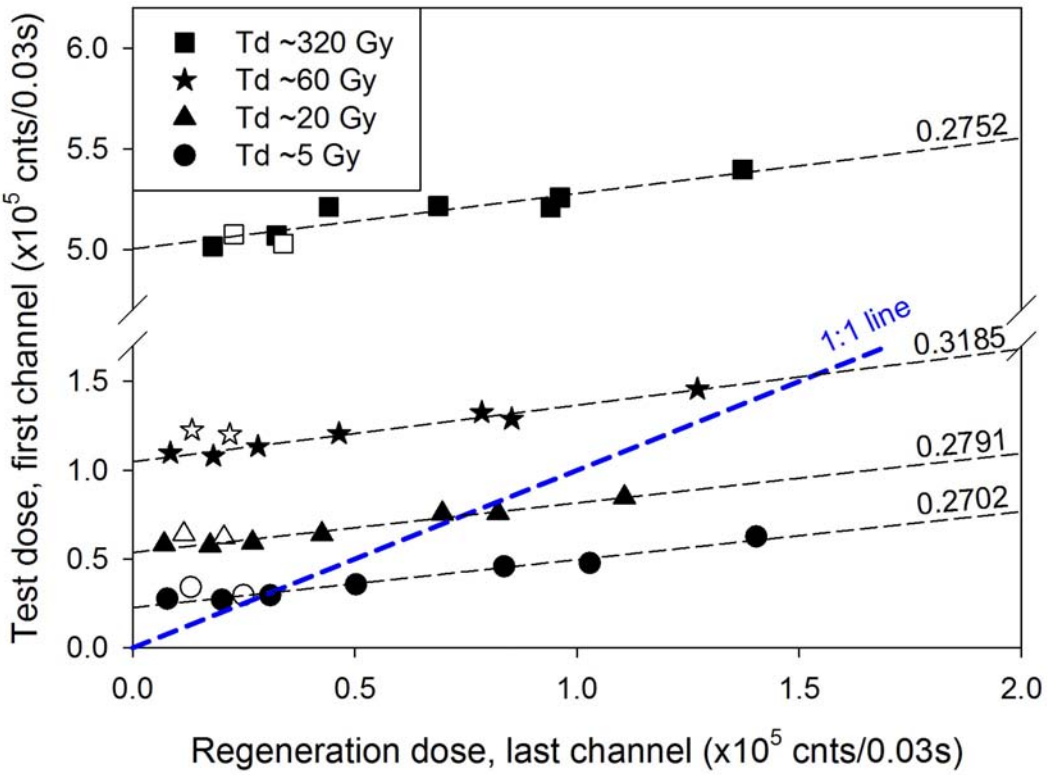

Figure 6.5: Quantifying the amount of signal transfer between the L_x and T_x measurements by directly comparing the last channel of L_x with the first channel of T_x from the IR laser stimulations for dose recovery experiment 3. The additional IR stimulation after both the L_x and T_x measurements in dose recovery experiment 3 has reduced the signal difference by a factor of 10 (see Figure 6.2). Data presented are for one synthetic aliquot.

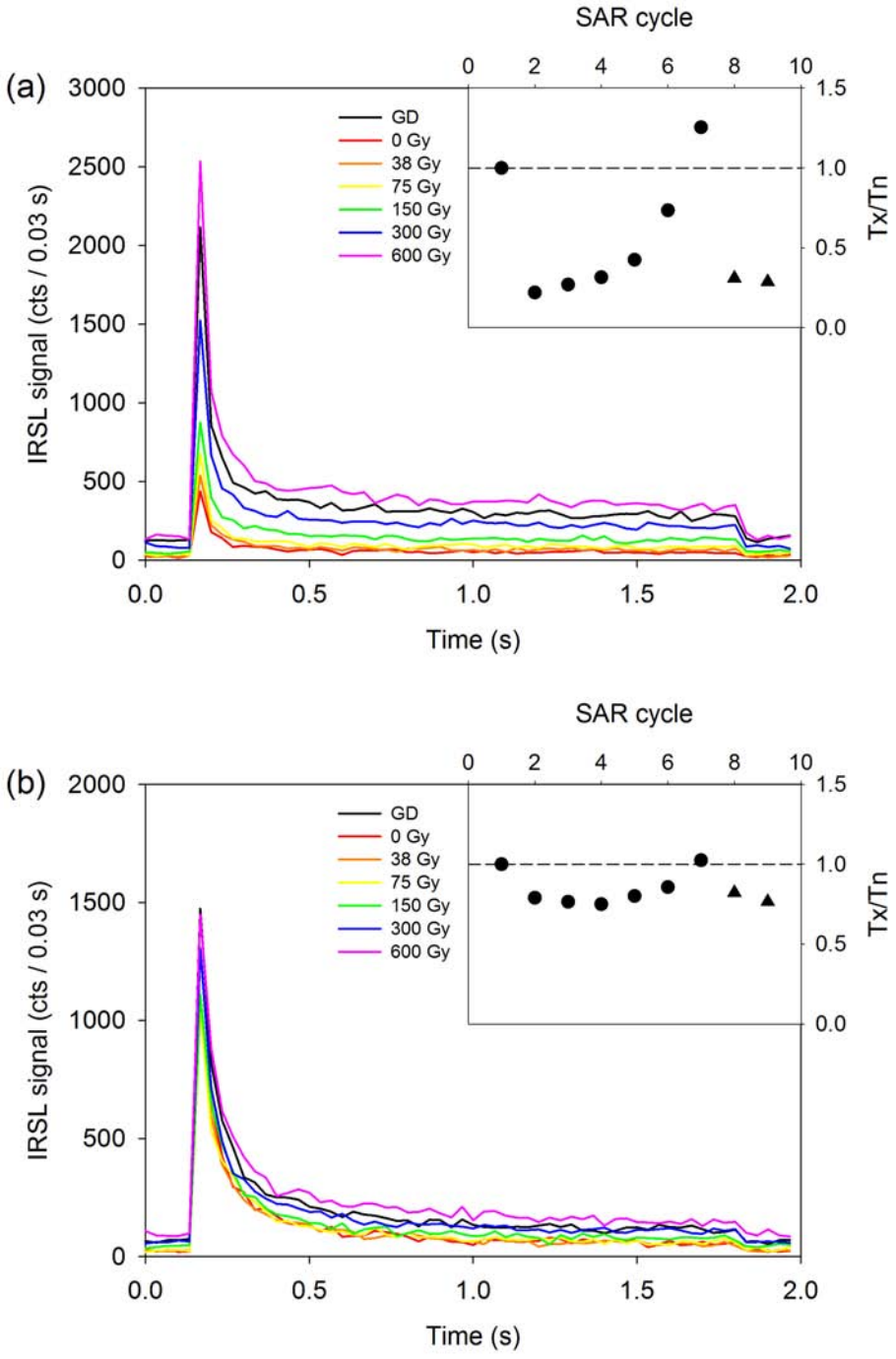

Figure 6.6: Comparison of the decay curves from T_x measurements for two single grains of K-feldspar measured with the a) post-IR IRSL protocol (dose recovery experiment 2) and the b) modified post-IR IRSL protocol (dose recovery experiment 3) for sample 162/MPT4. Both sets of curves were measured using a low (5 Gy) test dose and the inset shows the sensitivity plot for each grain. The additional IR stimulations reduce the 'stacking' effect and apparent sensitivity change, as increasing the size of the test dose did (see Figure 6.1).

signal being transferred into the test dose in this study is not transferred thermally, but is rather indicative of the post-IR $IRSL_{225}$ signal not being completely removed during the L_x measurement.

The effect of signal transfer during post-IR IRSL measurements can be dealt with in two ways. It can be masked by applying a large (30 % of the D_e) test dose (see Figure 6.1), or removed by using additional IR stimulations after the L_x and T_x measurements (Figures 6.5 and 6.6). The latter approach also prevents any thermally induced sensitivity change due to high temperature thermal treatments, such as the high temperature clean out at the end of each step, suggested by Buylaert et al. (2012).

6.6 Testing the modified post-IR $IRSL_{225}$ protocol

The modified post-IR $IRSL_{225}$ protocol was tested on a sample near the bottom of the sequence at Voordrag (215/VRD01). Two sets of single grain discs were prepared for D_e measurements; one set was measured using the post-IR $IRSL_{225}$ protocol (see Table 4.5) with a test dose magnitude of 30 % of the expected D_e value (~100 Gy) and the other set using the modified post-IR $IRSL_{225}$ with $t_1 = t_2 = 500$ s and a 20 Gy test dose (see Table 6.1). Recycling and recuperation values were almost identical (Table 6.3). The D_e distributions were similar, with OD values of 37 % and 40 % (Figure 6.7, Table 6.3). Furthermore, the mean D_e value and apparent ages for each distribution are within uncertainty (reported as one standard error) of one another; this applies to both the CAM and MAM values. Therefore, similar data can be obtained by (i) applying a test dose ~30 % of the expected D_e

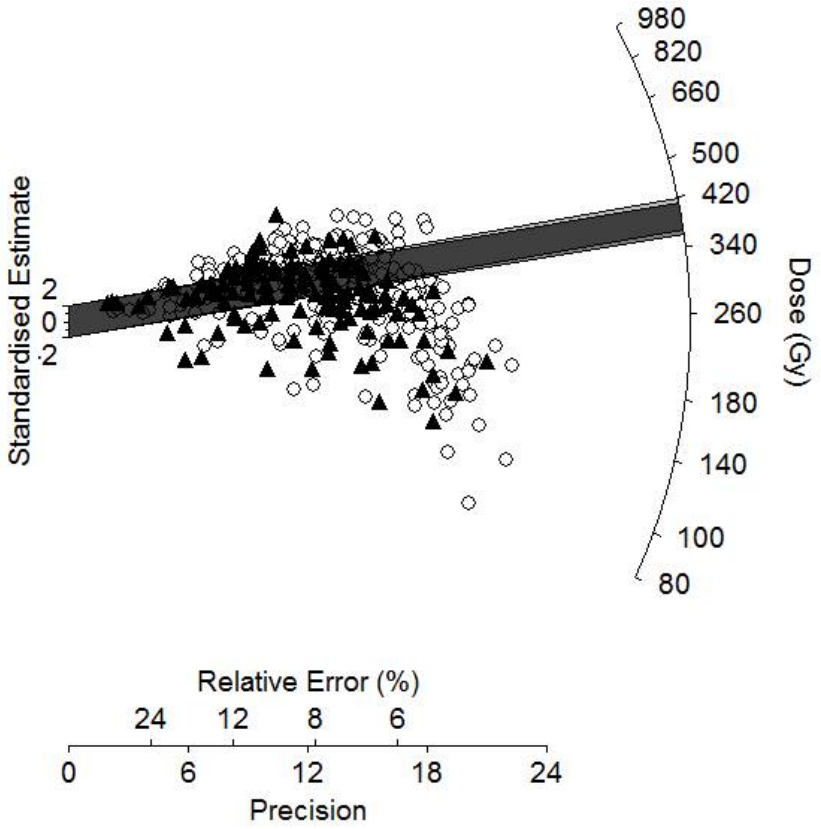

Figure 6.7: Radial plot of D_e distributions comparing the post-IR $IRSL_{225}$ (white circles) and the 'modified' post-IR $IRSL_{225}$ (black triangles) protocols. The light grey and dark grey bars represent the mean D_e values for the standard and modified distributions, respectively. See text for explanation of the two protocols.

value or (ii) applying the additional IR LED stimulations in combination with a test dose of ~20 Gy. These two methods yield more precise data, and with much lower apparent sensitivity change, than the method described in Table 4.5 using a small (~5 Gy) test dose.

6.7 Dating approach for the remaining sites

The dating approach applied to the remaining two sites, St Paul's and Goedgedacht, will be based on the findings from the Moopetsi tributary and

Table 6.3: Comparison of the post-IR $IRSL_{225}$ and 'modified' post-IR $IRSL_{225}$ protocols using sample 215/VRD01.

	Post-IR $IRSL_{225}$	Modified post-IR $IRSL_{225}$
N_T [a]	500	200
N [b]	365 (73%)	139 (70%)
n_{sat} [c]	3 (1%)	10 (7%)
n [d]	362 (99%)	129 (93%)
Recycling	1.00 ± 0.06	1.00 ± 0.01
Recuperation	1.22 ± 0.04	1.20 ± 0.06
OD (%)	37	40
Mean D_e (Gy)	391 ± 7	383 ± 14
Apparent age (ka)	118 ± 5	115 ± 6

[a] Total number of grains measured
[b] Number of grains that passed acceptance criteria
[c] Number of grains in saturation
[d] Number of grains in D_e distribution

Voordrag sites (Chapters 4 to 6). Therefore, single grain D_e measurements will be used for both quartz OSL and K-feldspar post-IR IRSL for all remaining samples. Full chronologies will not be measured for both minerals at the remaining sites, however, and instead the D_e distribution will be determined for a 'modern' sample using both dosimeters to quantify the degree of bleaching. Thereafter, quartz OSL will be applied down the stratigraphy until the effect of saturation is identified (i.e. $n_{sat} > 50$ %, and not proceeding beyond ~150 Gy), at which point the K-feldspar 'modified' post-IR $IRSL_{225}$ protocol will be applied to the remaining samples. A minimum of one cross-over point (i.e. both quartz OSL and K-feldspar post-IR IRSL) will be measured for a sample located above where saturation of the OSL signal was identified, not including the 'modern' sample.

The residual signal will be calculated for K-feldspar at each site by setting the 'modern' K-feldspar age to equal the paired quartz age, in

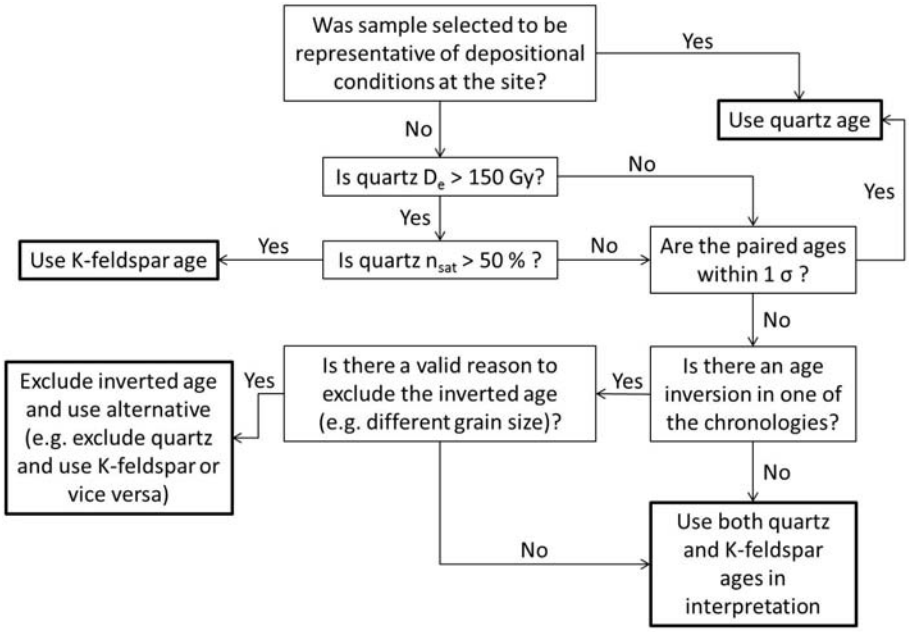

Figure 6.8: Flow diagram illustrating the decision process used to determine the final paired chronology for each site. Bold boxes indicate the end of the decision process for a particular sample.

order to assess the residual signal's impact on the D_e measurements on a site-by-site basis. To maintain consistency with the Moopetsi tributary and Voordrag sites, the calculated residual will be subtracted from the D_e values prior to age calculation, irrespective of the minimal effect this will have on the age of the old samples within the stratigraphy. Age models will be applied after consideration of (i) the likely depositional context for each site, (ii) the extent of heterogeneous bleaching observed in the 'modern' sample and (iii) the shape of the D_e distributions.

Once the final ages have been calculated for both quartz and K-feldspar, the two independent chronologies will be combined to produce a single complementary chronology for the site. Figure 6.8 is a flow diagram depicting the decision process applied to each set of paired ages in order to select

the most suitable age for the geomorphological interpretation presented in Chapter 8.

6.8 Summary

Observation of systematic underestimation of D_e values in Chapter 4, prompted an investigation into the effect of increasing test dose size on the post-IR $IRSL_{225}$ protocol. In this chapter, the ability to completely remove the IRSL signal between subsequent L_x and T_x measurements was explored, due to a significant amount of signal transfer observed in the T_x measurement. An alternative was sought to a high temperature clean out at the end of each step, which removes trapped charge prior to each L_x measurement but may potentially induce thermal transfer of signal into the subsequent T_x measurement (Section 6.3). This led to the inclusion of an additional IR LED stimulation after each L_x and T_x measurement, and lowering of the test dose from 30 % of the expected D_e value to a fixed value of 20 Gy. This approach was termed the 'modified' post-IR $IRSL_{225}$ protocol (Section 6.5). Finally the luminescence dating approach to be applied to the St Paul's and Goedgedacht sites based on the findings of Chapters 4 to 6 was presented (Section 6.7). The application of the modified post-IR $IRSL_{225}$ protocol to the K-feldspar samples from St Paul's and Goedgedacht, together with quartz OSL, will be the topic of the next chapter.

Chapter 7

Paired single grain dating at St Paul's and Goedgedacht

7.1 Introduction

Following the general investigation of quartz and K-feldspar single grain measurements, the modification of the post-IR IRSL protocol and the outlined optimal dating approach presented in Chapters 4 to 6, this chapter will present the detailed luminescence analysis of the St Paul's and Goedgedacht sites. First, D_e measurements undertaken at the St Paul's site using single grains of quartz (Section 7.2) and K-feldspar (Section 7.3) will be presented, followed by the resulting paired single grain chronology (Section 7.4). Subsequently, the data collected for the Goedgedacht site will be presented in the same order, starting with the single grain quartz measurements (Sections 7.5) followed by the single grain K-feldspar measurements (Section 7.6), and finally the paired single grain chronology (Section 7.7).

7.2 Single grain quartz OSL at St Paul's

An initial combined preheat and dose recovery test was undertaken on the sample collected from the uppermost colluvial unit (215/STP10) using small aliquots as described in Section 5.3; results are shown in Figure 7.1(a). A preheat plateau was identified between 180 °C and 240 °C and a Ph_{regen} of 220 °C was selected because it had the most successful dose recovery, returning a measured/given dose ratio of 0.99 ± 0.02. The SAR protocol used for the subsequent single grain quartz measurements was identical to the protocol used at Voordrag (see Table 5.1). An additional single grain dose recovery test was undertaken using the selected SAR protocol on sample 215/STP09, for 1400 grains using a given dose and test dose of ~5 Gy. The resulting distribution (n=207, n_{sat}=0, Figure 7.1 (b)) had an OD value of 7 % and a measured/given dose ratio of 1.00 ± 0.01. Therefore, the selected SAR protocol is suitable for these sediments as it is able to successfully correct for sensitivity changes and recover a given dose.

Single grain quartz OSL measurements were undertaken on the four uppermost samples collected from St Paul's; the remaining six samples were saturated and thus beyond the range of OSL. The quartz OSL signal was dominated by a fast component, illustrated by rapid decay of the signal. The same variability between DRCs for individual grains of the same sample was observed, as reported for the Voordrag OSL signal in Section 5.4. DRCs were built to ~150 Gy to sufficiently characterise the dose response and to determine a meaningful number for the proportion of saturated grains within the dose distribution. The total number of grains to pass the acceptance criteria (see Section 3.3.3) for the two uppermost samples (215/STP08 and

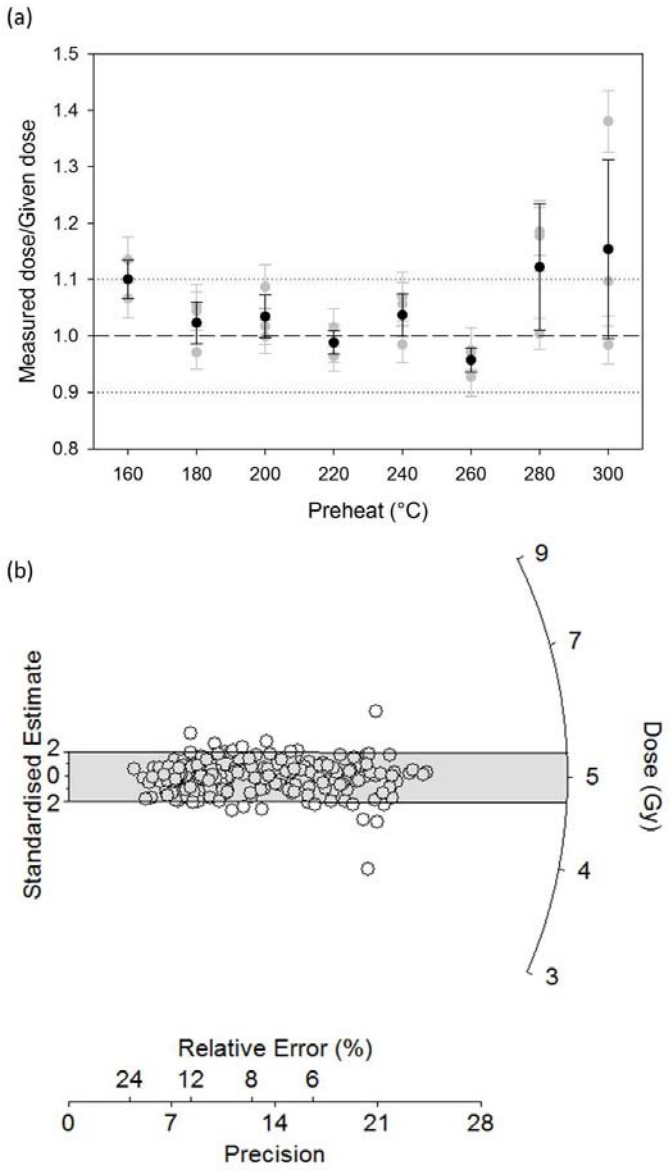

Figure 7.1: (a) Quartz OSL preheat-dose recovery test on small aliquots of quartz from the uppermost sample (215/STP10) within the stratigraphic section. Grey circles represent the measurements from individual aliquots and black circles represent the mean of the three measurements. (b) Single grain dose recovery test for sample 215/STP09. A standard test dose of ~5 Gy and a Ph_{test} of 160 °C for 10 s were used during the SAR measurement for both the small aliquot and single grain test.

215/STP10) was 6 – 7 %, whilst 13 – 15 % passed for the remaining two samples (215/STP09 and 215/STP07, Table 7.1).

7.2.1 D_e distributions

Dose distributions for three of the four samples are shown in Figure 7.2 and the statistical data in Table 7.1. The dose distribution for sample 215/STP07 was not included because the quartz OSL signal was clearly in saturation (n=5, n_{sat}=62 and $D_e > 2D_0$, Table 7.1) and any age determined would be unreliable. As expected, the young samples at St Paul's display the characteristic heterogeneous bleaching observed in the quartz distributions from the Moopetsi tributary and Voordrag sites, with a typical 'tail' visible in the histograms and a well-defined leading edge in the radial plots. A large amount of scatter is reflected in the high OD values (72 – 110 %, Table 7.1), coupled with both high positive skewness (3.19 – 3.87, Table 7.1) and high kurtosis (12.33 – 23.84, Table 7.1) values. Whilst the St Paul's donga extends over a larger geographical area than Voordrag, with potentially longer transport distances, colluvial sedimentation occurred via sheet wash at both sites. Heterogeneous bleaching means that the most bleached grains are those which will give the most accurate age and the MAM was used to determine the burial dose. This produced stratigraphically consistent ages (Table 7.1) for the top three samples, whilst 215/VRD07 was excluded due to saturation.

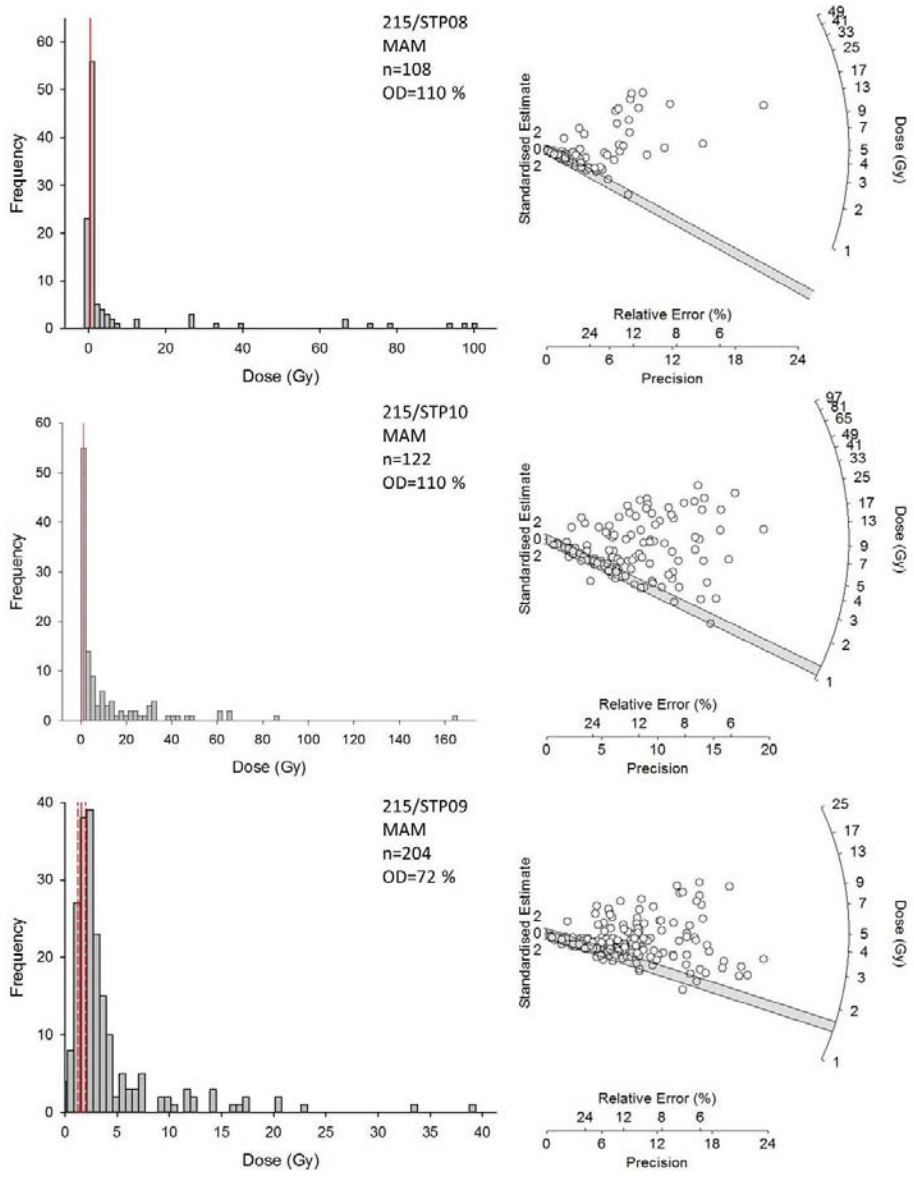

Figure 7.2: Histograms and radial plots of single grain quartz D_e distributions. The solid red line denotes the MAM D_e value with uncertainties (dashed red lines) and the grey bar on the radial plot shows the 2σ region about the MAM D_e value.

Table 7.1: Single grain quartz D_e measurements at St Paul's. Measurements were made using a SAR protocol on 180 – 212 μm grain size for all samples, except 215/STP07 where the 150 – 180 μm fraction was used. The minimum age model (MAM) was used to determine the D_e values for all samples except 215/STP07 which used the CAM (see discussion in text).

Sample ID	Number of grains							OD (%)	Skewness	Kurtosis	D_0 (Gy)[e]	D_e (Gy)[f]	Age (ka)
	N_T [a]	N[b]		n_{sat} [c]		n[d]							
215/STP08	2000	120	(6%)	12	(10%)	108	(90%)	110	3.19	12.33	35 ± 2	0.44 ± 0.04	0.08 ± 0.01
215/STP10	2000	144	(7%)	22	(15%)	122	(85%)	110	3.87	23.84	34 ± 2	1.18 ± 0.05	0.42 ± 0.03
215/STP09	1400	207	(15%)	3	(1%)	204	(99%)	72	3.62	19.82	29 ± 1	1.60 ± 0.37	0.51 ± 0.12
215/STP07	500	67	(13%)	62	(93%)	5	(7%)	19	0.12	1.03	44 ± 2	118 ± 16	42.3 ± 6.3

[a] Total number of grains measured

[b] Number of grains that passed acceptance criteria

[c] Number of grains in saturation (as % of N)

[d] Number of grains in D_e distribution (as % of N)

[e] Reported for DRCs fit with a single exponential function

[f] A sigma-b value of 0.2 was used in the MAM calculation

7.3 Single grain K-feldspar post-IR IRSL at St Paul's

Nine K-feldspar samples were dated at the St Paul's site; originally the sample collected from recent infill within the donga (215/STP08) was selected as the near-modern sample to determine the extent of bleaching in the K-feldspar grains, however the high dose rate (see Table 3.5) makes this sample stand out from the others. Thereafter, sample 215/STP10 was determined to be a better representative sample for the colluvial sediments, as it was collected from a colluvial fan (this will be discussed in more detail in Section 8.4). Sample 215/STP09 was not measured because it was within the range of quartz OSL. The seven remaining samples, stratigraphically including 215/STP07 and below, were all beyond the range of quartz OSL. The 'modified' post-IR IRSL protocol described in Section 6.5 and outlined in Table 7.2 was used for all single grain K-feldspar measurements. Instrumentation details, measurement parameters and acceptance criteria were discussed in Section 3.3.

Across all samples, the number of grains producing a luminescence signal was relatively high; 95 % of the total luminescence signal was produced by 65 – 84 % of the grains, with 54 – 87 % of the grains which were measured (Table 7.3) passing the acceptance criteria. An example of typical DRCs fit with a SSE and DSE function are shown in Figure 7.3, together with the corresponding natural signal. As in the quartz OSL measurements, there is a degree of variability in the DRCs of individual grains and in the brightness of the natural signal. The DRCs of the two grains shown in Figure 7.3 are almost identical in the linear region and diverge in the

Table 7.2: The 'modified' post-IR IRSL protocol used for the St Paul's and Goedgedacht K-feldspar measurements.

Step	Treatment	Measured
1	Dose	
2	Preheat 250 °C for 60 s	
3	IRSL at 50 °C for 200 s (LEDs)	
4	IRSL at 225 °C for 2 s (laser)	L_x
5	IRSL at 225 °C for 500 s (LEDs)	
6	Test dose	
7	Preheat 250 °C for 60 s	
8	IRSL at 50 °C for 200 s (LEDs)	
9	IRSL at 225 °C for 2 s (Laser)	T_x
10	IRSL at 225 °C for 500 s (LEDs)	
11	Return to step 1	

non-linear region, due to the different functions used to fit the DRCs. They produce respective D_e values of 611 ± 66 Gy (SSE, L_n/T_n = 11.83) and 685 ± 67 Gy (DSE, L_n/T_n = 12.72), which are within uncertainty of one another and yet the magnitude of the initial luminescence signal is vastly different for each grain; 103365 cts/0.03 s and 23611 cts/0.03 s respectively.

7.3.1 D_e distributions

The dose distribution (Figure 7.4 and Table 7.3) for the recent infill sample (215/STP08) is positively skewed (1.65, Table 7.3) with a well-defined leading edge of low dose values and a 'tail' of high dose values indicative of a typical single grain distribution from a heterogeneously bleached sample. It has a high OD value (110 %, Table 7.3) equivalent to the infill sample collected from the Moopetsi tributary site. In contrast, the distribution for the colluvial fan sample (215/STP10) appears to be more poorly bleached without a well-defined leading edge of low doses, but with comparable OD, skewness and kurtosis values (101 %, 1.61 and 7.06 respectively, Table 7.3).

Table 7.3: Single grain K-feldspar D_e measurements at St Paul's. Measurements were made using a modified post-IR $IRSL_{225}$ protocol on 180 – 212 μm grain size for all samples. The minimum age model (MAM) was used to determine the D_e values for all samples and reported D_e values have had a residual value of 11.30 ± 1.32 Gy subtracted.

Sample ID	Number of grains							OD (%)	Skewness	Kurtosis	D_0 (Gy)[e]	D_e (Gy)[f]	Age (ka)
	N_T [a]	N[b]		n_{sat} [c]		n[d]							
215/STP08	600	343	(57%)	10	(3%)	333	(97%)	110	1.65	6.10		1.51 ± 0.13	0.20 ± 0.02
215/STP10	300	163	(54%)	2	(1%)	161	(99%)	101	1.61	7.06	276 ± 6	1.59 ± 1.86	0.42 ± 0.05
215/STP07	200	161	(81%)	3	(2%)	158	(98%)	28	1.11	4.72	303 ± 5	239 ± 15	64.2 ± 4.8
215/STP04	300	229	(76%)	10	(4%)	219	(96%)	29	1.28	5.43	303 ± 6	274 ± 15	50.7 ± 3.7
215/STP06	300	220	(73%)	24	(11%)	196	(89%)	30	0.30	2.64	348 ± 6	413 ± 20	110 ± 7
215/STP05	300	199	(66%)	14	(7%)	185	(93%)	34	0.70	3.55	354 ± 8	276 ± 14	85.5 ± 5.6
215/STP03	300	196	(65%)	13	(7%)	183	(93%)	36	0.52	2.74	357 ± 9	433 ± 23	105 ± 7
215/STP01	300	224	(75%)	23	(10%)	201	(90%)	34	0.90	3.55	363 ± 8	463 ± 25	95.7 ± 6.7
215/STP02	300	260	(87%)	37	(14%)	223	(86%)	33	0.61	2.47	329 ± 7	590 ± 33	103 ± 7

[a] Total number of grains measured

[b] Number of grains that passed acceptance criteria

[c] Number of grains in saturation (as % of N)

[d] Number of grains in D_e distribution (as % of N)

[e] Reported for DRCs fit with a SSE function, excluding DRCs fit with a SEPL function

[f] A sigma-b value of 0.2 was used in the MAM calculation

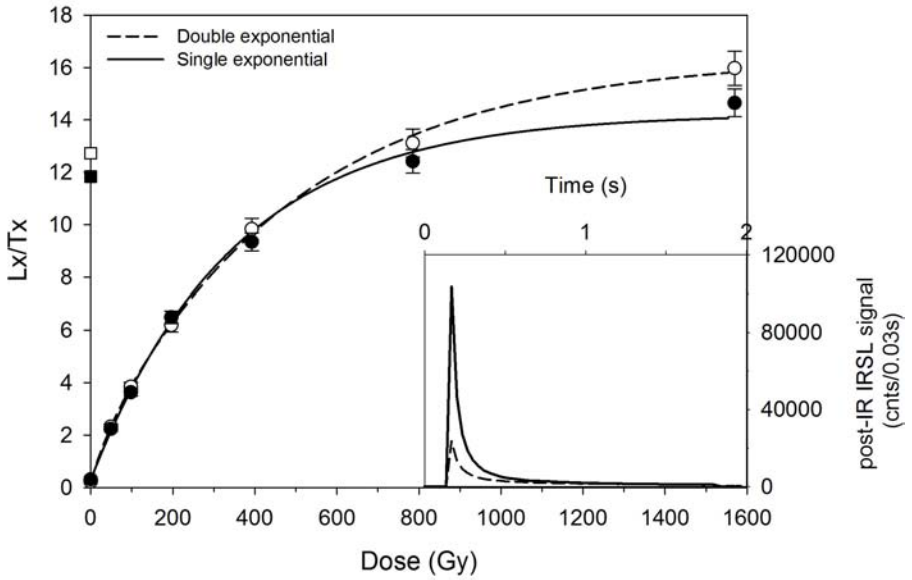

Figure 7.3: Typical DRCs for two grains of K-feldspar from sample 215/STP02 fit using a SSE and DSE function. The inset shows the corresponding natural signal for each grain.

Sample 215/STP10 also has a larger range in D_e values, 760 Gy as opposed to 412 Gy.

For samples below 215/STP07 the distributions become less scattered (OD drops to 28 – 36 %, Table 7.3) and tend progressively towards a normal distribution (skewness from 1.11 to 0.61, Table 7.3) moving down stratigraphy. The range in individual D_e values for single grains within a sample also increases consistently down stratigraphy, from 535 Gy (215/STP07) to 1440 Gy (215/STP02). The distributions no longer display an obvious leading edge of low dose values, however they do start to show a well-defined upper limit of high dose values in the radial plots, particularly from 215/STP05. This could possibly represent the effect of saturation of the post-IR IRSL signal, however saturation should not be problematic in these samples (the highest n_{sat} is 14 % for 215/STP02, which based on the quartz distributions at Voordrag is within acceptable limits).

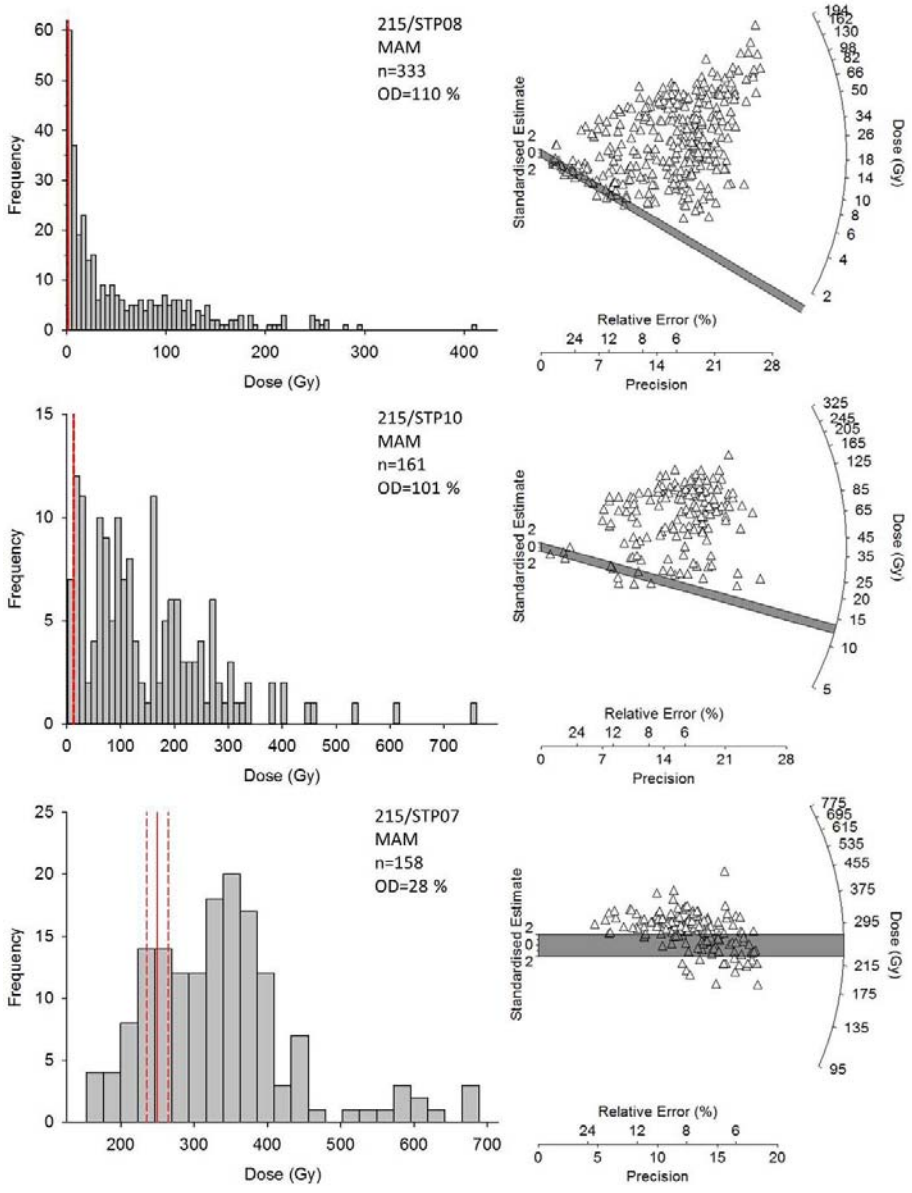

Figure 7.4: Histograms and radial plots of single grain K-feldspar D_e distributions at St Paul's. The solid red line denotes the MAM D_e value with uncertainties (dashed red lines) and the grey bar the 2σ region about the MAM D_e value. All data presented here are prior to subtraction of the calculated residual signal (see discussion in text).

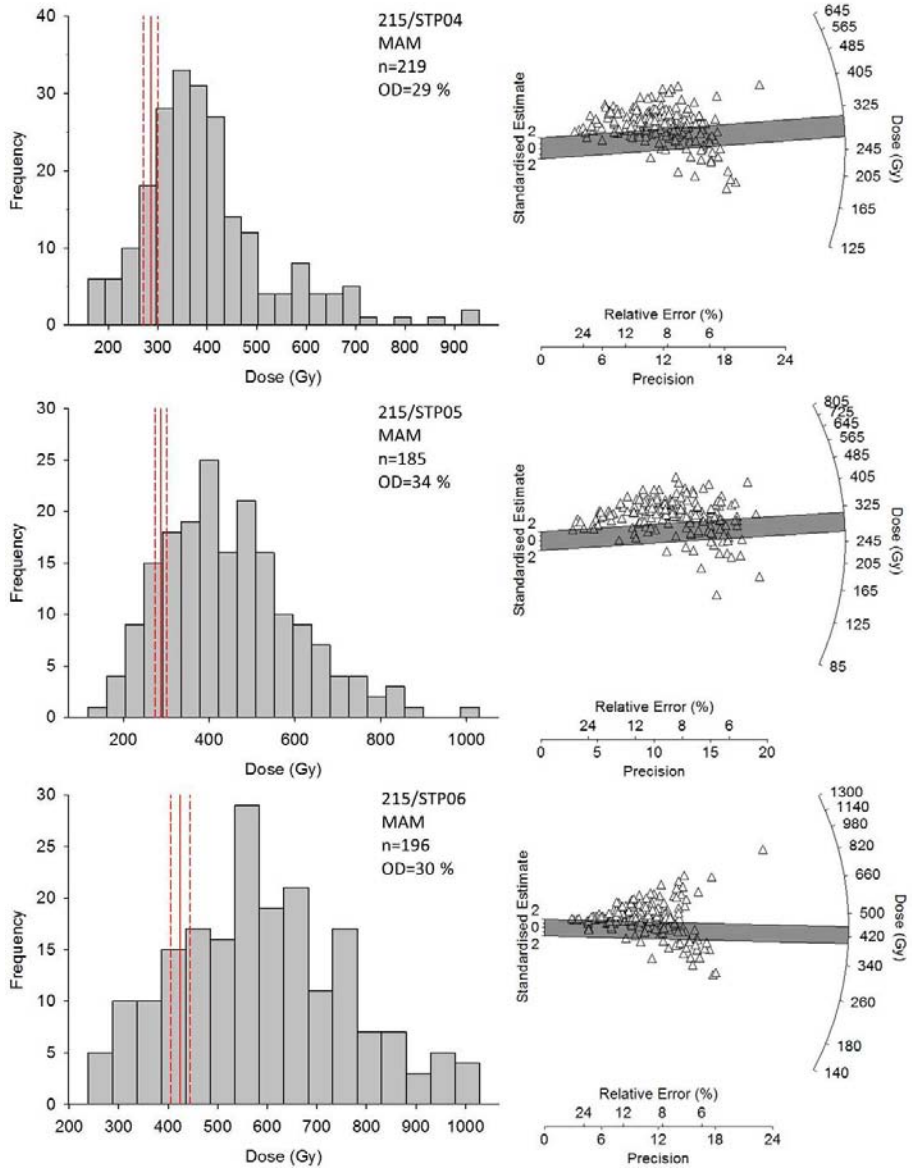

Figure 7.4: Histograms and radial plots of single grain K-feldspar D_e distributions at St Paul's (continued).

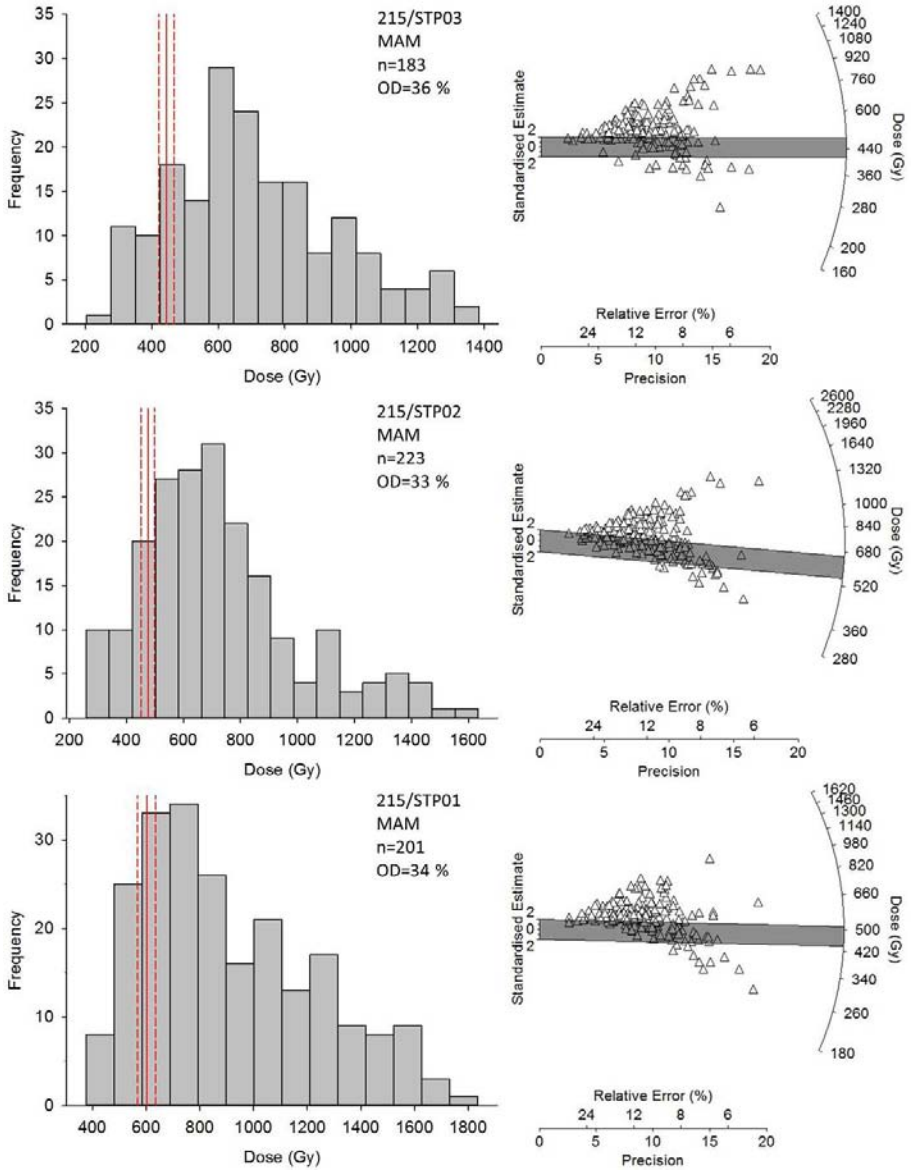

Figure 7.4: Histograms and radial plots of single grain K-feldspar D_e distributions at St Paul's (continued).

Furthermore, the reported D_e is well below the $2D_0$ for the uppermost eight samples. The D_e appears to be approaching the limit of $2D_0$ for the lowermost sample, however a significant proportion of DRCs for this sample were fit using a double saturating exponential function (n=75, 34 %). This population of grains produced two D_0 values, 125 ± 6 Gy and 883 ± 99 Gy, the latter giving a $2D_0$ value well above the D_e for the sample. Incidentally, a similar result applies to the overlying sample (215/STP01) where a larger proportion of grains were fit with a double saturating exponential (n=100, 50 %) which produced D_0 values of 117 ± 8 Gy and 829 ± 100 Gy. This is reassuring as these two samples were collected from the same stratigraphic unit.

Based on the exceptionally broad D_e distributions and the generally lower OD, skewness and kurtosis values when compared to the other three sites in this study, the K-feldspar sediments from St Paul's seem to be more poorly bleached than at the other sites. This may be due to the complex nature of the donga system, where numerous erosive events followed by subsequent deposition (visible as palaeodongas in the current donga wall) remobilised sediment which then had limited time to bleach during transport (see discussion in Section 8.4). The possible input of several populations of heterogeneously bleached grains may explain the very broad distributions and highlights the necessity to identify the most well-bleached proportion of grains. For this reason the MAM was applied to determine the burial dose for all samples within the section.

7.3.2 Residual calculation

Due to the possibility of a significant proportion of poorly bleached grains, it is important to ascertain whether a significant residual signal exists within the K-feldspar grains. The residual value was determined by setting the K-feldspar age for a young, representative sample (in this case 215/STP10, see Section 7.3) to equal the paired quartz age. The calculated residual of 11.30 ± 1.32 Gy was the largest residual value observed in this study, which seems to support the theory that the St Paul's K-feldspar sediments are more poorly-bleached than sediments at the other three sites. The residual was subtracted from the D_e value of each sample prior to age calculation, except in the case of 215/STP08 which is younger than 215/STP10.

7.3.3 Fading measurements

Fading measurements were undertaken as discussed in Section 4.3.2 for three samples located at the top (215/STP10), middle (215/STP04) and bottom (215/STP02) of the stratigraphic section. The mean measured g-value was 1.60 ± 0.35 %/decade, implying the post-IR $IRSL_{225}$ signal was not fading significantly (see Section 4.3.2). Therefore, fading corrections were not applied to these samples.

7.4 A paired single grain chronology for St Paul's

The final paired single grain chronology for St Paul's is comprised of three quartz OSL ages and nine K-feldspar post-IR IRSL ages (Table 7.4 and

Figure 7.5). Within the stratigraphy, only the three uppermost samples could be dated using quartz OSL. They represent the near-modern donga infill (215/STP08) deposited during the current phase of incision and the two topmost units of the Masotcheni Formation, the Batsche Alloformation (215/STP10) and the underlying Telezeni Alloformation (215/STP09). The paired ages for 215/STP07, collected from the Malonjeni Alloformation, show poor agreement, which was expected because > 50 % of the quartz dose distribution was in saturation. The quartz age was calculated using the CAM, based on the observation of Thomsen et al. (2016) that a sample in saturation (which has a dose distribution with 50 % saturated grains) will return an underestimated burial dose when applying the CAM. In this instance, the quartz age is ~22 ka younger than the paired K-feldspar age and is therefore excluded from the final chronology.

The central portion of the chronology features several age inversions. Sample 215/STP04, collected from the Nqutu Alloformation, should be older than 215/STP07 collected from the Malonjeni Alloformation based on their stratigraphic relationship. However, the K-feldspar ages determine 215/STP04 to be ~10 ka younger than 215/STP07. Stratigraphically, sample 215/STP05 should be older than 215/STP06 but is ~25 ka younger. Furthermore, the age for 215/STP06 is equivalent to the ages obtained for the basal sediments and is thus an overestimation of the true age based on the stratigraphic relationship. Sample 215/VRD03 was collected from the base of the Dingaanstad Alloformation and 215/STP01 and 215/STP02 from the St Augustine's Alloformation above the bedrock contact. These three samples are within 1 sigma of one another and provide the timing for the initiation of sedimentation at the St Paul's site.

Table 7.4: Final chronology based on single grain quartz and K-feldspar data for ten samples from the St Paul's site. Also shown are the number of aliquots used in the D_e estimate (n), the overdispersion (OD) of the D_e distribution and the grain size used for D_e measurements. Ages shown in red have been excluded from the final chronology (see discussion in text) and **bold** type denotes the preferred ages.

Sample ID	Quartz OSL					K-feldspar post-IR $IRSL_{225}$				
	n	OD (%)	Grain size (μm)	D_e (Gy)[a]	Age (ka)	n	OD (%)	Grain size (μm)	D_e (Gy)[a]	Age[b] (ka)
215/STP08	108	110	180-212	0.44 ± 0.04	**0.08± 0.01**	333	110	180-212	1.51 ± 0.13	0.20 ± 0.02
215/STP10	122	110	180-212	1.18 ± 0.05	**0.42± 0.03**	161	101	180-212	1.59 ± 1.86	0.42 ± 0.05
215/STP09	204	72	180-212	1.60 ± 0.37	**0.51± 0.12**					
215/STP07	5	19	150-180	118 ± 16	42.3 ± 6.3	158	28	180-212	239 ± 15	**64.2± 4.8**
215/STP04						219	29	180-212	274 ± 15	**50.7± 3.7**
215/STP06						196	30	180-212	413 ± 20	**110 ± 7**
215/STP05						185	34	180-212	276 ± 14	**85.5± 5.6**
215/STP03						183	36	180-212	433 ± 23	**105 ± 7**
215/STP01						201	34	180-212	463 ± 25	**95.7± 6.7**
215/STP02						223	33	180-212	590 ± 33	**103 ± 7**

[a] A sigma-b value of 0.20 was used for the MAM calculations for both quartz and K-feldspar measurements

[b] Ages using K-feldspar post-IR $IRSL_{225}$ measurements were calculated after subtracting a residual dose of 11.30 ± 1.32 Gy from the D_e as described in the text

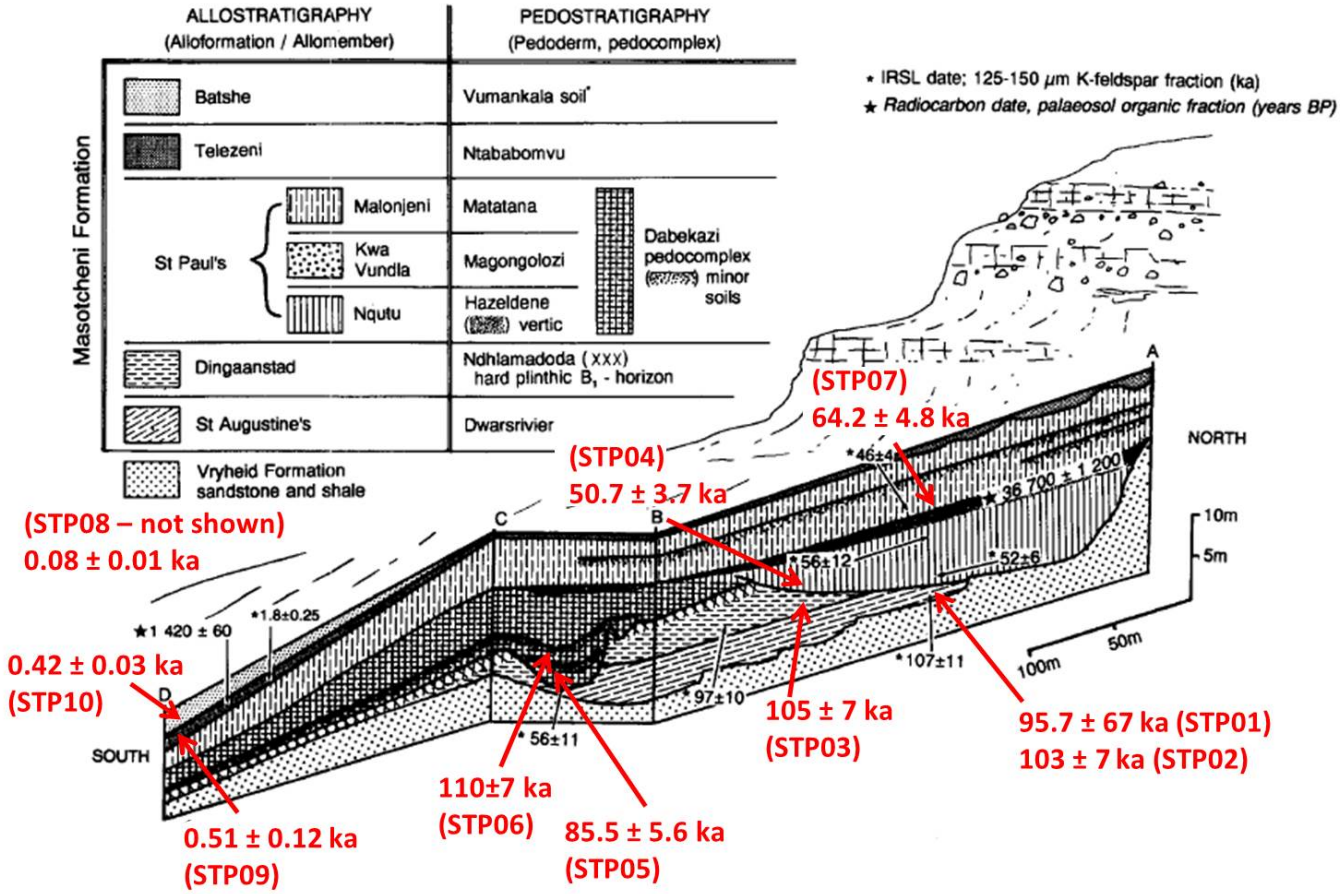

Figure 7.5: Single grain paired quartz-feldspar chronology (ages shown in red) determined for the St Paul's site (figure reproduced from Botha and Fedoroff, 1995). A detailed comparison with the previously published IRSL and ^{14}C chronology was not completed due to the uncertainty surrounding the causes of scatter in the K-feldspar distributions for this site.

The obvious age inversions and overestimation of ages in the central portion of this stratigraphic section could be due to a range of factors. Issues with sample preparation (e.g. sieving) are unlikely as all samples were prepared simultaneously and these problems are limited to a particular site. The inclusion of multiple grains into individual holes on the single grain discs would overestimate the burial dose, however all K-feldspar samples for this site were measured using the 180 – 212 μm grain size. Furthermore, even with the angular grains typical of these environments it is highly unlikely that more than two grains could fit within a hole. Similar age inversions are not observed in the Moopetsi tributary chronology and in the Voordrag chronology the inverted ages are within 1 σ of either the underlying or overlying age. This implies that the age inversions observed at St Paul's are most likely due to some sedimentological factor, the effect of which is either not present or is less pronounced at the other sites. Given the complex erosional and depositional history preserved at St Paul's, the extent of bleaching could be worse than originally thought. Repeat episodes of incision and redeposition of grains occurring over short distances within the donga, exacerbated by the relatively high dose rates measured for the site, may explain the very broad dose distributions observed for these samples. Furthermore, the calculated residual for the St Paul's K-feldspar samples was more than 10 times larger than those calculated for the Moopetsi tributary and Voordrag samples, which implies that the St Paul's sediments are more poorly bleached. One of the objectives of this study was to establish the timing of colluvial sedimentation during the late Quaternary with emphasis on the (i) initial pulse of sedimentation, (ii) the rate of sedimentary cut-and-fill episodes and (iii) the timing of the

most-recent phase of incision. Unfortunately, as it stands, the St Paul's paired chronology will provide a limited control on the timing of sedimentary cut-and-fill structures.

7.5 Single grain quartz OSL at Goedgedacht

An initial combined preheat and dose recovery test (see Section 5.3) was undertaken on the modern analogue sample (215/GGD00) using small aliquots (Figure 7.6). A preheat plateau was identified between 180 °C and 260 °C and a Ph_{regen} of 220 °C was selected because it had a successful dose recovery, returning a measured/given dose ratio of 1.03 ± 0.05 and it is consistent with the Ph_{regen} selected at the other two sites. Thus, the SAR protocol used for the subsequent single grain quartz measurements was identical to the protocol used at Voordrag (see Table 5.1). A more extensive series of single grain dose recovery tests were undertaken at the Goedgedacht site because nine of the ten samples are within the range of OSL dating. The selected SAR protocol was used on samples 218/GGD07, 218/GGD06 and 218/GGD01, using a given dose equal to the expected average D_e value (based on initial signal tests) and test dose of ~5 Gy. The resulting distributions (Figure 7.7) had low OD values of 6 – 12 % and measured/given dose ratios of 1.02 ± 0.02, 1.08 ± 0.03 and 0.98 ± 0.01 respectively. Therefore, the selected SAR protocol is suitable for application to the Goedgedacht sediments as it is able to successfully correct for sensitivity changes and recover a given dose.

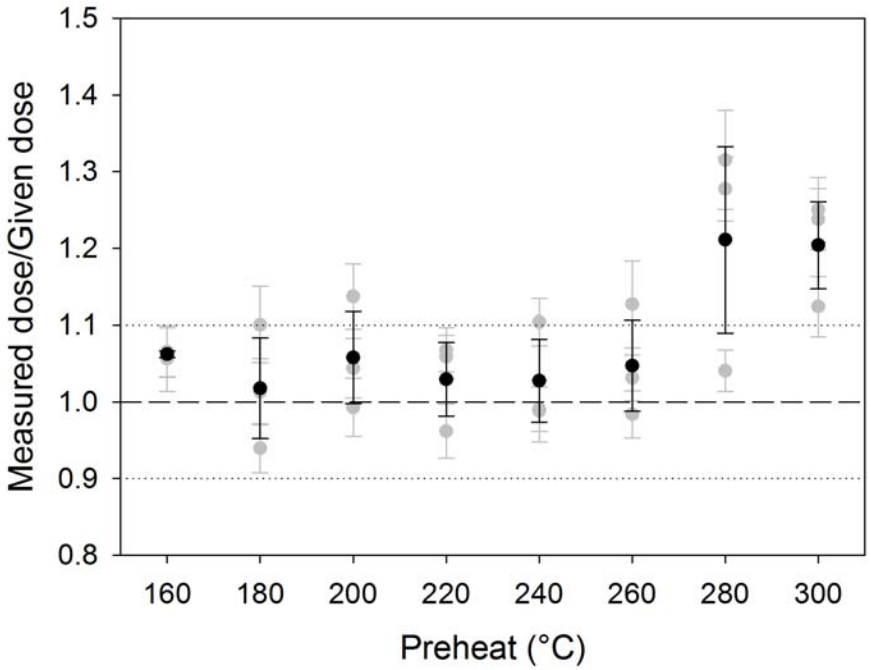

Figure 7.6: Preheat-dose recovery test on small aliquots of quartz from the modern analogue sample (215/GGD00). Grey circles represent the measurements from individual aliquots and black circles represent the mean of the three measurements. A standard test dose of ~5 Gy and a Ph_{test} of 160 °C for 10 s were used during the SAR measurement.

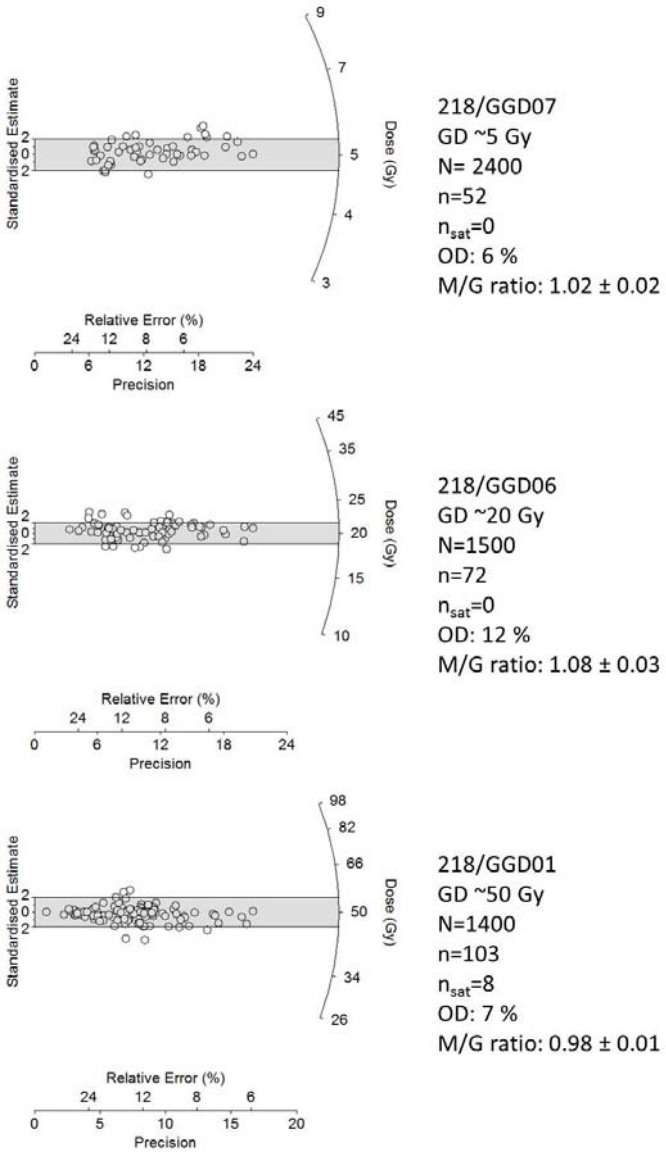

Figure 7.7: Single grain quartz OSL dose recovery tests on three young samples from Goedgedacht, (a) 218/GGD07, (b) 218/GGD06 and (c) 218/GGD01, selected based on their position within the stratigraphic section and expected average D_e values. A standard test dose of ~5 Gy and a Ph_{regen} of 220 °C for 10 s and Ph_{test} of 160 °C for 10 s were used during the SAR measurement. Also reported are the given dose (GD, illustrated by the grey bar), the total number of grains measured (N), the number of D_e values included in the distribution (n), the number of accepted grains in saturation (n_{sat}), the overdispersion (OD) and the measured/given dose ratio.

7.5.1 D_e distributions

Quartz OSL measurements were undertaken on all ten samples collected at Goedgedacht; dose distributions are shown in Figure 7.8 and the statistical data in Table 7.5. As at the previous sites, the near-modern samples (218/GGD04 and 218/GGD08) at Goedgedacht display characteristic heterogeneous bleaching, with a typical 'tail' visible in the histograms and a well-defined leading edge in the radial plots. High OD values (110 %, Table 7.5) reflect the large amount of scatter in the distributions, again coupled with both high positive skewness (5.11 – 6.68, Table 7.5) and high kurtosis (30.47 – 54.94, Table 7.5) values. The distributions of the young samples (ranging stratigraphically from 218/GGD03 down to 218/GGD01) are less skewed (0.85 – 2.06) with lower OD values (23 – 31 %) and a poorly defined leading edge. The data for the lowermost sample (218/GGD02) show the effects of saturation (n_{sat}=82 %, Table 7.5) on the quartz OSL signal and increased OD (56 %), thus any age determined would likely be an underestimation and this data is deemed unreliable.

The Goedgedacht donga complex occupies the largest area in this study and has a simpler stratigraphy than the other three sites. Evidence exists for rapid, massive sedimentation as well as the typical sheet-wash processes encountered at the other sites (this will be discussed in more detail in Chapter 8). However, it is once again apparent that the proportion of grains which are the most well-bleached are of interest at this site and the MAM was used to determine the representative D_e value for all nine samples measured with single grain quartz OSL. This approach has produced a single grain quartz chronology (Table 7.5) that is internally consistent,

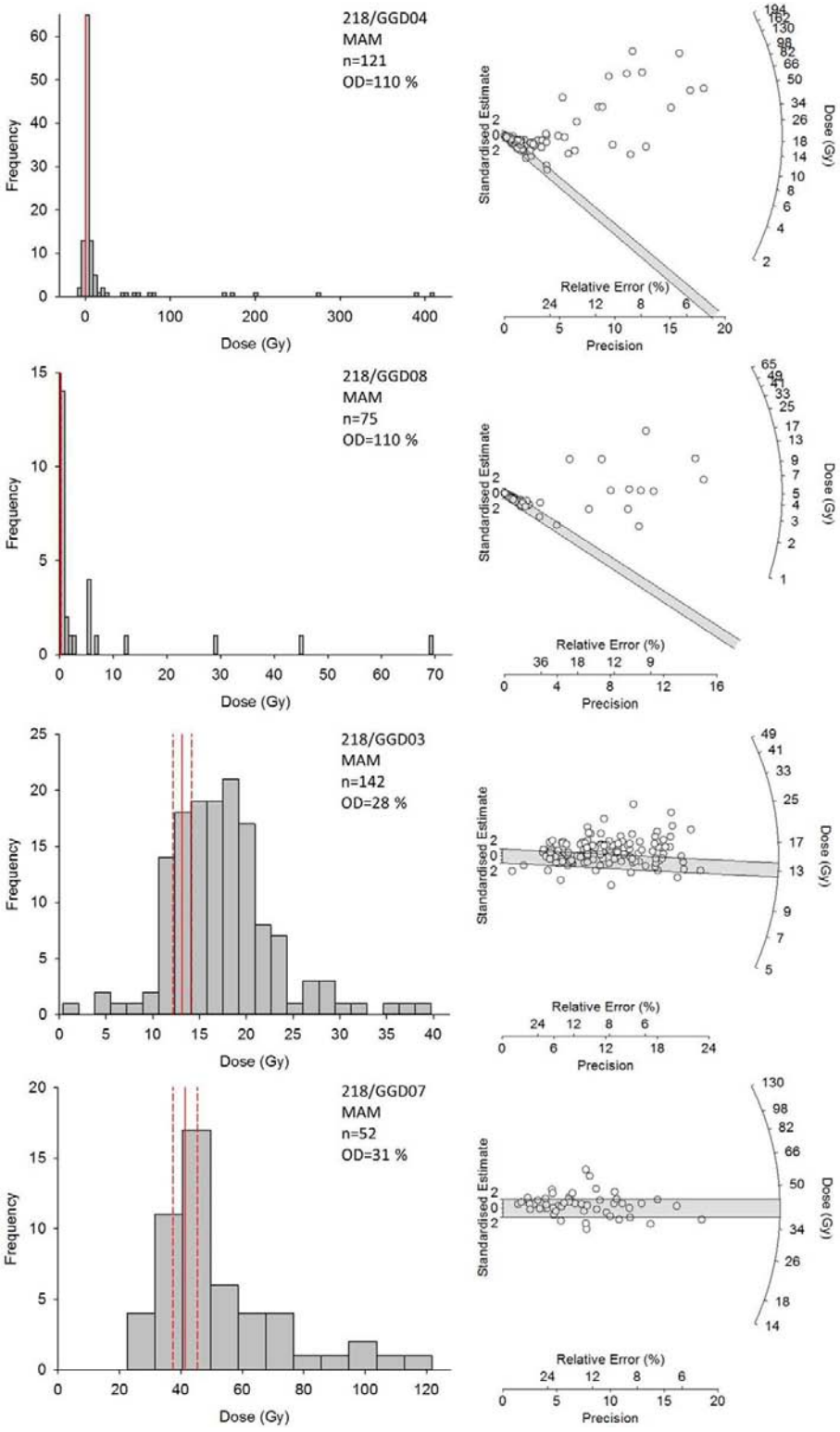

Figure 7.8: Histograms of single grain quartz D_e distributions. The solid red line denotes the MAM D_e value with uncertainties (dashed red lines) and the grey bar on the radial plot shows the 2σ region about the MAM D_e value.

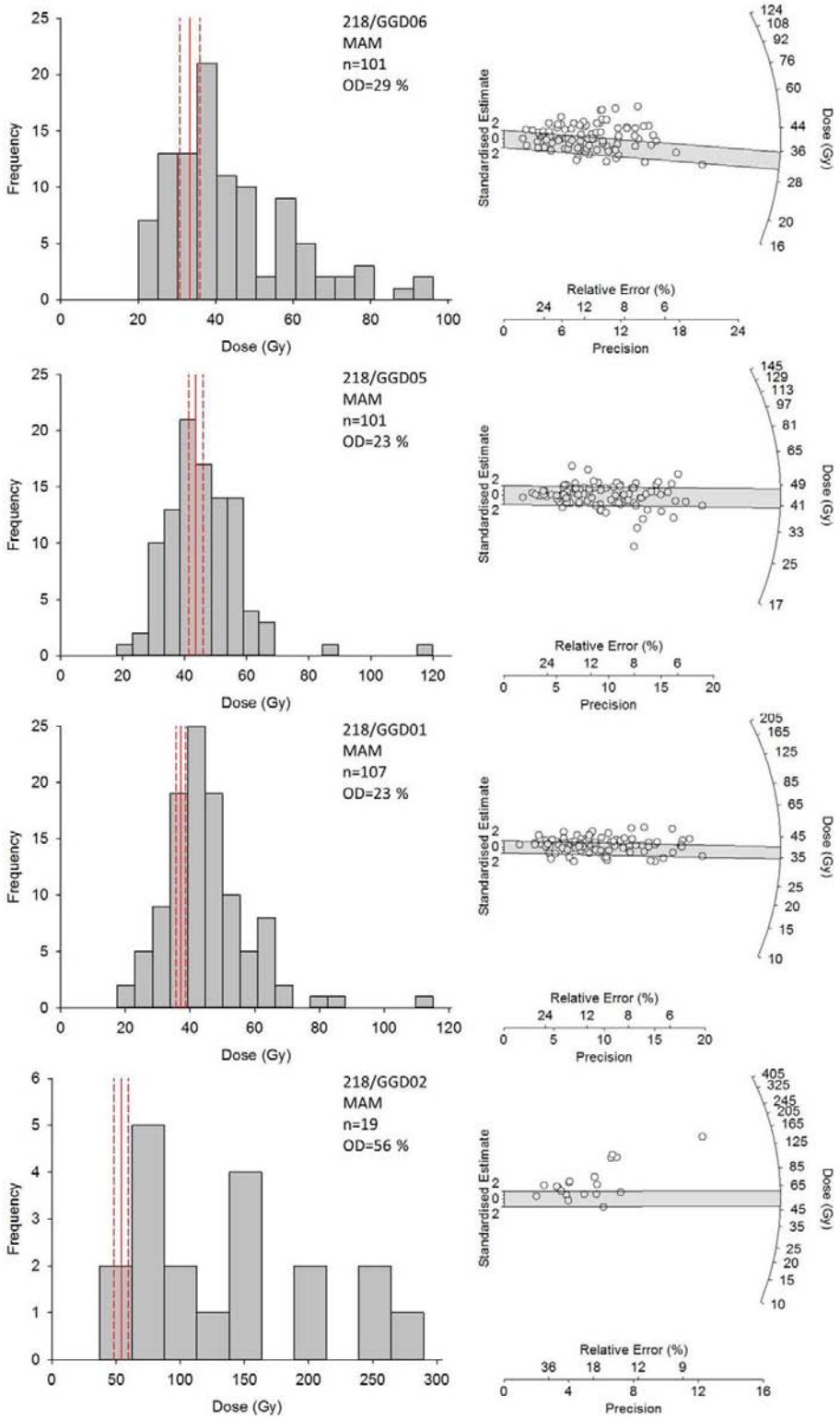

Figure 7.8: Histograms of single grain quartz D_e distributions (continued).

Table 7.5: Single grain quartz D_e measurements at Goedgedacht. Measurements were made using a SAR protocol on 180 – 212 μm grain size for all samples, except 218/GGD03 where the 150 – 180 μm fraction was used. The minimum age model (MAM) was used to determine the D_e values for all samples, except 218/GGD02 which used the central age model (CAM, see text for details).

Sample ID	Number of grains							OD (%)	Skewness	Kurtosis	D_0 (Gy)[e]	D_e (Gy)[f]	Age (ka)
	N_T [a]	N[b]		n_{sat} [c]		n[d]							
218/GGD04	2000	130	(7%)	9	(7%)	121	(93%)	110	6.68	54.94		0.40 ± 0.07	0.11 ± 0.02
218/GGD08	1800	75	(4%)	0	(0%)	75	(100%)	110	5.11	30.47		0.19 ± 0.04	0.06 ± 0.01
218/GGD03	1800	143	(8%)	1	(1%)	142	(99%)	28	0.85	5.42		13.1 ± 1.0	3.84 ± 0.34
218/GGD07	2000	63	(3%)	11	(17%)	52	(83%)	31	1.09	4.35		41.4 ± 4.0	11.2 ± 1.19
218/GGD06	2700	123	(5%)	22	(18%)	101	(82%)	29	0.88	3.70	42 ± 2	33.4 ± 2.6	10.2 ± 0.92
218/GGD05	2000	112	(6%)	11	(10%)	101	(90%)	23	2.06	12.53	43 ± 2	43.6 ± 2.3	14.6 ± 1.0
218/GGD01	1500	117	(8%)	10	(9%)	107	(91%)	23	1.58	8.36	46 ± 2	37.1 ± 1.4	13.2 ± 0.8
218/GGD02	1400	105	(8%)	86	(82%)	19	(18%)	56	0.59	2.06	49 ± 3	114 ± 16	37.6 ± 5.5

[a] Total number of grains measured

[b] Number of grains that passed acceptance criteria

[c] Number of grains in saturation (as % of N)

[d] Number of grains in D_e distribution (as % of N)

[e] Reported for DRCs fit with a single exponential function

[f] A sigma-b value of 0.2 was used in the MAM calculation

with the exception of an age inversion at 218/GGD06 (although the age for 218/GGD06 is within 2 sigma of 218/GGD07, the overlying sample). The age for the lowermost sample (218/GGD02) will be excluded from the final chronology because of potential underestimation due to the effect of saturation on the OSL signal. This age was calculated using the CAM based on the observation of Thomsen et al. (2016), that a sample in saturation will return an underestimated burial dose when applying the CAM. The resulting age of 37.6 ± 5.5 ka will be compared to the paired K-feldspar age to determine the extent of potential underestimation (similar to 215/STP07 in Section 7.4). It is worth noting that 218/GGD03 was measured using the 150 – 180 μm grain size, due to insufficient material in the preferred size fraction (180 – 212 μm). At Voordrag, two of the quartz ages were excluded due to age overestimation from D_e averaging, believed to be due to the smaller grain size allowing multiple grains within a hole on the single grain disc. Overestimation in 218/GGD03 is not expected because the Goedgedacht samples have consistently fewer grains passing the acceptance criteria (< 8 %) than the Voordrag samples and its D_e distribution and OD are comparable with the underlying sample 218/GGD07.

7.6 Single grain K-feldspar post-IR IRSL at Goedgedacht

Three of the eight samples collected from Goedgedacht were measured using single grains of K-feldspar. In Section 7.5, the lowermost sample (218/GGD02) was deemed to be beyond the limit of quartz OSL to date reliably and therefore obtaining an age requires the use of K-feldspar.

Sample 218/GGD01 was selected as a comparison sample because it is located directly above 218/GGD02 stratigraphically and sample 218/GGD04 was the near-modern sample selected to test the extent of heterogeneous bleaching in the K-feldspars at this site. The modified post-IR IRSL protocol (see Section 6.5) outlined in Table 7.2 was used for all single grain K-feldspar measurements. Instrumentation details, measurement parameters and acceptance criteria were discussed in Section 3.3.

The number of grains producing a luminescence signal was relatively high; 95 % of the total luminescence signal was produced by 56 – 69 % of the grains, with ~45 % of grains passing the acceptance criteria. An example of typical DRCs fit with a SSE and DSE function are shown in Figure 7.9, together with the corresponding natural signal. As in the quartz OSL measurements, there is a degree of variability in the DRCs of individual grains and in the brightness of the natural signal. The two grains shown in Figure 7.9 produce respective D_e values of 325 ± 19 Gy (SSE, L_n/T_n = 10.26) and 637 ± 49 Gy (DSE, L_n/T_n = 10.11) despite having similar L_n/T_n ratios. This is due to the difference in the shape of the DRCs.

7.6.1 D_e distributions

The dose distribution (see Figure 7.10 and Table 7.6) for the near-modern sample (218/GGD04) shows the extent of heterogeneous bleaching of the K-feldspar at Goedgedacht. Once again the distribution displays a well-defined leading edge of low dose values and a 'tail' of higher dose values, with high OD (110 %, Table 7.6), positive skewness (3.66, Table 7.6) and kurtosis (19.89, Table 7.6). Calculation of a residual dose by setting the K-feldspar age for a near-modern sample to equal the paired quartz age

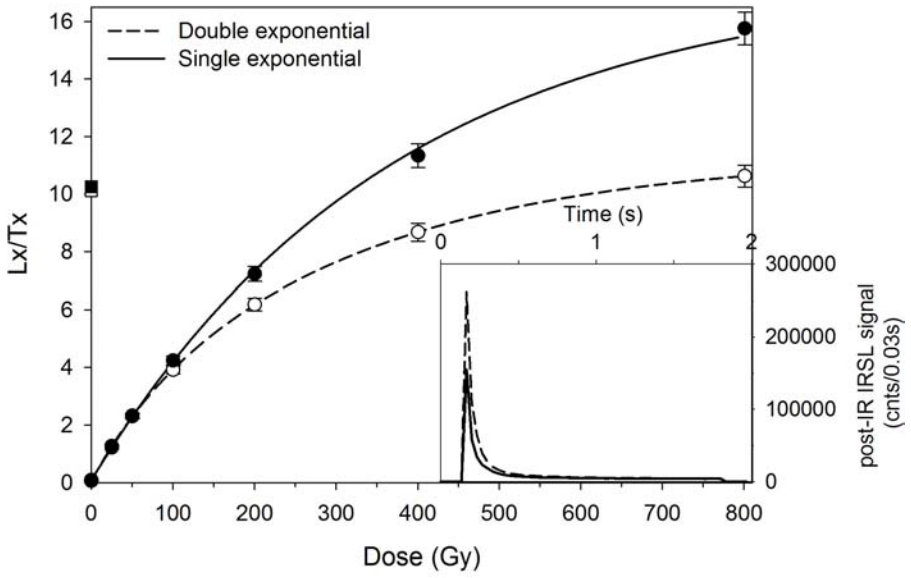

Figure 7.9: Typical DRCs for two grains of K-feldspar from sample 215/GGD02 fit using a SSE and DSE function. The inset shows the corresponding natural signal for each grain.

(see Section 4.3.3) provides a value of 1.57 ± 0.23 Gy, however the spread in the data implies that as much as ~750 Gy could be carried over in the least bleached grains. The dose distribution for sample 218/GGD01 also shows the effect of heterogeneous bleaching, although the OD is greatly reduced (49 %, Table 7.6) and the distribution is more positively skewed (5.02, Table 7.6). In contrast, the distribution for 218/GGD02 is different to the young samples and is instead comparable to the old K-feldspar distributions at the other three sites. It has a broad range (~825 Gy) with a relatively low OD value (38 %, Table 7.6), a poorly defined leading edge of low dose values and the typical 'tail' of high dose values is missing. Consideration of the radial plot (Figure 7.10) shows a well-defined upper limit to the distribution, which may indicate the truncation of the distribution due to saturation of the post-IR IRSL signal. However, only 16 % of accepted grains were in saturation, so a systematic underestimation is not expected for this sample

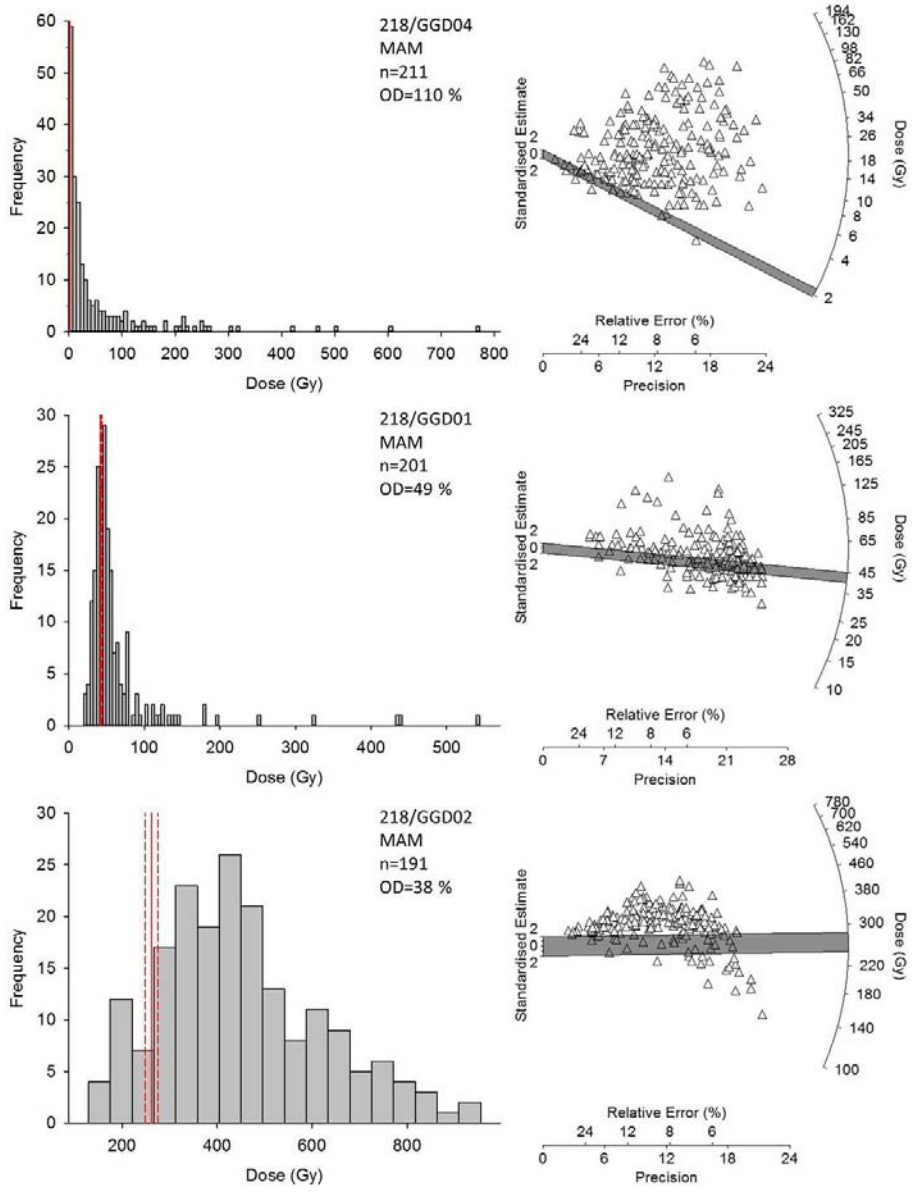

Figure 7.10: Histograms and radial plots of single grain K-feldspar D_e distributions at Goedgedacht. The solid red line denotes the MAM D_e value with uncertainties (dashed red lines) and the grey bar on the radial plot shows the 2σ region about the MAM D_e value. All data presented are prior to residual subtraction (see discussion in text).

Table 7.6: Single grain K-feldspar D_e measurements at Goedgedacht. Measurements were made using a modified post-IR $IRSL_{225}$ protocol on 180 – 212 μm grain size for all samples. The minimum age model (MAM) was used to determine the D_e values for all samples and reported D_e values have had a residual value of 1.57 ± 0.23 Gy subtracted.

Sample ID	Number of grains						OD (%)	Skewness	Kurtosis	D_0 (Gy)[e]	D_e (Gy)[f]	Age (ka)
	N_T [a]	N[b]		n_{sat} [c]		n[d]						
218/GGD04	500	226	(45%)	15	(7%)	211	(93%)	110	3.66	19.89		0.51 ± 0.30	0.11 ± 0.01
218/GGD01	500	206	(41%)	5	(2%)	201	(98%)	49	5.02	32.27	296 ± 34	41.0 ± 1.0	11.0 ± 0.5
218/GGD02	500	228	(46%)	37	(26%)	191	(84%)	38	0.59	2.93	310 ± 8	253 ± 13	65.7 ± 4.2

[a] Total number of grains measured

[b] Number of grains that passed acceptance criteria

[c] Number of grains in saturation (as % of N)

[d] Number of grains in D_e distribution (as % of N)

[e] Reported for DRCs fit with a single exponential function, excluding DRCs fit with a single exponential function with a linear component

[f] A sigma-b value of 0.2 was used in the MAM calculation

(quartz single grain distributions at Voordrag gave reliable ages up to 50 % saturation of the dose distribution, see Section 5.6.1). Furthermore, $D_e < 2D_0$ for all three samples.

7.6.2 Age calculation

As mentioned in Section 7.5.1, given the conditions during sediment deposition at Goedgedacht, the most well-bleached proportion of grains is of interest in dating this site. Therefore, the MAM was applied to all three single grain K-feldspar distributions to determine the true burial dose. In keeping with the previously discussed sites, a residual value (1.57 ± 0.23 Gy) was calculated and subtracted from the D_e value prior to age calculation, this was shown to improve the agreement between young ages at the Moopetsi tributary site (see Section 4.3.3) but had little effect on the old ages. Fading measurements were undertaken as discussed in Section 4.3.2 for two samples located at the top (215/GGD04) and bottom (215/GGD01) of the stratigraphic section. The mean measured g-value of 0.65 ± 0.32 %/decade is the lowest g-value obtained during this study and implies that the post-IR $IRSL_{225}$ signal is not fading significantly. Fading corrections were not applied to these samples.

7.7 A paired single grain chronology for Goedgedacht

The final paired chronology for Goedgedacht (Table 7.7) is based on eight quartz and three K-feldspar ages, making three direct comparisons between paired ages possible. The age of the near-modern sample (218/GGD04) was

Table 7.7: Final chronology based on single grain quartz and K-feldspar data for eight samples from the Goedgedacht site. Also shown are the number of aliquots used in the D_e estimate (n), the overdispersion (OD) of the D_e distribution and the grain size used for D_e measurements. Ages shown in red have been excluded from the final chronology (see discussion in text) and **bold** type denotes the preferred ages.

Sample ID	Quartz OSL					K-feldspar post-IR $IRSL_{225}$				
	n	OD (%)	Grain size (μm)	D_e (Gy)	Age (ka)	n	OD (%)	Grain size (μm)	D_e (Gy)	Age[b] (ka)
218/GGD04	121	110	180-212	0.40 ± 0.07	**0.11± 0.02**	211	110	180-212	0.51 ± 0.30	0.11 ± 0.01
218/GGD08	75	110	180-212	0.19 ± 0.04	**0.06± 0.01**					
218/GGD03	142	28	150-180	13.1 ± 1.0	**3.84± 0.34**					
218/GGD07	52	31	180-212	41.4 ± 4.0	**11.2± 1.19**					
218/GGD06	101	29	180-212	33.4 ± 2.6	**10.2± 0.92**					
218/GGD05	101	23	180-212	43.6 ± 2.3	**14.6± 1.0**					
218/GGD01	107	23	180-212	37.1 ± 1.4	**13.2± 0.8**	201	36	180-212	41.0 ± 1.0	11.0 ± 0.5
218/GGD02	19	56	180-212	114 ± 16	37.6 ± 5.5	191	36	180-212	253 ± 13	**65.7± 4.2**

[a] A sigma-b value of 0.20 was used for the MAM calculations for both quartz and K-feldspar measurements

[b] Ages using K-feldspar post-IR $IRSL_{225}$ measurements were calculated after subtracting a residual dose of 1.57 ± 0.23 Gy from the D_e as described in the text

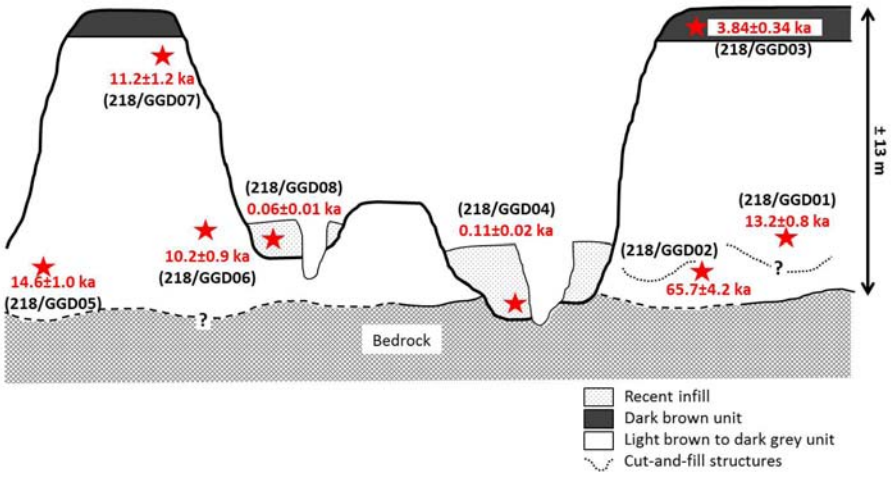

Figure 7.11: Schematic section showing the final paired single grain ages and their spatial relation to one another.

used to determine the residual signal stored in the K-feldspar grains due to their slower bleaching rate compared to quartz, and therefore the paired ages are identical. The paired ages for sample 218/GGD01 are within 2 sigma of one another, showing good agreement between the two chronometers. The paired ages for the lowermost sample 218/GGD02 show very poor agreement, as expected. The quartz age is almost 50 % younger than the paired K-feldspar age, due to the effect of saturation of the OSL signal (as discussed in Section 7.5.1). The final paired chronology has stratigraphic consistency throughout the section, with the one exception being the age for 218/GGD06 (Figure 7.11 and Table 7.7). The geomorphological context of the ages will be discussed in detail in Section 8.5.

7.8 Summary

This chapter applied the luminescence dating approach outlined in Section 6.7 to produce paired chronologies for the colluvial sediments sampled at St

Paul's and Goedgedacht. The paired chronology at St Paul's comprises three quartz ages (Section 7.2) and seven K-feldspar ages (Section 7.3). The ages are effective in constraining the timing of the initiation of sedimentation and the onset of the current phase of incision. However, the complex intervening cut-and-fill episodes are poorly constrained due to the poor bleaching of the K-feldspar in these sediments, considered to be the most poorly bleached of all the sites investigated during this study (Section 7.4).

The paired chronology for Goedgedacht is comprised of seven quartz ages (Section 7.5) and one K-feldspar age (Section 7.6). The stratigraphy at Goedgedacht is well constrained by the paired ages, constraining the timing of initiation of sedimentation, at least one subsequent erosive phase followed by deposition, and the current phase of incision. The following chapter will examine the geomorphological development of the four sites within the context of the paired chronologies presented in Chapters 4, 5 and 7.

Chapter 8

Geomorphic development of the landscape at selected sites across South Africa

8.1 Introduction

This chapter will outline the late Quaternary geomorphological development of the four sites investigated during this study, using the detailed chronological work that was undertaken and presented in Chapters 4 to 7 as the guiding framework. In keeping with research objective 3 (Chapter 1), focus will be placed on the (i) initiation of sedimentation, (ii) intervening phases of erosion, deposition and pedogenesis, and (iii) the cessation of deposition and initiation of the current phase of deep incision. These events will be outlined for the Moopetsi tributary (Section 8.2), Voordrag (Section 8.3), St Paul's (Section 8.4) and Goedgedacht (Section 8.5). Inter-site comparisons will be discussed in Chapter 9.

8.2 Moopetsi tributary site, Limpopo

The stratigraphy exposed at the Moopetsi tributary site (described in Section 2.3.1) can be observed across the Steelpoort region including at the Maandagshoek site (Kendall, 2000) and the Bridge site (see Figure 2.2). Across the region, the three sedimentary units (BSS, UGS and LGS) and two palaeosols (BT and OGP) vary in thickness, and the palaeosols vary in degree of development, but their regional expression implies that ages obtained at the Moopetsi tributary site can be extrapolated more widely. Furthermore, the previously determined radiocarbon ages for pedogenic carbonates from the Bridge site (see Table 8.1) can be directly compared to the paired luminescence chronology from this study.

Table 8.1: Radiocarbon ages originally published by Verster and van Rooyen (1999) recalibrated using the ShCal13 calibration curve.

Sample ID	C-14 age (years BP)[a]	Recalibrated (ka)[b]
Pta-4723	4220 ± 60	4.7 ± 0.2
Pta-4733	12280 ± 110	14.3 ± 0.5
Pta-5113	22500 ± 290	26.7 ± 0.6
Pta-4727	24100 ± 300	28.2 ± 0.5
Pta-5111	28600 ± 540	32.6 ± 1.2
Pta-5112	29800 ± 780	33.7 ± 1.8

[a] Radiocarbon ages published in Verster and van Rooyen (1999)
[b] Radiocarbon ages were recalibrated in Oxcal V4.2 (Bronk Ramsey, 2009) using ShCal13 (Hogg et al., 2013)

Lyons (2012) produced a conceptual model (Figure 8.1) for the sequence of events leading to the formation of the terrestrial archive preserved at the Moopetsi tributary site. In his model, deposition of the LGS over eroded bedrock began at ~117 ka (Stage 1, Figure 8.1). Aggradation of the

LGS continued until at least ~87 ka, but potentially until ~77 ka, based on extrapolation of the LGS sedimentation rate. This was followed by slowing or cessation of LGS sedimentation, and pedogenesis leading to the formation of the OGP (from LGS sediments) between ~77 ka and ~53 ka (Stage 2, Figure 8.1). Deposition of the UGS was initiated ~53 ka, locally leading to the truncation of the OGP and continued until ~5 ka, albeit with evidence of erosion and reworking of UGS preserved locally (Stage 3, Figure 8.1). Cessation of UGS deposition was followed by pedogenesis and formation of the BT, in the upper UGS between ~5 ka and ~2.7 ka (Stage 4, Figure 8.1). The BT palaeosol was locally truncated through erosion that preceded deposition of the BSS at ~2.7 ka, an event that represented the terminal phase of widespread alluvial aggradation in the region (Stage 5, Figure 8.1). Following the cessation of BSS deposition after ~2.7 ka, the Moopetsi tributary incised deeply into the succession, resulting in the formation of dongas. This was followed by a minor phase of channel aggradation ~0.22 ka (Stage 6, Figure 8.1) and then subsequent further incision of the tributary and dongas into bedrock (Stage 7, Figure 8.1).

Lyons (2012) used independent evidence, specifically aerial photographs and archaeological remains, to support the luminescence-constrained timing of donga formation near the Moopetsi tributary site. Comparison of modern aerial photographs with photographs from AD 1948 show no substantial increase in the areal extent of the dongas, and also provide another minimum age for donga formation. Additionally, the preservation of in-situ archaeological remains (including a series of stone circles, grinding stones and concentrations of iron slag) on the donga floor near the Bridge site provide a bracketing age for donga formation. These remains, believed

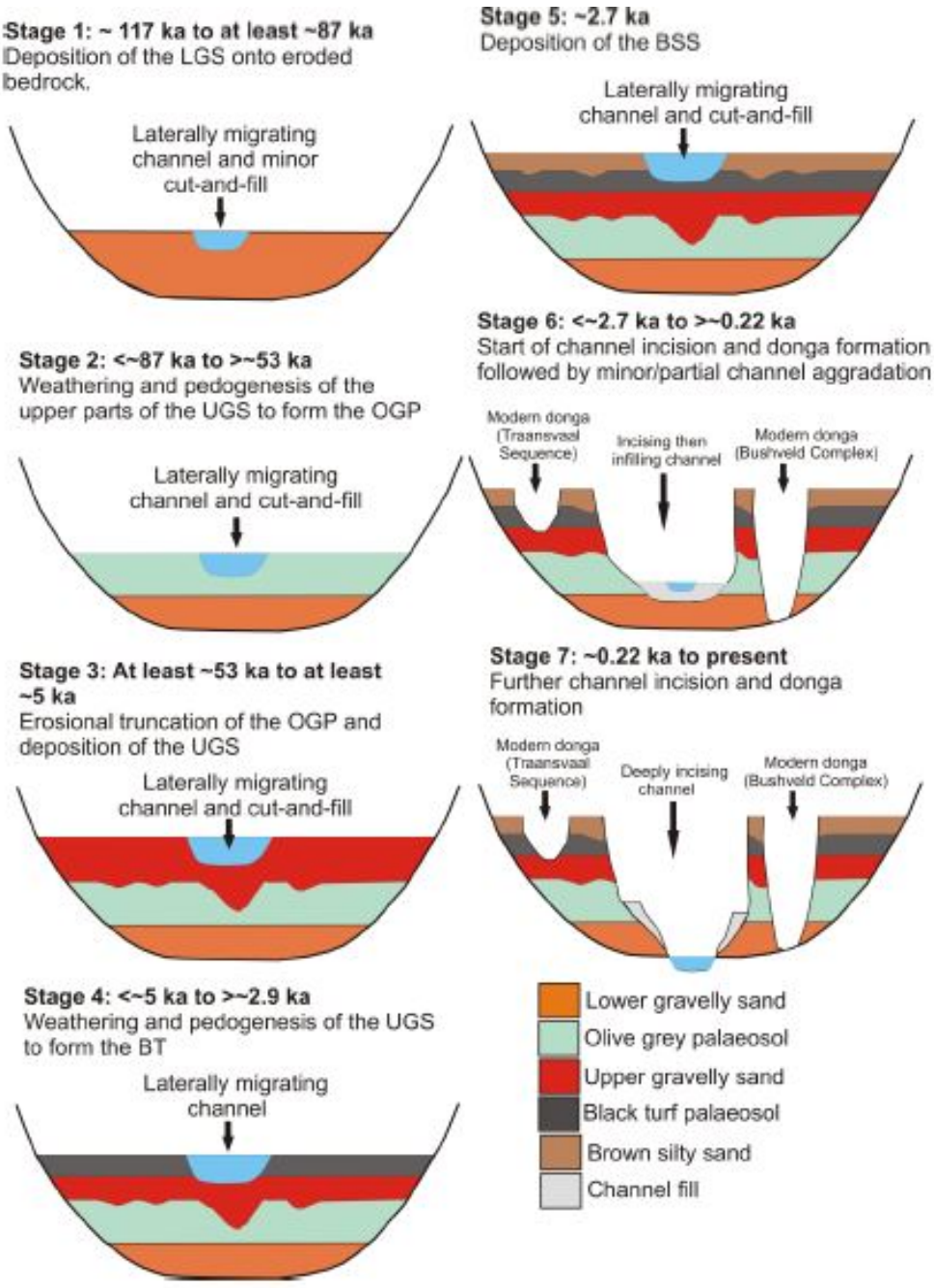

Figure 8.1: The conceptual model of Lyons (2012) describing the geomorphological development of the Moopetsi tributary site.

to be from the Late Iron Age (AD 1300 to 1820s), are similar to remains found within a donga ~60 km southeast of the Moopetsi tributary (Evers, 1975). Based on this and other studies (e.g. Maggs, 1974; Mason, 1973, 1974; Mason and van der Merwe, 1974) in northeastern South African, Lyons (2012) concluded that these dongas must have formed prior to AD 1820, and possibly as early as AD 1450.

The findings of this study largely support but nonetheless refine the findings of Lyons (2012). Whilst the sequence of events described by Lyons (2012) in Figure 8.1 remains the same, the ages of sedimentary units and therefore the timing of events are slightly different owing to the new chronologies derived during this study. These revised timings are outlined in the following sections.

8.2.1 Timing of initial sedimentation and pedogenesis

The timing of the initiation of deposition is provided by the basal sediments of the LGS unit (Figure 8.2), which were dated to ~153 ka by this study. Deposition of this unit continued until at least ~102 ka, as inferred from the age for 170/MPT9, which was collected just below the contact between the LGS and the overlying OGP. However, the OGP was formed through pedogenetic alteration of the uppermost section of the LGS. Therefore, deposition must have continued after 102 ka, prior to pedogenesis occurring. Given 2.8 m of deposition over 43 ka, which gives a projected sedimentation rate of 0.065 mm/year (assuming a constant rate of sedimentation) deposition may have occurred until ~78 ka.

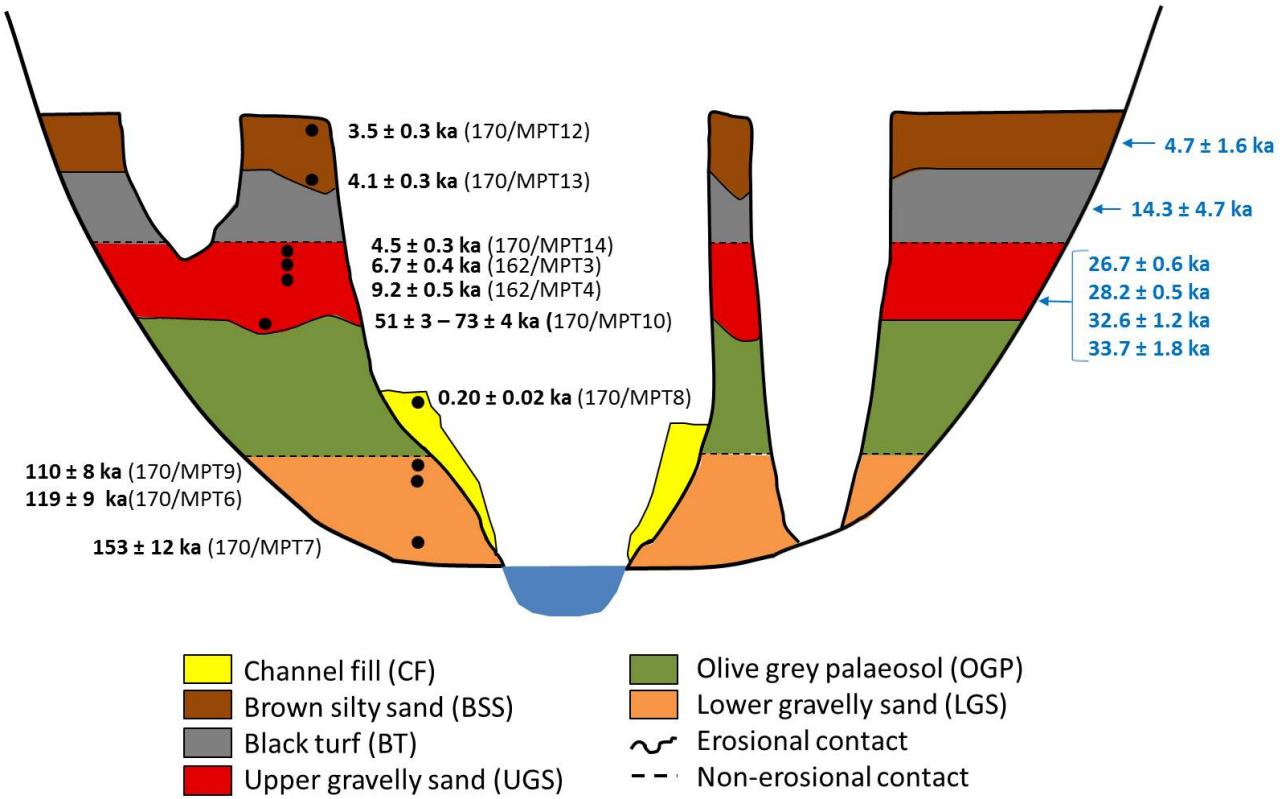

Figure 8.2: A schematic diagram showing the composite stratigraphy of the Moopetsi tributary site. This stratigraphy is expressed across the Steelpoort region, allowing extrapolation of ages between sites. Luminescence ages (from the tributary site) from this study are shown in black and the recalibrated radiocarbon ages (from the bridge site) of Verster and van Rooyen (1999) are shown in blue.

8.2.2 Timing of subsequent pedogenesis and depositional events

Cessation of OGP pedogenesis and the initiation of the subsequent phase of deposition began at least ~51 ka (possibly as early as ~73 ka based on the K-feldspar age) and continued until at least 4.5 ka (Figure 8.2). Owing to the fact that the BT palaeosol formed within the upper portion of the UGS, deposition of the UGS unit would have continued for some time after 4.5 ka. Ages for pedogenic carbonates (see Table 8.1) from the middle to lower part of the UGS lie between ~26.7 and 33.7 ka, which agrees with the luminescence ages from Lyons (2012) and this study. The subsequent phase of pedogenesis occurred over a period of ~400 years, with the formation of the overlying BT palaeosol constrained between 4.5 ka (underlying UGS age) and 4.1 ka (overlying BSS age).

Between ~4.1 ka and 3.5 ka, the BSS unit was deposited. This represents a final, relatively rapid phase of major sedimentation. Radiocarbon ages for carbonates from the BT palaeosol and BSS unit are older than the luminescence ages (see Figure 8.2). Verster and van Rooyen (1999) did not specify the nature of the carbonates that were dated, but they were likely pedogenic carbonates, so this overestimation may be due to incorporation or reworking of older calcrete nodules into younger palaeosols and younger sedimentary units. Lyons (2012) cited the erosive truncation of older units and abundant erosional unconformities as evidence of reworking of the succession at the Moopetsi tributary and other sites, and this could have resulted in the redistribution of pedogenic carbonates and incorporation into younger units.

8.2.3 Timing of the onset of current incision

Following deposition of the BSS, two phases of incision were separated by a phase of minor channel aggradation (Lyons, 2012). During the first phase of incision between 3.5 ka and 0.2 ka (Figure 8.2), dongas were formed on the steepened channel banks and extended headwards into the adjacent floodplain and adjoining pediments. This was more pronounced on the west bank floodplain (see Figure 2.7), as the sediments derived from the Bushveld Complex are more susceptible to erosion. This susceptibility may be due to several factors, such as the different weathering products of the two parent lithologies or the organic content and grain size of the soils (potential drivers of incision will be discussed in Section 9.5). Following deep incision, up to ~2 m of aggradation occurred ~0.20 ka, forming the minor channel fill. The second phase of incision occurred after ~0.20 ka, with the channel incising down to and locally into bedrock. In summary, this site has preserved a record of net aggradation interspersed with periods of minor erosion and pedogenesis from ~153 ka to ~3.4 ka, whilst the two phases of incision after 3.4 ka represent net erosion of a magnitude not seen at this site for at least the last ~150 ka.

8.2.4 Conceptual model for the sequence and timing of deposition, erosion and pedogenesis in the Steelpoort region

Figure 8.1 (originally in Lyons, 2012) summarised the sequence and timing of deposition, erosion and pedogenesis in the Steelpoort region, based on a combination of luminescence ages, aerial photographs an archaeological

evidence. Whilst the sequence of events in Figure 8.1 remains the same, the ages and therefore the timing of events are slightly different based on the single grain ages from this study. The revised timescale is as follows:

Stage 1: ~153 ka to at least ~110 ka Deposition of the LGS onto eroded bedrock began by at least ~153 ka, with aggradation continuing until at least ~110 ka and possibly until ~78 ka (based on the extrapolated LGS sedimentation rate).

Stage 2: <~78 ka to >~51 ka Subsequent to the cessation of LGS deposition, a period of slow or non-sedimentation resulted in pedogenic alteration of the LGS sediments to form the OGP. Based on the bracketing age of the LGS and UGS, and the extrapolated sedimentation rate of the LGS, the OGP formed sometime between ~78 ka and ~51 ka.

Stage 3: at least ~51 ka to ~4.5 ka Deposition of the UGS unit began by at least ~51 ka, leading to partial or complete truncation of the OGP, and continued until at least ~4.5 ka. There is evidence for phases of minor erosion and reworking of the UGS sediments in exposures across the region, particularly at the Maandagshoek fan site.

Stage 4: <~4.5 ka to >~4.1 ka Cessation of UGS deposition, was followed by formation of the BT through pedogenic alteration of the UGS sediments, occurred between ~4.5 ka and ~4.1 ka.

Stage 5: <~4.1 ka to >~3.5 ka The BT palaeosol was locally erosively truncated, with the initiation of BSS deposition at ~4.1 ka, which then continued until ~3.5 ka. Deposition of the BSS marked the terminal phase of widespread alluvial aggradation in the region.

Stage 6: <~3.5 ka to >~0.2 ka Cessation of BSS deposition occurred ~3.5 ka, following which the Moopetsi tributary incised deeply, and dongas

formed on the steepened channel banks. This was followed by a phase of minor (~2 m) channel aggradation at ~0.20 ka.

Stage 7: ~0.2 ka to present Following deposition of the minor channel fill ~0.2 ka, the channel incised through the entire succession down and into bedrock, resulting in further donga formation and/or expansion. A comparison by Lyons (2012) of the earliest aerial photographs of the region with later photographs showed that channel and donga incision was fully established by AD 1948. In addition, in situ archaeological remains on the floor of dongas points to Late Iron Age occupation, which suggests that the dongas were present prior to ~AD 1830 when the Late Iron Age ended. This current phase of incision appears to be of a magnitude greater than has been recorded previously in the preserved alluvial record in the region.

8.3 Voordrag, KwaZulu-Natal

As described in Section 2.2.2, Voordrag represents a sequence of intercalated colluvial units and buried palaeosols within a bowl-shaped depression underlain by Ecca Group argillites and a thick resistant sandstone unit. The preservation of several untruncated palaeosol A-horizons at Voordrag distinguishes it from typical Masotcheni Formation colluvium (Botha et al., 1992). More than 18 m of colluvium is exposed within the donga, but previous work was limited to the upper ~11 m within which the palaeosol units are preserved. Published luminescence ages for the site (Clarke et al., 2003) suggest that sedimentation began shortly after the end of the last interglacial (~100 ka) and the lack of any older colluvium was interpreted by Clarke et al. (2003) as evidence that hillslopes were largely stripped of their

colluvial mantle during the preceding interglacial (OIS 5e). Stripping was followed by successive pulses of colluvial deposition, separated by periods of slope stability during which pedogenesis occurred, giving rise to the intercalated stratigraphy of colluvium and buried soil profiles during OIS 2. Two subsequent depositional pulses occurred during the Holocene (OIS 1), and a final phase of slope stability and soil formation occurred prior to the current phase of incision. None of these OIS 1 events were dated by Clarke et al. (2003).

8.3.1 Mechanism and timing of initiation of sediment deposition

Results of the paired single grain chronology (Figure 8.3) show sedimentation to have been initiated ~65 – 70 ka, ~30 ka later than suggested by Clarke et al. (2003). Based on its stratigraphic position (~2.5 m below 215/VRD01), sample 215/VRD10 should be significantly older than 215/VRD01 but this is clearly not the case. The contact between colluvium and heavily weathered shale bedrock was observed ~15 m below the projected land surface (Figure 8.4(a)) and ~7 m away from the location of sample 215/VRD10 (see Figure 2.11), which was collected from a >5 m thick, massive, red (10R 4/8) colluvial unit underlying the main donga sequence reported in Clarke et al. (2003). Based on this contact, the red colluvial unit is likely the lowermost sedimentary unit preserved within the basin.

Investigation of the area surrounding the donga shows a missing section of the sandstone escarpment directly above the site, a dolerite dyke cross cutting the escarpment and a boulder field downslope of the donga (Figure 8.5). In combination, this array and spatial arrangement of factors is

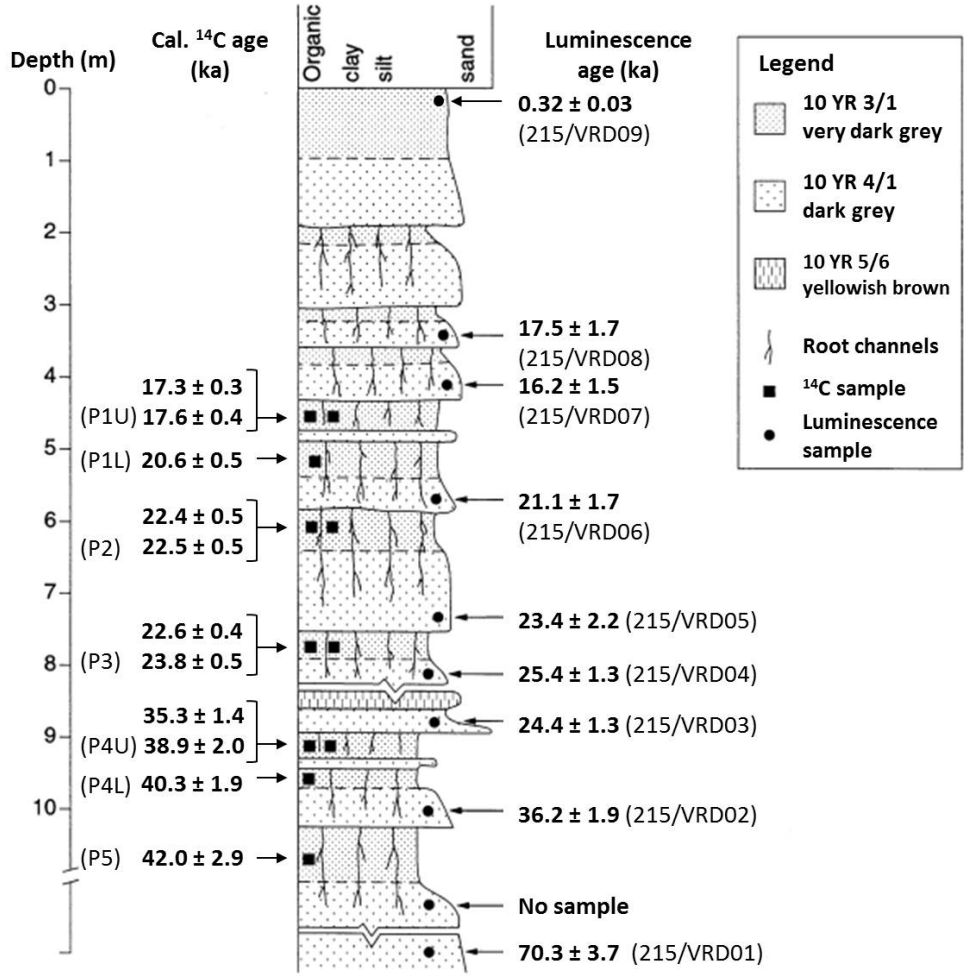

Figure 8.3: Composite stratigraphy of the Voordrag colluvial succession (redrawn from Clarke et al., 2003), showing the recalibrated (ShCal13) radiocarbon ages and the paired single grain luminescence chronology from this study. The lowermost sample from this study (215/VRD10, 64.6 ± 3.3 ka) does not appear on the stratigraphic log as it is located below the sediments exposed in the donga walls. This sample was collected to constrain the timing of the initiation of sedimentation in the main succession.

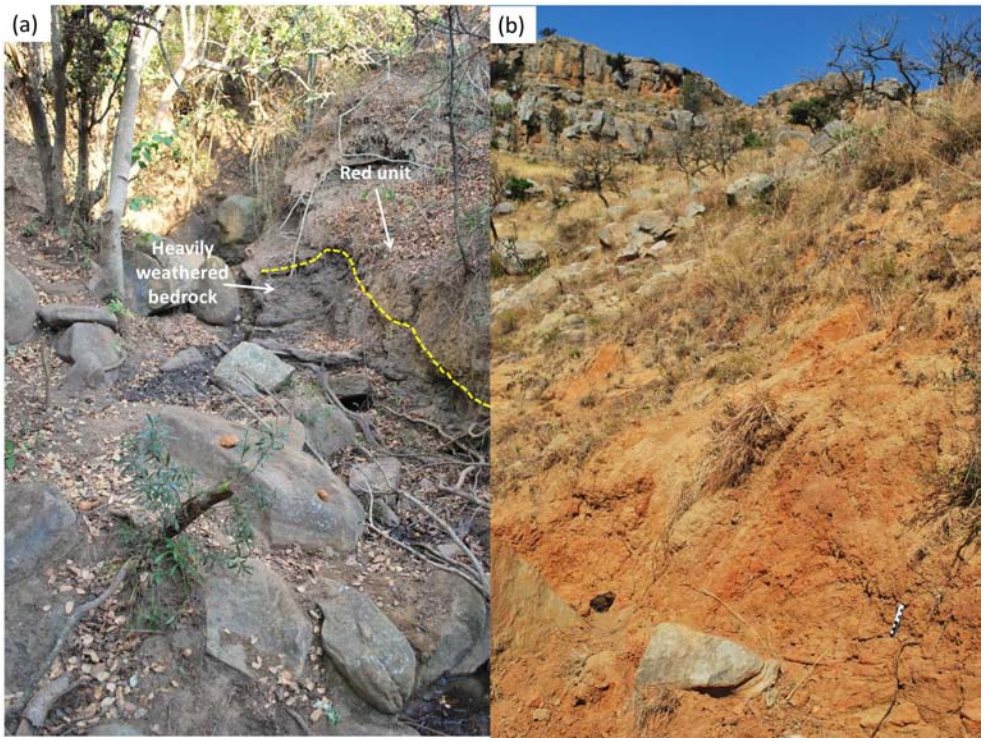

Figure 8.4: (a) The observed bedrock contact at Voordrag, with the red unit overlying heavily weathered Permian shales (view looking upstream along a small-incised channel) and (b) the red unit exposed near the top of the escarpment, with sandstone boulders from the bedrock hosted within the sediment unit.

strongly suggestive of a landslide. The sequence of events leading to such a postulated event is unknown but invites speculation. Sandstone tends to be more permeable than dolerite, thus water percolation may have occurred preferentially along the boundary of the dyke, leading to enhanced weathering. During heavy rainfall, increased pore water pressure within the weathered rock face could have led to eventual slope failure and generated a landslide. Some of the larger boulders emplaced down slope likely created a basin-shaped depression with a restricted outlet. The red colluvial unit is >5 m thick and is massive with almost no internal structure, and hosts sandstone and shale boulders of various sizes (Figure 8.4(b)), both of which imply rapid emplacement. The overlying unit is light orange brown (2.5Y 7/8), massive, and is distinct from the overlying colluvial sediments due to its lack of horizontal laminations, also implying rapid emplacement. The new single grain ages date the red unit (215/VRD10) and orange brown unit (215/VRD01) to within 1 sigma of each other, 64.6 ± 3.3 ka and 70.3 ± 3.7 ka respectively. The first period of landscape stability is denoted by the P5 palaeosol unit, which has a radiocarbon age of 42.0 ± 2.9 ka (Figure 8.3) and constrains the timing of palaeosol formation. This radiocarbon age is approaching the upper limit of the technique and should be treated as a minimum age for the palaeosol. Therefore, the most logical interpretation is that the landslide occurred ~70 ka and was associated with rapid deposition of the red and orange-brown units within the depression. The land surface eventually stabilised and pedogenesis occurred to form P5 by at least ~42 ka. This palaeosol was then buried by a pulse of colluvial deposition after 42 ka but before 36 ka, as shown by the luminescence age for the overlying unit.

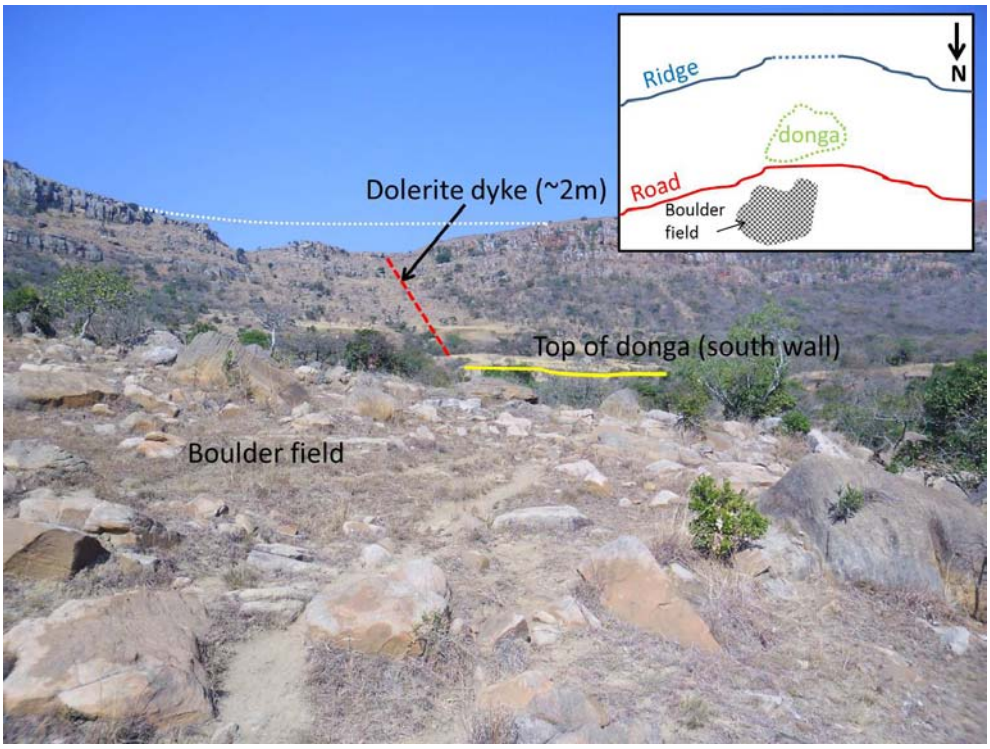

Figure 8.5: Ground-level photograph of the area around the Voordrag donga. The donga (see top surface marked by yellow line) is situated below eye level, between the sandstone ridge in the background and the boulder field in the foreground of the photograph. The dotted line shows the extent of the missing portion of the ridge, which was emplaced downslope during the landslide event to form the boulder field. This led to the formation of the bowl-shaped depression within which the colluvial sediments have accumulated.

8.3.2 Timing of interspersed colluvial deposition and palaeosol formation

Following the period of land surface stability ~42 ka, pulses of colluvial sedimentation occurred, interspersed by other periods of stability. The colluvial sediments are typically dark brown (10YR 4/1) and display stratification, micro-fault structures, fining upward successions at the cm-scale (Figure 8.6 (a)), and granules and local dolerite pebbles. The intervening periods of slope stability resulted in the formation of soil horizons which were buried by subsequent pulses of sedimentation. These units are typically dark grey (10YR 3/1) and organic-enriched, and have weakly developed ped structures and oxidised root traces (Figure 8.6 (b)). Granulometric data from Botha et al. (1992) shows a higher clay content in the soil A horizons than in the underlying subsoil horizons, which is indicative of poorly developed soils. Botha et al. (1992) also noted the enrichment of organic material within the A horizons which accounts for the dark grey colour, despite the low measured organic carbon contents ($<$ 1 %).

Through the central section of the stratigraphy there is good agreement between the luminescence and radiocarbon ages (Figure 8.3). The luminescence ages are dating the timing of colluvial deposition in each phase and therefore should be younger than the radiocarbon ages for underlying soil units, which are interpreted as representing the terminal phases of soil formation. Minor sedimentation occurred during two phases of overall stability, as evidenced by the split palaeosol units (i.e. P4 and P1, Figure 8.3; also see Figure 2.10) which are characterised by thin colluvial layers

sandwiched within thicker palaeosol units. Based on the short periods of time separating the split palaeosols (P4 upper and P4 lower) and the P2 and P3 palaeosols from one another, sediment accumulation and formation of the A horizons occurred within a period of ~1 ka (Botha et al., 1992).

Overall, during the late Quaternary, three major periods of rapid accumulation and pedogenesis can be identified at Voordrag (Figure 8.7). The first period, between ~36.2 ka and ~35.3 ka (1, Figure 8.7), represents 0.9 m of sediment accumulation and subsequent pedogenesis. Thus the rate of deposition must have been >1 mm/yr to allow time for the two minor phases of soil formation. The second period between ~24.4 ka and ~17.5 ka (2, Figure 8.7) represents 5.3 m of accumulation, with a rate of deposition of 0.768 mm/yr. The third period between ~17.5 ka and ~0.32 ka (3, Figure 8.7), includes most of the Holocene, and has a lower rate of deposition, of 0.180 mm/yr.

8.3.3 Final deposition and the onset of the current incision phase

The top unit exposed within the donga walls was dated to 0.32 ± 0.03 ka. This age provides an estimate of the end of the most recent period of hillslope stability, evidenced by the formation of a weak soil horizon. This age also provides a maximum limiting age for the current phase of incision, indicating that incision has occurred within the last few centuries. Unfortunately, Voordrag does not contain infill material suitable for dating, so a minimum limiting age on incision and donga formation cannot be constrained at this site. Historical aerial photographs taken in AD 1943 show the donga to have a similar areal extent to the present day donga, and

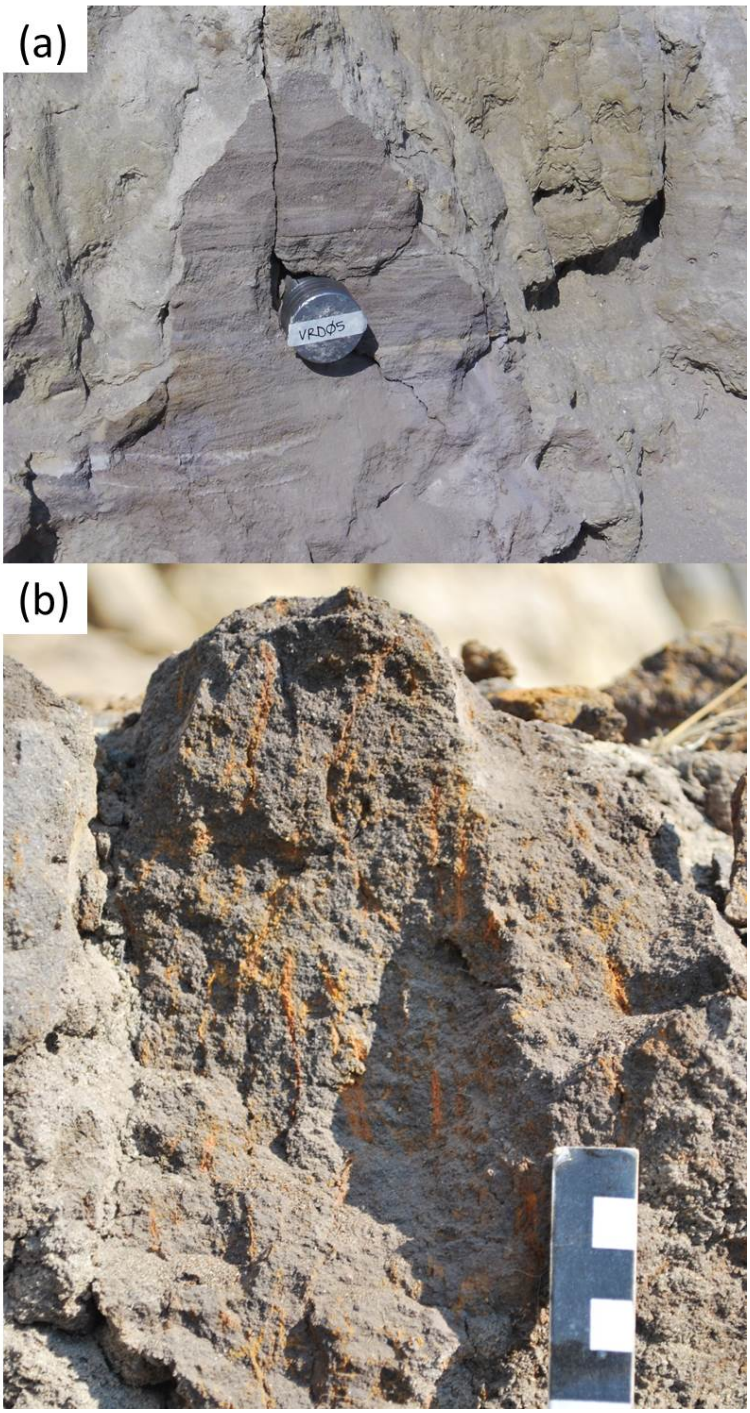

Figure 8.6: Typical sediments and palaeosols preserved at Voordrag, showing (a) the stratification of the colluvial unit, indicative of sediment emplacement by sheetwash, and (b) a dark-grey palaeosol with Fe-oxidised root traces.

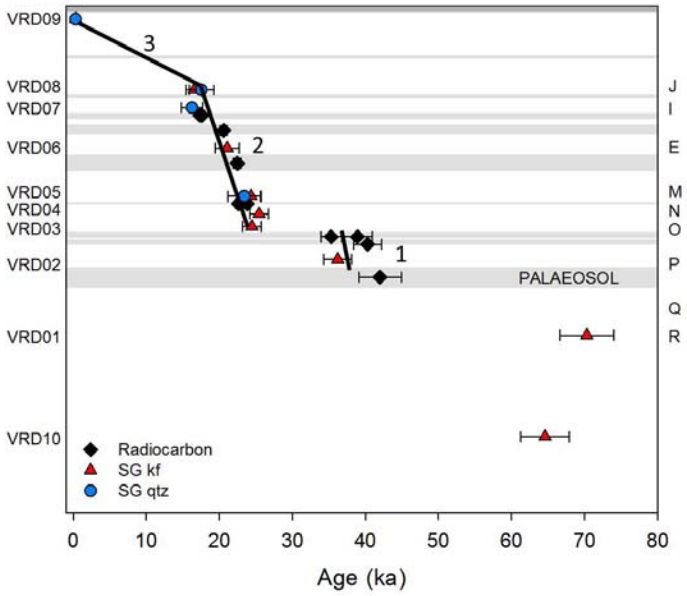

Figure 8.7: Three periods of rapid accumulation and pedogenesis identified during the Pleistocene and Holocene at Voordrag, between (1) 36.2 - 35.3 ka, (2) 24.4 - 17.5 ka and (3) 17.5 - 0.32 ka.

show channelised flow downslope, with a tributary connecting to the Mkuze River. Clearly, the donga pre-dates the earliest available aerial photographs. Collectively, the evidence constrains incision to sometime between AD 1700 and AD 1940.

Based on the landslide interpretation (Section 8.3.1), the colluvial depression likely had a restricted outlet for much of the Late Pleistocene and Holocene. Once sediment accumulated to the point where there was no remaining accommodation space, flow and sediment would have been more likely to have exited the basin. This may have initiated the breaching of the basin margin, leading to base level fall and triggering incision upslope. Thus incision may have been initiated by base level fall, although the timing appears to be broadly coincident with climate-driven incision elsewhere in South Africa (this will be discussed further in Chapter 9).

8.3.4 Conceptual model for the sequence and timing of subsequent pulses of deposition and pedogenesis

The sequence and timing of pulses of colluvial deposition and pedogenesis and subsequent donga formation are constrained using paired quartz-feldspar single grain luminescence ages, radiocarbon ages and aerial photographs and summarised in the schematic model shown in Figure 8.8. This model identifies nine key stages:

Stage 1: ~65 ka to 70 ka Approximately 65 ka to 70 ka a landslide occurred along a portion of the Ntumbane Hill, creating a bowl-shaped depression and rapidly emplacing the red unit and overlying light orange brown unit.

Stage 2: > 42 ka After emplacement of the orange brown unit, a period of non-deposition occurred, during which weathering and pedogenesis formed the P5 palaeosol unit.

Stage 3: >~36.2 ka to at least ~35.3 ka Colluvial deposition along the hillslope occurred from before ~36 ka. This was followed by a period of limited or non-deposition during which weathering and pedogenesis produced the P4 palaeosol unit. Pedogenesis was briefly interrupted by a minor phase of colluvial deposition, resulting in a split palaeosol layer (P4U and P4L).

Stage 4: >~25.4 ka to 22.6 ka Colluvial deposition along the hillslope occurred from before ~25.4 ka. This was followed by a period of non-deposition between ~23.8 ka and ~22.6 ka during which weathering and pedogenesis produced the P3 palaeosol unit.

Stage 5: >~23.4 ka to ~22.5 ka Colluvial deposition occurred from before ~23.4 ka. This was followed by a period of non-deposition ~22.5 ka during which weathering and pedogenesis produced the P2 palaeosol unit. The timing of the events in Stage 5 overlap with those of Stage 4, possibly implying short, rapid pulses of deposition and pedogenesis.

Stage 6: >~21.1 ka to ~20.6 ka Colluvial deposition occurred from before ~21.1 ka. This was followed by a period of limited or non-deposition between ~20.6 ka and ~17.3 ka during which weathering and pedogenesis produced the P1 palaeosol unit. Pedogenesis was briefly interrupted by a minor phase of colluvial deposition, resulting in a split palaeosol layer (P1U and P1L).

Stage 7: >~17.5 ka to <0.32 ka Colluvial deposition occurred from before ~17.5 ka, followed by a minor phase of pedogenesis and a second phase of colluvial deposition. The interpretation that two rapid pulses of deposition interrupted by an abrupt phase of pedogenesis which produced a weakly developed palaeosol layer (undated) is based on two consecutive luminescence ages within uncertainty of one another.

Stage 8: <~16.5 ka to ~0.32 ka The final phase of deposition began at some point after ~16.5 ka (likely during the late Pleistocene or early Holocene) and ended prior to ~0.32 ka, at which point weathering and pedogenesis formed the uppermost soil layer ~0.32 ka.

Stage 9: <~0.32 ka to present The current phase of incision began after ~0.32 ka and continues until the present. Aerial photographs from the region show that the Voordrag donga was established prior to AD 1940. No intervening phase of accumulation during donga formation has been preserved.

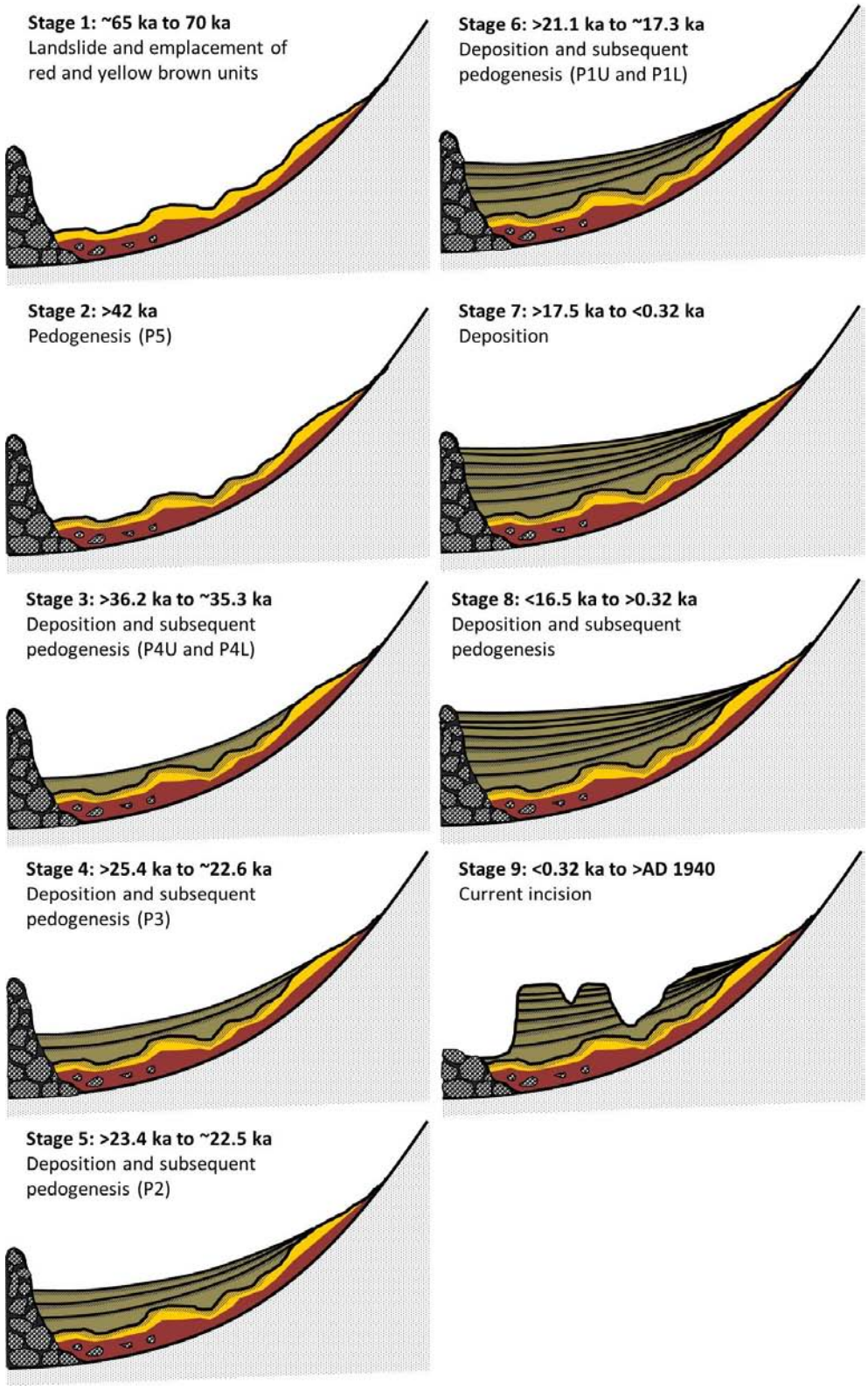

Figure 8.8: Conceptual model summarising the key phases of colluvial deposition and pedogenesis, and subsequent incision and donga formation, at the Voordrag site.

8.4 St Paul's, KwaZulu-Natal

As described in Section 2.2.3, the St Paul's site preserves one of the most complex records of successive cycles of colluviation, pedogenesis and donga incision within the Masotcheni Formation pedostratigraphy (see Table 2.3). Independent IRSL ages suggest the Masotcheni Formation sediments were deposited post-OIS 5e (i.e. over much of the last 110 ka) although prior to this study, deposition through the late Holocene had been largely inferred (Wintle et al., 1995a).

8.4.1 Timing of the initiation of sedimentation

Permian sandstone bedrock is exposed in the donga floor as a series of local knickpoints (Figure 8.9). A basal sediment sample was collected from sediments directly overlying this contact. Based on the single grain ages from this study, initial sedimentation began ~100 – 110 ka (Figure 8.10). Sediment accumulation emplaced the St Augustine's Alloformation and then the Dingaanstad Alloformation shortly thereafter (105 ± 7 ka).

8.4.2 Timing of subsequent phases of erosion, deposition and pedogenesis

Evidence of multiple erosional and subsequent deposition events are preserved as palaeodongas (i.e. cut-and-fill structures) within the donga side walls (Figure 8.11). Constraining the timing of these events proved difficult due to the poor bleaching of the post-IR IRSL signal (see Section 7.4). Following deposition of the Dingaanstad Alloformation, Wintle et al. (1995a)

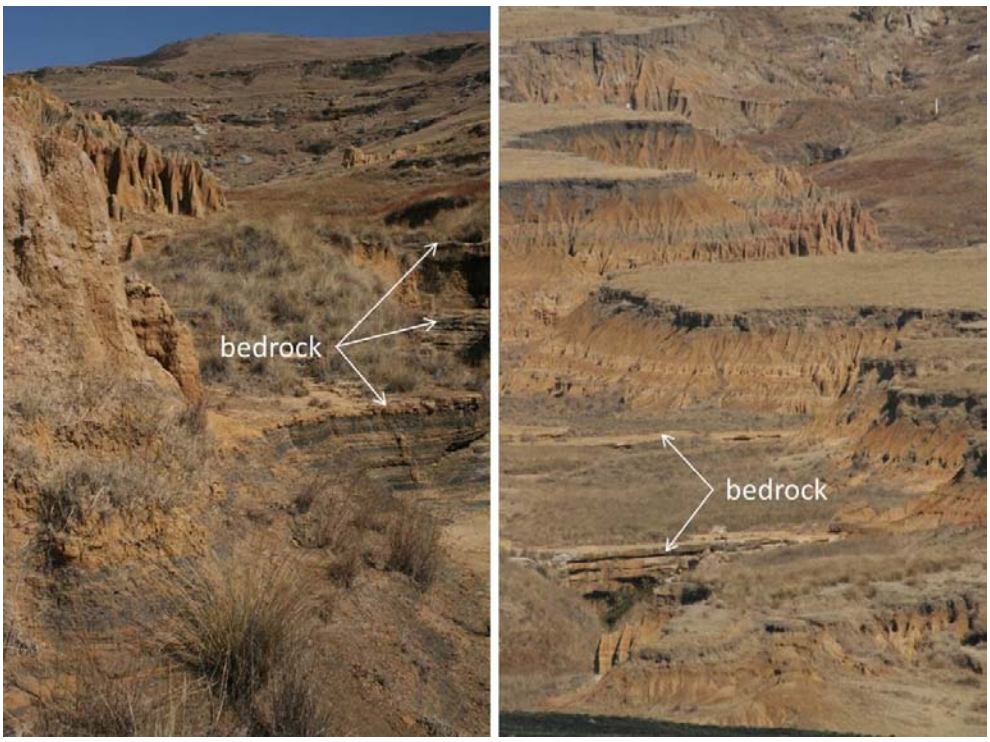

Figure 8.9: Permian sandstone bedrock exposed in the floor of the Dabekazi donga at St Paul's as a series of local knickpoints.

constrained the subsequent erosional event to later than 60 ka, with rapid deposition of the overlying Nqutu Alloformation then occurring between 52 – 56 ka (see Figure 8.10). In this study, an age of 50.7 ± 3.7 ka (215/STP04) from the base of the Nqutu Alloformation broadly supports this previous interpretation for the timing of deposition. In contrast, the other ages from the Nqutu Alloformation of 85.5 ± 5.6 ka (215/STP05) and 110 ± 7 ka (215/STP06) are substantially older than the age of sample 215/STP04 (Figure 8.10). This could mean that both ages (for samples 215/STP05 and 215/STP06) are overestimations. Alternatively, if only the age for sample 215/STP06 is an overestimation, then the erosional event preceding the deposition of the Nqutu Alloformation may have occurred as early as ~90 ka.

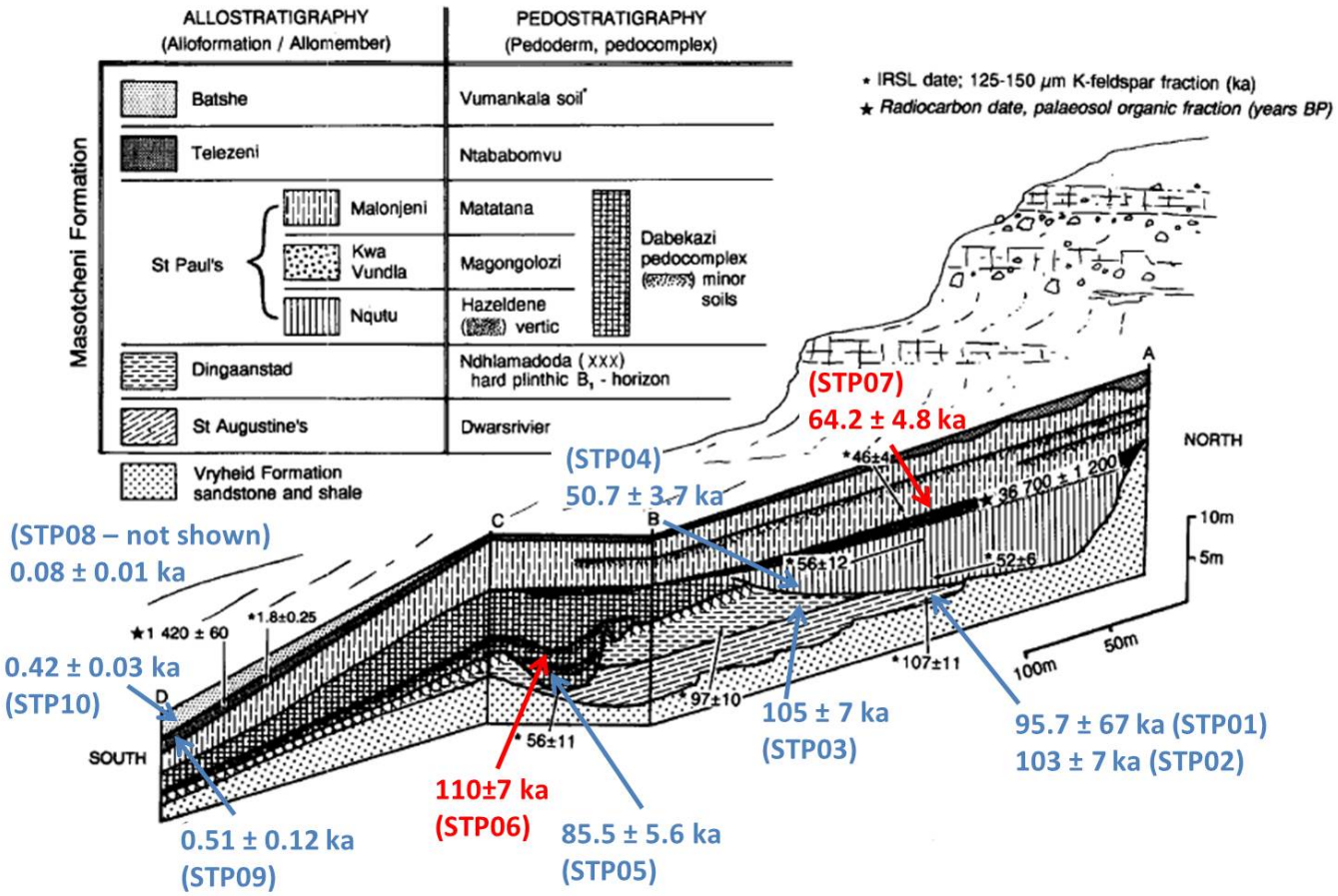

Figure 8.10: Schematic section showing the single grain ages for the St Paul's site. Ages shown in blue are in stratigraphic order, while the two ages shown in red are deemed to be overestimations based on their location within the stratigraphy. The diagram was reproduced from Botha and Fedoroff (1995) and the IRSL and ^{14}C ages shown in black are from the original IRSL dating studies presented in Wintle et al. (1993), Wintle et al. (1995a) and Wintle et al. (1995b).

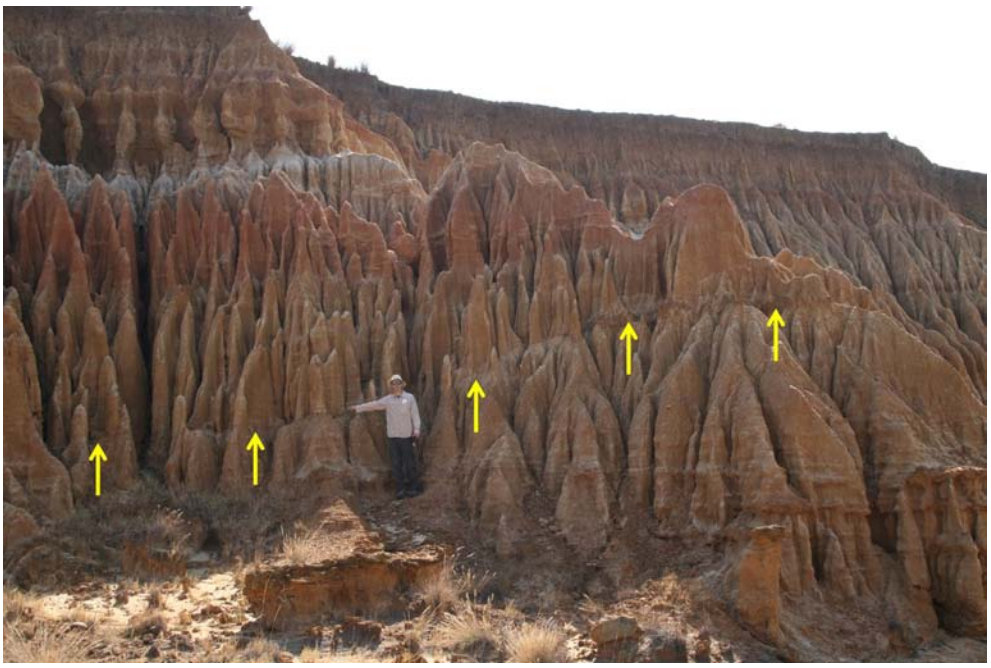

Figure 8.11: Example of one of the cut-and-fill structures preserved within the side walls of the Dabekazi donga. The figure is pointing to the basal contact of a palaeodonga that incised into older sediments before refilling, with arrows indicating the contact.

The upper limit of the Nqutu Alloformation is marked by the Hazeldene Pedoderm (Figure 8.10), which represents a period of stability during which pedogenesis occurred. The Hazeldene Pedoderm, and thus pedogenesis, was radiocarbon dated to 36700 ± 1200 years BP (36.7 ± 1.2 ka) by Botha and Fedoroff (1995). This was followed by another period of deposition ~45 ka, interrupted by minor periods of stability during which the Malonjeni Alloformation with its interspersed minor soil horizons was formed. The age of 64.2 ± 4.8 ka (215/STP07, Figure 8.10) derived in this study for the Malonjeni Alloformation is clearly an overestimation. The Malonjeni is overlain by the Telezeni Alloformation, dated at 0.51 ± 0.12 ka. This age is substantially younger than the 1.7 ± 0.2 ka age reported by Wintle et al. (1995a) for this unit. This offset is likely due to the fact that the younger

age from this study was measured using quartz OSL, which is more reliable for young ages because of the faster bleaching rate of the OSL signal (see Section 4.2).

8.4.3 Timing of the current phase of incision

The current donga has incised into a colluvial fan/drape on the slope of the Telezeni Hill. Directly north of the Dabekazi donga, a series of smaller gullies along the hillslope are visible, which appear to indicate the beginning stages of more widespread donga formation in this environment (Figure 8.12, inset A). Minor incision on the mid-slope eventually produces larger gullies which capture and direct water flow, increasing erosion and sediment movement downslope. This material is deposited as small fans on the foot of the slope. Continued incision deepens, widens and lengthens the gullies (Figure 8.12, inset B)), eventually forming a more extensive donga complex, through which large amounts of sediment can be moved downslope. To constrain the timing of donga formation, sample 215/STP10 was collected from a fan drape overlying the previous surface layer and 215/STP08 was collected from a recent infill deposit within the donga. These two samples constrain the timing of donga formation to between 0.42 ka and 0.08 ka. The oldest aerial photograph available for this site was taken in AD 1964 and shows the Dabekazi donga to have a similar areal extent to present, thus providing some support for the timing based on luminescence ages.

Overall, this site has preserved a complex record of net aggradation interspersed with periods of pedogenesis and periods of net erosion from ~105 ka to ~0.42 ka. Although multiple phases of erosion have been preserved within the sedimentary record, the current phase of incision after 0.42

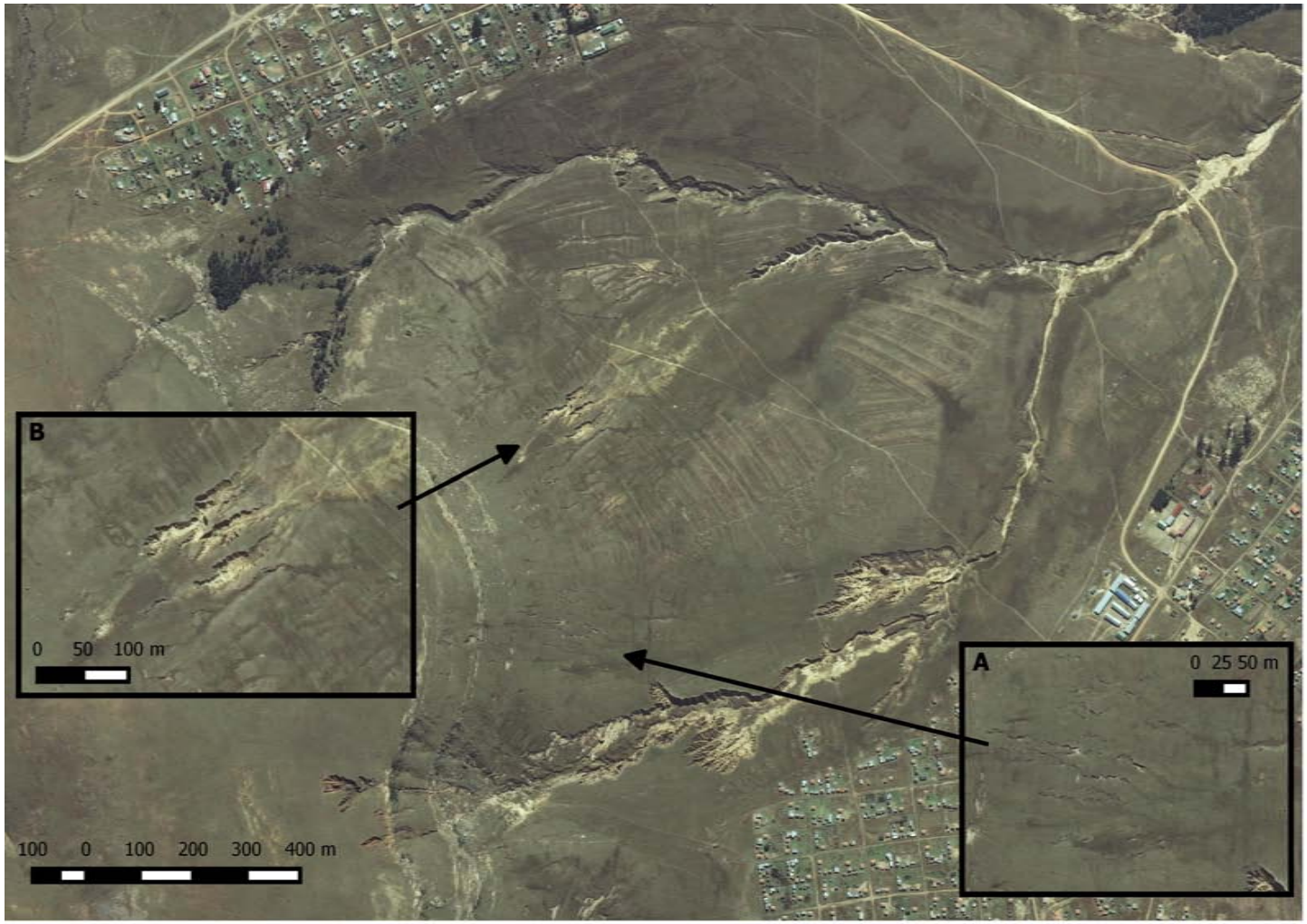

Figure 8.12: Evidence of the progression of donga incision visible on the Telezeni hillside. Minor incision creates long, thin discontinuous gullies (inset A) which eventually expand and join to form small, individual dongas (inset B). Continued incision will eventually result in extensive donga systems such as Dabekazi.

ka represents net erosion of a magnitude that has not occurred in the late Quaternary history of the site. Previous phases of erosion, preserved as palaeodongas, incised into older sediment but did not erode through the entire succession into bedrock. This current phase of net erosion is characterised by deep incision down to and into bedrock, donga formation, and apparent valley sediment evacuation on a scale that has not occurred since prior to the last interglacial.

8.4.4 Conceptual model for the sequence and timing of deposition, erosion and pedogenesis at St Paul's

The sequence and timing of pulses of colluvial deposition, pedogenesis and erosion are constrained using paired quartz-feldspar single grain luminescence ages and aerial photographs, and summarised in the schematic model shown in Figure 8.13. This model identifies eight key stages:

Stage 1: ~105 ka to <85.5 ka Deposition of the sediments comprising the St Augustine's Alloformation and the overlying Dingaanstad Alloformation occurred from ~105 ka until some time before ~85.5 ka.

Stage 2: > ~85.5 ka A phase of incision cut into the sediments of the St Augustine's Alloformation but not into bedrock, at some point before 85.5 ka.

Stage 3: ~85.5 ka to ~36.6 ka Deposition of the Nqutu Alloformation sediments occurred from ~85.5 ka until <~36.6 ka. Deposition was interrupted by at least two phases of pedogenesis, and followed by a major phase of pedogenesis ~36.6 ka, resulting in the formation of the Hazeldene

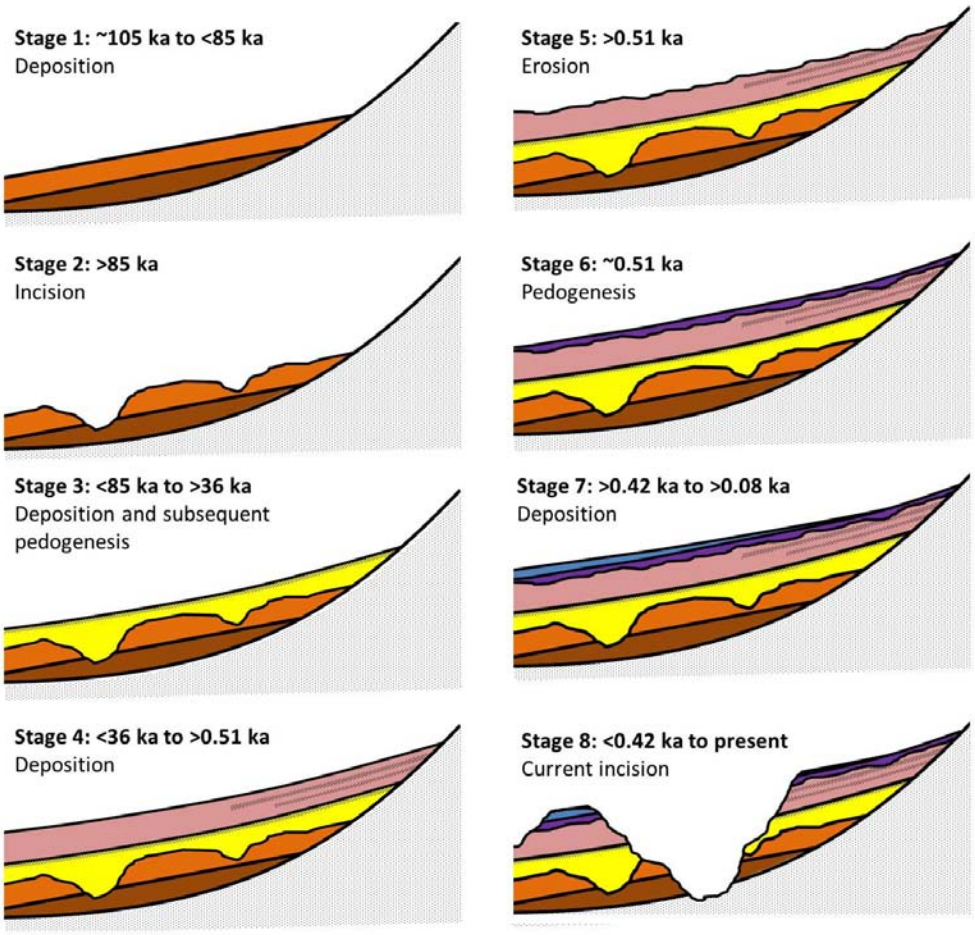

Figure 8.13: Conceptual model summarising the key phases of colluvial deposition, pedogenesis and erosion at the St Paul's site.

pedoderm.

Stage 4: <∼36 ka to >∼0.51 ka Deposition of the Malonjeni Alloformation sediments began after ∼36 ka and may have continued until as recently as 0.51 ka. Deposition was interrupted by multiple phases of pedogenesis.

Stage 5: >∼0.51 ka Erosive truncation of the Malonjeni Alloformation, prior to ∼0.51 ka.

Stage 6: ∼0.51 ka A phase of pedogenesis ∼0.51 ka, resulted in the formation of the Telezeni Alloformation.

Stage 7: >∼0.42 ka to >∼0.08 ka Deposition ∼0.42 ka resulted in the emplacement of the Batshe Alloformation sediments.

Stage 8: <∼0.42 ka to present The current phase of incision began after 0.42 ka and continued until present, and was interrupted by minor deposition within the donga ∼0.08 ka. The current phase of incision has incised through the entire sedimentary succession and into bedrock.

8.5 Goedgedacht, Mpumalanga

The Goedgedacht donga complex is located along an unnamed tributary of the lower Klip River. Whilst geomorphological (e.g. Tooth et al., 2002, 2007) and optical dating studies (e.g. Keen-Zebert et al., 2013; Rodnight et al., 2006, 2005) have been undertaken on the upper Klip River, no prior work exists along the lower Klip River or within the Goedgedacht donga system itself. As described in Section 2.3.4, the stratigraphy at Goedgedacht is relatively simple, with underlying bedrock exposed at several locations within the dongas (Figures 8.14 and 8.15).

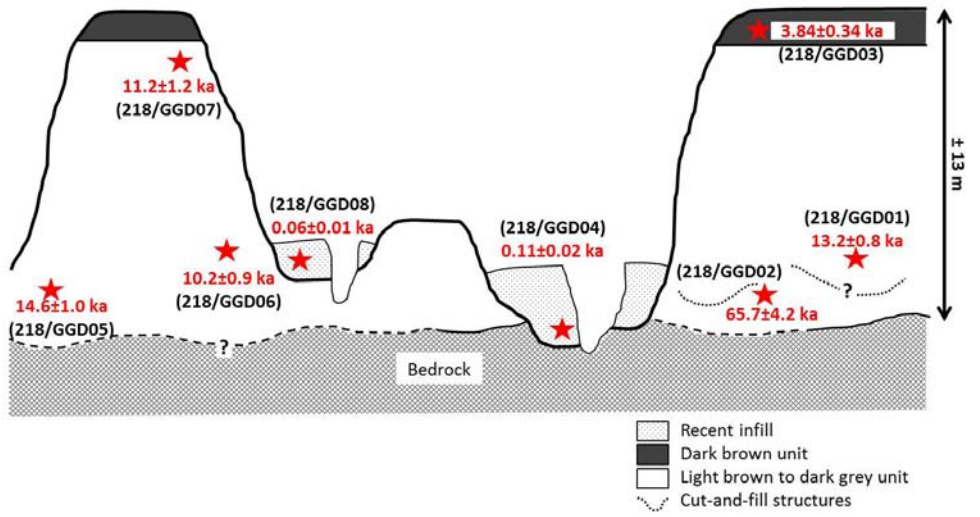

Figure 8.14: Schematic section of Goedgedacht showing the final single grain ages (reproduced from Chapter 7).

8.5.1 Overview of the development of Goedgedacht

Field observation identified an undulating, erosive contact between heavily weathered shale bedrock and the overlying light brown (10YR 5/3) to dark grey (10YR 4/1) unit, visible across large sections of the donga (Figure 8.15). The paired single grain chronology (Figure 8.14, also see Section 7.7) constrains the timing of the initiation of sedimentation to ~65 ka. This implies an earlier erosional event, prior to 65 ka, had stripped any pre-existing sediment cover from the landscape. Sediment accumulation starting at ~65 ka was followed by one or more erosional events, which led to partial stripping of the sediment. Indeed, numerous cut-and-fill sequences were observed within the light brown to dark grey unit, particularly in the lower sections within 1 – 2 m of bedrock (Figure 8.16(a)). The single grain chronology shows that above this basal cut-and-fill structure the upper parts of the ~12 m thick, light brown to dark grey unit were deposited fairly rapidly between ~15 ka and ~10 ka (Figure 8.14).

Figure 8.15: The basic stratigraphy preserved at the Goedgedacht donga site. The dark grey unit in the foreground is heavily weathered shale bedrock, which is overlain by the light brown to dark grey unit. The view is looking downslope towards the central sample collection site.

The uppermost dark brown (10YR 4/3) unit has a sharp, erosional lower contact and a weakly-developed soil structure with blocky peds and disseminated roots throughout the top 20 cm, implying a period of stability long enough for pedogenesis to occur. This upper unit provides a minimum limiting age for the final phase of deposition at ~3.8 ka (Figure 8.14) and a maximum limiting age for the current phase of incision. Incision began sometime after 3.8 ka, but has been interrupted by a minor phase of partial infilling, as reflected by an age of 0.11 – 0.06 ka for sedimentary infill (Figure 8.16(b)). As with the other sites, the oldest aerial photographs (from AD 1956) show the donga complex to have a similar areal extent to present, thereby providing another minimum limiting age on donga formation. As is the case at St Paul's and Moopetsi, while previous phases of incision at

Goedgedacht cut only into older sediments, the current phase of incision has incised down to and into bedrock (see Figure 8.16(b)).

8.5.2 Geological control on deposition

Based on the luminescence ages, the light brown to dark grey unit was deposited by two main depositional events that were separated by a period of incision. Besides the local cut-and-fill structures, the most obvious distinguishing feature of this unit is the colouring, with broad bands of light brown grading into dark grey and back again (see Figure 8.15). Close examination reveals that the unit is dominated by horizontally laminated fine to medium sand interspersed with gravel lenses (Figure 8.17) and these grain size variations and subtle variations in organic content could account for the colour banding. The mechanism driving deposition at this site is of interest, as clearly it resulted in accumulation of a large sedimentary package in a relatively short interval of time (i.e. ~11.3 m in ~3.4 ka, giving a rate of deposition of 3.325 mm/year).

In their work on South African rivers, Keen-Zebert et al. (2013) showed that variation in lithological resistance along a river's course is a key control on the degree of valley confinement, incision and local base levels. In turn, these factors can influence the formation and preservation of alluvial sedimentary archives. When local base level is stable, vertical aggradation and lateral migration in reaches upstream result in the construction and reworking of alluvial archives. In contrast, when local base level is lowered, incision occurs upstream. This results in erosion of part of the archive but may also preserve other parts of the floodplains (terraces) adjacent to the incised channel. For tributary channels, the trunk river is effectively the

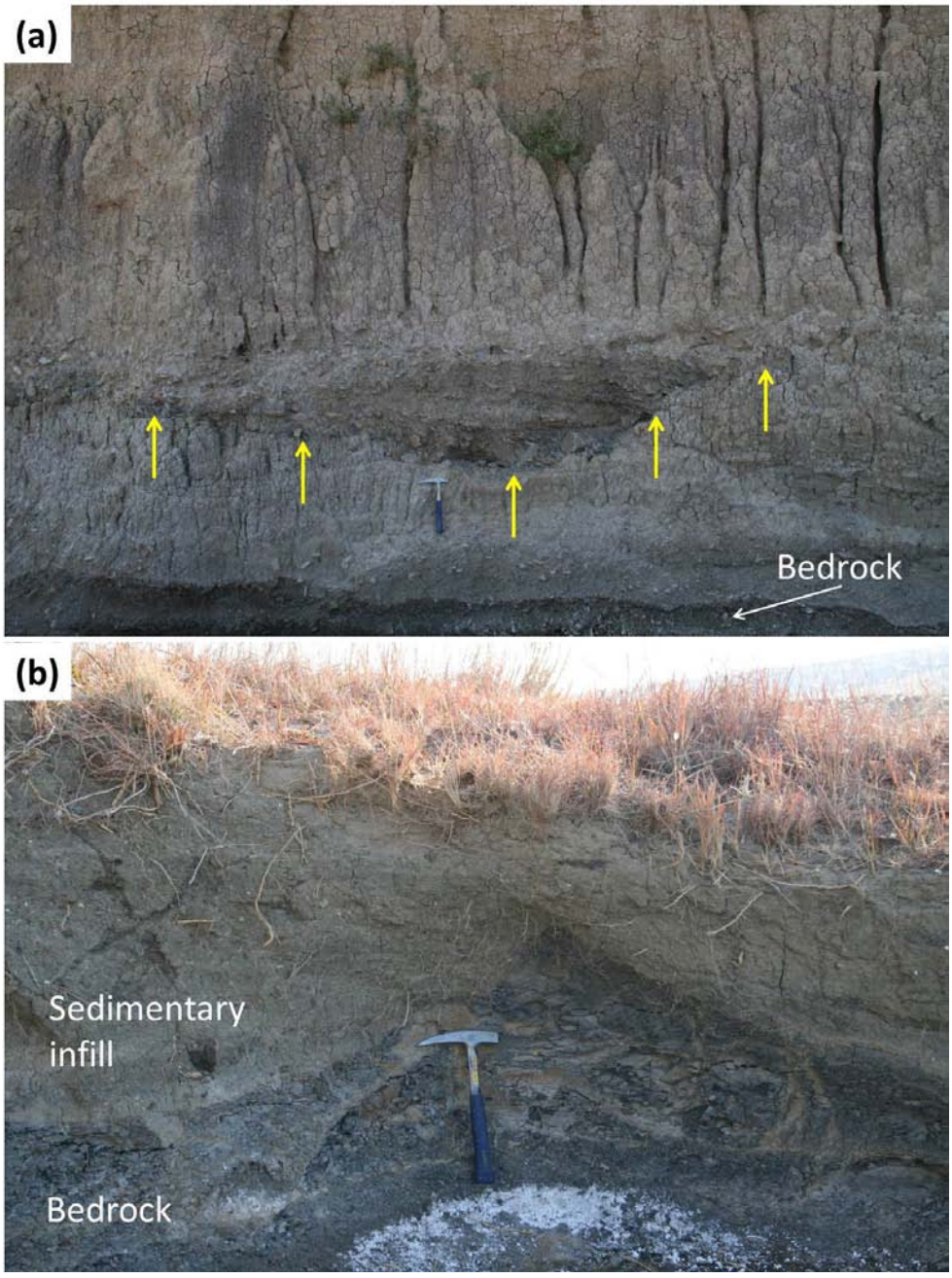

Figure 8.16: Cut and fill structures preserved within the sedimentary record at Goedgedacht. Scours are observed into a) older sediments (basal contact indicated by yellow arrows) and b) heavily weathered bedrock (contact above the geopick).

Figure 8.17: cm-scale horizontal laminations observed in the light brown to dark grey unit at Goedgedacht.

local base level, so aggradation or incision can result in base level rise or fall along tributaries respectively. Thus, lowering of base level along an incising Klip River potentially could lead to substantial incision along its tributaries, such as Goedgedacht. Aerial surveys and ground-level investigations in fact reveal deep incision along the Klip River (Figure 8.18(a)) suggesting a history of base level fall. Deep incision along sediment-filled tributary valleys such as Goedgedacht potentially would have provided a large amount of sediment. As incision progressed upstream through headward migration, this would lead to deposition downstream. Once the headcut reached the lower-order tributaries, however, and the sediment supply began to be exhausted, the system reverted back to net erosion. At this site, therefore falling base level along the Klip River could have driven alternating phases of incision and deposition along the donga system (Figure 8.18 (b)), perhaps

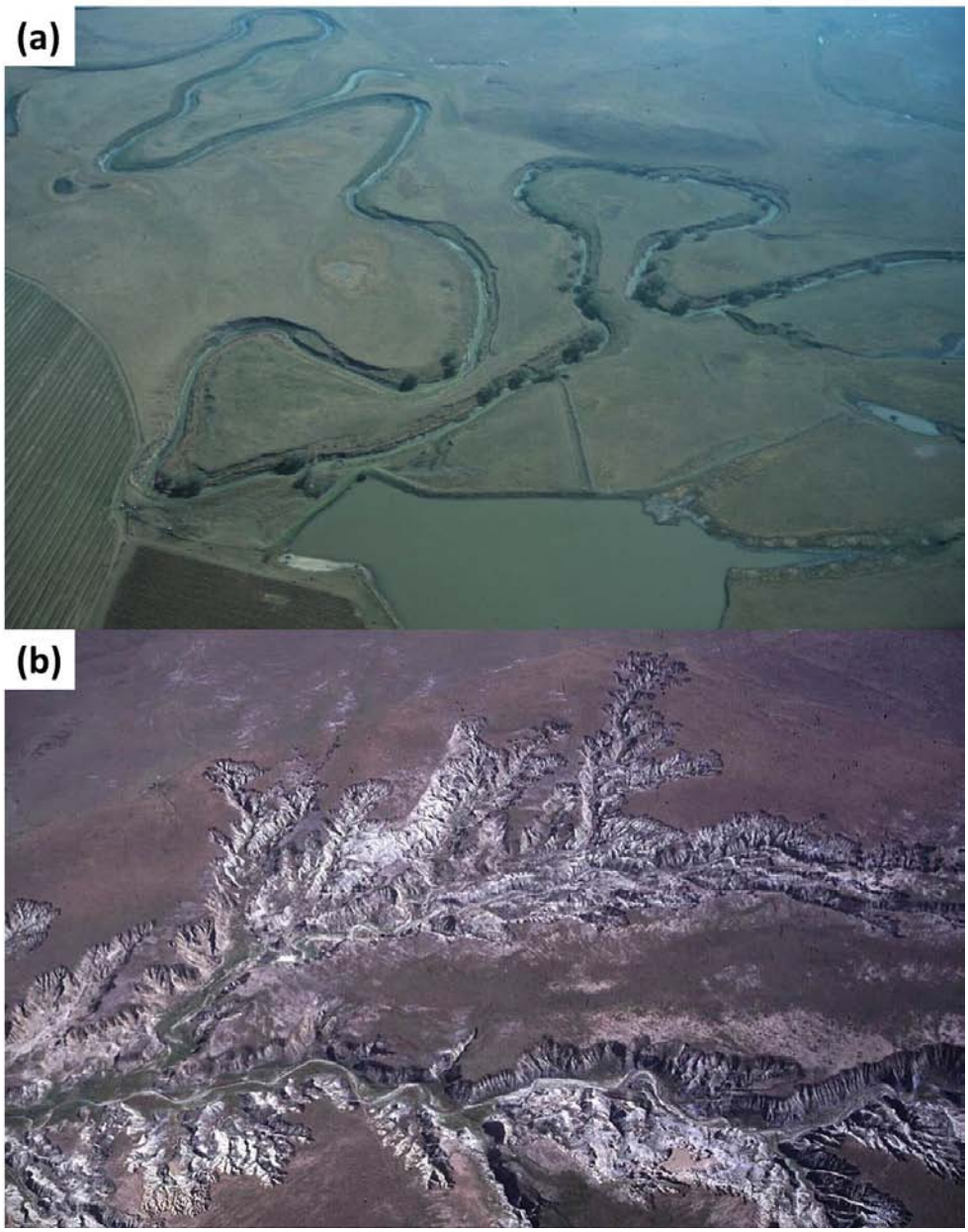

Figure 8.18: a) View of the lower Klip River, showing deep (5 – 6 m) incision and headward erosion along its sinuous course (view looking downvalley). b) Incision and base level lowering on the Klip River would have led incision and headward erosion along tributaries, leading to the formation of Goedgedacht and other donga complexes.

largely or partially independent of regional climate trends.

8.5.3 Conceptual model for the sequence and timing of deposition, erosion and pedogenesis at Goedgedacht

The sequence and timing of pulses of colluvial deposition and pedogenesis and subsequent donga formation are constrained using paired quartz-feldspar single grain luminescence ages and aerial photographs and summarised in the schematic model shown in Figure 8.19. This model identifies four key stages:

Stage 1: from ~65 ka to >14 ka Deposition of the light brown to dark grey unit onto eroded bedrock began at least ~65 ka and continued for an unknown amount of time prior to ~14 ka.

Stage 2: <~65 ka to >~14 ka A major phase of erosion incised almost down to bedrock at some point between ~65 ka and ~14 ka. This was followed by continued deposition of the light brown to dark grey unit from ~14 ka until prior to 3.8 ka.

Stage 3: <~3.8 ka Erosional truncation of the light brown to dark grey unit was followed by deposition of the final sedimentary unit ~3.8 ka, after which weathering and pedogenesis lead to the formation of the dark brown unit.

Stage 4: <~3.8 ka to present The current phase of incision began after ~3.8 ka and continued until the present, but was interrupted by partial aggradation between ~0.11 ka and ~0.06 ka.

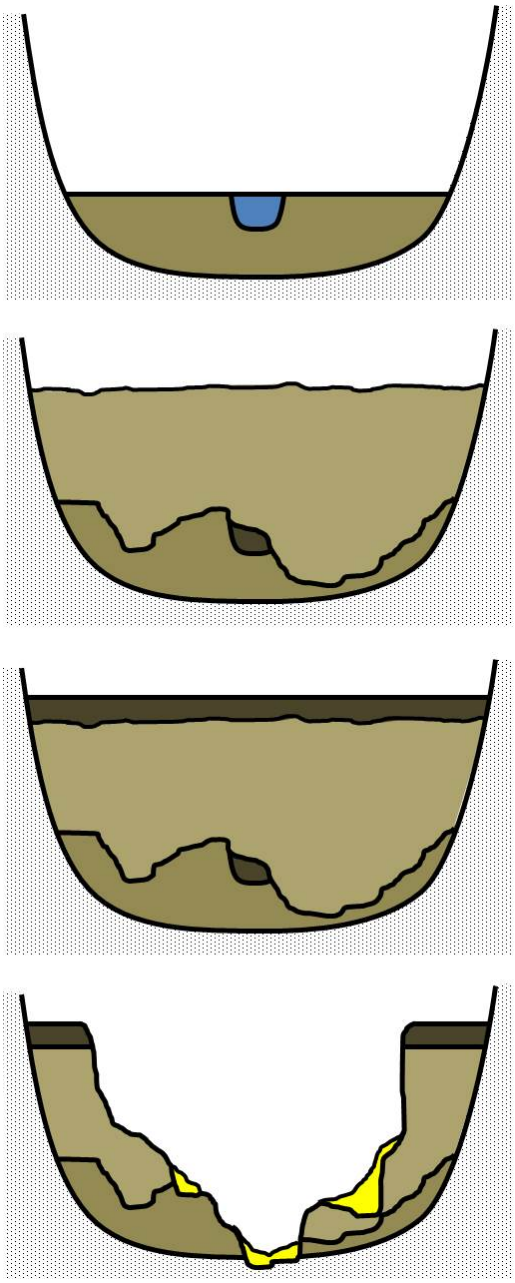

Stage 1: ~65 ka to >14 ka
Deposition onto eroded bedrock

Stage 2: <65 ka to ~3.8 ka
Erosion of stage 1 sediments, locally close to bedrock, followed by deposition <14 ka but >3.8 ka

Stage 3: >3.8 ka
Erosional truncation of stage 2 sediments, followed by deposition ~3.8 ka and then weathering and pedogenesis

Stage 4: <3.8 ka to present
Incision, interrupted by minor partial aggradation between 0.11 ka and 0.06 ka

Figure 8.19: Conceptual model summarising the key phases of deposition, pedogenesis and erosion at the Goedgedacht site.

8.6 Summary

In this chapter, the geomorphologic development of each of the study sites was outlined. The sedimentary record preserved at the Moopetsi tributary site shows net aggradation interspersed with periods of pedogenesis over the last ~153 ka (Section 8.2). The record at Voordrag is near-continuous over the last ~70 ka and shows net aggradation, with pulses of colluvial deposition interspersed with periods of pedogenesis (Section 8.3). Whilst the record preserved at St Paul's shows net aggradation, it also reveals a more complex series of erosional, depositional and pedogenetic phases covering the last ~105 ka (Section 8.4). The record at Goedgedacht also preserves net aggradation for the last ~66 ka (Section 8.5). Varied geomorphic controls on the initiation of sedimentation at each site were outlined. It was also noted that the current phase of erosion is characterised by deep incision and extensive donga formation. Although the drivers of incision may have varied at each site, this scale and extent of erosion has not occurred since prior to the last interglacial. The following chapter will attempt to place the geomorphic development of these sites into the larger South African context.

Chapter 9

Timing and controls of late Quaternary landscape dynamics

9.1 Introduction

In Chapter 8, the geomorphological development of the individual sites was discussed within the constraints provided by the single grain chronologies developed in Chapters 4 to 7. This chapter will undertake an inter-site comparison (Section 9.2), once again focusing on the timing of the (i) initiation of sedimentation, (ii) intervening phases of deposition, pedogenesis and erosion, and (iii) the cessation of sedimentation and initiation of the current phase of incision. This will be followed by a discussion of the findings against the backdrop of similar research undertaken elsewhere within South Africa (Sections 9.3, 9.4 and 9.5). Due to the relatively large uncertainties on some of the ages and following the approach taken by many

other researchers (e.g. Thomas and Shaw, 2002), the central age will be used when discussing the timing of events.

9.2 Inter-site comparison

9.2.1 Timing of initiation of sedimentation

An inter-site comparison shows that, at least across the four study sites, deposition did not begin simultaneously (Figure 9.1). For northern KwaZulu-Natal, the prevailing theory is that hillslopes were stripped of their colluvial mantle during the last interglacial (OIS 5e), and subsequent deposition began during OIS 5d, ~100 ka (Clarke et al., 2003). The ages for basal sediments from the Voordrag, St Paul's and Goedgedacht sites broadly support this hypothesis, with the timing of the onset of deposition on stripped bedrock occurring at ~70 ka, ~105 ka and ~66 ka respectively (Figure 9.1). In contrast, at the Moopetsi tributary site, the ages for the basal LGS sediments establish the onset of deposition ~153 ka and provide evidence for deposition throughout the last interglacial (Figure 9.1). Overall, the evidence lends support to an hypothesis that whilst many hillslopes were being stripped during the last interglacial, sediments were being deposited and preserved within at least some river valleys.

9.2.2 Timing of intervening periods of erosion, deposition and pedogenesis

To constrain the timing of subsequent periods of incision, deposition and pedogenesis, preserved cut-and-fill structures were targeted for dating at St

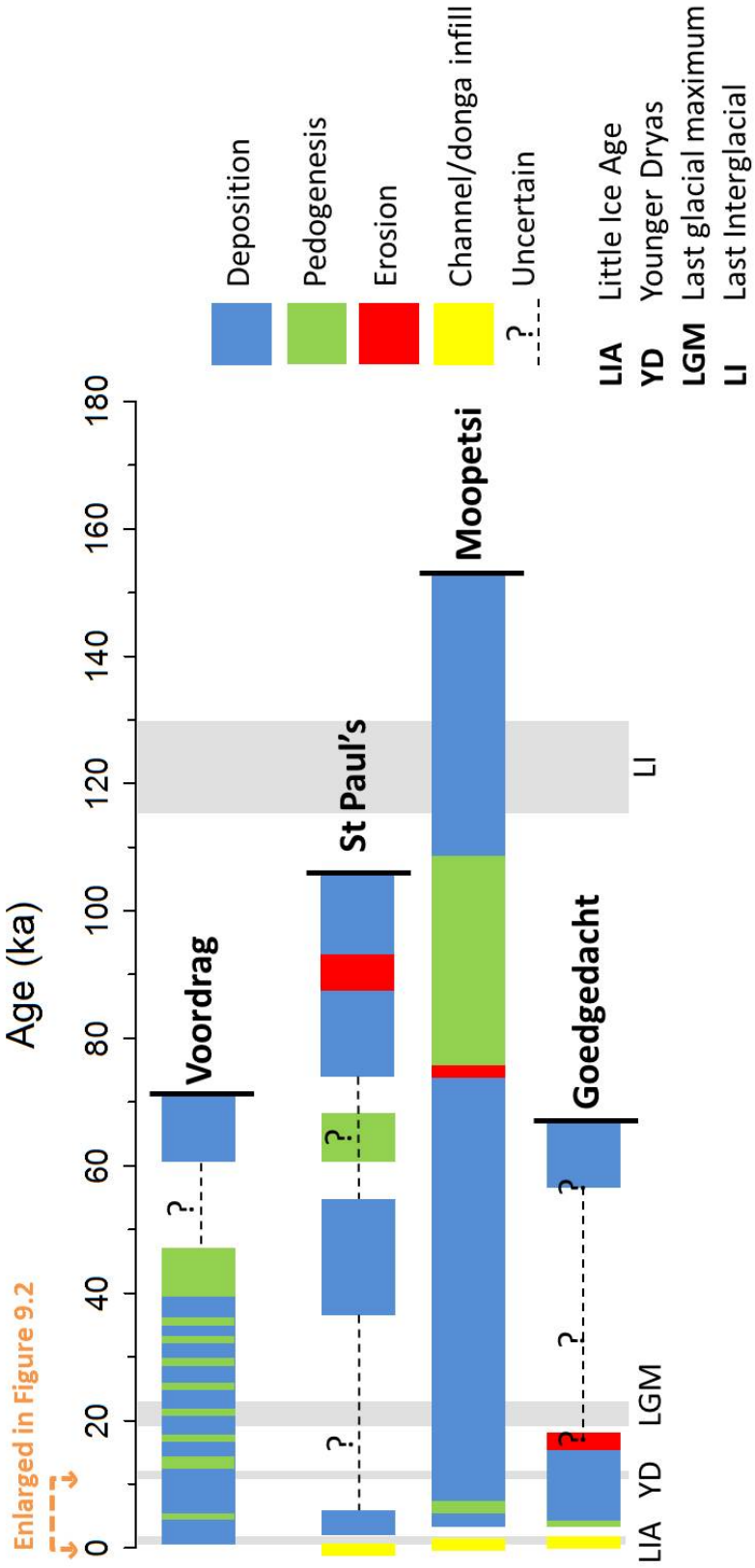

Figure 9.1: Schematic diagram showing the general timing of deposition, pedogenesis and incision during the Late Pleistocene and Holocene at all four study sites. The initiation of deposition at each site is demarcated by a vertical black line, and periods where processes are uncertain due to limitations in the dating and sediment record are marked by a dashed line and question mark.

Paul's (Section 2.3.3) and Goedgedacht (Section 2.3.4), and layer boundaries were targeted at Voordrag (Section 2.3.2) and Moopetsi (Section 2.3.1). Constraining these events proved challenging due to the nature of the sedimentary records. For example, at Goedgedacht the missing portion of the sedimentary record resulting from cut-and-fills near the base of the light brown to dark grey unit spans ~51 ka (Figure 9.1). Within that timespan, extensive deposition and erosion may have occurred but reworking has meant that there is no preserved record, with only a minimum limiting age for one of the more recent erosive episodes (~14.6 ka) being provided by the age for the overlying sediments. In addition, the preserved record of deposition at St Paul's is more complex than originally thought, with erosion having led to apparent loss of parts of the record. Resolving the full history of erosion, deposition and pedogenesis at this site will require more extensive sampling to determine the timing of events than was achievable during the scope of this study.

The Moopetsi tributary preserves the longest record of aggradation, pedogenesis and erosion throughout the late Pleistocene and the Holocene (see Figure 9.1 and Section 8.2). The Voordrag terrestrial record preserves a shorter but largely complete record showing pulses of colluvial deposition interspersed with periods of pedogenesis throughout the late Pleistocene and Holocene (see Figure 9.1 and Section 8.3). Goedgedacht preserves a partially-complete record of major aggradation, at least one intervening phase of incision, and a minor phase of pedogenesis (see Figure 9.1 and Section 8.5). As documented in Section 8.4 and noted above, the terrestrial record preserved at St Paul's is by far the most complex, with evidence for multiple phases of erosion, deposition and pedogenesis, several of which

remain either poorly constrained or completely unconstrained (see Figure 9.1 and Section 8.4). It is noteworthy that at the three sites where previous phases of incision occurred during the late Pleistocene and/or the earlier part of the Holocene, incision did not occur down to bedrock.

9.2.3 Timing of the current phase of incision

The cessation of the most recent phase of deposition, at these four sites, has potentially occurred over two broad time periods (Figure 9.2). Deposition ceased at the Moopetsi tributary site ~3.45 ka and at Goedgedacht ~3.84 ka. In contrast, colluvial deposition along hillslopes in KwaZulu-Natal ended more recently, ~0.32 ka at Voordrag and ~0.42 ka at St Paul's.

At St Paul's, Moopetsi and Goedgedacht incision was interrupted by a recent phase of minor aggradation (Figure 9.2; also see Figures 8.2 and 8.14). At all three sites, infill deposits have been dated (yellow boxes, Figure 9.2) and provide minimum limiting ages for donga formation of 0.08 ± 0.01 ka at St Paul's, 0.20 ± 0.02 ka at Moopetsi and from 0.11 ± 0.02 ka to 0.06 ± 0.01 ka at Goedgedacht. No infill sediments were available for dating at Voordrag. At all four study sites, aerial photographs taken between AD 1943 and AD 1964 show all the donga systems to have a similar areal extent to present, providing additional minimum limiting ages for donga formation that lend broad support to the available luminescence ages. At all study sites, the current phase of incision has incised down to and into bedrock, either locally or more extensively.

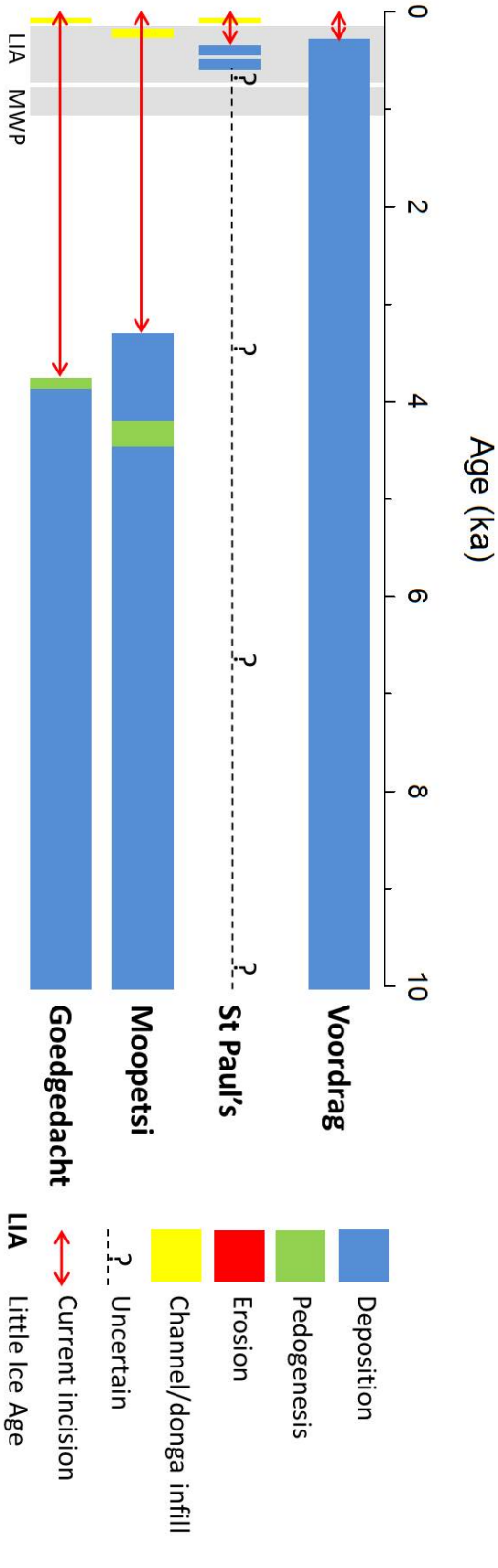

Figure 9.2: Schematic diagram showing the general timing of deposition, pedogenesis and incision over the last 10 ka at all four sites.

9.3 Controls on the initiation of deposition

Geoproxies are a potential source of palaeoenvironmental data in the dominantly arid and semi-arid regions of South Africa, where traditional organic-based proxy records are scarce (see Section 1.1). They can be used to extract palaeoenvironmental data because their sedimentology, morphology and spatial distributions were likely controlled by past environmental changes (Lyons et al., 2014; Thomas and Burrough, 2012). Given the nature of landforming processes and the uncertainties associated with dating techniques, geoproxies are typically of lower resolution than other types of palaeoclimate proxy records (e.g. speleothems, marine cores), but broad correlations nonetheless can be drawn between them. The main records used for comparison with the derived single grain luminescence chronologies in this study are: (i) the EPICA Dome C temperature record (Jouzel et al., 2007); (ii) the Lake Tswaing (previously the Pretoria saltpan) rainfall record (Partridge et al., 1997); (iii) the marine sediment core of Ziegler et al. (2013); (iv) the stable isotope speleothem records from Makapansgat (Holmgren et al., 2003); and (v) the temperature and humidity indices from Wonderkrater (Truc et al., 2013). These records are shown in Figures 9.3 and 9.4, whilst their geographic locations are shown in Figure 2.1.

Establishing the controls on the initiation of deposition across the interior of South Africa is a complex undertaking, because the overriding geomorphological controls are different between the four sites investigated in this study. Commonly assumed climatic and vegetative controls on deposition (e.g. rainfall and vegetation cover) can be conditioned or overprinted by non-climatic, 'random' controls (e.g. landslides). For

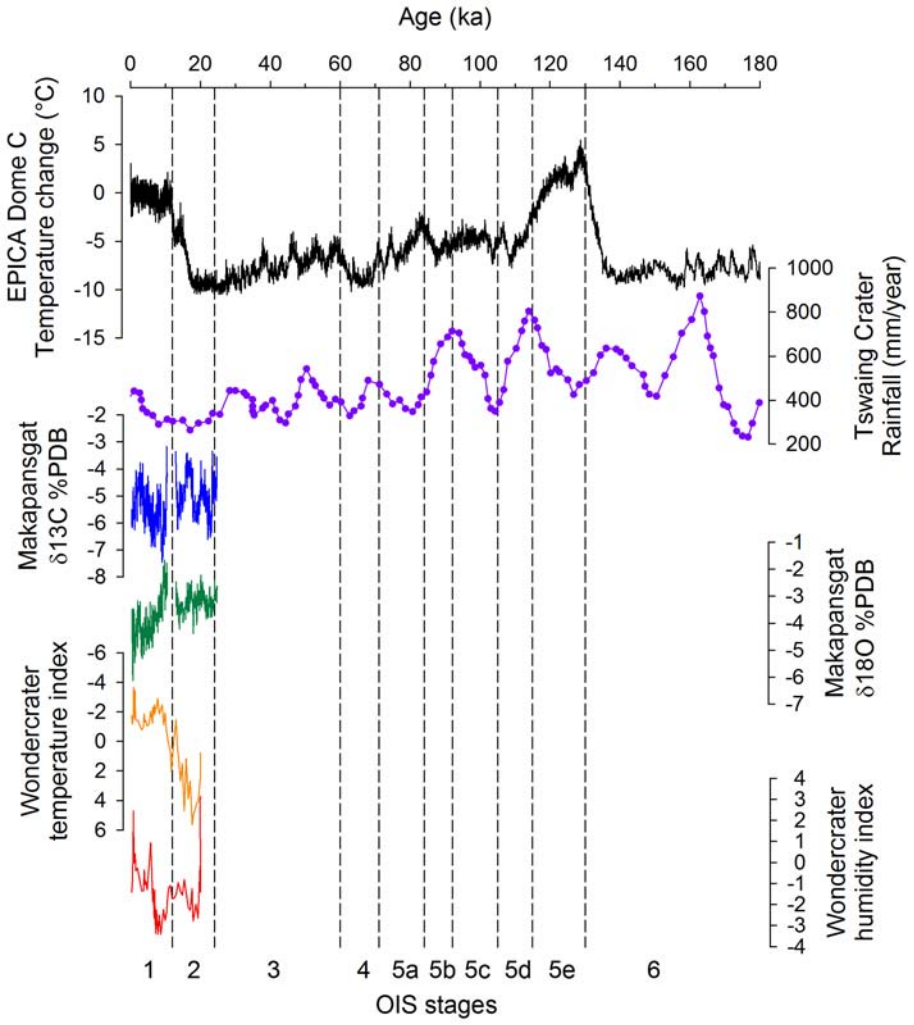

Figure 9.3: Comparison of some available proxy records, illustrating the variable time spans covered. The EPICA Dome C temperature record spans ~800 ka (Jouzel et al., 2007), the Lake Tswaing record ~200 ka (Partridge et al., 1997), the speleothem record from Makapansgat ~25 ka (Holmgren et al., 2003) and the pollen record from Wonderkrater ~20 ka (Truc et al., 2013).

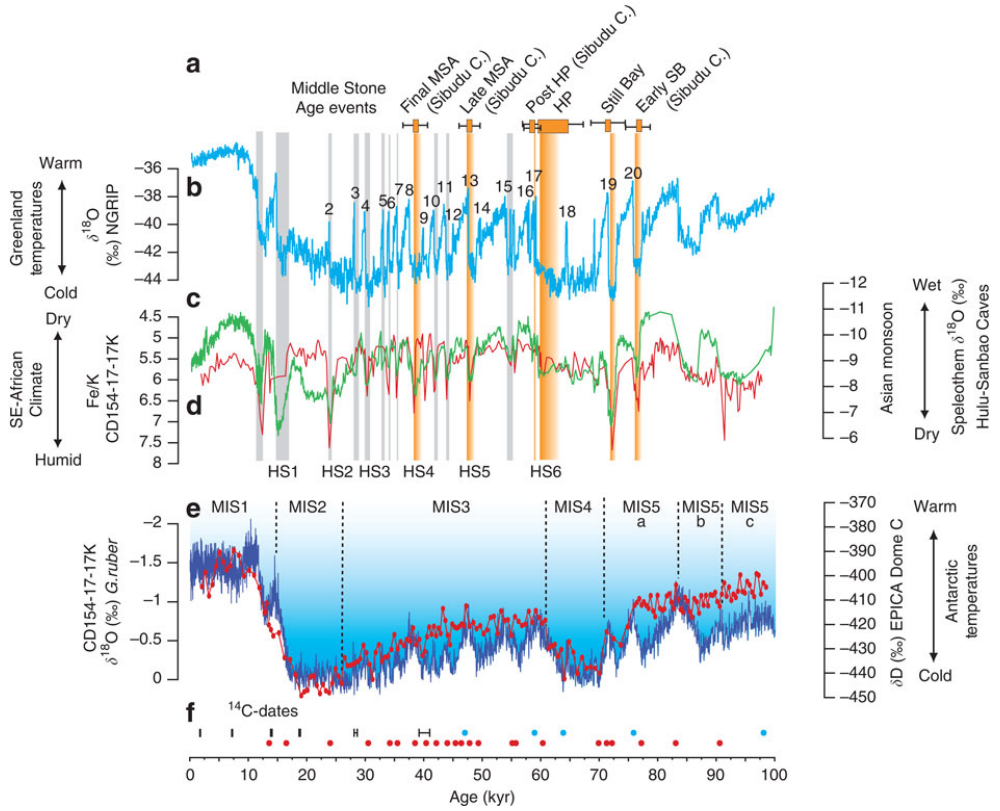

Figure 9.4: The comparative proxy record from Ziegler et al. (2013) (their Figure 4) showing (a) ages of southeast African Middle Stone Age events; (b) the δ^{18}O record from Greenland ice core NGRIP; (c) the δ^{18}O splice from Chinese speleothems (green); (d) Fe/K of marine core CD154-17-17K (red); (e) planktonic foraminiferal (*G. ruber*) δ^{18}O record from CD154-17-17K (red) with EPICA Dome C deuterium record (blue) and (f) age control points for CD154-17-17K including radiocarbon dates (black), tuning of the foraminiferal record.

example, generation and preservation of the Voordrag terrestrial record may not have occurred without the proposed landslide event (see Section 8.3.1) that created the bowl-shaped depression in which the sediments accumulated.

Hillslopes in northern and central KwaZulu-Natal are commonly mantled by colluvial sediments from the Masotcheni Formation. There have been extensive investigations into the stratigraphic subdivisions based on the intercalated palaeosols and colluvial layers, with the aim of relating intervening periods of colluvial deposition, pedogenesis and erosion to late Quaternary palaeoclimate records (Botha and Fedoroff, 1995; Botha et al., 1992; Botha, 1996; Botha et al., 1994; Clarke et al., 2003). More recently, the landscape processes and drivers leading to net aggradation of the Masotcheni sediments during the late Quaternary have been investigated by Temme et al. (2008).

The regional expression of the Masotcheni Formation across much of KwaZulu-Natal has led to the dating of individual layers by stratigraphic correlation across several sites. Although the previously reported IRSL luminescence ages (Botha and Fedoroff, 1995; Wintle et al., 1995a,b) were only re-analysed at the St Paul's site, the single grain luminescence ages from this study were in broad agreement with the previous basal ages. The initiation of sedimentation at St Paul's was dated to ~105 ka in this study compared to ~107 ka by Wintle et al. (1995a). This lowermost unit (the St Augustine's Alloformation) was dated at two other sites and produced ages of ~96 ka at the Nqutu donga and ~135 ka at the Masotcheni donga sites (Botha, 1996). Furthermore, ages from this study from the overlying Dingaanstad Alloformation (see Figure 8.10) are within uncertainty of those

from the underlying unit, implying rapid accumulation of these two basal units. This constraint on the timing of initiation of deposition led to the hypothesis of Clarke et al. (2003) that hillslopes were largely stripped of their colluvial mantle during the last interglacial (OIS 5e, 130 – 115 ka) and that subsequent deposition began during OIS 5d. OIS 5d, from 115 – 105 ka, was cooler and drier than the preceding interglacial based on the Dome C temperature record and Lake Tswaing rainfall record (Figure 9.3).

Section 9.2.1 outlined an hypothesis that, during the last interglacial, sediments were simultaneously being stripped from many hillslopes whilst being preserved within at least some river valleys. This was based on the evidence for deposition of LGS sediments at the Moopetsi tributary site during the last interglacial, but is supported by evidence for deposition and preservation of fluvial sediments during the time frame in some other South African river valleys (Tooth et al., 2013). However, the initiation of deposition for the LGS sediments is dated to ~153 ka, and possibly as early as ~165 ka if taking account of uncertainties. Ziegler et al. (2013) identified two periods of very weak East Asian monsoon activity at ~120 ka and ~165 ka, based on δ^{18}O records from Chinese speleothems from Hulu and Sanbao Cave (Wang et al., 2008, 2001). These periods coincided with occupational phases at Pinnacle Point Cave in the Western Cape Province, which were linked to variation in sea level by Marean (2010), and interpreted by Ziegler et al. (2013) as representing wetter conditions in South Africa. Increased runoff during these intervals could have led to stripping of hillslope colluvium, whilst simultaneously reworking and depositing the sediment within river valleys, an interpretation that is supported by the

coarse-grained nature of the fluvial sediments at places like Erfkroon (Tooth et al., 2013).

Initiation of sedimentation at Goedgedacht began much later, ~66 ka, during OIS 4 (71 – 60 ka). Chase (2010) report cold and wet conditions during this period, whilst variable conditions have been reported by Bar-Matthews et al. (2010) at Pinnacle Point Cave. Ziegler et al. (2013) argue that wet and humid conditions prevailed across the Eastern Cape during the latter half of OIS 4 (coinciding with a cold North Atlantic Ocean and a dry phase in Asia) which transitioned rapidly into drier conditions ~59.5 ka. Deposition at Goedgedacht began around the same time as the sediments of the UGS unit at the Moopetsi tributary site were being deposited (see Figure 9.1). This phase of deposition at the Moopetsi tributary site began after the extensive erosional truncation of the OGP, possibly due to the abrupt shift to drier conditions in eastern South Africa beginning early in OIS 3 (60 – 24 ka). The gap in the St Paul's record at this time is unfortunate, as it is possible that deposition may have been occurring during this interval. However, based on the sedimentary record a period of pedogenesis had to have occurred during this period of dating uncertainty i.e. between ~75 – 55 ka (shown on Figure 9.1). Furthermore, deposition began at Voordrag ~70 ka. Based on the landslide theory (see Section 8.3.1) this could be coincidental, or it may indicate that the wetter conditions during OIS 4 were responsible for initiating the landslide.

Clearly, the ability to constrain the initiation of sedimentation across South Africa is dependent on the preservation of the records selected for dating. In this study, luminescence dating has been used to highlight the variable timing of deposition of sediments at multiple sites and when

compared to other luminescence-dated South African records, even greater variability is found. However, very few studies have specifically targeted basal sediments in an attempt to tightly constrain the timing of initiation of deposition, so making comprehensive comparisons remains difficult.

9.4 Controls on intervening phases of deposition, pedogenesis and erosion

Given the difficulty of dating the cut-and-fill structures at St Paul's (see Section 7.4) and the largely uncertain nature of the associated time period (see Figure 9.1) this section will focus on the records preserved at the Voordrag, Moopetsi and Goedgedacht sites. The sedimentary record preserved at Voordrag cannot be directly correlated with the regional stratigraphy of the Masotcheni Formation (see Section 2.3.2). The Voordrag record is of particular interest because it represents a largely complete record of colluvial deposition, with intervening periods of pedogenesis, over the last ~70 ka, covering the late Pleistocene and most of the Holocene.

Based on their ages, Clarke et al. (2003) concluded that temperature was not a controlling factor for either colluvial accretion or soil formation because both occurred during the cold LGM (19 – 23 ka, Gasse et al., 2008) and warm Early Holocene. This conclusion is supported by the single grain ages derived in this study. Instead, they identified the influence of regional precipitation on the Voordrag record, by comparing it to the Lake Tswaing rainfall record of Partridge et al. (1997). Their conclusion was that colluvial deposition occurred during arid stages and pedogenesis during more humid phases. More recently, Ziegler et al. (2013) identified

generally dry conditions interrupted by multiple short pulses of wetter conditions during OIS 3 (~60 – 24 ka, see Figure 9.4), which may support the conclusion of Clarke et al. (2003). During the Holocene (OIS 1, 12 – 0 ka), minor, less well-defined phases of pedogenesis are observed in the Voordrag sedimentary record. The EPICA Dome C and Wonderkrater records (see Figure 9.3) both show an increase in temperature, and the latter an increase in humidity during OIS 1. In contrast, the pollen and sediment record from Lake Eteza in eastern KwaZulu-Natal (Neumann et al., 2010) indicates humid, wet, woodland conditions at ~10200 cal yr BP (10.2 ka) changing to drier grassy environments ~6800 cal yr BP (6.8 ka), with maximum humidity and higher precipitation between 6800 – 3600 cal yr BP (6.8 – 3.6 ka), followed by a shift to drier conditions after 3600 cal yr BP (3.6 ka). The Lake Eteza record agrees with sea surface temperature (SST) fluctuations, which influence precipitation in coastal Natal, recorded in a marine core from the Mozambique Channel (Neumann et al., 2010).

At Voordrag, and also at St Paul's and Moopetsi, the process of pedogenesis occurred during periods of land surface stability. During more humid phases, for instance, conditions likely would have promoted greater vegetation growth (especially grasses), which lead to increased slope stability owing to anchoring of the upper sediment layer by root systems (typical rooting zones of hillslope grasses under modern conditions are ~20 – 30 cm). An abrupt shift to drier climatic conditions may have lead to a decrease in vegetation cover and eventual slope surface instability, leading to a renewed pulse of colluvial sedimentation. However, this climatic control is by no means a universal indicator of pedogenesis across the South African interior. For instance, Lyons et al. (2014) reported that pedogenesis

occurred contemporaneously with floodplain sedimentation at the Erfkroon site. Here the sedimentation rate was sufficiently low (~0.15 mm/yr) that pedogenesis occurred contemporaneously with sediment deposition, resulting in a broadly continuous record of sediment and soil formation from >44 ka to ~0.83 ka under variable climates. These changing climatic conditions were, however, recorded in the palaeosol characteristics, including colour, secondary pedogenic minerals and mineral magnetic assemblages.

9.5 Controls on the current phase of incision

9.5.1 Cessation of the most recent phase of deposition

As outlined in previous chapters, the timing of the cessation of the most recent phase of deposition (e.g. sample 9, Figure 2.5) offers a maximum limiting age for the beginning of the current phase of incision and associated donga formation. In addition to ages derived in this study, other ages exist from several other sites across South Africa (Table 9.1). Considering all sites together, the Moopetsi tributary and Goedgedacht sites record the earliest evidence for cessation of deposition at ~3.45 ka and ~3.84 ka, respectively (see Figure 9.2). These ages coincide with, or slightly post-date, a period of global rapid climate change between 4.2 and 3.8 ka, characterised by polar cooling, tropical aridity and major atmospheric circulation changes (Mayewski et al., 2004). Within South Africa, several proxies record drier conditions over this time span (e.g. Beaumont et al., 1984; Holmes et al., 2008; Jolly et al., 1998). Thus, at the Moopetsi tributary and Goedgedacht

Table 9.1: Timing of the cessation of the most recent depositional phase, and the current phase of incision and subsequent donga formation in South Africa. Ages from Voordrag, St Paul's, Moopetsi and Goedgedacht are from this study. Ages for Erkroon are from Lyons et al. (2014), for Blood River are from Lyons et al. (2013), for Okhombe valley are from Temme et al. (2008) and for Heelbo are from Evans (2016).

Site	Timing of cessation of deposition	Timing of donga formation	Timing of minor sedimentation
Voordrag	~0.32 ka	<0.32 ka, >0.07 ka[a]	
St Paul's	~0.42 ka	<0.42 ka, >0.08 ka	~0.08 ka
Moopetsi	~3.45 ka	<0.56 ka[b], >0.19 ka[b]	~0.20 ka
Goedgedacht	~3.84 ka	<3.84 ka, >0.11 ka	~0.11 - 0.06 ka
Erfkroon	~0.83 ka	<0.83 ka, >0.30 ka	~0.30 ka
Blood River	~1.83 - 1.62 ka	<1.62 ka, >0.29 ka	~0.29 ka
Okhombe	>0.17 ka		
Heelbo	<2.50 ka		

[a] Date based on aerial photographs

[b] Date based on archaeological interpretations

sites, the final stage of deposition may have been linked to this period of rapid climate change.

At many other sites however, the cessation of deposition occurs much later. At the Blood River the cessation of deposition occurs between ~1.83 – 1.62 ka and predates the MWP (AD 900 – 1300), another prominent climatic interval. Cessation of deposition at Voordrag, St Paul's and Erfkroon occurs later and coincides with the LIA (AD 1300 – 1800). In the Okhombe Valley the topmost layer of the fluvially-redistributed sediments was dated to 0.169 ± 0.025 ka by Temme et al. (2008). However, they assert that deposition ceased well before 0.17 ka, citing ongoing bleaching of the current A-horizon in support. At Heelbo, the maximum limiting age is from the depositional layer below the surface soil profile, implying a period of pedogenesis post-

deposition but prior to incision. Thus cessation at this site occurred at some undefined time after ~2.5 ka (Evans, 2016).

9.5.2 Current channel incision and donga formation

Having considered the maximum limiting age for constraining the current phase of incision and associated donga formation, consideration can also be given to the minimum limiting age. In this study, the minimum age was based on dating sediment packages infilling the incised channels and dongas (e.g. sample 10, Figure 2.5). Where infill samples were not available, aerial photographs were used to determine a minimum limiting age for donga formation. For each site, this approach provided a bracketing window during which incision must have occurred (see Table 9.1 and Figure 9.2). At Moopetsi and Goedgedacht, the early cessation of deposition means that this bracketing window is relatively large (e.g. from 3.84 – 0.11 ka at Goedgedacht). The window for incision at Moopetsi, however, can be narrowed through the use of archeological remains preserved on the floor of the donga (see Section 8.2) from 3.45 – 0.20 ka to 0.56 – 0.19 ka. This tighter bracketing window is in keeping with the potential timing of incision at many other sites, most of which coincide with the timing of the LIA.

The LIA, characterised by overall cool and dry conditions globally, represents an abrupt shift in climate from the preceding MWP, which was characterised by above average warming and high variability (Holmgren et al., 1999; Tyson et al., 2000). Based on the Wonderkrater pollen and Makapansgat $\delta^{18}O$ records (Holmgren et al., 2003; Scott, 1999), in South Africa, conditions during the LIA were up to 1 °C cooler than present

and significantly drier, albeit with frequent intense storms. Alteration of vegetation systems linked to repeated droughts during the LIA have been reported from across South Africa (e.g. Ekblom et al., 2012; Ekblom and Stabell, 2008; Holmgren et al., 2003; Scott, 1989, 1996; Smith, 1992; Tyson et al., 2000; Woodborne et al., 2015). This led Lyons (2012) and Lyons et al. (2013) to suggest that incision at many sites was likely initiated during the transition to the LIA, due to the combination of increased aridity, sparse vegetation cover, and the possible occurrence of intense storms and floods. The constraints on the timing of current incision at Voordrag, St Paul's and the Moopetsi tributary site (see Table 9.1) all suggest the onset of incision and donga formation during the LIA. Incision at Goedgedacht may also have begun during the LIA, but here the timing is less tightly constrained and so it remains possible that incision began earlier based on the maximum limiting age of 3.84 ka (see Table 9.1 and Figure 9.2).

9.5.3 Alternative controls on channel incision and donga formation

Although a climate control on channel incision and donga formation is highly suggestive, abrupt climate change is by no means the only possible driver of incision and donga formation in South Africa. Based on a review of previously published studies, Lyons (2012) undertook a detailed analysis of incision in South Africa, and highlighted three additional potential drivers. These include: (i) human impact on the landscape; (ii) local base level fall along the trunk river channel; and (iii) the inherent susceptibility of sediments to water erosion. Each of these will be discussed briefly in the following section.

Soil erosion in South Africa has traditionally been ascribed to the role of human impact on the landscape. This was linked, in particular, to the arrival and dispersal of European settlers from the second half of the 18^{th} century and attributed to the effects of overgrazing by domestic livestock and the intensification of agropastoralism (e.g. Boardman et al., 2003; Hoffman et al., 1999; Keay-Bright and Boardman, 2009; Meadows, 2001). However, Bantu-speaking farming communities settled south of the Limpopo River during the Early Iron Age (AD 200 – 900) and introduced domestic livestock ~AD 300. Occupation by Iron Age populations has been linked to climate change, with population expansion and increased farming occuring during the MWP in the Shashe-Limpopo River Basin (Huffman, 2000), and the abandonment of Mapungubwe corresponding with the onset of cooler, drier conditions associated with the LIA (Tyson et al., 2002; Vogel and Fuls, 1999). A recent study (AD 1945 – 2000) in the Okhombe valley showed that erosion of the Masotcheni Formation sediments varied with rainfall, grazing regime and population density (Sonneveld et al., 2005). In contrast, Lyons (2012) argued that human impact was not the main driver of erosion at his field sites (Erfkroon, Steelpoort and Blood River) because (i) Iron Age populations could not be linked to incision along the Modder or Moopetsi Rivers; (ii) in-situ archaeological remains located on donga floors across the Steelpoort region imply incision pre-dated human occupation; (iii) the onset of incision pre-dated agropastoral intensification associated with European settlement; and (iv) historical aerial photographs of the Blood River and Moopetsi tributary sites showed almost no change in the areal extent of dongas since the early 20^{th} century despite an ~600 % increase in population density in the Steelpoort region.

Local base level fall is another potential driver of incision. Tooth et al. (2004) presented a model illustrating how breaching of a resistant rock barrier exposed within a channel bed can lead to baselevel fall and knickpoint retreat through upstream reaches underlain by softer sedimentary rocks. This leads to channel incision and floodplain abandonment. Floodplains gradually desiccate, and donga formation occurs as a result of headward incision on the steepened channel banks. Tooth et al. (2013) applied this basic model to the Modder River, and identified a potential location for the former rock barrier (a dolerite sill or dyke) ~11 km downstream from the Erfkroon site. Lyons (2012) asserted that rock barrier breaching was a secondary driver of incision along the Modder River, but possibly a primary driver along the Venterspruit and Schoonspruit Rivers (see also Keen-Zebert et al., 2013). Base level fall can also operate in other geomorphic contexts; for instance, in Section 8.5.2, the possibility of base level fall on the trunk river was presented as a plausible driver of incision within the Goedgedacht donga system.

The inherent susceptibility of soils/sediments to erosion has also been linked to donga formation across South Africa, with different studies identifying the content of sodium (Watson et al., 1984), clay (Hanvey et al., 1991) and organic matter (De Villiers et al., 2002; Oluwole and Sikhalazo, 2008) as relevant properties. In addition, Rienks et al. (2000) correlated the erodibility of the Masotcheni Formation sediments to electrical conductivity and the sodium absorption ratio, and cited landscape position and geomorphic threshold conditions as factors that co-determine erosion. As an example, Lyons (2012) highlighted the contrast in the extent of donga formation on the east and west banks at the Moopetsi tributary

site (see Figure 2.7 in this thesis), and noted the apparent predisposition to weathering of sediment sourced from the mafic Bushveld Complex as opposed to sediments derived from the quartz-rich Transvaal Supergoup.

In an attempt to reconcile the different drivers, Lyons (2012) presented a conceptual model in which he identified primary, secondary and intrinsic drivers of channel incision and donga formation (Figure 9.5). His primary driver was abrupt climate change brought about by the rapidly changing conditions at the MWP-LIA transition. Secondary drivers, that may or may not apply at particular sites, were identified as: (i) indigenous population expansion and agropastoralism contributing to localised erosion from ~AD 300; (ii) European population expansion and intensification of agropastoralism contributing to localised donga formation from late 18^{th} century; (iii) local susceptibility of soils/sediments to erosion controlling the extent of the dongas, and (iv) rock barrier breaching and local base level fall controlling the depth of channel and donga incision. He also identified an intrinsic driver, which creates a positive feedback loop, for as channels deepen and widen during incision, their potential to contain large flows is enhanced, which leads to further potential for incision. The findings from this study, derived from four sites that cover a wide range of physiographic, geological, climatic, vegetative and land use conditions (Chapter 2) provide additional empirical support for the underpinning concepts outlined by Lyons (2012).

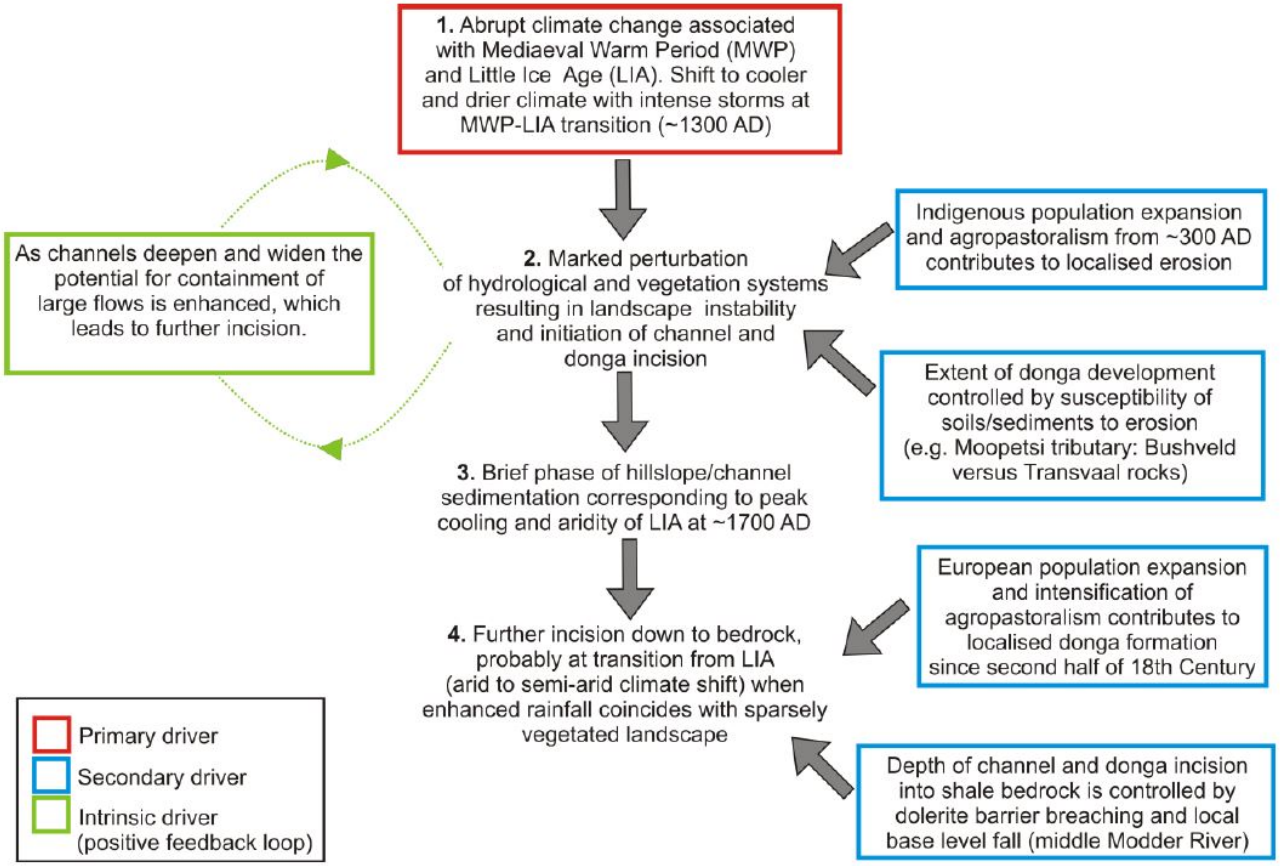

Figure 9.5: Conceptual model summarising the key stages (1-4) and drivers (primary, secondary and intrinsic) of channel incision and donga formation across the South African interior (reproduced from Lyons, 2012).

9.6 Summary

This chapter began with an inter-site comparison which showed that during the initiation of deposition, no clear regional synchrony can be identified across the four widely dispersed study sites. The oldest preserved sediments dated in this study were from the Moopetsi river system in Limpopo Province and were deposited during OIS 6 and 5e. The next oldest preserved sediments are found on hillslopes in KwaZulu-Natal Province and have been dated to OIS 5d. This implies that deposition occurred during OIS 6 and continued through OIS 5e within some river valleys, even whilst the colluvial mantles were being stripped from many hillslopes during OIS 5e. At several sites, the full history of subsequent phases of deposition, erosion and pedogenesis through OIS 5d to OIS 2 are difficult to constrain, tightly or fully, in part due to limited sampling density and in part due to the large uncertainties inherent in the single grain luminescence ages. Cessation of the most recent phase of deposition appears to correspond to two main time periods in the mid-late Holocene, one coincidental with the 3.8 – 4.2 ka global aridification event and one coincidental with the LIA event. Both events are related to abrupt climate change. At most sites, the start of the current phase of incision and donga formation largely coincides with the LIA, although a variety of other factors (e.g. human impacts, base level fall, soil properties) complicate a straightforward or simplistic interpretation of a climatic driver of incision and donga formation.

Chapter 10

Conclusion

The primary aim of this study was to develop the use of luminescence chronometers to establish the timing of colluvial/alluvial sedimentation during the late Quaternary in South Africa. Two chronometers were selected for investigation in this study. Quartz OSL has previously been used in the dating of geoproxy records in South Africa, but is limited by the low saturation level of the fast component used for dating (Chapter 1). In contrast, K-feldspar post-IR IRSL is a relatively new technique, capable of extending the maximum age limit, but prior to this study had not been widely applied to sediments from South Africa.

During this study, multiple grain (small aliquot) D_e measurements were shown to be overestimating for both quartz (Chapter 5) and K-feldspar (Chapter 4). This was as a result of heterogeneous bleaching and the large proportion of grains producing a luminescence signal, so that a range of highly variable D_e values were averaged on each individual aliquot and produced an overly large D_e value. Overestimation of multiple grain measurements have previously been attributed to averaging effects in both

quartz (Russell and Armitage, 2012) and K-feldspar (Reimann et al., 2012, 2011). Thus it was concluded that in environments where heterogeneous bleaching is expected, such as colluvial hillslopes, it is highly likely that single grain measurements will be required in order to obtain an accurate estimation of the burial dose and the apparent age. Based on this conclusion, all subsequent measurements in this study were made on single grains of quartz and K-feldspar.

The issue of saturation of the luminescence signal is of particular importance as it determines the maximum age limit for the technique. This is especially relevant for the quartz OSL signal, which has a low saturation level for the component used in OSL dating. The unusual depositional environment at Voordrag produced a near-continuous record of pulsed deposition and pedogenesis, facilitating the investigation of the saturation level of the quartz OSL signal within the confines of a paired K-feldspar chronology and an extensive existing radiocarbon chronology (Chapter 5). Single grain measurements showed that the quartz OSL signal saturated at ~60 Gy (equivalent age ~24 ka), which is well below the 150 Gy threshold limit suggested by Chapot et al. (2012) and $2D_0$ for the sample (~98 Gy). However, >50 % of the single grain dose population was in saturation. Furthermore, comparison with the paired K-feldspar ages and the interspersed radiocarbon ages showed a systematic underestimation of the quartz ages, similar to that reported in studies attempting to date quartz beyond the last interglacial (e.g. Buylaert et al., 2007; Lai, 2010; Lowick et al., 2010a; Murray et al., 2007; Timar et al., 2010). Thus, given the difficultly associated with identifying saturation of the quartz OSL signal, particularly without any form of independent age control, it is suggested

that paired quartz-feldspar ages could be used to identify the point at which quartz OSL ages begin to underestimate relative to the K-feldspar ages. Obviously, this approach would be limited to environments where both minerals are present in sufficient quantities to be datable.

K-feldspar single grain D_e measurements using the post-IR $IRSL_{225}$ protocol with a low test dose (~5 Gy) were shown to be underestimating the burial dose (Chapter 4), based on their comparison to the quartz OSL ages. The underlying cause of the D_e underestimation was shown to be signal transfer between the L_x and T_x measurements (Chapter 6) and two alternatives were explored to prevent systematic underestimation, (i) increasing the size of the test dose (Chapter 4) and (ii) increasing the stimulation time during measurement (Chapter 6). Both approaches were successful in reducing the apparent sensitivity change, but for different reasons. Increasing the size of the test dose dilutes the effect of the transferred charge on the T_x measurement, and an optimum test dose of ~30 % of the expected D_e value was selected for high test dose measurements. In contrast, increasing the stimulation time removes the excess signal, thereby reducing the amount of signal transferred between L_x and T_x measurements. This led to the proposal of a modified post-IR $IRSL_{225}$ protocol (Chapter 6) which minimised signal transfer between measurements and recuperation values. Although both approaches are equally effective, the modified protocol with additional IRSL stimulations is the preferred approach, because it also avoids possible thermal transfer (by removing the high temperature clean out step) and it reduces the total amount of measurement time on the reader.

The use of paired ages to produce combined chronologies (i.e. using quartz OSL to date the younger sediments and K-feldspar post-IR IRSL to date the older sediments) was the approach taken in this study. This approach was used to successfully date four sites across the eastern interior South Africa. The focus was on establishing the timing of (i) the initiation of deposition, (ii) the intervening phases of erosion, deposition and pedogenesis, and (iii) the cessation of sedimentation and initiation of the current phase of deep incision (Chapter 1). The initiation of deposition was not synchronous across the interior and was shown to have started earlier than previously thought at the Moopetsi tributary site (~153 ka), based on the underestimation of the quartz ages when considered in combination with the K-feldspar ages (Chapter 4). In contrast, the initiation of deposition at St Paul's was constrained to ~110 ka (Chapter 7), whilst at Voordrag and Geodgedacht the initiation of deposition occurred much later, ~70 ka and ~65 ka respectively. Thus deposition and aggradation of sediments began during OIS 6 (>153 ka) when conditions were cool and wet. The shift into the warmer, moister OIS 5e resulted in more available water, and hillslopes were stripped of their colluvial mantles across a large portion of South Africa, whilst sediments were reworked and potentially preserved within river valleys. Deposition of sediments on hillslopes resumed during OIS 5d, and was followed by a complex series of erosional, depositional and pedogenetic phases (Chapters 8 and 9). The timing of these phases were difficult to constrain, owing to limited sampling density, and the poorly bleached nature of the sediments, particularly at St Paul's (Chapter 7). Some broad relationships were drawn between the four sites, for instance where simultaneous deposition may have occurred ~60 ka. The initiation of

the current phase of incision was better constrained and appears to coincide with two periods of abrupt climatic changes: a cool, dry arid period ~4.2 – 3.8 ka, and the LIA (~AD1300 – 1800). The timing of the initiation of incision is also in agreement with several other donga sites that have been dated across South Africa and implies at least a partial climatic control on incision and donga formation (Chapter 9).

The extended chronologies produced during this research improved the constraints on the timing of deposition, pedogenesis and erosion, and were used to refine the detailed geomorphic development for each individual site (Chapter 8). The subsequent inter-site comparison (Chapter 9) illustrated that whilst there are time periods that may suggest a regional climatic control on deposition, pedogenesis and erosion of sediments (for example the current phase of deep incision), there is also strong evidence of individual sites preferentially preserving local conditions as opposed to regional climatic conditions. The Voordrag site, where there is evidence of deposition and pedogenesis occurring during both wet and dry phases, provides the most obvious example of the preservation of local conditions.

The chronology from Voordrag is of particular importance, as it indicates almost continual aggradation throughout the late Pleistocene and Holocene in contrast to the records preserved at the other three sites (Moopetsi, St Paul's and Goedgedacht). The existing theory states that colluvial layers formed during drier conditions and palaeosols formed during wetter conditions. However, this is a potentially oversimplified explanation based on the assumption of a large-scale regional climatic control on the formation of these sedimentary features. For example, thick colluvial layers could have been deposited during short, intense rainfall events, whilst pedogenesis may

have occurred during less intense rainfall events. Thus it could be, at this particular site, that deposition and pedogenesis are linked to the intensity of local rainfall events, irrespective of the regional climate.

The Voordrag chronology also has the highest resolution of the four sites investigated during this research. Unfortunately, the relatively large uncertainties on the luminescence ages preclude direct comparisons between geoproxies and higher resolution proxy records (e.g. vegetation records) available for the region. Thus, the refinement of luminescence measurement protocols with a view to improving both the precision and accuracy of the resultant dates is of the utmost importance if geoproxy records are to be utilised to their full potential.

In conclusion, the use of paired chronologies showed good agreement between quartz OSL and K-feldspar post-IR $IRSL_{225}$ single grain ages up to ~24 ka (Chapters 4, 5 and 7). By far the most valuable record in this study is the terrestrial record at Voordrag, which has now yielded extensive quartz, K-feldspar and radiocarbon chronologies. The investigations based on this record confirm that the single grain post-IR $IRSL_{225}$ signal is a viable chronometer, and one which can be used to date environments characterised by heterogeneously bleached sediments. However, beyond the age range of radiocarbon (~40 ka) there is limited opportunity to compare post-IR IRSL ages with independent age controls, either within the South African context or worldwide. Future research will be needed to address this limitation by determining an appropriate independent chronometer that can test the maximum age limit of the post-IR IRSL protocol. Tephra deposits are one such possibility; for instance the Tochigi tephras in Japan, have been

dated to 660 ± 40 ka (Watanuki et al., 2005) and could potentially facilitate comparisons of up to 2 kGy, depending on the environmental dose rate.

Appendix A: Multiple grain D_e distributions from the Moopetsi tributary site

Radial plots constructed from small aliquot D_e measurements at the Moopetsi tributary site, Limpopo Province. Plots show the quartz OSL D_e values (black circles) together with the post-IR $IRSL_{225}$ D_e values (white triangles). The light and dark grey shaded regions represent the D_e defined by the relevant age model for each distribution, respectively.

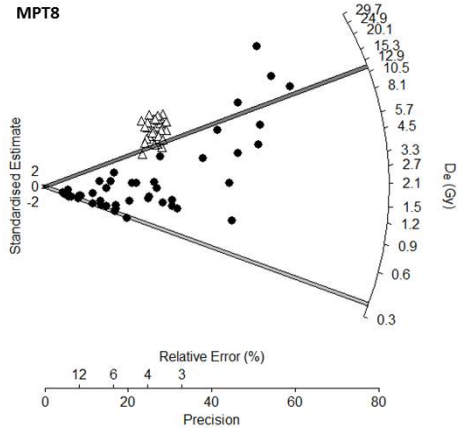
MPT8
Standardised Estimate
De (Gy)
Relative Error (%)
Precision

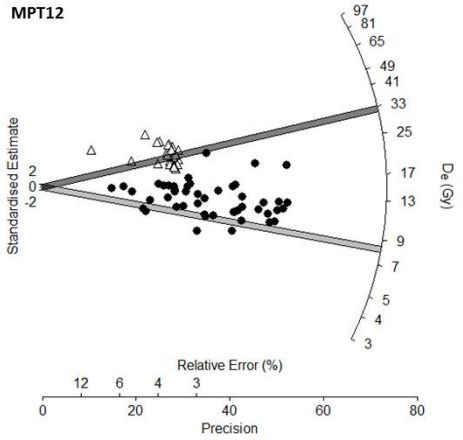
MPT12
Standardised Estimate
De (Gy)
Relative Error (%)
Precision

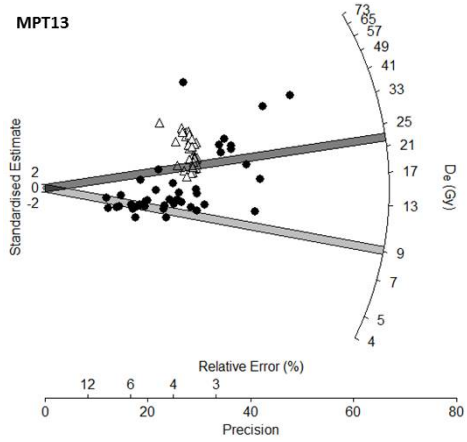
MPT13
Standardised Estimate
De (Gy)
Relative Error (%)
Precision

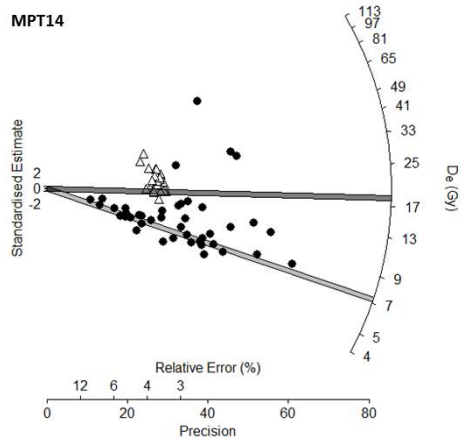
MPT14
Standardised Estimate
De (Gy)
Relative Error (%)
Precision

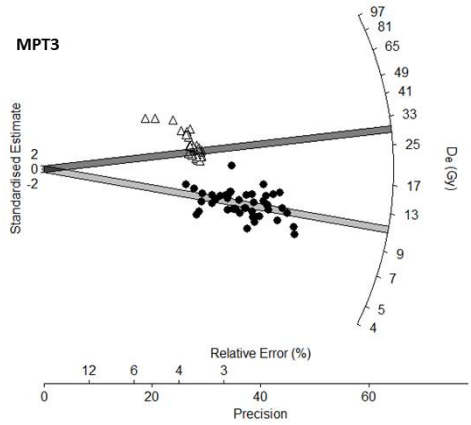
MPT3
Standardised Estimate
De (Gy)
Relative Error (%)
Precision

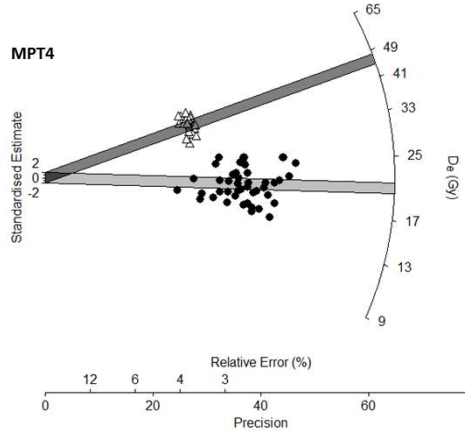
MPT4
Standardised Estimate
De (Gy)
Relative Error (%)
Precision

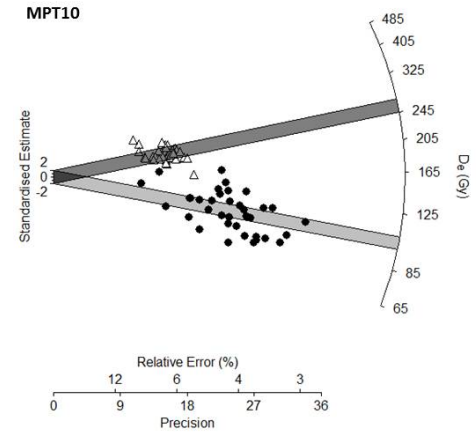
MPT10
Standardised Estimate
2
0
-2
De (Gy)
485
405
325
245
205
165
125
85
65
Relative Error (%)
12
6
4
3
0
9
18
27
36
Precision

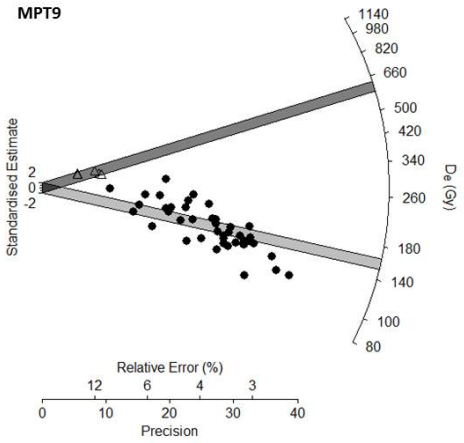
MPT9
Standardised Estimate
2
0
-2
De (Gy)
1140
980
820
660
500
420
340
260
180
140
100
80
Relative Error (%)
12
6
4
3
0
10
20
30
40
Precision

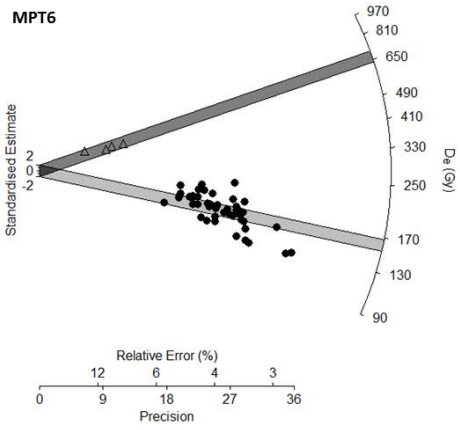
MPT6
Standardised Estimate
2
0
-2
De (Gy)
970
810
650
490
410
330
250
170
130
90
Relative Error (%)
12
6
4
3
0
9
18
27
36
Precision

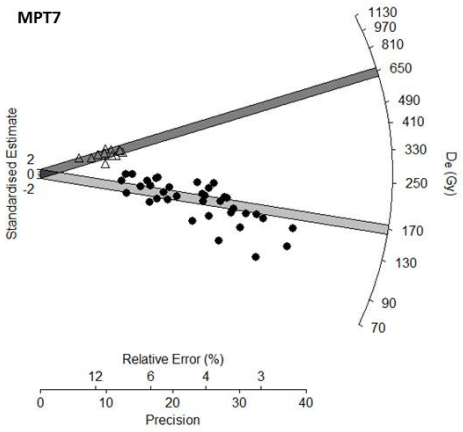
MPT7
Standardised Estimate
2
0
-2
De (Gy)
1130
970
810
650
490
410
330
250
170
130
90
70
Relative Error (%)
12
6
4
3
0
10
20
30
40
Precision

References

Adamiec, G. and Aitken, M. (1998). Dose-rate conversion factors: update. *Ancient TL*, 16(2):37–50.

Aitken, M. (1985). *Thermoluminescence dating*. Academic Press.

Aitken, M. (1998). *An Introduction to Optical Dating: The Dating of Quaternary Sediments by the Use of Photon-Stimulated Luminescence*. Oxford University Press.

Aitken, M. and Xie, J. (1990). Moisture correction for annual gamma dose. *Ancient TL*, 8(2):6–9.

Aitken, M. J. (1994). Optical dating: a non-specialist review. *Quaternary Science Reviews*, 13(5-7):503–508.

Ankjærgaard, C. and Murray, A. S. (2007). Total beta and gamma dose rates in trapped charge dating based on beta counting. *Radiation Measurements*, 42(3):352–359.

Armitage, S. J., Duller, G. A. T., and Wintle, A. G. (2000). Quartz from southern Africa: sensitivity changes as a result of thermal pretreatment. *Radiation Measurements*, 32(5-6):571–577.

Armitage, S. J., Jasim, S. A., Marks, A. E., Parker, A. G., Usik, V. I., and Uerpmann, H.-P. (2011). The Southern Route 'Out of Africa': Evidence for an Early Expansion of Modern Humans into Arabia. *Science*, 331(6016):453–456.

Arnold, L. J., Bailey, R. M., and Tucker, G. E. (2007). Statistical treatment of fluvial dose distributions from southern Colorado arroyo deposits. *Quaternary Geochronology*, 2(1-4):162–167.

Arnold, L. J., Demuro, M., and Ruiz, M. N. (2012). Empirical insights into multi-grain averaging effects from 'pseudo' single-grain OSL measurements. *Radiation Measurements*, 47(9):652–658.

Auclair, M., Lamothe, M., and Huot, S. (2003). Measurement of anomalous fading for feldspar IRSL using SAR. *Radiation Measurements*, 37(4-5):487–492.

Bailey, R. M. and Arnold, L. J. (2006). Statistical modelling of single grain quartz De distributions and an assessment of procedures for estimating burial dose. *Quaternary Science Reviews*, 25(19-20):2475–2502.

Balescu, S. and Lamothe, M. (1993). Thermoluminescence dating of the holsteinian marine formation of Herzeele, northern France. *Journal of Quaternary Science*, 8(2):117–124.

Balescu, S. and Lamothe, M. (1994). Comparison of TL and IRSL age estimates of feldspar coarse grains from waterlain sediments. *Quaternary Science Reviews*, 13(5-7):437–444.

Balescu, S., Ritz, J. F., Lamothe, M., Auclair, M., and Todbileg, M. (2007). Luminescence dating of a gigantic palaeolandslide in the Gobi-Altay mountains, Mongolia. *Quaternary Geochronology*, 2(1-4):290–295.

Bar-Matthews, M., Marean, C. W., Jacobs, Z., Karkanas, P., Fisher, E. C., Herries, A. I. R., Brown, K., Williams, H. M., Bernatchez, J., Ayalon, A., and Nilssen, P. J. (2010). A high resolution and continuous isotopic speleothem record of paleoclimate and paleoenvironment from 90 to 53 ka from Pinnacle Point on the south coast of South Africa. *Quaternary Science Reviews*, 29(17-18):2131–2145.

Barbouti, A. and Rastin, B. (1983). A study of the absolute intensity of muons at sea level and under various thicknesses of absorber. *Journal of Physics G: Nuclear Physics*, 9:1577–1595.

Barr, M. and Lamothe, M. (2010). Luminescence dating of archaeosediments: A comparison of K-feldspar and plagioclase IRSL ages. *Quaternary Geochronology*, 5(2-3):324–328.

Beaumont, P., van Zinderen Bakker, E., and Vogel, J. (1984). Environmental changes since 32 000 BP at Kathu Pan, northern Cape. In Vogel, J., editor, *Late Cainozoic Palaeoclimates of the Southern Hemisphere*, pages 329–338. Balkema, Rotterdam.

Bell, W. (1979). Attenuation Factors for the Absorbed Radiation Dose in Quartz Inclusions for Thermoluminescence Dating. *Ancient TL*, 8:2–13.

Bell, W. (1980). Alpha dose attenuation in quartz grains for thermoluminescence dating. *Ancient TL*, 12:4–8.

Berger, G. W. and Chen, G. (2011). Error analysis and modelling of double saturating exponential dose response curves from SAR OSL dating. *Ancient TL*, 29(1):9–14.

Berger, G. W. and Huntley, D. J. (1994). Tests for optically stimulated luminescence from tephra glass. *Quaternary Science Reviews*, 13(5-7):509–511.

Boardman, J., Parsons, A. J., Holland, R., Holmes, P. J., and Washington, R. (2003). Development of badlands and gullies in the Sneeuberg, Great Karoo, South Africa. *Catena*, 50(2-4):165–184.

Botha, G. (1992). *The geology and palaeopedology of late Quaternary colluvial sediments in northen Natal, South Africa*. PhD thesis, University of Natal.

Botha, G. and Fedoroff, N. (1995). Palaeosols in Late Quaternary colluvium, northern KwaZulu-Natal, South Africa. *Journal of African Earth Sciences*, 21(2):291–311.

Botha, G., Scott, L., Vogel, J., and von Brunn, V. (1992). Palaeosols and palaeoenvironments during the Late Pleistocene Hypothermal in northern Natal. *South African Journal of Science*, 88:508–512.

Botha, G. A. (1996). *The geology and palaeopedology of Late Quaternary colluvial sediments in northern Kwazulu/Natal*. Memoir 83 of the Geological Survey of South Africa. Council for Geoscience.

Botha, G. A., Wintle, A. G., and Vogel, J. C. (1994). Episodic late quaternary palaeogully erosion in northern KwaZulu-Natal, South Africa. *Catena*, 23(3-4):327–340.

Bøtter-Jensen, L., Bulur, E., Duller, G. A. T., and Murray, A. S. (2000). Advances in luminescence instrument systems. *Radiation Measurements*, 32(5-6):523–528.

Bøtter-Jensen, L. and Mejdahl, V. (1988). Assessment of beta dose-rate using a GM multicounter system. *International Journal of Radiation Applications and Instrumentation. Part D. Nuclear Tracks and Radiation Measurements*, 14(1-2):187–191.

Bøtter-Jensen, L., Thomsen, K. J., and Jain, M. (2010). Review of optically stimulated luminescence (OSL) instrumental developments for retrospective dosimetry. *Radiation Measurements*, 45(3-6):253–257.

Brennan, B. (2003). Beta doses to spherical grains. *Radiation Measurements*, 37:299–303.

Brennan, B. (2006). Variation of the alpha dose rate to grains in heterogeneous sediments. *Radiation Measurements*, 41:1026–1031.

Bronk Ramsey, C. (2009). Bayesian analysis of radiocarbon dates. *Radiocarbon*, 51(1):337–360.

Burrough, S. L., Thomas, D., Shaw, P., and Bailey, R. M. (2007). Multiphase Quaternary highstands at Lake Ngami, Kalahari, northern Botswana. *Palaeogeography, Palaeoclimatology, Palaeoecology*, 253(3-4):280–299.

Buylaert, J.-P., Huot, S., Murray, A. S., and Van Den Haute, P. (2011a). Infrared stimulated luminescence dating of an Eemian (MIS 5e) site in Denmark using K-feldspar. *Boreas*, 40(1):46–56.

Buylaert, J.-P., Jain, M., Murray, A. S., Thomsen, K. J., Thiel, C., and Sohbati, R. (2012). A robust feldspar luminescence dating method for Middle and Late Pleistocene sediments. *Boreas*, 41(3):435–451.

Buylaert, J. P., Murray, A. S., Gebhardt, A. C., Sohbati, R., Ohlendorf, C., Thiel, C., Wastegård, S., and Zolitschka, B. (2013). Luminescence dating of the PASADO core 5022-1D from Laguna Potrok Aike (Argentina) using IRSL signals from feldspar. *Quaternary Science Reviews*, 71:70–80.

Buylaert, J. P., Murray, A. S., Thomsen, K. J., and Jain, M. (2009). Testing the potential of an elevated temperature IRSL signal from K-feldspar. *Radiation Measurements*, 44(5-6):560–565.

Buylaert, J.-P., Thiel, C., Murray, A. S., Vandenberghe, D. G., Yi, S., and Lu, H. (2011b). IRSL and post-IR IRSL residual doses recorded in modern dust samples from the Chinese Loess Plateau. *Geochronometria*, 38(4):432–440.

Buylaert, J. P., Vandenberghe, D., Murray, A. S., Huot, S., De Corte, F., and Van den Haute, P. (2007). Luminescence dating of old (> 70 ka) Chinese loess: A comparison of single-aliquot OSL and IRSL techniques. *Quaternary Geochronology*, 2(1-4):9–14.

Buylaert, J.-P., Yeo, E.-Y., Thiel, C., Yi, S., Stevens, T., Thompson, W., Frechen, M., Murray, A., and Lu, H. (2015). A detailed post-IR IRSL chronology for the last interglacial soil at the Jingbian loess site (northern China). *Quaternary Geochronology*, 30, Part B:194–199.

Carr, A. S., Bateman, M. D., and Holmes, P. J. (2007). Developing a 150ka luminescence chronology for the barrier dunes of the southern Cape, South Africa. *Quaternary Geochronology*, 2(1-4):110–116.

Cawthorn, R. G. and Ashwal, L. D. (2009). Origin of Anorthosite and Magnetitite Layers in the Bushveld Complex, Constrained by Major Element Compositions of Plagioclase. *Journal of Petrology*, 50(9):1607–1637.

Chapot, M. S., Roberts, H. M., Duller, G. A. T., and Lai, Z. P. (2012). A comparison of natural- and laboratory-generated dose response curves for quartz optically stimulated luminescence signals from Chinese Loess. *Radiation Measurements*, 47(11-12):1045–1052.

Chase, B. (2009). Evaluating the use of dune sediments as a proxy for palaeo-aridity: A southern African case study. *Earth-Science Reviews*, 93(1-2):31–45.

Chase, B. (2010). South African palaeoenvironments during marine oxygen isotope stage 4: a context for Howiesons poort and Still Bay industries. *Journal of Archaeological Science*, 37:1359–1366.

Chase, B. M. and Meadows, M. E. (2007). Late Quaternary dynamics of southern Africa's winter rainfall zone. *Earth-Science Reviews*, 84(3-4):103–138.

Clarke, M. L., Vogel, J. C., Botha, G. A., and Wintle, A. G. (2003). Late Quaternary hillslope evolution recorded in eastern South African colluvial badlands. *Palaeogeography, Palaeoclimatology, Palaeoecology*, 197(3-4):199–212.

Colarossi, D., Duller, G. A. T., Roberts, H. M., Tooth, S., and Lyons, R. (2015). Comparison of paired quartz OSL and feldspar post-IR IRSL dose distributions in poorly bleached fluvial sediments from South Africa. *Quaternary Geochronology*, 30, Part B:233–238.

De Corte, F., Vandenberghe, D., Hossain, S. M., De Wispelaere, A., Buylaert, J. P., and Van den Haute, P. (2007). Preparation and characterization of loess sediment for use as a reference material in the annual radiation dose determination for luminescence dating. *Journal of Radioanalytical and Nuclear Chemistry*, 272(2):311–319.

De Villiers, M., Pretorius, D., Barnard, R., van Zyl, A., and leClus, C. (2002). Land degradation assessment in dryland areas: South Africa. Paper for Land Degradation Assessment in Dryland Project (FAO). Technical report, Rome, Italy.

Duller, G. (1991). Equivalent dose determination using single aliquots. *International Journal of Radiation Applications and Instrumentation Part D Nuclear Tracks and Radiation Measurements*, 18(4):371–378.

Duller, G. (1994). Luminescence dating of sediments using single aliquots: New procedures. *Quaternary Science Reviews*, 13(2):149–156.

Duller, G. (2015). The Analyst software package for luminescence data: overview and recent improvements. *Ancient TL*, 33(1):35–42.

Duller, G. (2016). Challenges involved in obtaining luminescence ages for long records of aridity: Examples from the Arabian Peninsula. *Quaternary International*, 410, Part B:69–74.

Duller, G. A. T. (1992). *Luminescence Chronology of Raised Marine Terraces, South-West North Island, New Zealand*. PhD thesis, University of Wales, Aberystwyth.

Duller, G. A. T. (2003). Distinguishing quartz and feldspar in single grain luminescence measurements. *Radiation Measurements*, 37(2):161–165.

Duller, G. A. T. (2004). Luminescence dating of Quaternary sediments: recent advances. *Journal of Quaternary Science*, 19(2):183–192.

Duller, G. A. T. (2008a). *Luminescence Dating: guidelines on using luminescence dating in archaeology*. English Heritage, Swindon.

Duller, G. A. T. (2008b). Single-grain optical dating of Quaternary sediments: why aliquot size matters in luminescence dating. *Boreas*, 37(4):589–612.

Duller, G. A. T. (2011). What date is it? Should there be an agreed datum for luminescence ages? *Ancient TL*, 29(1):1–4.

Duller, G. A. T. (2012a). Cross-talk during single grain optically stimulated luminescence measurements of quartz and feldspar. *Radiation Measurements*, 47(3):219–224.

Duller, G. A. T. (2012b). Improving the accuracy and precision of equivalent doses determined using the optically stimulated luminescence signal from single grains of quartz. *Radiation Measurements*, 47(9):770–777.

Duller, G. A. T., Bøtter-Jensen, L., and Murray, A. S. (2000). Optical dating of single sand-sized grains of quartz: sources of variability. *Radiation Measurements*, 32(5-6):453–457.

Duller, G. A. T., Bøtter-Jensen, L., and Murray, A. S. (2003). Combining infrared- and green-laser stimulation sources in single-grain luminescence measurements of feldspar and quartz. *Radiation Measurements*, 37(4-5):543–550.

Duller, G. A. T., Penkman, K. E. H., and Wintle, A. G. (2009). Assessing the potential for using biogenic calcites as dosemeters for luminescence dating. *Radiation Measurements*, 44(5-6):429–433.

Ekblom, A., Gillson, L., Risberg, J., Holmgren, K., and Chidoub, Z. (2012). Rainfall variability and vegetation dynamics of the lower Limpopo Valley, Southern Africa, 500 AD to present. *Palaeogeography, Palaeoclimatology, Palaeoecology*, 363-364:69–78.

Ekblom, A. and Stabell, B. (2008). Paleohydrology of Lake Nhaucati (southern Mozambique), 400 AD to present. *Journal of Paleolimnology*, 40(4):1127–1141.

Evans, M. (2016). *The geology, sedimentology, geochronology and palaeo-environmental reconstruction of the Heelbo hillslope deposit, Free State Province, South Africa*. PhD thesis, University of the Witwatersrand.

Evers, T. (1975). Recent Iron Age research in the eastern Transvaal, South Africa. *South African Archaeological Bulletin*, 30:71–83.

Fain, J., Soumana, S., Montret, M., Miallier, D., Pilleyre, T., and Sanzelle, S. (1999). Luminescence and ESR dating: Beta-dose attenuation for various grain shapes calculated by a Monte-Carlo method. *Quaternary Science Reviews*, 18(2):231–234.

Feathers, J. and Migliorini, E. (2001). Luminescence dating of Middle Stone Age deposits at Die Kelders. *Journal of Human Evolution*, 38:91–119.

Feathers, J. K. (2002). Luminescence dating in less than ideal conditions: Case studies from Klasies River Main Site and Duinefontein, South Africa. *Journal of Archaeological Science*, 29(2):177–194.

Feathers, J. K. and Pagonis, V. (2015). Dating quartz near saturation - Simulations and application at archaeological sites in South Africa and South Carolina. *Quaternary Geochronology*, 30, Part B:416–421.

Folz, E., Bodu, P., Bonte, P., Joron, J.-L., Mercier, N., and Reyss, J.-L. (2001). OSL dating of fluvial quartz from Le Closeau, a Late Paleolithic site near Paris - comparison with 14C chronology. *Quaternary Science Reviews*, 20(5-9):927–933.

Fu, X., Li, S.-H., and Li, B. (2015). Optical dating of aeolian and fluvial sediments in north Tian Shan range, China: Luminescence characteristics and methodological aspects. *Quaternary Geochronology*, 30, Part B:161–167.

Fuchs, M. and Lang, A. (2009). Luminescence dating of hillslope deposits - A review. *Geomorphology*, 109(1-2):17–26.

Fuchs, M. and Owen, L. A. (2008). Luminescence dating of glacial and associated sediments: review, recommendations and future directions. *Boreas*, 37(4):636–659.

Galbraith, R. F. and Green, P. F. (1990). Estimating the component ages in a finite mixture. *International Journal of Radiation Applications and*

Instrumentation. Part D. Nuclear Tracks and Radiation Measurements, 17(3):197–206.

Galbraith, R. F. and Roberts, R. G. (2012). Statistical aspects of equivalent dose and error calculation and display in OSL dating: An overview and some recommendations. *Quaternary Geochronology*, 11:1–27.

Galbraith, R. F., Roberts, R. G., Laslett, G. M., Yoshida, H., and Olley, J. M. (1999). Optical dating of single and multiple grains of quartz from Jinmium rock shelter, northern Australia: Part I, experimental design and statistical models. *Archaeometry*, 41(2):339–364.

Gasse, F., Chali, F., Vincens, A., Williams, M. A. J., and Williamson, D. (2008). Climatic patterns in equatorial and southern Africa from 30,000 to 10,000 years ago reconstructed from terrestrial and near-shore proxy data. *Quaternary Science Reviews*, 27(25-26):2316–2340.

Geach, M. R., Thomsen, K. J., Buylaert, J. P., Murray, A. S., Mather, A. E., Telfer, M. W., and Stokes, M. (2015). Single-grain and multi-grain OSL dating of river terrace sediments in the Tabernas Basin, SE Spain. *Quaternary Geochronology*, 30, Part B:213–218.

Godfrey-Smith, D. I., Huntley, D. J., and Chen, W. H. (1988). Optical dating studies of quartz and feldspar sediment extracts. *Quaternary Science Reviews*, 7(3-4):373–380.

Guérin, G., Combès, B., Lahaye, C., Thomsen, K. J., Tribolo, C., Urbanova, P., Guibert, P., Mercier, N., and Valladas, H. (2015a). Testing the accuracy of a Bayesian central-dose model for single-grain OSL, using known-age samples. *Radiation Measurements*, 81:62–70.

Guérin, G., Frouin, M., Talamo, S., Aldeias, V., Bruxelles, L., Chiotti, L., Dibble, H. L., Goldberg, P., Hublin, J.-J., Jain, M., Lahaye, C., Madelaine, S., Maureille, B., McPherron, S. J. P., Mercier, N., Murray, A. S., Sandgathe, D., Steele, T. E., Thomsen, K. J., and Turq, A. (2015b). A multi-method luminescence dating of the Palaeolithic sequence of La Ferrassie based on new excavations adjacent to the La Ferrassie 1 and 2 skeletons. *Journal of Archaeological Science*, 58:147–166.

Guérin, G., Mercier, N., and Adamiec, G. (2011). Dose-rate conversion factors: update. *Ancient TL*, 29(1):5–8.

Guérin, G., Mercier, N., Nathan, R., Adamiec, G., and Lefrais, Y. (2012). On the use of the infinite matrix assumption and associated concepts: A critical review. *Radiation Measurements*, 47:778–785.

Guérin, G. and Visocekas, R. (2015). Volcanic feldspars anomalous fading: Evidence for two different mechanisms. *Radiation Measurements*, 79:1–6.

Hanvey, P., Dardis, G., and Beckedahl, H. (1991). Soil erosion on a sub-tropical coastal dune complex, Transkei, southern Africa. *GeoJournal*, 1:41–48.

Hoffman, M., Todd, S., Ntshona, Z., and Turner, S. (1999). *Land degradation in South Africa*. Department of Environmental Affairs and Tourism, Pretoria.

Hogg, A., Hua, Q., Blackwell, P., Niu, M., Buck, C., Guilderson, T., Heaton, T., Palmer, J., Reimer, P., Reimer, R., Turney, C., and Zimmerman, S. (2013). SHCal13 Southern Hemisphere Calibration, 0-50,000 Years cal BP. *Radiocarbon*, 55(4):1889–1903.

Holmes, P. J., Bateman, M. D., Thomas, D. S., Telfer, M. W., Barker, C. H., and Lawson, M. P. (2008). A Holocene - late Pleistocene aeolian record from lunette dunes of the western Free State panfield, South Africa. *The Holocene*, 18(8):1193–1205.

Holmgren, K., Karlén, W., Lauritzen, S. E., Lee-Thorp, J. A., Partridge, T. C., Piketh, S., Repinski, P., Stevenson, C., Svanered, O., and Tyson, P. D. (1999). A 3000-year high-resolution stalagmite based record of palaeoclimate for northeastern South Africa. *The Holocene*, 9(3):295–309.

Holmgren, K., Lee-Thorp, J. A., Cooper, G. R. J., Lundblad, K., Partridge, T. C., Scott, L., Sithaldeen, R., Siep Talma, A., and Tyson, P. D. (2003). Persistent millennial-scale climatic variability over the past 25,000 years in Southern Africa. *Quaternary Science Reviews*, 22(21-22):2311–2326.

Holzkämper, S., Holmgren, K., Lee-Thorp, J., Talma, S., Mangini, A., and Partridge, T. (2009). Late Pleistocene stalagmite growth in Wolkberg Cave, South Africa. *Earth and Planetary Science Letters*, 282(1-4):212–221.

Huffman, T. (2000). Mapungubwe and the origins of the Zimbabwe culture. In Leslie, M. and Maggs, T., editors, *African Naissance: The LImpopo Valley 1000 Years Ago*, pages 14–29. South African Archeological Society Goodwin Series 8.

Huntley, D. J. and Baril, M. (1997). The K content of the K-feldspars being measured in optical dating or in thermoluminescence dating. *Ancient TL*, 15:11–13.

Huntley, D. J., Godfrey-Smith, D. I., and Haskell, E. H. (1991). Light-induced emission spectra from some quartz and feldspars. *International Journal of Radiation Applications and Instrumentation. Part D. Nuclear Tracks and Radiation Measurements*, 18(1-2):127–131.

Huntley, D. J. and Hancock, R. (2001). The Rb contents of the K-feldspar grains being measured in optical dating. *Ancient TL*, 19(2):43–46.

Huntley, D. J. and Lamothe, M. (2001). Ubiquity of anomalous fading in K-feldspars and the measurement and correction for it in optical dating. *Canadian Journal of Earth Sciences*, 38(7):1093–1106.

Hütt, G., Jaek, I., and Tchonka, J. (1988). Optical dating: K-feldspars optical response stimulation spectra. *Quaternary Science Reviews*, 7(3-4):381–385.

Jacobs, Z. (2004). *Development of luminescence techniques for dating Middle Stone Age sites in South Africa*. PhD thesis, Aberystwyth University.

Jacobs, Z. (2008). Luminescence chronologies for coastal and marine sediments. *Boreas*, 37(4):508–535.

Jacobs, Z., Duller, G. A. T., and Wintle, A. G. (2003). Optical dating of dune sand from Blombos Cave, South Africa: II - single grain data. *Journal of Human Evolution*, 44(5):613–625.

Jacobs, Z., Duller, G. A. T., and Wintle, A. G. (2006a). Interpretation of single grain D_e distributions and calculation of D_e. *Radiation Measurements*, 41(3):264–277.

Jacobs, Z., Duller, G. A. T., Wintle, A. G., and Henshilwood, C. S. (2006b). Extending the chronology of deposits at Blombos Cave, South Africa,

back to 140 ka using optical dating of single and multiple grains of quartz. *Journal of Human Evolution*, 51(3):255–273.

Jacobs, Z., Hayes, E. H., Roberts, R. G., Galbraith, R. F., and Henshilwood, C. S. (2013). An improved OSL chronology for the Still Bay layers at Blombos Cave, South Africa: further tests of single-grain dating procedures and a re-evaluation of the timing of the Still Bay industry across southern Africa. *Journal of Archaeological Science*, 40(1):579–594.

Jacobs, Z., Wintle, A. G., Duller, G. A. T., Roberts, R. G., and Wadley, L. (2008a). New ages for the post-Howiesons Poort, late and final Middle Stone Age at Sibudu, South Africa. *Journal of Archaeological Science*, 35(7):1790–1807.

Jacobs, Z., Wintle, A. G., Roberts, R. G., and Duller, G. A. T. (2008b). Equivalent dose distributions from single grains of quartz at Sibudu, South Africa: context, causes and consequences for optical dating of archaeological deposits. *Journal of Archaeological Science*, 35(7):1808–1820.

Jain, M. and Ankjærgaard, C. (2011). Towards a non-fading signal in feldspar: Insight into charge transport and tunnelling from time-resolved optically stimulated luminescence. *Radiation Measurements*, 46(3):292–309.

Jolly, D., Prentice, I., Bonnefille, R., Ballouche, A., Bengo, M., Brenac, P., Buchet, G., Burney, D., Cazet, J.-P., Cheddadi, R., Edorh, T., Elenga, H., Elmoutaki, S., Guiot, J., Laarif, F., Lamb, H., Lezine, A.-M., Maley, J., Mbenza, M., Peyron, O., Reille, M., Reynaud-Farrera, I., Riollet, G.,

Ritchie, J., Roche, E., Scott, L., Ssemmanda, I., Straka, H., Umer, M., Van Campo, E., Vilimumbalo, S., Vincens, A., and Waller, M. (1998). Biome reconstruction from pollen and plant macrofossil data for Africa and the Arabian peninsula at 0 and 6000 years. *Journal of Biogeography*, 25(6):1007–1027.

Jouzel, J., Masson-Delmotte, V., Cattani, O., Dreyfus, G., Falourd, S., Hoffmann, G., Minster, B., Nouet, J., Barnola, J. M., Chappellaz, J., Fischer, H., Gallet, J. C., Johnsen, S., Leuenberger, M., Loulergue, L., Luethi, D., Oerter, H., Parrenin, F., Raisbeck, G., Raynaud, D., Schilt, A., Schwander, J., Selmo, E., Souchez, R., Spahni, R., Stauffer, B., Steffensen, J. P., Stenni, B., Stocker, T. F., Tison, J. L., Werner, M., and Wolff, E. W. (2007). Orbital and millennial Antarctic climate variability over the past 800,000 years. *Science*, 317(5839):793–796.

Kars, R. H., Busschers, F. S., and Wallinga, J. (2012). Validating post IR-IRSL dating on K-feldspars through comparison with quartz OSL ages. *Quaternary Geochronology*, 12:74–86.

Kars, R. H. and Wallinga, J. (2009). IRSL dating of K-feldspars: Modelling natural dose response curves to deal with anomalous fading and trap competition. *Radiation Measurements*, 44(5-6):594–599.

Kars, R. H., Wallinga, J., and Cohen, K. M. (2008). A new approach towards anomalous fading correction for feldspar IRSL dating tests on samples in field saturation. *Radiation Measurements*, 43(2-6):786–790.

Keay-Bright, J. and Boardman, J. (2009). Evidence from field-based studies of rates of soil erosion on degraded land in the central Karoo. *Geomorphology*, 103(3):455–465.

Keen-Zebert, A., Tooth, S., Rodnight, H., Duller, G. A. T., Roberts, H. M., and Grenfell, M. (2013). Late Quaternary floodplain reworking and the preservation of alluvial sedimentary archives in unconfined and confined river valleys in the eastern interior of South Africa. *Geomorphology*, 185:54–66.

Kendall, G. (2000). *The Maandagshoek alluvial fan: a cyclical history of erosion, sedimentation and pedogenesis*. BSc Honours thesis, University of the Witwatersrand.

Kim, J., Roberts, H., Duller, G., Lee, Y., and Yi, S. (2009). Assessment of diagnostic tests for evaluating the reliability of SAR De values from polymineral and quartz fine grains. *Radiation Measurements*, 44(2):149–157.

Kolstrup, E. and Mejdahl, V. (1986). Three frost wedge casts from Jutland (Denmark) and TL dating of their infill. *Boreas*, 15(4):311–321.

Kreutzer, S., Schmidt, C., DeWitt, R., and Fuchs, M. (2014). The a-value of polymineral fine grain samples measured with the post-IR IRSL protocol. *Radiation Measurements*, 69:18–29.

Lai, Z. (2010). Chronology and the upper dating limit for loess samples from Luochuan section in the Chinese Loess Plateau using quartz OSL SAR protocol. *Journal of Asian Earth Sciences*, 37(2):176–185.

Lai, Z., Brückner, H., Fülling, A., and Zöller, L. (2008). Effects of thermal treatment on the growth curve shape for OSL of quartz extracted from Chinese loess. *Radiation Measurements*, 43(26):763–766.

Lamothe, M. and Auclair, M. (2000). The fadia method: a new approach in luminescence dating using the analysis of single feldspar grains. *Radiation Measurements*, 32(5-6):433–438.

Lamothe, M., Auclair, M., Hamzaoui, C., and Huot, S. (2003). Towards a prediction of long-term anomalous fading of feldspar IRSL. *Radiation Measurements*, 37(4-5):493–498.

Lamothe, M., Balescu, S., and Auclair, M. (1994). Natural IRSL intensities and apparent luminescence ages of single feldspar grains extracted from partially bleached sediments. *Radiation Measurements*, 23(2-3):555–561.

Lamothe, M., Barr, M., Huot, S., and Ouimet, S. (2012). Natural luminescence and anomalous fading in K-feldspar. *Radiation Measurements*, 47(9):682–687.

Li, B., Jacobs, Z., Roberts, R., and Li, S.-H. (2014). Review and assessment of the potential of post-IR IRSL dating methods to circumvent the problem of anomalous fading in feldspar luminescence. *Geochronometria*, 41:178–201.

Li, B., Jacobs, Z., Roberts, R. G., and Li, S.-H. (2013). Extending the age limit of luminescence dating using the dose-dependent sensitivity of MET-pIRIR signals from K-feldspar. *Quaternary Geochronology*, 17:55–67.

Li, B. and Li, S.-H. (2008). Investigations of the dose-dependent anomalous fading rate of feldspar from sediments. *Journal of Physics D: Applied Physics*, 41(22):F02026.

Liritzis, I., Singhvi, A. K., Feathers, J., Wagner, G. A., Kadereit, A., Zacharias, N., and Li, S.-H. (2013). *Luminescence dating in archaeology,*

anthropology, and geoarchaeology: An overview. SpringerBriefs in Earth System Science. Springer Science and Business.

Løvborg, L. and Kirke (1974). Response of 3" x 3" NaI(TL) detectors to terrestrial gamma radiation. *Nuclear Instruments and Methods*, 121:239–251.

Lowick, S. E. and Preusser, F. (2011). Investigating age underestimation in the high dose region of optically stimulated luminescence using fine grain quartz. *Quaternary Geochronology*, 6(1):33–41.

Lowick, S. E., Preusser, F., Pini, R., and Ravazzi, C. (2010a). Underestimation of fine grain quartz OSL dating towards the Eemian: Comparison with palynostratigraphy from Azzano Decimo, northeastern Italy. *Quaternary Geochronology*, 5(5):583–590.

Lowick, S. E., Preusser, F., and Wintle, A. G. (2010b). Investigating quartz optically stimulated luminescence dose - response curves at high doses. *Radiation Measurements*, 45(9):975–984.

Lowick, S. E., Trauerstein, M., and Preusser, F. (2012). Testing the application of post IR-IRSL dating to fine grain waterlain sediments. *Quaternary Geochronology*, 8:33–40.

Lynch, S. (2004). Development of a raster database of annual, monthly and daily rainfall for southern Africa. Technical Report WRC Report No. 1156/1/04, Water Research Commission.

Lyons, R. (2012). *Chronology and controls of Late Quaternary sedimentation, pedogenesis and erosion across interior South Africa*. PhD thesis, Aberystwyth University.

Lyons, R., Tooth, S., and Duller, G. (2013). Chronology and controls of donga (gully) formation in the upper Blood River catchment, KwaZulu-Natal, South Africa: Evidence for a climatic driver of erosion. *The Holocene*, 23(12):1875–1887.

Lyons, R., Tooth, S., and Duller, G. A. T. (2014). Late Quaternary climatic changes revealed by luminescence dating, mineral magnetism and diffuse reflectance spectroscopy of river terrace palaeosols: a new form of geoproxy data for the southern African interior. *Quaternary Science Reviews*, 95:43–59.

Madsen, A. T., Buylaert, J.-P., and Murray, A. S. (2011). Luminescence dating of young coastal deposits from New Zealand using feldspar. *Geochronometria*, 38(4):379–390.

Madsen, A. T. and Murray, A. S. (2009). Optically stimulated luminescence dating of young sediments: A review. *Geomorphology*, 109(1-2):3–16.

Maggs, T. (1974). *Early framing communities on the southern Highveld: a study of Iron Age settlement*. PhD thesis, University of Cape Town.

Mararakanye, N. and Le Roux, J. (2012). Gully location mapping at a national scale for South Africa. *South African Geographical Journal*, 94(2):208–218.

Marean, C. (2010). Pinnacle Point Cave 13B (Western Cape Province, South Afirca) in context: The Cape Floral kingdom, shellfish, and modern human origins. *Journal of Human Evolution*, 59:425443.

Mason, R. (1973). Iron Age research in the western Transvaal, South Africa. *Current Anthropology*, 14:485–487.

Mason, R. (1974). Background to the Transvaal Iron Age new discoveries at Olifantspoort and Broederstroom. *Journal of the South African Institute of Mining and Metallurgy*, 74:211–216.

Mason, R. and van der Merwe, N. (1974). Radiocarbon dating of Iron Age sites in the southern Transvaal: Melville Koppies and Uitkomst Cave. *South African Journal of Science*, 60:142.

Mayewski, P. A., Rohling, E. E., Curt Stager, J., Karlén, W., Maasch, K. A., David Meeker, L., Meyerson, E. A., Gasse, F., van Kreveld, S., Holmgren, K., Lee-Thorp, J., Rosqvist, G., Rack, F., Staubwasser, M., Schneider, R. R., and Steig, E. J. (2004). Holocene climate variability. *Quaternary Research*, 62(3):243–255.

Meadows, M. (2001). The role of Quaternary environmental change in the evolution of landscapes: case studies from southern Africa. *Catena*, 42:39–57.

Meadows, M. E. and Finch, J. M. (2016). The history and development of Quaternary Science in South Africa. *South African Geographical Journal*, 98(3):472–482.

Medialdea, A., Thomsen, K. J., Murray, A. S., and Benito, G. (2014). Reliability of equivalent-dose determination and age-models in the OSL dating of historical and modern palaeoflood sediments. *Quaternary Geochronology*, 22:11–24.

Mejdahl, V. (1979). Thermoluminescence dating: beta-dose attenuation in quartz grains. *Archaeometry*, 21(1):61–72.

Mejdahl, V. (1983). Feldspar inclusion dating of ceramics and burnt stones. *PACT*, 9:351–364.

Mejdahl, V. (1987). Internal radioactivity in quartz and feldspar grains. *Ancient TL*, 5(2):10–17.

Mercier, N. and Falgures, C. (2007). Field gamma dose-rate measurement with a NaI(Tl) detector: re-evaluation of the 'threshold' technique. *Ancient TL*, 25(1):1–4.

Mikutta, R., Kleber, M., Kaiser, K., and Jahn, R. (2005). Review: Organic Matter Removal from Soils using Hydrogen Peroxide, Sodium Hypochlorite, and Disodium Peroxodisulfate. *Soil Science Society of America Journal*, 69:120–135.

Mucina, L. and Rutherford, M. (2006). *The Vegetation of South Africa, Lesotho and Swaziland. Strelitzia 19*. South African National Biodiversity Institute.

Murray, A., Bowman, S., and Aitken, M. (1978). Evaluation of the gamma dose rate contribution. *PACT*, 2:84–96.

Murray, A., Buylaert, J.-P., Henriksen, M., Svendsen, J.-I., and Mangerud, J. (2008). Testing the reliability of quartz OSL ages beyond the Eemian. *Radiation Measurements*, 43(2-6):776–780.

Murray, A. S. and Funder, S. (2003). Optically stimulated luminescence dating of a Danish Eemian coastal marine deposit: a test of accuracy. *Quaternary Science Reviews*, 22(10-13):1177–1183.

Murray, A. S. and Roberts, R. G. (1997). Determining the burial time of single grains of quartz using optically stimulated luminescence. *Earth and Planetary Science Letters*, 152(1-4):163–180.

Murray, A. S., Svendsen, J. I., Mangerud, J., and Astakhov, V. I. (2007). Testing the accuracy of quartz OSL dating using a known-age Eemian site on the river Sula, northern Russia. *Quaternary Geochronology*, 2(1-4):102–109.

Murray, A. S., Thomsen, K. J., Masuda, N., Buylaert, J. P., and Jain, M. (2012). Identifying well-bleached quartz using the different bleaching rates of quartz and feldspar luminescence signals. *Radiation Measurements*, 47(9):688–695.

Murray, A. S. and Wintle, A. G. (2000). Luminescence dating of quartz using an improved single-aliquot regenerative-dose protocol. *Radiation Measurements*, 32(1):57–73.

Nathan, R. P. and Mauz, B. (2008). On the dose-rate estimate of carbonate-rich sediments for trapped charge dating. *Radiation Measurements*, 43(1):14–25.

Neudorf, C. M., Roberts, R. G., and Jacobs, Z. (2012). Sources of overdispersion in a K-rich feldspar sample from north-central India: Insights from De, K content and IRSL age distributions for individual grains. *Radiation Measurements*, 47(9):696–702.

Neumann, F. H., Scott, L., Bousman, C. B., and van As, L. (2010). A Holocene sequence of vegetation change at Lake Eteza, coastal KwaZulu-

Natal, South Africa. *Review of Palaeobotany and Palynology*, 162(1):39–53.

Nian, X., Bailey, R. M., and Zhou, L. (2012). Investigations of the post-IR IRSL protocol applied to single K-feldspar grains from fluvial sediment samples. *Radiation Measurements*, 47(9):703–709.

Nielsen, A., Murray, A. S., Pejrup, M., and Elberling, B. (2006). Optically stimulated luminescence dating of a Holocene beach ridge plain in Northern Jutland, Denmark. *Quaternary Geochronology*, 1(4):305–312.

Olley, J. M., Caitcheon, G., and Murray, A. (1998). The distribution of apparent dose as determined by Optically Stimulated Luminescence in small aliquots of fluvial quartz: Implications for dating young sediments. *Quaternary Geochronology*, 17(11):1033–1040.

Olley, J. M., De Deckker, P., Roberts, R. G., Fifield, L., Yoshida, H., and Hancock, G. J. (2004a). Optical dating of deep-sea sediments using single grains of quartz: a comparison with radiocarbon. *Sedimentary Geology*, 169:175–189.

Olley, J. M., Pietsch, T., and Roberts, R. G. (2004b). Optical dating of Holocene sediments from a variety of geomorphic settings using single grains of quartz. *Geomorphology*, 60(3-4):337–358.

Oluwole, F. and Sikhalazo, D. (2008). Land degradation evaluation in a game reserve in Eastern Cape of South Africa: soil properties and vegetation cover. *Scientific Research and Essay*, 3(3):111–119.

Ou, X., Duller, G. A. T., Roberts, H. M., Zhou, S., Lai, Z., Chen, R., Chen, R., and Zeng, L. (2015). Single grain optically stimulated luminescence

dating of glacial sediments from the Baiyu Valley, southeastern Tibet. *Quaternary Geochronology*, 30, Part B:314–319.

Parish, R. (1994). The influence of feldspar weathering on luminescence signals and the implications for luminescence dating of sediments. In Robinson, D. and Williams, R., editors, *Rock weathering and landform evolution*, chapter 15, pages 243–258. Wiley.

Partridge, T. C., Demenocal, P. B., Lorentz, S. A., Paiker, M. J., and Vogel, J. C. (1997). Orbital forcing of climate over South Africa: A 200,000-year rainfall record from the pretoria saltpan. *Quaternary Science Reviews*, 16(10):1125–1133.

Pawley, S. M., Bailey, R. M., Rose, J., Moorlock, B. S., Hamblin, R. J., Booth, S. J., and Lee, J. R. (2008). Age limits on Middle Pleistocene glacial sediments from OSL dating, north Norfolk, UK. *Quaternary Science Reviews*, 27(1314):1363–1377.

Poolton, H. R. J., Ozanyan, K. B., Wallinga, J., Murray, A. S., and Bøtter-Jensen, L. (2002a). Electrons in feldspar II: A consideration of the influence of conduction band-tail states on luminescence processes. *Physics and Chemistry of Minerals*, 29(3):217–225.

Poolton, N. R. J., Wallinga, J., Murray, A. S., Bulur, E., and Bøtter-Jensen, L. (2002b). Electrons in feldspar I: on the wavefunction of electrons trapped at simple lattice defects. *Physics and Chemistry of Minerals*, 29(3):210–216.

Porat, N., Chazan, M., Grün, R., Aubert, M., Eisenmann, V., and Horwitz, L. K. (2010). New radiometric ages for the Fauresmith industry from

Kathu Pan, southern Africa: Implications for the Earlier to Middle Stone Age transition. *Journal of Archaeological Science*, 37(2):269–283.

Prescott, J. R. and Hutton, J. T. (1988). Cosmic ray and gamma ray dosimetry for TL and ESR. *International Journal of Radiation Applications and Instrumentation. Part D. Nuclear Tracks and Radiation Measurements*, 14(12):223–227.

Prescott, J. R. and Hutton, J. T. (1994). Cosmic ray contributions to dose rates for luminescence and ESR dating: Large depths and long-term time variations. *Radiation Measurements*, 23(23):497–500.

Prescott, J. R. and Robertson, G. B. (1997). Sediment dating by luminescence: a review. *Radiation Measurements*, 27(5-6):893–922.

Preusser, F., Chithambo, M. L., Götte, T., Martini, M., Ramseyer, K., Sendezera, E. J., Susino, G. J., and Wintle, A. G. (2009). Quartz as a natural luminescence dosimeter. *Earth-Science Reviews*, 97(1-4):184–214.

Preusser, F., Degering, D., Fuchs, M., Hilgers, A., Kadereit, A., Klasen, N., Krbetschek, M. R., Richter, D., and Spencer, J. Q. G. (2008). Luminescence dating: basics, methods and applications. *Quaternary Science Journal*, 57(1-2):95–149.

Qin, J. T. and Zhou, L. P. (2012). Effects of thermally transferred signals in the post-IR IRSL SAR protocol. *Radiation Measurements*, 47(9):710–715.

Reimann, T., Thomsen, K. J., Jain, M., Murray, A. S., and Frechen, M. (2012). Single-grain dating of young sediments using the pIRIR signal from feldspar. *Quaternary Geochronology*, 11:28–41.

Reimann, T. and Tsukamoto, S. (2012). Dating the recent past (<500 years) by post-IR IRSL feldspar - Examples from the North Sea and Baltic Sea coast. *Quaternary Geochronology*, 10:180–187.

Reimann, T., Tsukamoto, S., Naumann, M., and Frechen, M. (2011). The potential of using K-rich feldspars for optical dating of young coastal sediments - A test case from Darss-Zingst peninsula (southern Baltic Sea coast). *Quaternary Geochronology*, 6(2):207–222.

Rhodes, E. J. (2015). Dating sediments using potassium feldspar single-grain IRSL: Initial methodological considerations. *Quaternary International*, 362:14–22.

Rhodes, E. J. and Schwenninger, J. (2007). Dose rates and radioisotope concentrations in the concrete calibration blocks at Oxford. *Ancient TL*, 25(1):5–8.

Rienks, S. M., Botha, G. A., and Hughes, J. C. (2000). Some physical and chemical properties of sediments exposed in a gully (donga) in northern KwaZulu-Natal, South Africa and their relationship to the erodibility of the colluvial layers. *Catena*, 39(1):11–31.

Rittenour, T. M. (2008). Luminescence dating of fluvial deposits: applications to geomorphic, palaeoseismic and archaeological research. *Boreas*, 37(4):613–635.

Roberts, H. M. and Duller, G. A. T. (2004). Standardised growth curves for optical dating of sediment using multiple-grain aliquots. *Radiation Measurements*, 38(2):241–252.

Roberts, H. M., Durcan, J. A., and Duller, G. A. (2009). Exploring procedures for the rapid assessment of optically stimulated luminescence range-finder ages. *Radiation Measurements*, 44(56):582–587.

Roberts, R. G., Galbraith, R. F., Olley, J. M., Yoshida, H., and Laslett, G. M. (1999). Optical dating of single and multiple grains of quartz from Jinmium rock shelter, northern Australia: Part II, results and implications. *Archaeometry*, 41(2):365–395.

Rodnight, H. (2006). *Developing a luminescence chronology for late Quaternary fluvial change in South African floodplain wetlands*. PhD thesis, Univeristy of Wales, Aberystwyth.

Rodnight, H., Duller, G., Wintle, A., and Tooth, S. (2006). Assessing the reproducibility and accuracy of optical dating of fluvial deposits. *Quaternary Geochronology*, 1(2):109–120.

Rodnight, H., Duller, G. A., Tooth, S., and Wintle, A. G. (2005). Optical dating of a scroll-bar sequence on the Klip River, South Africa, to derive the lateral migration rate of a meander bend. *The Holocene*, 15(6):802–811.

Roskosch, J., Tsukamoto, S., Meinsen, J., Frechen, M., and Winsemann, J. (2012). Luminescence dating of an Upper Pleistocene alluvial fan and aeolian sandsheet complex: The Senne in the Münsterland Embayment, NW Germany. *Quaternary Geochronology*, 10:94–101.

Russell, N. J. and Armitage, S. J. (2012). A comparison of single-grain and small aliquot dating of fine sand from Cyrenaica, northern Libya. *Quaternary Geochronology*, 10:62–67.

Schulze, R. (1997). *South African Atlas of Agrohydrology and Climatology*. University of Natal.

Scott, L. (1989). Climatic conditions in Southern Africa since the last glacial maximum, inferred from pollen analysis. *Palaeogeography, Palaeoclimatology, Palaeoecology*, 70(4):345–353.

Scott, L. (1996). Palynology of hyrax middens: 2000 years of palaeo-environmental history in Namibia. *Quaternary International*, 33:73–79.

Scott, L. (1999). Vegetation history and climate in the Savanna biome South Africa since 190,000 ka: a comparison of pollen data from the Tswaing Crater (the Pretoria Saltpan) and Wonderkrater. *Quaternary International*, 57-58:215–223.

Scott, L., Neumann, F. H., Brook, G. A., Bousman, C. B., Norstrm, E., and Metwally, A. A. (2012). Terrestrial fossil-pollen evidence of climate change during the last 26 thousand years in Southern Africa. *Quaternary Science Reviews*, 32:100–118.

Shen, H., Yu, L., Zhang, H., Zhao, M., and Lai, Z. (2015). OSL and radiocarbon dating of flood deposits and its paleoclimatic and archaeological implications in the Yihe River Basin, East China. *Quaternary Geochronology*, 30, Part B:398–404.

Singhvi, A. K. and Porat, N. (2008). Impact of luminescence dating on geomorphological and palaeoclimate research in drylands. *Boreas*, 37(4):536–558.

Smedley, R., Glasser, N., and Duller, G. (2016). Luminescence dating of glacial advances at Lago Buenos Aires (~46 °S), Patagonia. *Quaternary Science Reviews*, 134:59–73.

Smedley, R. and Pearce, N. J. G. (2016). Internal U, Th and Rb concentrations of alkali-feldspar grains: Implications for luminescence dating. *Quaternary Geochronology*, 35:16–25.

Smedley, R. K. and Duller, G. A. T. (2013). Optimising the reproducibility of measurements of the post-IR IRSL signal from single-grains of K-feldspar for dating. *Ancient TL*, 31(2):49–58.

Smedley, R. K., Duller, G. A. T., Pearce, N. J. G., and Roberts, H. M. (2012). Determining the K-content of single-grains of feldspar for luminescence dating. *Radiation Measurements*, 47(9):790–796.

Smith, A. M. (1992). Holocene palaeoclimatic trends from palaeoflood analysis. *Palaeogeography, Palaeoclimatology, Palaeoecology*, 97(3):235–240.

Smith, B., Aitken, M., Rhodes, E., Robinson, P., and Geldard, D. (1986). Optical Dating: Methodological Aspects. *Radiation Protection Dosimetry*, 17(1-4):229–233.

Smith, B. W. (1988). Zircon from sediments: A combined OSL and TL auto-regenerative dating technique. *Quaternary Science Reviews*, 7(3-4):401–406.

Sohbati, R., Murray, A. S., Buylaert, J.-P., Ortuño, M., Cunha, P. P., and Masana, E. (2012). Luminescence dating of Pleistocene alluvial sediments affected by the Alhama de Murcia fault (eastern Betics, Spain)

- a comparison between OSL, IRSL and post-IR IRSL ages. *Boreas*, 41(2):250–262.

Sonneveld, M., Everson, T., and Veldkamp, A. (2005). Multi-scale analysis of soil erosion dynamics in Kwazulu-Natal, South Africa. *Land Degradation and Development*, 16:287–301.

Spooner, N. A. (1994). The anomalous fading of infrared-stimulated luminescence from feldspars. *Radiation Measurements*, 23(2-3):625–632.

Srivastava, P. and Misra, D. K. (2012). Optically stimulated luminescence chronology of terrace sediments of Siang River, Higher NE Himalaya: Comparison of Quartz and Feldspar chronometers. *Journal of the Geological Society of India*, 79(3):252–258.

Stirling, R. J., Duller, G. A. T., and Roberts, H. M. (2012). Developing a single-aliquot protocol for measuring equivalent dose in biogenic carbonates. *Radiation Measurements*, 47(9):725–731.

Stokes, S., Colls, A., Fattahi, M., and Rich, J. (2000). Investigations of the performance of quartz single aliquot D_E determination procedures . *Radiation Measurements*, 32(56):585–594.

Telfer, M. and Thomas, D. (2006). Complex Holocene lunette dune development, South Africa: Implications for paleoclimate and models of pan development in arid regions. *Geology*, 34(10):853–856.

Temme, A. J. A. M., Baartman, J. E. M., Botha, G. A., Veldkamp, A., Jongmans, A. G., and Wallinga, J. (2008). Climate controls on late Pleistocene landscape evolution of the Okhombe valley, KwaZulu-Natal, South Africa. *Geomorphology*, 99(1-4):280–295.

Thiel, C., Buylaert, J.-P., Murray, A., Terhorst, B., Hofer, I., Tsukamoto, S., and Frechen, M. (2011). Luminescence dating of the Stratzing loess profile (Austria) - Testing the potential of an elevated temperature post-IR IRSL protocol. *Quaternary International*, 234(1-2):23–31.

Thiel, C., Buylaert, J.-P., Murray, A. S., Elmejdoub, N., and Jedoui, Y. (2012). A comparison of TT-OSL and post-IR IRSL dating of coastal deposits on Cap Bon peninsula, north-eastern Tunisia. *Quaternary Geochronology*, 10:209–217.

Thiel, C., Coltorti, M., Tsukamoto, S., and Frechen, M. (2010). Geochronology for some key sites along the coast of Sardinia (Italy). *Quaternary International*, 222(1-2):36–47.

Thomas, D. S. G. and Burrough, S. L. (2012). Interpreting geoproxies of late Quaternary climate change in African drylands: Implications for understanding environmental change and early human behaviour. *Quaternary International*, 253:5–17.

Thomas, D. S. G. and Shaw, P. A. (2002). Late Quaternary environmental change in central southern Africa: new data, synthesis, issues and prospects. *Quaternary Science Reviews*, 21(7):783–797.

Thomas, P. J., Jain, M., Juyal, N., and Singhvi, A. K. (2005). Comparison of single-grain and small-aliquot OSL dose estimates in years old river sediments from South India. *Radiation Measurements*, 39(5):457–469.

Thomsen, K. J., Jain, M., Bøtter-Jensen, L., Murray, A. S., and Jungner, H. (2003). Variation with depth of dose distributions in single grains of quartz

extracted from an irradiated concrete block. *Radiation Measurements*, 37(4-5):315–321.

Thomsen, K. J., Murray, A. S., Bøtter-Jensen, L., and Kinahan, J. (2007). Determination of burial dose in incompletely bleached fluvial samples using single grains of quartz. *Radiation Measurements*, 42(3):370–379.

Thomsen, K. J., Murray, A. S., Buylaert, J. P., Jain, M., Hansen, J. H., and Aubry, T. (2016). Testing single-grain quartz OSL methods using sediment samples with independent age control from the Bordes-Fitte rockshelter (Roches d'Abilly site, Central France). *Quaternary Geochronology*, 31:77–96.

Thomsen, K. J., Murray, A. S., Jain, M., and Bøtter-Jensen, L. (2008). Laboratory fading rates of various luminescence signals from feldspar-rich sediment extracts. *Radiation Measurements*, 43(9-10):1474–1486.

Timar, A., Vandenberghe, D., Panaiotu, E., Panaiotu, C., Necula, C., Cosma, C., and van den haute, P. (2010). Optical dating of Romanian loess using fine-grained quartz. *Quaternary Geochronology*, 5(23):143–148.

Timar-Gabor, A., Vasiliniuc, S., Vandenberghe, D. A. G., Cosma, C., and Wintle, A. G. (2012). Investigations into the reliability of SAR-OSL equivalent doses obtained for quartz samples displaying dose response curves with more than one component. *Radiation Measurements*, 47(9):740–745.

Tooth, S. (2015). Luminescence, geomorphological processes. In Rink, W. and Thompson, J., editors, *Encyclopedia of Scientific Dating Methods*, pages 470–475. Springer.

Tooth, S., Brandt, D., Hancox, P. J., and McCarthy, T. S. (2004). Geological controls on alluvial river behaviour: a comparative study of three rivers on the South African Highveld. *Journal of African Earth Sciences*, 38(1):79–97.

Tooth, S., Hancox, P. J., Brandt, D., McCarthy, T. S., Jacobs, Z., and Woodborne, S. (2013). Controls On the genesis, sedimentary architecture, and preservation potential of dryland alluvial successions in stable continental interiors: Insights from the incising Modder River, South Africa. *Journal of Sedimentary Research*, 83(7):541–561.

Tooth, S., McCarthy, T. S., Brandt, D., Hancox, P. J., and Morris, R. (2002). Geological controls on the formation of alluvial meanders and floodplain wetlands: the example of the Klip River, eastern Free State, South Africa. *Earth Surface Processes and Landforms*, 27(8):797–815.

Tooth, S., Rodnight, H., Duller, G., McCarthy, T., Marren, P., and Brandt, D. (2007). Chronology and controls of avulsion along a mixed bedrock-alluvial river. *Geological Society of America Bulletin*, 119(3-4):452–461.

Trauerstein, M., Lowick, S. E., Preusser, F., and Schlunegger, F. (2014). Small aliquot and single grain IRSL and post-IR IRSL dating of fluvial and alluvial sediments from the Pativilca valley, Peru. *Quaternary Geochronology*, 22:163–174.

Truc, L., Chevalier, M., Favier, C., Cheddadi, R., Meadows, M. E., Scott, L., Carr, A. S., Smith, G. F., and Chase, B. M. (2013). Quantification of climate change for the last 20,000 years from Wonderkrater, South Africa: Implications for the long-term dynamics of the Intertropical Convergence Zone. *Palaeogeography, Palaeoclimatology, Palaeoecology*, 386:575–587.

Tyson, P., Karlen, W., Holmgren, K., and Heiss, G. (2000). The Little Ice Age and medieval warming in South Africa. *South African Journal of Science*, 96:121–126.

Tyson, P., Lee-Thorp, J., Holmgren, K., and Thackeray, J. (2002). Changing gradients of climate change in southern Africa during the past millenium: implications for population movements. *Climatic change*, 52:129–135.

Verster, E. and van Rooyen, T. H. (1999). Palaeosols on a fluvial terrace at Driekop, Northern Province, South Africa as indicators of climatic changes during the Late Quaternary. *Quaternary International*, 57-58:229–235.

Vogel, J. and Fuls, A. (1999). Spatial distribution of radiocarbon dates for the Iron Age in southern Africa. *South African Archeological Bulletin*, 54:97–101.

Walker, M. (2005). *Quaternary Dating Methods*. J. Wiley.

Wallinga, J. (2002a). On the detection of OSL age overestimation using single-aliquot techniques. *Geochronometria*, 21:17–26.

Wallinga, J. (2002b). Optically stimulated luminescence dating of fluvial deposits: a review. *Boreas*, 31(4):303–322.

Wallinga, J., Murray, A. S., Duller, G. A. T., and Törnqvist, T. E. (2001). Testing optically stimulated luminescence dating of sand-sized quartz and feldspar from fluvial deposits. *Earth and Planetary Science Letters*, 193(3-4):617–630.

Wang, Y., Cheng, H., Edwards, R., Kong, X., Shao, X., Chen, S., Wu, J., Jiang, X., Wang, X., and An, Z. (2008). Millennial- and orbital-scale

changes in the East Asian monsoon over the past 224,000 years. *Nature*, 451:1090–1093.

Wang, Y. J., Cheng, H., Edwards, R., An, Z., Wu, J., Shen, C.-C., and Dorale, J. (2001). A high-resolution absolute-dated late pleistocene monsoon record from Hulu Cave, China. *Science*, 294:2345–2348.

Warren, S. E. (1978). Thermoluminescence dating of pottery: an assessment of the dose-rate from Rubidium. *Archaeometry*, 20(1):71–72.

Watanuki, T., Murray, A. S., and Tsukamoto, S. (2005). Quartz and polymineral luminescence dating of Japanese loess over the last 0.6 Ma: comparison with an independent chronology. *Earth and Planetary Science Letters*, 240:774–789.

Watson, A., Price-Williams, D., and Goudie, A. (1984). The palaeoenvironmental interpretation of colluvial sediments and palaeosols of the late Pleistocene hypothermal in southern Africa. *Palaeogeography, Palaeoclimatology, Palaeoecology*, 45:225–249.

Wessels, K., Prince, S., Malherbe, J., Small, J., Frost, P., and Zyl, D. V. (2007). Can human-induced land degradation be distinguished from the effects of rainfall variability? A case study in South Africa. *Journal of Arid Environments*, 68(2):271–297.

Wintle, A., Botha, G. A., Li, S. H., and Vogel, J. C. (1995a). A chronological framework for colluviation during the last 110kyr in Kwazulu/Natal. *South African Journal of Science*, 91:134–139.

Wintle, A., Li, S., Botha, G., and Vogel, J. (1995b). Evaluation of luminescence-dating procedures applied to late-Holocene colluvium near St Paul's Mission, Natal, South Africa. *The Holocene*, 5(1):97–102.

Wintle, A., Li, S. H., and Botha, G. A. (1993). Luminescence dating of colluvial deposits from Natal, South Africa. *South African Journal of Science*, 89(2):77–82.

Wintle, A. G. (1973). Anomalous Fading of Thermo-luminescence in Mineral Samples. *Nature*, 245(5421):143–144.

Wintle, A. G. (1997). Luminescence dating: laboratory procedures and protocols. *Radiation Measurements*, 27(56):769–817.

Wintle, A. G. (2008). Luminescence dating: where it has been and where it is going. *Boreas*, 37(4):471–482.

Wintle, A. G. and Murray, A. S. (2006). A review of quartz optically stimulated luminescence characteristics and their relevance in single-aliquot regeneration dating protocols. *Radiation Measurements*, 41(4):369–391.

Woodborne, S., Hall, G., Robertson, I., Patrut, A., Rouault, M., Loader, N. J., and Hofmeyer, M. (2015). 1000-Year Carbon Isotope Rainfall Proxy Record from South African Baobab Trees (Adansonia digitata L.). *PLoS ONE*, 10(5):e0124202.

Yi, S., Buylaert, J.-P., Murray, A. S., Lu, H., Thiel, C., and Zeng, L. (2016). A detailed post-IR IRSL dating study of the Niuyangzigou loess site in northeastern China. *Boreas*, pages 1–14.

Yi, S., Buylaert, J.-P., Murray, A. S., Thiel, C., Zeng, L., and Lu, H. (2015). High resolution OSL and post-IR IRSL dating of the last interglacial-glacial cycle at the Sanbahuo loess site (northeastern China). *Quaternary Geochronology*, 30, Part B:200–206.

Zhao, H., Li, S.-H., and Murray, A. S. (2003). Comparison of SAAD and SAR procedures for equivalent dose determination using quartz. *Radiation Measurements*, 37(4-5):417–424.

Ziegler, M., Simon, M. H., Hall, I. R., Barker, S., Stringer, C., and Zahn, R. (2013). Development of Middle Stone Age innovation linked to rapid climate change. *Nature Communications*, 4:1905.

Zimmerman, D. W. (1971). Thermoluminescent dating using fine grains from pottery. *Archaeometry*, 13(1):29–52.